

Monoatomic Metal Doped Nanomaterials for Hydrogen Production and Storage

By

Chengguang Lang

BSc, MSc



School of Environment and Science

Queensland Micro- and Nanotechnology Centre

Griffith University

Submitted in fulfilment of the requirements of the degree of

Doctor of Philosophy

August 2022

Abstract

Hydrogen production and storage play a critical role in energy transformation from fossil fuels to green energy. To realize the carbon neutralization target by increasing the competitiveness of hydrogen as an energy vector, production and storage of hydrogen must be made more efficient, safer, and cheaper, which is essential for future energy security and economic development.

Water splitting via electrolysis holds great promise for hydrogen production, due to its simplicity, sustainability, and high purity for industrial hydrogen production. Recently, despite tremendous efforts have been devoted, platinum (Pt)-based catalysts are still considered to be the most effective electrocatalysts for hydrogen evolution reaction (HER). However, the high cost and low reserves of platinum-based catalysts greatly limit their commercial application. To make hydrogen derived from water splitting more cost-competitive, it is thus highly desirable to exploit low-cost, highly efficient electrocatalysts to replace the expensive Pt-based catalysts. Furthermore, after hydrogen production, the gaseous hydrogen needs to be stored safely and efficiently for utilization by end-users. The current mainstream methods of solid-state hydrogen storage including molecular physisorption and atomic chemisorption, both possess either too high or too low enthalpy of hydrogen adsorption, which are not suitable for practical application. The ideal hydrogen storage materials should be reversibly absorb/desorbing hydrogen under mild temperatures with high hydrogen capacities. To this end, it is extremely essential to design and construct new solid-state hydrogen storage materials at atomic levels. Recently, the atomic metal-site (AMS) nanomaterials are found to be promising catalysts and solid-state media for both the H_2 production and storage, which is not only ascribed to the maximized atomic metals utilization but also the unique electronic structure of various metal-site coordination motifs at atomic scales. The aim of this project is to develop efficient and inexpensive AMS nanomaterials that are expected to create new knowledge of atomic interface catalysis and develop

practical applications of solid-state hydrogen storage materials, reducing carbon dioxide emissions and alleviating the air pollution.

First of all, with respect to hydrogen evolution, we demonstrate a straightforward, eco-friendly, and scalable ball milling strategy for the synthesis of atomic Ru doped defective MoS₂ catalysts (denoted as Ru₁@D-MoS₂). The results indicate that single atom Ru doping induces the generation of S vacancies, which could break the symmetrical structures around the Ru atoms, resulting in an asymmetrical distribution of electron. Accordingly, the performance tests confirm that the Ru₁@D-MoS₂ exhibits superb HER performance, exceeding that of C-MoS₂ by a factor of 9. Furthermore, density functional theory (DFT) calculations unravel that the vacancy coupled single Ru can induce much higher asymmetry degree of electronic distribution, which could regulate the adsorption energy of intermediates, favoring the water dissociation and the adsorption/desorption of H*. In addition, the electronic structure of the Ru₁@MoS₂ is delicately tailored, effectively promoting the electrical conductivity of the catalyst.

Secondly, we use non-noble metal Co to replace Ru to directly modify the electrochemical performance of the commercial MoS₂ for hydrogen evolution. Through high-energy mechanochemical milling with CoO, the MoS₂ can expose more active sites due to the reduced size, abundant defects, and strain. Meanwhile, the isolated Co atoms are found to be decorated onto MoS₂ (verified by HADDF-STEM and XANE spectra), which can further engineer the inert basal planes of MoS₂ to make them electrochemically active. The optimal HER performance of Co_{0.4}O@MoS₂-0.4 reaches an overpotential of 94 mV at a current density of 10 mA cm⁻². This strategy provides an economic and viable route to the batch preparation of efficient MoS₂-based catalysts for industrial HER applications.

The atomic metal sites nanomaterials also possess great potential to be used for hydrogen storage as compared to the bulk metal counterparts. Herein, we propose a defect engineering technique to modulate the coordination structure of interfacial Ti atom for hydrogen storage. It is found that the uniquely unsaturated Ti atom can bind

H₂ molecules via molecular chemisorption fashion. Differing from the weak Van der Waals force and strong chemical bonding, the molecular chemisorption involves a strong electronic interaction between Ti atom and molecular H₂. Combined with the DFT analysis, it is revealed that the binding energy of H₂ for four-coordinates Ti atom is determined to be 0.3 eV, which is evidently larger than that of the five-coordinates Ti atom (0.18 eV). Besides, the hydrogen adsorbed remains the molecule form readily facilitating the hydrogen desorption, while high temperature is required for titanium hydride.

To further increase the density of atomic metal site for hydrogen storage, we select the lightweight carbon-based material as the support to construct the atomic metal decorated solid-state hydrogen storage material. It is found that the atomic Ti doped carbon black (CB) nanomaterials exhibit increased hydrogen adsorption capacity as compared to the pure CB. Meanwhile, the adsorbed hydrogen remains stable near the room temperature, reflecting a molecular chemisorption fashion (weak chemisorption). Notably, charging or discharging hydrogen can be easily manipulated via simply increasing or decreasing the hydrogen pressure.

In summary, this thesis mainly focusses on designing and fabricating cost-effective, efficient, and scalable AMS nanomaterials for both hydrogen production and storage, and the reaction mechanisms of atomic metal sites in hydrogen production and storage are also systematically studied.

Statement of Originality

This work has not previously been submitted for a degree or diploma in any university. To the best of my knowledge and belief, the thesis contains no material previously published or written by another person except where due reference is made in the thesis itself.

Signature of Candidate

A solid black rectangular box used to redact the candidate's signature.

Chengguang Lang

ALL PAPERS INCLUDED ARE CO-AUTHORED

Acknowledgement of Papers included in this Thesis

Included in this thesis are papers in *Chapters 2 (2.3.3), 4, 5, 6 and 7* which are co-authored with other researchers. My contribution to each co-authored paper is outlined at the front of the relevant chapter. The bibliographic details and status for these papers including all authors, are:

Chapter 2:

Chengguang Lang, Yi Jia, Xuecheng Yan, Liuzhang Ouyang, Min Zhu, Xiangdong Yao, Molecular chemisorption: a new conceptual paradigm for hydrogen storage, *Chemical Synthesis*, 2022, 2, 1.

Chapter 4:

Chengguang Lang, Wenbin Jiang, Cheng-Jie Yang, Hao Zhong, Peirong Chen, Chung-Li Dong, Yue Lin, Xuecheng Yan, Liuzhang Ouyang, Yi Jia, Xiangdong Yao. Facile and Scalable Mechanochemical Synthesis of Defective MoS₂ with Single Atoms toward Highly Efficient Hydrogen Evolution (To be submitted)

Chapter 5:

Chengguang Lang, Lei Zhang, Cheng-Jie Yang, Hao Zhong, Peirong Chen, Chung-Li Dong, Jun Chen, Aijun Du, Xuecheng Yan, Liuzhang Ouyang, Yi Jia, Xiangdong Yao. Mechanochemical preparation of defective MoS₂ with Co and O co-doping for electrochemical hydrogen evolution. (To be submitted)

Chapter 6:

Chengguang Lang, Lei Zhang, Cheng-Jie Yang, Hao Zhong, Hanwu Dong, Chung-Li Dong, Aijun Du, Xuecheng Yan, Liuzhang Ouyang, Yi Jia, Xiangdong Yao. Crossover from physisorption to chemisorption: a rational design for H₂ storage. (To be submitted)

Chapter 7:

Chengguang Lang, Lei Zhang, Cheng-Jie Yang, Hao Zhong, Yue Lin, Chung-Li Dong, Aijun Du, Xuecheng Yan, Liuzhang Ouyang, Yi Jia, Xiangdong Yao. Isolated Ti atom grafting carbon material for advanced hydrogen storage. (To be submitted)

Appropriate acknowledgements of those who contributed to the research but did not qualify as authors are included in each paper.

(Signed) _____

(Date) 31/07/2022

Name of Student: Chengguang Lang

(Countersigned) _____

(Date) 31/07/2022

Supervisor: Xuecheng Yan

Table of Contents

Abstract.....	i
Statement of Originality	iv
Table of Contents	vi
List of Figures.....	ix
List of Abbreviations	xiv
List of Publications	xv
Acknowledgements	xvi
Chapter 1. Introduction.....	1
1.1 Background	2
1.2 Objectives	3
1.3 Structure of Thesis	4
1.4 References.....	5
Chapter 2. Literature Review	7
2.1 Hydrogen Production via Water Splitting.....	9
2.1.1 Hydrogen Evolution Reaction Mechanism.....	9
2.1.2 Metal-based Catalysts for HER	11
2.1.3 Metal-free Catalysts for HER	14
2.2 Hydrogen Storage	17
2.2.1 Hydrogen Storage Materials	17
2.2.2 Regulations of Thermodynamics and Kinetics	19
2.3 Atomic Metal-site (AMS) Nanomaterials.....	26
2.3.1 Advantages and Synthetic Strategies of AMS Nanomaterials.....	26
2.3.2 AMS Nanomaterials for Hydrogen Production	35
2.3.3 AMS Nanomaterials for Hydrogen Storage.....	37
2.4 Conclusions.....	42
2.5 References.....	43
Chapter 3. Experimental Methodologies	57
3.1 Materials	58

3.2 Synthesis of Samples	58
3.3 Characterization	59
3.4 Electrochemical Performance Evaluation.....	61
3.5 Hydrogen Storage Performance Test.....	62
3.6 DFT Calculations	62
3.7 References.....	64
Chapter 4. Facile and Scalable Mechanochemical Synthesis of Defective MoS₂ with Single Atoms toward Highly Efficient Hydrogen Evolution	65
4.1 Introduction.....	67
4.2 Results and discussion	69
4.3 Conclusions.....	79
4.4 References.....	79
4.5 Supporting Information.....	84
Chapter 5. Mechanochemical preparation of defective MoS₂ with Co and O co-doping for electrochemical hydrogen evolution	98
5.1 Introduction.....	100
5.2 Results and discussion	102
5.3 Conclusions.....	112
5.4 References.....	112
5.5 Supporting Information.....	117
Chapter 6. Crossover from physisorption to chemisorption: a rational design for H₂ storage.....	128
6.1 Introduction.....	130
6.2 Results and Discussion	131
6.3 Conclusions.....	140
6.4 References.....	141
6.5 Supporting Information.....	145
Chapter 7. Isolated Ti atom grafting carbon material for advanced hydrogen storage.....	150
7.1 Introduction.....	152
7.2 Results and Discussion	153
7.3 Conclusions.....	160
7.4 References.....	161

7.5 Supporting Information.....	163
Chapter 8. Conclusions and Perspectives	170
8.1 Conclusions.....	171
8.2 Recommendations for Future Work.....	172

List of Figures

Figure 2-1. A volcano plot of j_0 vs. Gibbs free energy (ΔG_{H^*}) of adsorption of hydrogen on individual catalyst.	11
Figure 2-2. Elements selected for constructing HER catalysts.	12
Figure 2-3. (a) Schematic of the top (upper panel) and side (lower panel) views of MoS ₂ with strained S-vacancies on the basal plane. (b) Free energy versus the reaction coordinate of HER for the S-vacancy range of 0–25% 16. (c) Electrochemical HER performance of P-MoS ₂ and MoS _{2-x} s (x: 10–150) . (d) Polarization curves obtained with several catalysts.	13
Figure 2-4. Schematic energy image for the HER pathway on defective graphene in acidic media.	15
Figure 2-5. The calculated free energy (ΔG_{H^*}) profile for HER at the equilibrium potential for heteroatom doped graphene models.	16
Figure 2-6. (a) Hydrogen storage capacity of commonly used materials with respect to operating temperature. (b) Volumetric and gravimetric hydrogen density of some selected hydrides.	19
Figure 2-7. Schematic illustration of thermodynamic and kinetic barrier for de-/hydriding reactions of metal hydrides.	20
Figure 2-8. Pressure-composition isotherm curves and corresponding van't Hoff plot related to the phase transition from metal to metal hydride.	21
Figure 2-9. The reaction process of hydrogen with storage material.	22
Figure 2-10 (a) Building a bridge between heterogeneous and homogeneous catalyst. (b) Specific activity vs. metal loadings/sizes.	27
Figure 2-11. (a) The mechanism illustration of the formation of Co AMSs/N-C; (b) Co K ₃ -weighted $\chi(k)$ function of the EXAFS spectra; (c) The corresponding EXAFS fitting curves for Co AMSs/N-C treated under 800°C. Insets are the proposed Co-N ₄ architectures.	29

Figure 2-12 (a) Schematic illustration of the synthetic process for Mn/C-NO; (b) The HAADF-STEM images of Mn/C-NO; (c) The schematic illustration of the formation W-AMS; (d) The corresponding HAADF-STEM image of the W-AMSs.30

Figure 2-13. Schematic illustration of the preparation of Cu-SAs/N-C. (a) Apparatus diagram; (b) Proposed reaction mechanism. (c) Apparatus diagram for synthesizing Pt SAs/DG.32

Figure 2-14. Schematic illustration of the Ar-plasma-induced exfoliation of CoSe₂-origin and the loading of single Pt by UV irradiation. 33

Figure 2-15. Schematic illustration of the ALD method for synthesizing atomically dispersed Pt on graphene nanosheet.35

Figure 2-16. The zoomed-in image of the defective area with atomic Ni trapped (a) and corresponding HER performance (b).36

Figure 2-17. Schematic diagram showing three orbital interactions between the central element and ligand. Type I: TM-olefin complexes. Type II: Kubas-type H₂ complexes.38

Figure 2-18. Hydrogen storage performance (via molecular chemisorption). (a) Schematic representation of the grafting of benzyl Ti species onto the surface of mesoporous silica. (b) Hydrogen adsorption isotherms at 77 K for mesoporous silica treated with various molar equivalents of tribenzyl titanium. (c) Possible mechanism for the reaction between V(Mes)₃ · THF and N₂H₄. (d) Hydrogen adsorption-desorption isotherms of vanadium hydrazide samples.40

Figure 4-1. Preparation and morphology characterization of Ru₁@D-MoS₂. (a) Schematic illustration for the synthetic process of Ru₁@D-MoS₂. (b) HRTEM image of commercial MoS₂. (c) HRTEM image of D-MoS₂. (d and e) TEM (d) and HRTEM (e) image of Ru₁@D-MoS₂. (f) EDS mapping of Ru₁@D-MoS₂. (g) XRD patterns of C-MoS₂, D-MoS₂ and Ru₁@D-MoS₂. (h) Representative Raman spectra for C-MoS₂, D-MoS₂ and Ru₁@D-MoS₂, respectively. (i) The Brunauer–Emmett–Teller (BET) measurements for C-MoS₂, D-MoS₂ and Ru₁@D-MoS₂, respectively.69

Figure 4-2. Characterization of atomically dispersed Ru₁@D-MoS₂ catalysts. (a) Aberration-

corrected atomic resolution HAADF-STEM image of Ru₁@D-MoS₂. (b) Intensity profile along the line 1 and 2 in Fig. 1a. (c) The schematic diagram of Ru occupation corresponding to line 1 and 2. (d) High-resolution X-ray photoelectron spectroscopy of Mo 3d of C-MoS₂, D-MoS₂ and Ru₁@D-MoS₂. (e) Normalized XAFS spectra of the Mo K-edge for the C-MoS₂, D-MoS₂ and Ru₁@D-MoS₂ samples. (f) Corresponding FT-EXAFS spectra from (e). (g) Normalized NEXAFS spectra of the Ru K-edge for the C-MoS₂, D-MoS₂ and Ru₁@D-MoS₂ samples. (h) Corresponding FT-EXAFS spectra from (g). (i) The fitting of k₃-weighted Fourier transforms EXAFS spectra of the Ru K-edge for Ru₁@D-MoS₂. Inset is the model of Ru₁@D-MoS₂. The dashed circle represents the S vacancy.73

Figure 4-3. Catalytic HER performances. (a) Linear sweep voltammetry (LSV) curves (scan rate: 5 mV s⁻¹) of C-MoS₂, D-MoS₂, Ru₁@D-MoS₂, and Ru@C-MoS₂ as catalysts toward HER in 1.0 M KOH. (b) Tafel plots derived from the LSV curves for HER. (c) ECSA-normalized polarization curves of C-MoS₂, D-MoS₂, Ru₁@D-MoS₂, and Ru@C-MoS₂. (d) Overpotential at ECSA-normalized current density of 0.04 mA cm⁻² for Ru₁@D-MoS₂ in comparison with those of C-MoS₂, D-MoS₂, Ru₁@D-MoS₂, and Ru@C-MoS₂. (e) Comparison of the η₁₀ values between Ru₁@D-MoS₂ and other hydrogen evolution electrocatalysts. (f) HER polarization curves of Ru₁@MoS₂ coated on carbon cloth. (g) Stability test of Ru₁@MoS₂ at a current density of 500 mA cm⁻².75

Figure 4-4. DFT calculations. (a-c) The geometries of MoS₂, MoS₂-Sv, and Ru₁@D-MoS₂ and their 3D charge density differences calculated by DFT. (d) Comparison of the total DOS for MoS₂, MoS₂-Sv, and Ru₁@D-MoS₂. (e) Free energy diagrams of the MoS₂, MoS₂-Sv, Ru₁(S)@MoS₂, Ru₁(Mo)@MoS₂ and Ru₁@D-MoS₂ under alkaline solution. (f) The optimized structures of the intermediates on Ru₁@D-MoS₂.77

Figure 5-1. Schematic drawing of scalable catalyst preparation for hydrogen production. ...102

Figure 5-2. (a) XRD patterns of C-MoS₂, M-MoS₂ and Co₃O₄@MoS₂. (b-d) SEM images of C-MoS₂ (b), M-MoS₂ (c) and Co₃O₄@MoS₂ (d). (e) The enlarged SEM image of Co₃O₄@MoS₂. (f and g) HRTEM images of C-MoS₂ and M-MoS₂. (h) Representative Raman spectra for C-MoS₂, M-MoS₂ and Co₃O₄@MoS₂, respectively.103

Figure 5-3. Structure characterizations of Co,O@MoS₂. (a) Aberration-corrected atomic resolution HAADF-STEM image of Co,O@MoS₂. (b) Intensity profiles along line 1 and 2 indicated in image (a). (c) EDS mapping of Co,O@MoS₂. (d) Normalized Co K-edge X-ray absorption near-edge structure spectra (XANES) of the Co K-edge for the Co foil, CoO and Co,O@MoS₂, respectively. (e) Fourier transform (FT) k^3 -weighted XANES of Co,O@MoS₂, CoO and Co foil. (f) Wavelet transform (WT) for the k^3 -weighted EXAFS signals of Co,O@MoS₂, CoO and Co foil, respectively. (g). The corresponding experimental and best-fitted EXAFS spectra in R space for Co,O@MoS₂. (h) The simulation model of Co,O@MoS₂. The dashed circle represents the S vacancy.106

Figure 5-4. Catalytic HER performances. (a) Linear sweep voltammetry (LSV) curves of C-MoS₂, CoO, M-MoS₂, Co,O@MoS₂ and 20 wt% Pt/C in 1.0 M KOH at a scan rate of 5 mV s⁻¹. (b) Tafel plots derived from the LSV curves in (a). (c) Nyquist plot of electrochemical impedance spectra for C-MoS₂, M-MoS₂ and Co,O@MoS₂. (d) HER polarization curves of Co,O@MoS₂ coated on carbon cloth. (e) Long-term stability test of Co,O@MoS₂ at 500 mA cm². (f) Comparison of the η_{10} values between Co,O@MoS₂ and hydrogen evolution electrocatalysts. (g) Stability test of Ru₁@MoS₂ at 500 mA cm⁻².109

Figure 5-5. (a) The hydrogen adsorption free energy diagrams of the C-MoS₂, Co,O@MoS₂, strained Co,O@MoS₂. (b) Comparison of the DOS for C-MoS₂, Co,O@MoS₂, and strained Co,O@MoS₂, respectively.111

Figure 6-1. (a) Types of hydrogen interaction with adsorption sites. (b) The average adsorption energy of H₂ onto Ti atoms with different coordination number. (c) Corresponding Structural model of hydrogen adsorption. (d) The distance between Ti and hydrogen. The red, blue, green, and grey balls represent O atom, Ti atom, H atom and O vacancy, respectively.132

Figure 6-2. (a) Schematic illustration of synthetic defective titanium oxide. (b) XRD patterns of TiO₂-P and annealed TiO₂ under H₂ atmosphere. (c) High-resolution XPS spectra of Ti 2p of TiO₂ before and after annealing. (d) and (e) UV-vis absorption spectra and Valence band XPS (VB-XPS) spectra of TiO₂-P and annealed TiO₂-x. (f) the band gap of TiO₂-P and annealed TiO₂-x. (g) band energy diagram of TiO₂-P and annealed TiO₂-400.133

Figure 6-3. (a) HR-TEM image of TiO₂-400. (b) HAADF-STEM images and (c) corresponding intensity line profile extracted from HAADF-STEM image of TiO₂-400. (d) EELS spectra of TiO₂-P and TiO₂-400. (e) Experimental and best-fitted EXAFS spectra in R space for TiO₂-400. (f) Schematic model of tetra-coordinated Ti atom. (g) Experimental and best-fitted EXAFS spectra in k space for TiO₂-400. (h) Nitrogen adsorption desorption isotherms and (i) corresponding pore size distribution of TiO₂-P and annealed TiO₂-x. (h) Hydrogen adsorption curves for all TiO₂ samples under liquid temperature.135

Figure 6-4. (a-c) Structural model of hydrogen adsorbed onto Ti atom with different coordination. (d-f) Crystal orbital Hamilton population (COHP) charts of H₂ adsorbed onto 5c-Ti, 4c-Ti and 2c-Ti, respectively. (g-i) The charge densities of H₂ adsorbed onto 5c-Ti, 4c-Ti and 2c-Ti, respectively. Yellow and cyan color represents the accumulation and depletion of charge density.138

Figure 7-1. (a) XRD patterns of TiOPc, CB and as-prepared Ti₁@C-x (x=50, 100 and 170). (b) Raman spectra of CB and Ti₁@CB-170.153

Figure 7-2. (a to c) HRTEM images of Ti₁@C-50, Ti₁@C-100 and Ti₁@C-170, respectively. (b) HAADF-STEM images of Ti₁@C-50, Ti₁@C-100 and Ti₁@C-170, respectively. (c) Corresponding EDS mapping of Ti₁@CB-170.155

Figure 7-3. (a) Survey scan XPS spectra of CB and Ti₁@CB-170. (b) Ti 2p high resolution XPS spectrum of Ti₁@CB-170. (c) O1s high resolution XPS spectrum of Ti₁@CB-170. (d) Ti K-edge x-ray absorption near-edge structure (XANES) spectra of Ti foil, Ti₁@CB-x, TiOPc, anatase TiO₂.156

Figure7-4. (a) Nitrogen adsorption desorption isotherms and (b) corresponding pore size distribution of CB and Ti₁@CB-x. (c) Hydrogen adsorption/desorption curves for CB and Ti₁@CB-x samples at -20°C. (d) Hydrogen adsorption/desorption cycling curves.158

List of Abbreviations

Abbreviation	Full Name
ACTEM	Aberration Corrected Transmission Electron Microscopy
AMS	Atomic Metal Site
BET	Brunauer Emmett Teller
CB	Carbon Black
CV	Cyclic Voltammetry
DFT	Density Functional Theory
ECSA	Electrochemical Active Surface Area
EDS	Energy Dispersive Spectroscopy
EELS	Electron Energy Loss Spectroscopy
EIS	Electrochemical Impedance Spectroscopy
EXAFS	Extended X-ray Absorption Fine Structure
HAADF	High-Angle Annular Dark-Field
HER	Hydrogen Evolution Reaction
HRTEM	High-Resolution Transmission Electron Microscopy
ICP	Inductively Coupled Plasma
ICP-AES	Inductively Coupled Plasma Atomic Emission Spectroscopy
LSV	Linear Sweep Voltammetry
SEM	Scanning Electron Microscopy
TEM	Scanning Electron Microscopy
UV-vis	Ultraviolet and Visible Spectrophotometry
VB-XPS	Valence-Band XPS
XANES	X-ray Absorption Near Edge Structure
XAS	X-ray Absorption Spectroscopy
XPS	X-ray Photoelectron Spectroscopy

List of Publications

1. **Chengguang Lang**, Yi Jia, Xuecheng Yan, Liuzhang Ouyang, Min Zhu, Xiangdong Yao. Molecular chemisorption: a new conceptual paradigm for hydrogen storage. *Chemical Synthesis*, 2022, 2, 1.

(Incorporated in Chapter 2.3.3)

2. **Chengguang Lang**, Yi Jia, Xiangdong Yao, Recent advances in liquid-phase chemical hydrogen storage, *Energy Storage Materials*, 2020, 26, 290-312.

3. Longzhou Zhang, Yi Jia, Hongli Liu, Linzhou Zhuang, Xuecheng Yan, **Chengguang Lang**, Xin Wang, Dongjiang Yang, Keke Huang, Shouhua Feng, Xiangdong Yao, Charge Polarization from Atomic Metals on Adjacent Graphitic Layers for Enhancing the Hydrogen Evolution Reaction, *Angewandte Chemie International Edition*, 2019, 58, 9404-9408.

Acknowledgements

First and foremost, I would like to express sincere appreciation to my principal supervisors, Prof. Xiangdong Yao and Dr. Yi Jia. Thank you very much to Prof. Xiangdong Yao. You are a phenomenal researcher who has the deepest influence on me academically. I am so incredibly grateful for giving me the great opportunity to undertake my PhD research and for your support and guidance along my candidature. No matter in work or in life, whenever I encounter problems, you are always enthusiastic and willing to help me. Also, I want to give special thanks to Dr. Yi Jia. He kept discussion with me every week even during the difficult epidemic period, so that I can successfully complete all my milestones on time. Dr. Yi Jia taught me how to conceive innovative research plans, draft academic writings, and create opportunities to communicate with other researchers in the field.

I would like to express my sincere appreciation to Prof. Nam-Trung Nguyen and Dr. Xuecheng Yan on my thesis submission and revision. I also sincerely appreciate my external supervisor, Prof. Liuzhang Ouyang from South China University of Technology (SCUT). Thank you very much to Prof. Liuzhang Ouyang for providing the great opportunity to continue my PhD research in SCUT during the epidemic period. It is his kind support and guidance that I can successfully complete my PhD research.

I would like to express my gratitude to those who provided technical support and assistance on my experimental work. Thank you very much to Prof. Chung-Li Dong and Dr. Cheng-Jie Yang from Taiwan National Synchrotron Radiation Research Centre

for providing XAS equipment access and data analysis. Thanks also goes to Dr. Barry Wood and Ms. Ying Yu from the University of Queensland, who are very kindly and supportive during the training of XPS and SEM. Prof. Jun Chen from University of Wollongong and Prof. Yue Lin from University of Science and Technology of China are also highly appreciated for the support of ACTEM characterizations.

I also wish to thank my colleagues Dr. Xuecheng Yan, Dr. Lei Zhang, Dr. Wenbin Jiang, Dr. Kang Chen. Mr. Qilong Wu, Dr. Hao Zhong, Dr. Xin Wang, and Dr. Shicheng Yan. They gave me a lot of assistance in experiments. I also want to thank my friends Dr. Nguyen Van Nhi Tran and Dr. Donghwan Kim. They made my life in Australia colorful. I will never forget the time with them at Griffith. I would like to acknowledge the financial support from Griffith University (Griffith University Postgraduate Research Scholarship and Griffith University International Postgraduate Research Scholarship), which covered not only the tuition fees but also my living allowance.

Last but not least, I would like to express my sincere appreciation to my family for their encouragement, support and love. Special thanks are given to my wife, Mrs. Dongdong Wang, who is the one I want to spend my life with.

Chapter 1. Introduction

1.1 Background

The better mastery of energy resulting from scientific and technological progress is to improve the living quality and to lead a better world. However, considering the constantly consumed fossil energy reserves, immoderate reliance on fossil fuels has now become a pivotal global challenge in today's economy. Presumably, the demand for energy will increase ten-fold in the next 100 years^[1], while the current fossil fuel reserves are speculated to last at most 40 years for petroleum and 60 years for natural gas^[2]. Moreover, on the concern about the environmental issues and climate changes caused by the combustion of fossil fuels, decarbonization of the energy supply is highly urgent to shift from conventional carbon-based energy resource to alternatively clean and renewable energy. Thus, the supply and utilization of low-priced and clean fuels are particularly significant.

Up to now, among various alternatives, hydrogen has been considered as a promising energy carrier to substitute fossil fuels, owing to its high energy density of 142 MJ/kg^[3-5], environmentally friendly by-product, abundant reserves in earth and various sources. Based on these merits, the successful development of hydrogen economy not only can replace the scarce fossil fuels and simultaneously decrease the ever-increasing emissions of hydrocarbon-based fuel combustion, but also benefit the economic growth in a sustainable fashion^[6, 7]. To achieve the hydrogen economy in the future, technological challenges should be addressed in advance, including the fabrication of hydrogen, storage and conveyance, as well as utilization. Nowadays, the well-developed fuel cell technologies pave the way for the practical application of hydrogen. However, the secure and efficient production and storage of hydrogen are still the bottleneck of hydrogen economy.

To achieve the up-coming hydrogen economy, as mentioned above, one of the major challenges is to fabricating hydrogen in an efficient, cost-effective and secure way. Over the past decades, abundant feedstocks are available for hydrogen production with various methods including hydrocarbon reforming, hydrocarbon pyrolysis, biomass

conversion and water electrolysis^[8, 9]. Currently, hydrogen production from fossil fuels, such as hydrocarbon reforming and pyrolysis, is still the main pathway to meet almost the entire hydrogen demand^[10]. Over 90% of the global hydrogen supply is produced by the reformation of fossil fuels, which involves the CO₂ emission and still in short supply^[11, 12]. Water electrolysis, as a sustainable and green hydrogen production pathway, has the advantage of producing extremely pure hydrogen (>99.9%). Moreover, hydrogen produced by water electrolysis can serve as the ideal energy carrier to adjust the balance between the power generation from the renewable resource and end-use energy demand^[13]. Thus, hydrogen evolution via water electrolysis has inspired a great scientific interest. Currently, the benchmark catalysts for catalytic hydrogen evolution are still the noble Pt-based metal catalysts. Unfortunately, the utilization of Pt-based cathode contributes over 55% of the total cost of the fuel cell system, and thus is not practical for large-scale applications^[14]. Besides the high cost, the low abundance also impedes the commercialization of Pt-based electrocatalysts. Therefore, low-cost, scalable synthesis of efficient and stable catalysts for practical applications is still a great challenge at present.

After production, hydrogen must be safely and efficiently packaged and stored, to bring it for final use, while the efficient and secure hydrogen storage is still an indomitable challenge for the hydrogen economy. Currently, the established techniques can enable the hydrogen to be stored as compressed hydrogen, liquid hydrogen and as storage material. Because of the safety consideration and high volumetric capacity, solid-state storage via materials is considered as a promising transformative technology. However, although various hydrogen storage materials have been developed, none of them can satisfy the practical application due to the unsuitable enthalpy. Designing and constructing new solid-state hydrogen storage materials is extremely important.

1.2 Objectives

The aim of this project is to design, optimize and controllably synthesize AMS catalysts for hydrogen production and storage. To this end, the critical issues for hydrogen

storage in metal-based materials are the poor thermodynamics and sluggish kinetics. In addition, cost-effective catalysts with long durability are of great importance for hydrogen production from water splitting. Monoatomic metal doped nanomaterials have the advantage of bridging homogeneous and heterogeneous catalysts, which allows the metal utilization up to 100%. Besides, the tunable electronic structures of monoatomic metal doped nanomaterials are beneficial for the targeting reactions. The specific objectives are listed below.

- (1) Develop simple, efficient and scalable strategies for fabricating atomically dispersed metal-based nanomaterials with controllable loadings.
- (2) Regulate the coordination structures and morphology of AMS to evaluate the hydrogen production and hydrogen storage performance of AMS nanomaterials.
- (3) Understand the underlying structure-property relationship of different reaction processes.

1.3 Structure of Thesis

The structure of this thesis is described as below, which is broken down into the subjects covered in each individual chapter.

Chapter 1 gives an introduction of the thesis and describes the scope and key contributions to the field of research.

Chapter 2 is a literature review, which covers the developments in hydrogen production and storage, and the AMS nanomaterials

Chapter 3 summarizes various strategies applied in this project to develop and evaluate the AMS nanomaterials for hydrogen production and storage, including sample synthesis, structure and morphology characterization, electrochemical performance tests, and density functional theory (DFT) calculations.

Chapter 4 describes a facile and scalable high-energy mechanochemical ball milling method, which is applied to synthesize atomic Ru doped defective MoS₂ for hydrogen

evolution.

Chapter 5 introduces the one-step batch preparation of non-noble metal Co doped MoS₂ nanomaterials for hydrogen production.

Chapter 6 presents a new hydrogen adsorption fashion via molecular chemisorption by regulating the coordination number of the Ti atom.

Chapter 7 introduces the design and construction of the atomic metal site doped carbon nanomaterials as solid-state hydrogen storage materials, which shows excellent hydrogen storage performance.

Chapter 8 summarizes the key findings of this research and makes recommendations for further development in this field.

1.4 References

1. P. Poizot and F. Dolhem, *Energy Environ. Sci.*, 2011, **4**, 2003-2019.
2. J. O. Abe, A. P. I. Popoola, E. Ajenifuja and O. M. Popoola, *Int. J. Hydrogen Energy* 2019, **44**, 15072-15086.
3. A. O. Dudoladov, O. A. Buryakovskaya, M. S. Vlaskin, A. Z. Zhuk and E. I. Shkolnikov, *Int. J. Hydrogen Energy* 2016, **41**, 2230-2237.
4. A. Bulut, M. Yurderi, I. E. Ertas, M. Celebi, M. Kaya and M. Zahmakiran, *Applied Catalysis B-Environmental*, 2016, **180**, 121-129.
5. L. Ouyang, H. Zhong, H.-W. Li and M. Zhu, *Inorganics*, 2018, **6**.
6. A. Demirbas, *Energy Sources Part B-Economics Planning and Policy*, 2017, **12**, 172-181.
7. Y. Dou, L. Sun, J. Z. Ren and L. Dong, *Hydrogen Economy: Supply Chain, Life Cycle Analysis and Energy Transition for Sustainability*, 2017, DOI: 10.1016/B978-0-12-811132-1.00010-9, 277-305.
8. P. Nikolaidis and A. Poullikkas, *Renewable & Sustainable Energy Reviews*,

- 2017, **67**, 597-611.
9. J. A. Turner, *Science*, 2004, **305**, 972-974.
 10. P. Nikolaidis and A. Poullikkas, *Renewable Sustainable Energy Rev.* , 2017, **67**, 597-611.
 11. M. D. Symes and L. Cronin, *Nature Chemistry*, 2013, **5**, 403-409.
 12. N. Mahmood, Y. Yao, J.-W. Zhang, L. Pan, X. Zhang and J.-J. Zou, *Advanced Science*, 2018, **5**, 1700464.
 13. M. Wang, Z. Wang, X. Gong and Z. Guo, *Renewable Sustainable Energy Rev.* , 2014, **29**, 573-588.
 14. Y. Bing, H. Liu, L. Zhang, D. Ghosh and J. Zhang, *Chem. Soc. Rev.* , 2010, **39**, 2184-2202.

Chapter 2. Literature Review

STATEMENT OF CONTRIBUTION TO CO-AUTHORED PUBLISHED PAPER


This chapter includes a co-authored paper, incorporated in **section 2.3.3**. The bibliographic details of the co-authored paper, including all authors, are:

Chengguang Lang, Yi Jia, Xuecheng Yan, Liuzhang Ouyang, Min Zhu, Xiangdong Yao, Molecular chemisorption: a new conceptual paradigm for hydrogen storage, *Chemical Synthesis*, 2022, 2, 1.

My contribution to the paper involved:

- Literature survey
- Concept and design
- Drafting and writing

(Signed)  (Date) 31/07/2022
Chengguang Lang

(Countersigned)  (Date) 02/08/2022
Corresponding author of paper: Dr. Xuecheng Yan

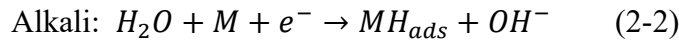
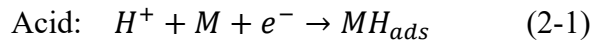
(Countersigned)  (Date) 31/07/2022
Supervisor: Dr. Xuecheng Yan

2.1 Hydrogen Production via Water Splitting

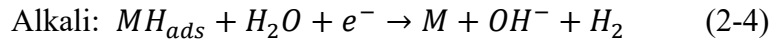
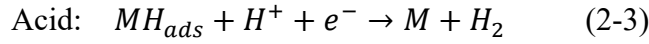
2.1.1 Hydrogen Evolution Reaction Mechanism

Electrocatalytic HER is the cathodic half reaction of water splitting, where redox reactions take place at the electrode/electrolyte interface. Electrocatalytic hydrogen evolution can be realized in electrolytes with various pH values. Generally, the electrochemical HER involves three steps, including Volmer reaction, Heyrovsky reaction and Tafel reaction. Depending on the pH value of the electrolyte, the HER process can be described as follows:

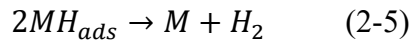
Volmer reaction (discharge step):



Heyrovsky reaction (desorption step):



Tafel reaction (recombination step):



Here, M represents the catalytic sites and H_{ads} means the adsorbed hydrogen.

The difference of coverage of H_{ads} on the catalyst surface will lead to different reaction pathways. The H_{ads} prefers to combine with a proton and an electron to generate a H_2 molecule under low coverage of H_{ads} on the catalyst surface, leading to a Volmer–Heyrovsky reaction pathway. In contrast, the high H_{ads} coverage is preferable for the Volmer–Tafel pathway that a H_2 molecule is generated via the binding of two adjacent H_{ads} atoms^[1, 2].

Tafel slopes are commonly utilized to reflect the dominant mechanism, which can be obtained by replotting the polarization plots into Tafel plots. At 25 °C, the Tafel slope for Tafel reaction is calculated to be 29 mV/dec. For Heyrovsky reaction, the minimum Tafel plot is 38 mV/dec. While the rate determining step is the Volmer reaction, the Tafel slope will be determined as 116 mV/dec^[3].

Irrespective of HER occurring by Volmer–Heyrovsky pathway or Volmer–Tafel pathway, the discharge step to form the intermediate H_{ads} is always involved. Thus, the Gibbs free energy for hydrogen adsorption (ΔG_{H^*}) is a vital descriptor to evaluate the activities of a selected HER catalyst. For an ideal HER catalyst, the ΔG_{H^*} should be neither too strong nor too weak^[1]. The weak bonding strength between hydrogen atom and catalyst surface is disadvantageous to the Volmer reaction step, while the strong bonding strength makes the Tafel reaction or Heyrovsky reaction difficult, thus unfavourable the release of H_2 molecular^[2]. Figure 2-1 presents a volcano plot of exchange current density (j_0) vs. Gibbs free energy (ΔG_{H^*}) of adsorption of hydrogen on individual catalyst. Apparently, Pt group metals possess the highest exchange current density located at the summit of the volcano, exhibiting the highest activity, and the Gibbs free energy of adsorption of hydrogen is close to zero.

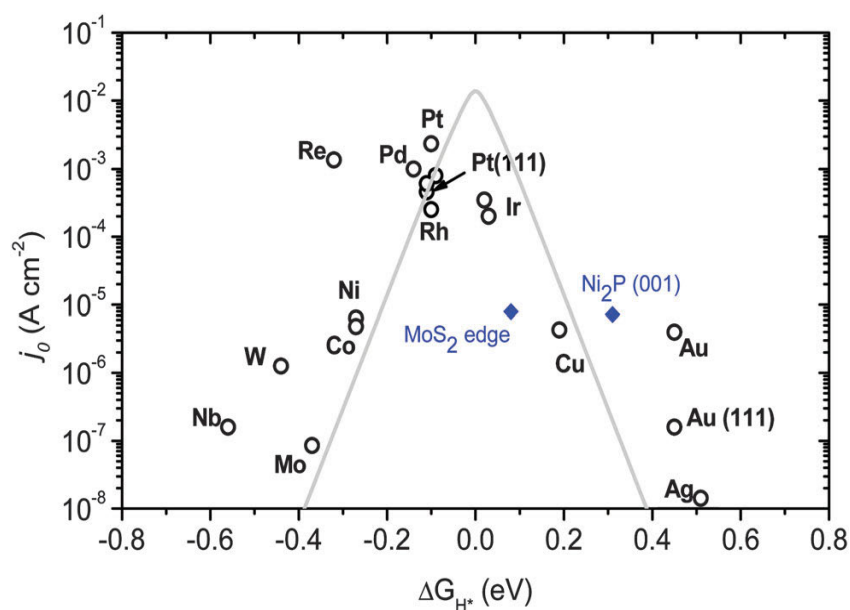


Figure 2-1. A volcano plot of j_0 vs. Gibbs free energy (ΔG_{H^*}) of adsorption of hydrogen on individual catalyst^[3].

2.1.2 Metal-based Catalysts for HER

As discussed above, Pt family materials are located at the summit of the volcano plot, possess a ΔG_{H^*} close to zero, indicating extremely high exchange current density (shown in Figure 2-1). These features render the Pt group catalysts as the benchmark electrocatalyst for HER. However, the limited reserve, high cost and poor stability have impeded their broad commercial application. Various methods have been proposed to address the issues, such as reducing the loading amount of noble metals, alloying or hybridizing with other inexpensive transition metals^[4]. Lou *et al.* reported sub-nanometre Pt clusters confined in hollow mesoporous carbon spheres (Pt₅/HMCS) for hydrogen evolution^[5]. Due to their high surface-to-volume ratio, the Pt clusters possess high ratio of surface atoms, tunable composition, and electronic structure, resulting in higher catalytic activity, as compared to the nanoparticles. It is reported that the electrocatalytic activity of Pt₅/HMCS with a Pt loading of 5.08 wt% exceeds that of the commercial 20 wt% Pt/C, and the calculated mass activity of Pt₅/HMCS is 12 times higher than that of the commercial Pt/C. Alloying can modulate the electronic structure of catalysts via bimetallic synergistic effect, which promises significantly enhanced catalytic activity^[6]. To date, various Pt-based alloys are reported, such as Pt-M (M=Ni, Co, Fe)^[7] and PtRuNi^[8], which display outstanding catalytic activity.

However, while considering commercial application, affordability, facile synthesis, high durability and catalytic activity are normally involved^[9]. As a result, non-precious metal catalysts have emerged and developed as alternatives. Up to now, metal sulphides, carbides, nitrides, selenides, and phosphides (shown in Figure 2-2) have been developed as promising candidates^[10].

1	2	3	4	5	6	7	8	9	10	11	12	13	14	15	16	17	18
H	Periodic Table of Elements																He
Li	Be											B	C	N	O	F	Ne
Na	Mg											Al	Si	P	S	Cl	Ar
K	Ca	Sc	Ti	V	Cr	Mn	Fe	Co	Ni	Cu	Zn	Ga	Ge	As	Se	Br	Kr
Rb	Sr	Y	Zr	Nb	Mo	Tc	Ru	Rh	Pd	Ag	Cd	In	Sn	Sb	Te	I	Xe
Cs	Ba	La	Hf	Ta	W	Re	Os	Ir	Pt	Au	Hg	Tl	Pb	Bi	Po	At	Rn

■ Pt-containing noble metal HER catalysts
■ Metals that are used for constructing noble metal-free HER catalysts
■ Nonmetals that are used for constructing noble metal-free HER catalysts

Figure 2-2. Elements selected for constructing HER catalysts^[11].

Molybdenum sulphide (MoS₂) is a well-studied electrocatalyst because of its intriguing structural and electronic properties. It is experimentally and computationally confirmed that the HER activity of MoS₂ correlates linearly with the number of edge sites^[12, 13]. However, the 2D structure of MoS₂ is prone to stacking and aggregation owing to the high surface energy and interlayer van der Waals attraction, which is adverse to HER^[13, 14]. Engineering the surface structure of MoS₂ to expose more active edge sites could effectively enhance the electrocatalysis HER activity. Feng *et al.* reported an interface engineering of novel MoS₂/Ni₃S₂ heterostructures, in which the outer MoS₂ nanosheets are decorated on the surface of the inner Ni₃S₂ nanoparticles, exposing abundant interfaces^[15]. The observed cell voltage is only 1.56 V to deliver a current density of 10 mA cm⁻².

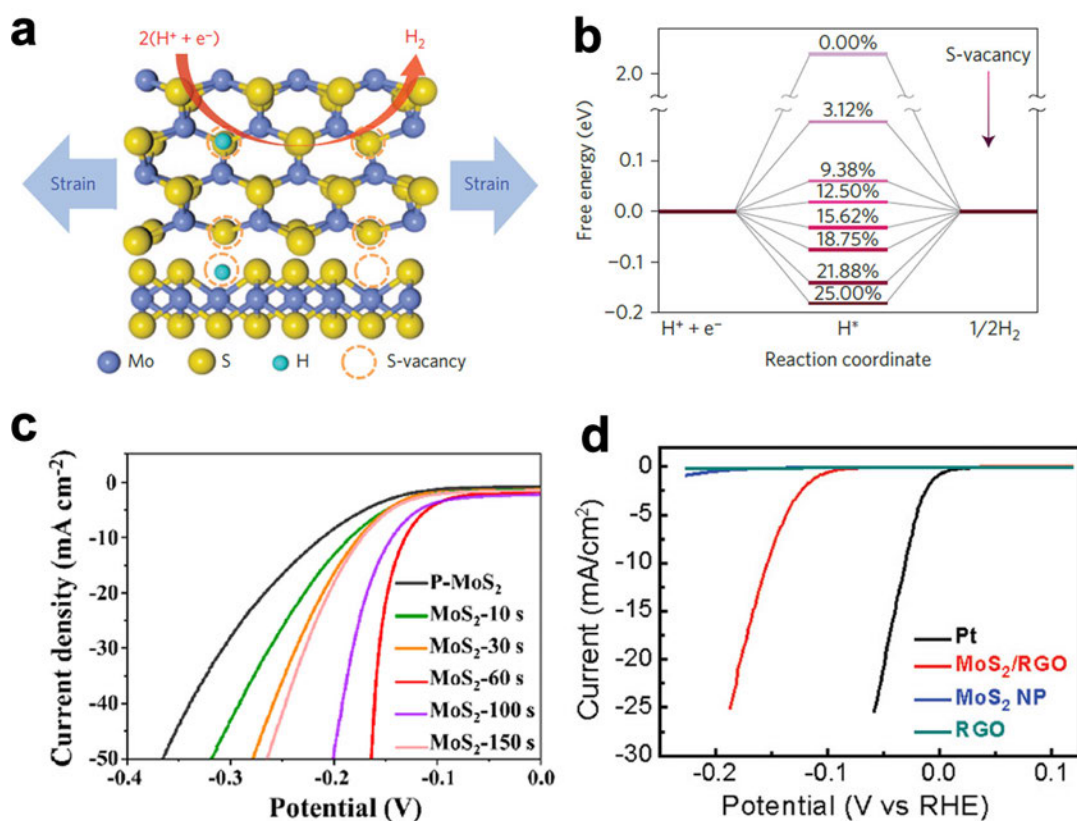


Figure 2-3. (a) Schematic of the top (upper panel) and side (lower panel) views of MoS₂ with strained S-vacancies on the basal plane. (b) Free energy versus the reaction coordinate of HER for the S-vacancy range of 0–25%^[16]. (c) Electrochemical HER performance of P-MoS₂ and MoS₂-x s (x: 10–150)^[17]. (d) Polarization curves obtained with several catalysts^[18].

Constructing active sites via defect engineering has emerged as a new perspective and has been demonstrated to be an effective strategy to enhance the hydrogen evolution performance by several groups^[19–22]. The introduction of defects can effectively tune the electrocatalytic performance of catalysts by regulating their electronic structures, and thus improving the catalytic activity^[23–26]. For example, Zheng *et al.* reported a strained S vacancy engineer via exposing MoS₂ to Ar plasma (Figure 2-3a)^[16]. Combining DFT calculations, it is found that the strained S-vacancy sites can manipulate the gap states even closer to the Fermi level, thus yielding an optimal ΔG_H (Figure 2-3b). Besides the plasma engraving, chemical etching agent (such as H₂O₂) is

also reported to creating S-vacancy defects on the basal plane^[17]. By regulating the etching duration, etching solution, and etching temperature, a homogeneously distributed single S-vacancy onto the MoS₂ is obtained, resulting in an overpotential decreased from 220 mV to 131 mV at the current density of 10 mA cm⁻² (Figure 2-3c).

Besides the defect engineering for improving the numbers of active sites, doping heteroatoms or coupling conductive substrates are also applied to tune the electrocatalysis performance of MoS₂. For example, it is reported that Co-doped MoS₂ could reduce the free energy of hydrogen adsorption at the Co-promoted S-edge and simultaneously increase the number of active sites, showing a low overpotential of 124 mV at 10 mA cm⁻²^[27]. Embedding MoS₂ on conductive substrate could improve the electronic conductivity. Dai *et al.* reported a MoS₂/RGO (reduced graphene oxide) hybrid catalyst with low overpotential and small Tafel slopes (Figure 2-3d)^[18]. It is believed that the strong chemical and electronic coupling between the GO sheets and MoS₂ contributed to the excellent HER performance, which could not only favour the electron transport but also expose massive edges of MoS₂.

2.1.3 Metal-free Catalysts for HER

Metal-based catalysts are efficient in electrocatalytic hydrogen evolution. However, the disadvantages of metal-based catalysts include poor durability and stability, susceptibility to gas poisoning, and low selectivity. Besides, the limited availability and high cost of metal-based catalysts, especially the noble-metal-based catalysts have blocked their large-scale commercial preparation and application^[28]. Moreover, the use of metal-based catalysts will lead to the release of metal ions, damaging the environment^[29]. Thus, metal-free catalysts are also considered for electrochemical hydrogen evolution in acid/alkaline environments, such as graphene, carbon nanotube, and C₃N₄^[30-33]. Compared with metal-based catalysts, the abundance, tunable molecular structures, and strong tolerance to acidic/alkaline environments endows these carbon-based materials highly potential to be used as electrocatalysts.

For pure carbon, its activity towards HER is very low owing to the lack of 3d orbital which could transfer the electrons. Regulating the electron structure of carbon-based materials by creating defects^[21, 34, 35] or doping with heteroatoms such as N, P and S can enhance the electrocatalytic hydrogen evolution effectively. Yao *et al.* firstly reported a defect-derived active carbon (D-AC) with high activity to HER^[35]. The defects in D-AC were obtained via a simple removal of the doped nitrogen. The observed overpotential of D-AC at 10 mA cm⁻² is 334 mV, which is almost 60 mV lower than that of the original high surface area activated carbon. The authors contributed the enhanced HER activity to its defective and metal-free nature. However, the catalytic reaction mechanism has not clarified. Later, the authors further conducted a deep understanding on the origin of activity using a defective graphene fabricated by a facile nitrogen removal procedure from a N-doped precursor^[34]. It is reported that the existence of defects in graphene could modulate the local electronic environment and perturb the surface properties of graphene such as the specific surface area and surface hydrophobicity. Density function theory (DFT) calculations were further conducted to reveal the underlying catalytic mechanisms. It was found that 7557 defects are the most active sites for HER with a lowest $\Delta G_{H^*}^0$ of -0.187 eV, as shown in Figure 2-4.

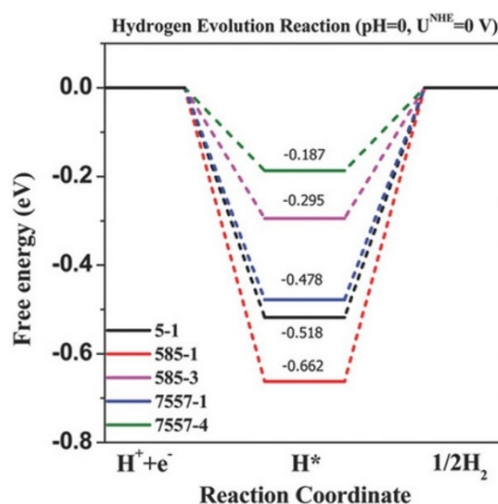


Figure 2-4. Schematic energy image for the HER pathway on defective graphene in acidic media ^[34].

Heteroatom doping such as N, B, P and S, is also an effective method to alter the electronic structures and electrochemical properties of carbon-based materials. Typically, co-doping two heteroatoms possessing different electronegativities to that of carbon, like P-N and S-N, could result in a unique electron-donor property of carbon via a synergistic coupling effect^[36]. As shown in Figure 2-5, the DFT calculations show that the N and P co-doping in graphene matrix could significantly narrow the Gibbs free energy of the hydrogen adsorption as compared to single doped counterparts^[31]. The electrocatalytic activity enhancement via N, P co-doping is also confirmed by electrochemical measurements in both acidic and alkaline solutions. Both the electrochemical measurements and theoretical calculations elucidate that heteroatom doping could create more active sites and lower the Gibbs free energy of the hydrogen adsorption by tailoring the density of states near Fermi level. However, the stability (like defects in carbon-based materials) and activity of metal-free catalysts still need to be considered before practical application.

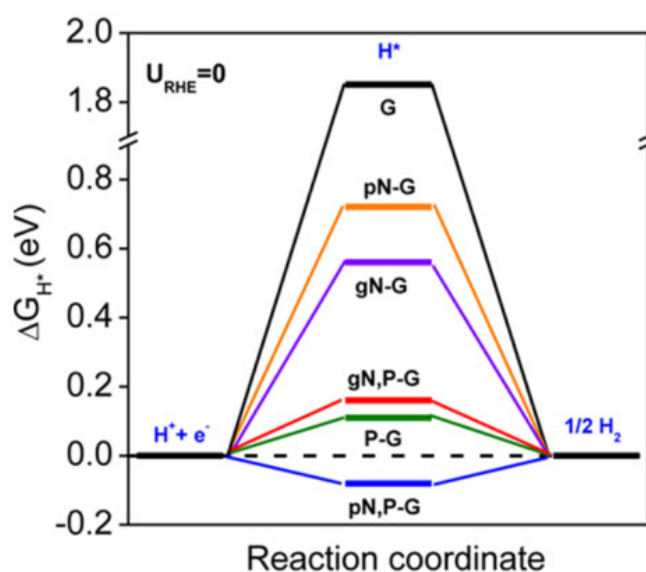


Figure 2-5. The calculated free energy (ΔG_{H^*}) profile for HER at the equilibrium potential for heteroatom doped graphene models^[31].

2.2 Hydrogen Storage

2.2.1 Hydrogen Storage Materials

After hydrogen production, how to store hydrogen in an efficient and safe way is the other bottleneck which needs to be addressed in advance for achieving hydrogen economy. Currently, the established technique of hydrogen storage consists of three means: compression, cryogenics and material-based hydrogen storage. Early in 2003, the U.S. Department of Energy (DOE) released the set targets for hydrogen storage system every five years starting in 2005. The set technical standards include gravimetric and volumetric capacities, cycle life, costs, refuelling time and loss of usable hydrogen^[37]. Figure 2-6a presents hydrogen storage capacity of commonly used materials with respect to the operating temperatures^[37]. According to the DOE, the set target for automotive hydrogen storage systems is to achieve 5.5 wt% hydrogen in gravimetric capacity for 2020^[38, 39]. Though the mass energy density of hydrogen is about three times higher than that of gasoline, its volumetric energy density is only 10.1 MJ/l (liquid) compared with 34.2 MJ/l of gasoline^[40]. In this case, compression or liquefaction is a direct and easy way to improve the volumetric energy density. Compression is a conventional and common method to store hydrogen through a fixed cylinder with enhanced pressure. Recently, the commercially available hydrogen cylinder is achieved a 70 MPa capacity, but the process of compression requires electrical consumption, and the security is still under consideration^[40]. This is because of the nature of the hydrogen as the smallest molecule which is highly buoyant and diffuse. In addition, the volumetric hydrogen storage densities of compressed hydrogen system are still low^[41]. By comparison, liquid hydrogen has a much higher volumetric energy density compared to that of the compressed hydrogen. However, the severe preparation condition and high storage criterion require a considerable energy input and specific container as well as specialized management, making it unsuitable for mobile practical utilization.

Research interest was further transferred to the hydrogen storage materials, including physical adsorption materials like metal-organic frameworks^[42], carbon nanotubes^[43], zeolites^[44], and chemical materials such as metal hydrides^[45] and complex hydrides^[46]. Hydrogen storage materials via physisorption will be beneficial to the fast refuel and release of hydrogen. However, physisorption materials, such as the typical representatives of carbon nanotube and classical MOFs, their adsorption enthalpies are determined to be 4~7 kJ/mol^[47], which can only stabilize considerable hydrogen under cryogenic temperature. Room temperature will lead to a sharp decrease on the hydrogen storage capacity. Compared with classical physisorption materials, enhanced physisorption materials such as heteroatom (such as O) doped carbon-based materials, possesses elevated sorption enthalpies^[48]. However, the improvement of adsorption enthalpy is limited, generally lower than 15 kJ/mol.

Different from physical adsorption materials of which hydrogen exists in the form of molecules, chemical materials such as metal hydrides are chemically bonded to hydrogen atom in their solid state by an absorption process. Storing hydrogen in metal hydrides has many advantages as compared to compression, liquefaction and physical adsorption method. The first merit is safety. Metal hydrides can be operated at relatively mild conditions with low temperatures and pressures compared with compression and liquefaction. The second advantage is that metal hydrides are capable of storing high volumetric and gravimetric hydrogen storage densities. Figure 2-6b shows the volumetric versus gravimetric hydrogen density for the various materials^[49, 50]. For example, MgH₂ has a gravimetric hydrogen storage density of 7.6 wt% which well-meet the target set by the DOE. Besides, metal hydrides possess good reversibility that hydrogen could be charged/discharged by altering the temperature or pressure. However, the poor thermodynamics and/or sluggish dynamics hinder their practical application.

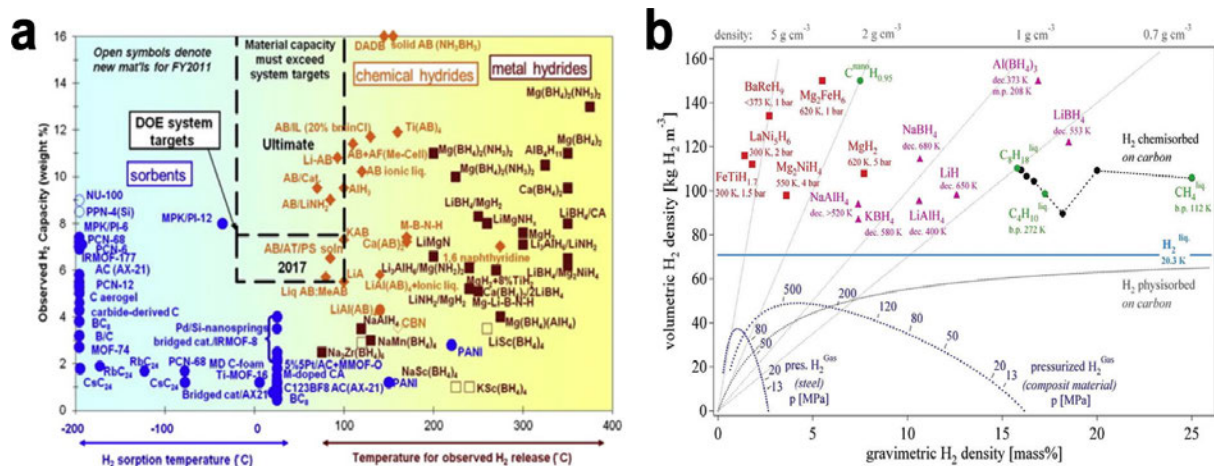


Figure 2-6. (a) Hydrogen storage capacity of commonly used materials with respect to operating temperature^[37]. (b) Volumetric and gravimetric hydrogen density of some selected hydrides^[49].

2.2.2 Regulations of Thermodynamics and Kinetics

Metals or alloys can reversibly react with hydrogen under certain conditions (temperature and pressure) forming metal hydrides (MH). The reaction formula is shown as below:



Where the M represents metal.

Hydrogen storage performance of metal hydrides is normally characterized by thermodynamics and dynamics, which reflects the barrier for de-/hydriding reaction of metal hydrides. Currently, the regulation of the thermodynamic and dynamic characteristics of metal hydrides is still a big challenge. Here, the thermodynamics and dynamics of in hydrogen storage materials will be introduced briefly. For a specific metal hydride, the entropy (ΔS) and formation enthalpy (ΔH) are used to characterize the thermodynamic stability, while the activation energy of reaction (E_a) is used to describe the kinetic barrier. Figure 2-7 clearly illustrates the two factors influencing the hydrogen storage performance. High ΔH normally leads to high desorption temperature

under a specific hydrogen pressure, and the high E_a means sluggish kinetics, namely low absorption/desorption rate and high reaction temperature.

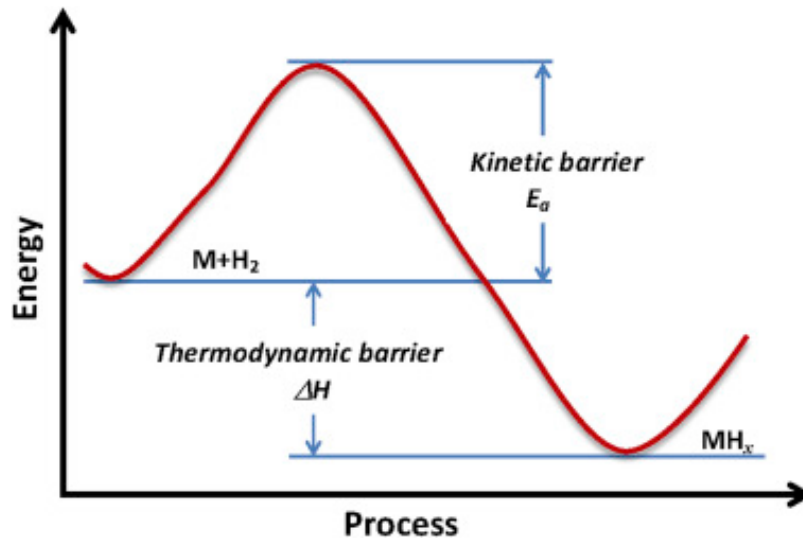


Figure 2-7. Schematic illustration of thermodynamic and kinetic barrier for de/hydrating reactions of metal hydrides ^[51].

2.2.2.1 Thermodynamics

In respect to the thermodynamic, the formation of metal hydrides can be described by pressure-composition isotherms, shown in Figure 2-8. The equilibrium of the Reaction (2-7) is influenced by the interaction of three factors between hydrogen pressure (P), concentration of hydrogen in the solid phase (C) and temperature (T)^[52]. When the reaction reaches the equilibrium under isothermal process, a “plateau” phenomenon will occur in the metal-hydrogen system. The host metal would firstly transfer to a solid solution (α -phase) by dissolving hydrogen. While reaching the solubility limit, the nucleation and growth of the hydride phase (β -phase) will be induced. The flat plateau zone indicates the coexistence of two phases (α and β), and the width of the plateau reflects the reversible amount of hydrogen storage^[53]. The equilibrium pressure in the plateau region is a function of temperature (T), which can be described by the van’t Hoff equation shown below:

$$\ln P_{H_2}^{eq} = \frac{\Delta H}{RT} - \frac{\Delta S}{R} \quad (2-7)$$

where, the $P_{H_2}^{eq}$ means the plateau pressure, ΔH means the enthalpy which reflects the metal-hydrogen bond energy, i.e., the hydride stability, ΔS is entropy, R is the gas constant, and T is the reaction temperature.

Obviously, experimental values of the enthalpy of hydride formation ΔH can be evaluated through the slope of the van't Hoff plot, as shown in Figure 2-8.

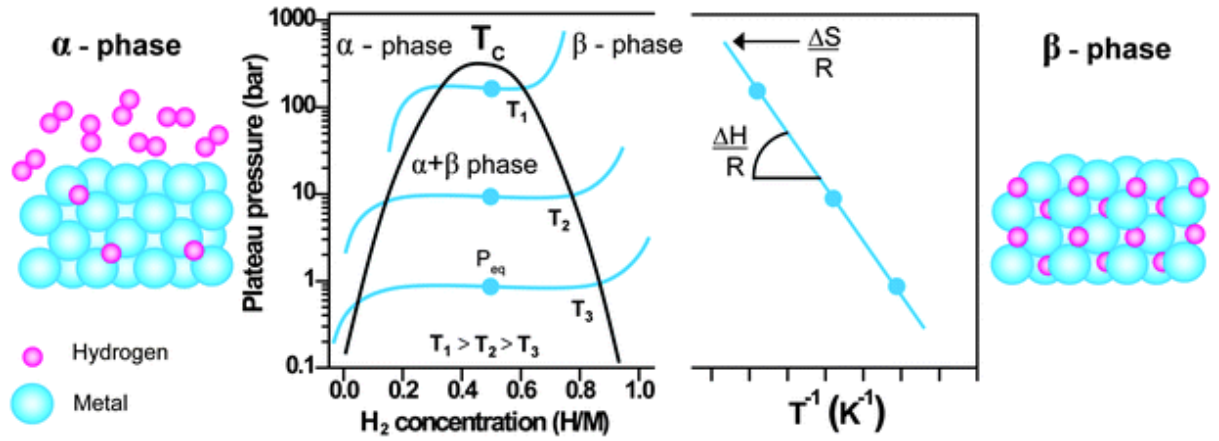


Figure 2-8. Pressure-composition isotherm curves and corresponding Van't Hoff plot related to the phase transition from metal to metal hydride [53, 54].

2.2.2.2 Dynamics

The system kinetics is also a vital factor in a selected hydrogen storage material. The hydriding and dehydriding kinetics of a target material is directly related to the time required for given materials to uptake and release hydrogen at a certain temperature and pressure.

Figure 2-9 depicts a typical process of hydrogenation between hydrogen and metal, which includes several dynamic steps. Firstly, hydrogen is attracted to the surface of the metal. Then, hydrogen will interact with the metal on the surface through van der

Waals interactions and the hydrogen molecules are dissociated into atoms. Afterward, the dissociated hydrogen atoms will diffuse from the surface into the bulk through a surface layer. Lastly, the metal hydrides are formed^[55-57]. During the hydride formation process, the slowest process dominates the overall reaction kinetics, which is known as the rate-limiting step or kinetic barrier^[58]. To evaluate the dynamics of system, Johnson–Mehl–Avrami–Kolmogorov (JMAK) model is widely used, equation shown as below ^[55, 59-61]:

$$\alpha = 1 - e^{-(kt)^\eta} \quad (2-8)$$

where α is the reaction fraction, k is the constant of reaction rate, t is the reaction time, and η is the reaction order used to understand the dehydrogenation mechanism. Thus, the Avrami exponent n and the rate constant k can also be determined by fitting the desorption curve. The obtained k values are further used for estimating the apparent activation energy E_a by Arrhenius equation:

$$K = Ae^{-E_a/RT} \quad (2-9)$$

where A is the pre-exponential factor, R is the gas constant, and T is the Kelvin temperature.

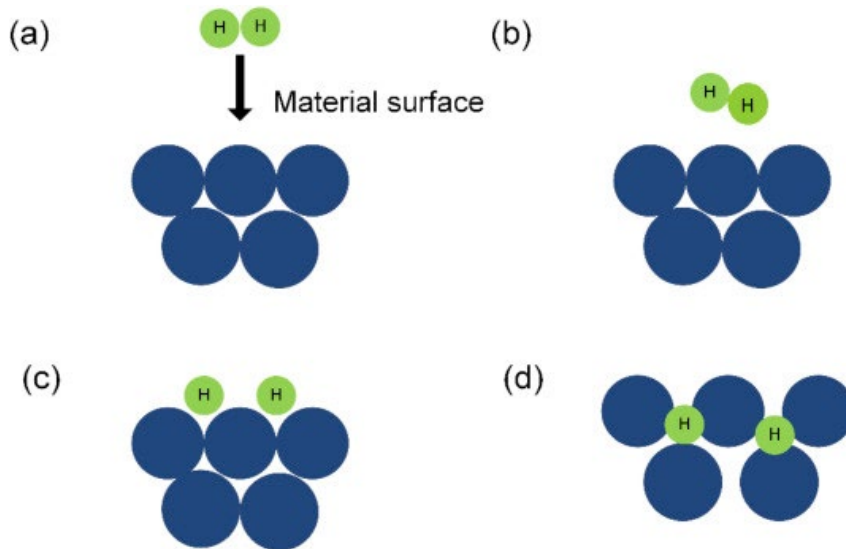


Figure 2-9. The reaction process of hydrogen with storage material^[56].

2.2.2.3 Regulations of Thermodynamics and Kinetics

Though metal hydrides possess high mass hydrogen storage density, their poor thermodynamics and/or sluggish kinetics cannot meet the end requirement of DOE for hydrogen storage system standards, it is therefore cannot be commercialized. For example, the high stable magnesium hydride possesses a heat of formation of $-74.5 \text{ kJ}\cdot\text{mol}^{-1}\cdot\text{H}_2$ and an entropy variation of $-135 \text{ J}\cdot\text{mol}^{-1}\cdot\text{H}_2\cdot\text{K}^{-1}$, leading to a dehydrogenation temperature up to 300°C . Thus, great efforts have been devoted to improving the thermodynamics and sluggish kinetics of hydrides.

The unfavourable thermodynamic stability of metal hydrides is rooted in the strong bonding nature between metal and H. Till now, strategies for destabilizing hydrides and improving the kinetics include alloying with another elements or forming solid solution [62-65], doping catalysts, nanosizing and so on. Altering the binding energy of Mg with H in MgH_2 by partial substitution with elements to form alloys could weaken the bonds with H, such as transition metals (Fe, Ni, etc.) [66-68]. For example, the hydride formation enthalpy of typical Mg_2Ni alloy decreased to $-64 \text{ kJ}\cdot\text{mol}^{-1}\cdot\text{H}_2$ as compared with $-74.5 \text{ kJ}\cdot\text{mol}^{-1}\cdot\text{H}_2$ of MgH_2 [62]. It was found that the interaction between Ni and H is stronger than that of Mg and H in Mg_2NiH_4 , but this Ni–H interaction in Mg_2NiH_4 is much weaker compared with the Mg–H interaction in pure MgH_2 , resulting in a lower formation enthalpy of Mg_2NiH_4 [50, 51, 69]. Destabilizing metal hydrides by adding a reactive additive B to change the reaction pathway could optimise the thermodynamics as well. For example, Vajo *et al.* reported a Si doped MgH_2 system, in which the desorption enthalpy was sharply decreased to $36.4 \text{ kJ}\cdot\text{mol}^{-1}$ owing to the formation of Mg_2Si .

Adding catalysts such as metal oxides and transition metals, is also an effective strategy to optimize the hydrogen sorption/desorption kinetics of magnesium [70]. For example, researchers found that Nb_2O_5 doped MgH_2 could adsorb 7 wt% H_2 within only 1 min and desorb hydrogen within 2.2 min at 300°C [71]. It was found that Nb_2O_5 is active at the surface by accelerating the pathway of hydrogen diffusion through the surface

barriers in the reaction^[56]. Transition metal fluorides, such as TiF_3 and NbF_5 , are also used as catalysts introducing into MgH_2 to improve its kinetics^[72-74]. The desorption temperature was decreased by 64 K in the $\text{MgH}_2 + 2 \text{ mol\% NbF}_5$ system as compared to pure MgH_2 detected by diffraction scanning calorimetry (DSC) examination and the activation energy for hydrogen desorption is estimated to be $\sim 90 \text{ kJ/mol}$. It was claimed that both metal and fluorine anions contribute to the kinetic enhancement of MgH_2 . Specifically, during the desorption, Nb atom of the catalyst could activate the Mg–H bond of MgH_2 by which the unoccupied orbitals of the catalyst could accept the electrons of the bonding orbitals of MgH_2 accompanied by a back-donation from the electrons of the occupied orbitals of the catalyst to the anti-bonding orbitals of MgH_2 . The electronic exchange reactions could facilitate the Mg–H dissociation, thus accelerating recombination of hydrogen atoms. In addition, the introduction of F^- anion would lead to the formation of MgF , which is highly reactive and protective toward H uptake. Alternatively, F^- anion may also directly acts on the generation of the catalytically active species. Similarly, Yu *et al.* reported an enhanced hydrogen sorption property in Ni and Co-catalyzed MgH_2 ^[75]. The obtained activation energy from the desorption data of $\text{MgH}_2/\text{NiCl}_2$ and $\text{MgH}_2/\text{CoCl}_2$ is 55.9 kJ/mol and 37.2 kJ/mol , respectively, smaller than that of pure MgH_2 sample. Moreover, further kinetic investigation illustrated that the slow, random nucleation and growth process-controlled hydrogen desorption process was transferred to two-dimensional growth after the addition of NiCl_2 or CoCl_2 , indicating a reduced barrier and lowered driving forces for nucleation as compared to the pure MgH_2 , thus enhanced the kinetics.

The negative impact of the above strategies is the decrease in hydrogen storage capacity. Moreover, systems with additives like Si may suffer from poor reversibility. In contrast, nanosizing is a promising method which could not only maintain its hydrogen storage capacity, but also destabilize the thermodynamics, and improve the dynamics of metal hydrides. Compared with their corresponding bulk materials, nanoscale particles possess distinct physical and chemical properties originating from the increased surface energy and lower atom coordination as well as the appearance of unsatisfied bonds^[53].

As to the desorption/absorption process of a nanostructured materials, the free energy of formation can be expressed below^[76]:

$$\Delta G(r) = \Delta G_0(r) + RT \ln \left(\frac{a_{MH_2}}{a_M P_{H_2}} \right) + \frac{3V_M \Delta_{M \rightarrow MH_2}(r)}{r} \quad (2-10)$$

Where the volume-adjusted surface energy difference is given by ^[76, 77]

$$E_{M \rightarrow MH_2}(r) = \left[\gamma_{MH_2}(r) \left(\frac{V_{MH_2}}{V_M} \right)^{\frac{2}{3}} - \gamma_M(r) \right] + E_{ads} \quad (2-11)$$

Here, V_M means the molar volume accounting for volume changes. Inclusion of these surface energy terms gives a new van't Hoff relation, showing that size reduction lowers the heat released ($\Delta H'$) as long as $E_{M \rightarrow MH_2}$ is positive (ΔH is a negative quantity) illustrated as below:

$$\ln P_{H_2}^{eq} = \frac{\Delta H'}{RT} - \frac{\Delta S_0}{R} \quad (2-12)$$

$$\Delta H' = \Delta H_0 + \frac{3v_M E_{M \rightarrow MH_2}}{r} \quad (2-13)$$

Here, $E_{M \rightarrow MH_2}$ will be positive as a volume expansion is usually accompanied with the hydriding reaction. A smaller magnitude for $\Delta H'$ means that MH_2 nanoparticles will be destabilized with respect to the bulk MH_2 ^[77].

Size-dependent effect from the nanostructure is also favourable for enhancing the kinetics via optimizing the dissociation and penetration of hydrogen at the interface and the nucleation of β -phase. Decreasing the particle size could increase the surface area and porosity which will be beneficial for the dissociation of hydrogen atoms via offering a larger number of dissociation sites and allowing fast gaseous diffusion to the center of the material. In addition, the increased volume in the amorphous grain boundary by decreasing size could weaken the binding between metal and hydrogen atoms, which favours the site-to-site hopping and diffusion of hydrogen^[76].

2.3 Atomic Metal-site (AMS) Nanomaterials

2.3.1 Advantages and Synthetic Strategies of AMS Nanomaterials

2.3.1.1 Advantages

The research and development of catalysts is presently undergoing a rapid growth both in academic research and industrial applications. In fact, more than 80% of industrial products involve the application of catalysts to accelerate the target reaction^[78]. The central role of a catalyst is to activate the reactants, improve the reaction kinetics, and deactivate undesired side reactions. Hence, the properties of catalysts such as activity, cost, efficiency, selectivity and durability are widely considered and designed by scientists for a given reaction. Conventional heterogeneous catalysts seem to be a possible solution to overcome the issues above, but the catalytic activation would decrease significantly owing to the limited atomic utilization and the uncontrollable coordination structure.

One promising solution is to embed atomic metals on solid supports thereby creating typical atomic metal-sites (AMS) nanomaterials^[79] (Figure 2-10a). The AMS nanomaterials are conceptually building a bridge between homogeneous and heterogeneous catalysis, which naturally inherit the merits of both homogeneous and heterogeneous catalysts. The typically structure feature of AMS nanomaterials is the maximization of the metal utilization (up to 100%), the well-defined active centers and unique electronic structures, which allows utility of AMS nanomaterials in a broad scope. The exhibited catalytic activity of AMS catalysts is markedly higher than that of the nanostructured catalysts, owing to the maximized atomic utilization efficiency and high specific/mass activity (Figure 2-10b)^[80, 81]. Moreover, the tunable coordination configuration and unsaturated coordination environments of the active centers in ACs have demonstrated excellent catalytic performance for CO oxidation^[82], water–gas shift (WGS) reaction^[83, 84], and (photo)electrochemical reactions^[85, 86].

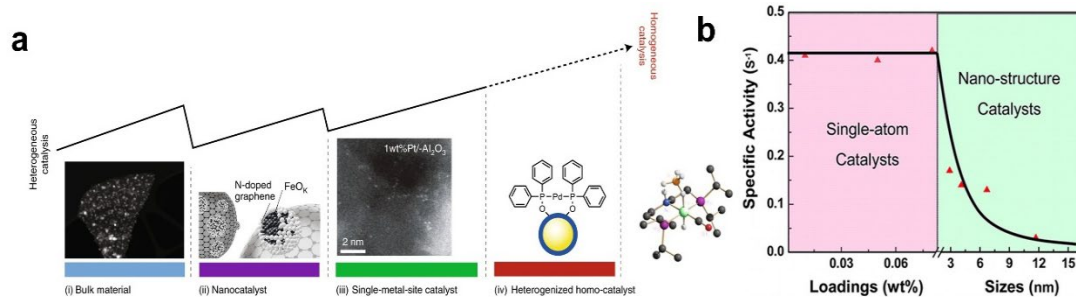


Figure 2-10 (a) Building a bridge between heterogeneous and homogeneous catalyst [79]. (b) Specific activity vs. metal loadings/sizes [87].

2.3.1.2 Synthetic Strategies

Great efforts have been devoted to developing AMS nanomaterials in the past decade, and various methods are reported, including wet-chemistry method, metal organic framework derived AMS, thermal emitting method, photo-chemical method, and atomic layer deposition (ALD).

Wet-Chemistry Method

Wet chemistry method is a commonly used strategy for constructing desired metal atoms on selected support because of their facile operation and sustainable nature. Generally, the wet-chemistry method consists of three consecutive processes: (1) dispersion of a desired metal precursor on the support; (2) calcination after drying; (3) reduction^[88, 89]. Although its general versatility to diverse supports, the wet-chemistry method may be inappropriate to fabricate high metal loading catalysts. Li *et al.* reported isolated Pt single atoms anchored on a graphitic carbon nitride with a weight content of 0.16 wt%^[90]. Pt atoms would become dense and form the sub-nanometer clusters while the loading content reached 0.38 wt%.

Metal Organic Framework Derived AMS

Metal organic frameworks (MOFs) are organic-inorganic hybrid porous materials that consist of uniformly distributed metal nodes coordinated to organic linkers. They are

considered as ideal precursors for fabricating AMSs supported on MOFs-derived carbons^[91-96]. The authigenic nitrogen sources in MOFs could anchor and stabilize the target metal atoms by forming strong metal-nitrogen coordination bonds. Pyrolysis is an essential approach to transfer MOFs into metal atom anchored carbon-based materials. However, constructing isolated metal sites and avoiding aggregation during high temperature are still big challenges. According to Han *et al.*, there are two synthetic methods for constructing MOF-derived carbon-supported AMS nanomaterials^[97].

The first strategy is to prohibit the aggregation of the target metal atoms during the synthesis process by pyrolyzing predesigned MOFs. In this method, bimetallic zeolitic imidazole frameworks (ZIFs) with target metal are designed, in which one of the metals acts as a sacrificial agent^[94, 98-100]. Recently, zinc-based zeolitic imidazole frameworks (ZIF-8) are commonly used, in which zinc acts as the sacrificial metal owing to its low boiling point (≈ 906 °C). The target metals such as Fe^{2+} , Co^{2+} , Ni^{2+} , etc., which have similar ionic size and charge with Zn^{2+} , could coordinate with 2-methyl imidazole and homogeneously distribute in the Zn-based metal-organic framework, resulting in bimetallic ZIFs. Thus, bimetallic ZIF-derived carbon supported individual metal atoms are synthesized by evaporating zinc under high temperature treatment. As an example, Yin *et al.*^[98] achieved stable Co single atom with high metal loading over 4 wt% supported on N-doped porous carbon (Co AMSs/N-C) through carbonized Zn/Co ZIF under a high temperature. The mechanistic illustration of the formation of Co AMSs/N-C is summarized in Figure 2-11a. The added Co^{2+} can replace a certain proportion of Zn^{2+} , and the existence of Zn^{2+} could serve as a “fence” to further enlarge the adjacent distance of Co atom, thus preventing Co aggregation under high temperatures. During pyrolysis, low boiling point Zn atoms are evaporated, and Co nodes are in situ reduced by the carbonization of the organic linkers. The Co EXAFS spectra and the corresponding EXAFS fitting curves for Co AMSs/N-C in Figure 2-11b and c showed that no Co-Co peaks were found, and the coordination numbers of the Co-N within Co

AMSS/N-C treated under 800 °C is 4, indicating the atomically dispersed Co on N-doped carbon.

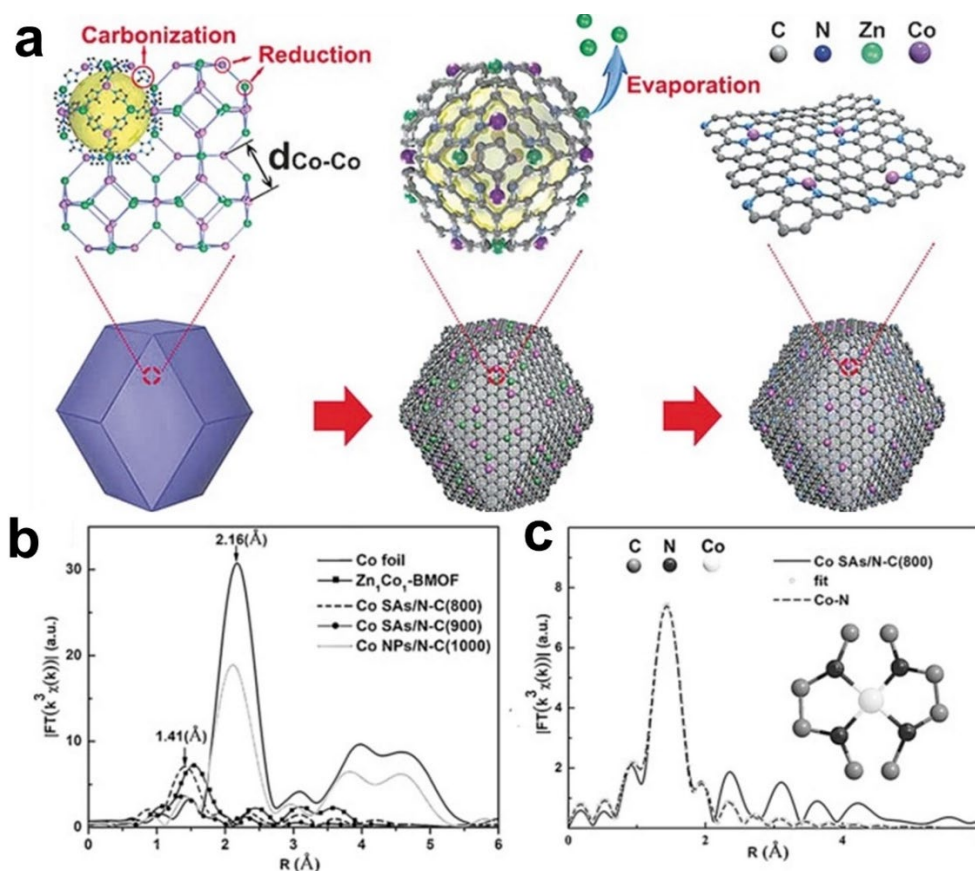


Figure 2-11. (a) The mechanism illustration of the formation of Co AMSs/N-C; (b) Co K₃-weighted $\chi(k)$ function of the EXAFS spectra; (c) The corresponding EXAFS fitting curves for Co AMSs/N-C treated under 800°C. Insets are the proposed Co-N₄ architectures^[98].

The second method is to remove metal nanoparticles via acid treatment, leaving individually dispersed metal sites on MOF-derived carbon support, if aggregation cannot be avoided during pyrolysis. For example, Yang *et al.* reported a monoatomic Mn supported on the 3D graphene framework obtained through Mn based MOFs (Mn-BTC) with post-treatments^[101]. As illustrated in Figure 2-12a, the calcination of Mn-BTC resulted in ultrafine MnO nanoparticles embedded on graphene framework. The following HCl etching treatment could effectively remove the MnO nanoparticle and

the annealing process under NH_3 atmosphere ensure the Mn atom atomically dispersed on graphene skeleton (Mn/C-NO). The HAADF-STEM image of the Mn/C-NO in Figure 2-12b confirmed the homogeneously and individually dispersed Mn atom incorporated within MOF-derived carbon support. Chen *et al.* also reported a MOF-derived N-doped carbon anchoring single tungsten catalyst for electrochemical hydrogen evolution^[102]. The synthetic route is shown in Figure 2-12c that the MOF (UiO-66- NH_2) is applied to encapsulate tungsten precursor (WCl_5). The pyrolysis followed by hydrofluoric acid treatment strategy successfully synthesized single W atom embedded on N-doped carbon. The uniform dispersion was evidenced by the HAADF-STEM image (Figure 2-12d) of the W AMSs. The ICP-OES analysis indicated that the loading content of W is 1.21 wt%.

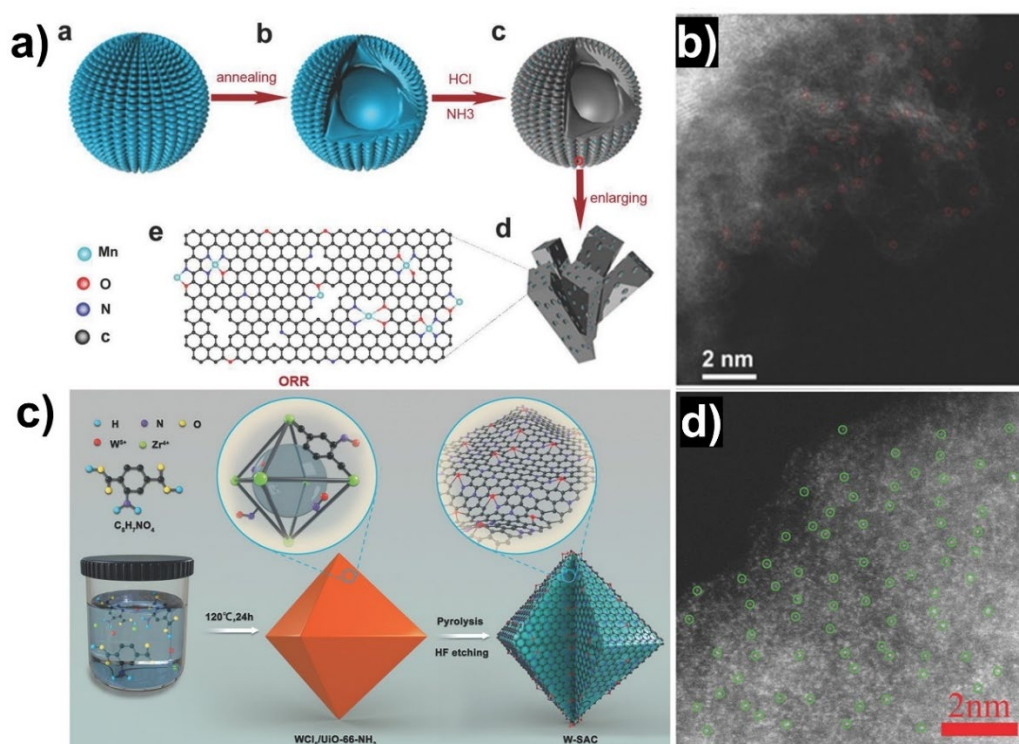


Figure 2-12 (a) Schematic illustration of the synthetic process for Mn/C-NO; (b) The HAADF-STEM images of Mn/C-NO^[101]; (c) The schematic illustration of the formation of W-AMSs; (d) The corresponding HAADF-STEM image of the W-AMSs^[102].

Thermal Emitting Method

Thermal emitting method is a facile gas-migration strategy which directly transform bulk metal materials into single atoms onto a substrate. Li's group firstly reported this method for fabricating individually dispersed Co atom onto nitrogen-rich porous carbon with the assistance of ammonia^[103]. The schematic illustration of thermal emitting method for trapping Cu atoms is presented in Figure 2-13a and b. Specifically, zeolitic imidazolate framework (ZIF-8) and Cu foam were placed separately in a porcelain boat. Then, the porcelain boat was placed into the tubular furnace, in which the Cu foam was placed in front of the airflow. During heating, the ZIF-8 was firstly pyrolyzed under argon atmosphere at 1173 K, forming N-rich porous carbon with abundant defects and empty zinc nodes. Afterward, the Ar was converted to NH₃ which could react with Cu under high temperatures based on the strong Lewis acid-base interaction, forming volatile Cu(NH₃)_x species. The resulting Cu(NH₃)_x species can immigrate to the carbonized ZIF-8 and be trapped by the defects on the N-rich carbon substrate, resulting in atomically dispersed Cu on N-doped carbon(Cu-SAs/N-C). The ICP-AES was used to identify the copper content, in which 0.54 wt% Cu was obtained. The authors also indicated the generality of this gas-migration method for fabricating a variety of functional SACs (such as Co and Ni).

Subsequently, Li's group modified the thermal emitting method for fabricating atomically dispersed Pt on graphene oxidation (GO)^[104]. As shown in Figure 2-13c, dicyandiamide (DCD), Pt net, and GO were placed sequentially in a porcelain boat, in which DCD, Pt net and GO served as NH₃ source, Pt source and support, respectively. The pyrolysis process was carried out under Ar atmosphere. The formation mechanism is similar to the Cu-SAs/N-C, involving the generation of ammonia gas under high temperatures by the decomposition of DCD, then forming strong coordination interaction with Pt atoms and lastly oxidized by oxygen-containing functional group on the surface of GO. The removed oxygen-containing functional group during pyrolysis can create a large number of defects (DG) which could further anchor the Pt atoms (Pt

SAs/DG). The Pt content in PtSAs/DG reached 2.1 wt% as measured by the ICP-AES, obviously higher than that of the Cu-SAs/N-C.

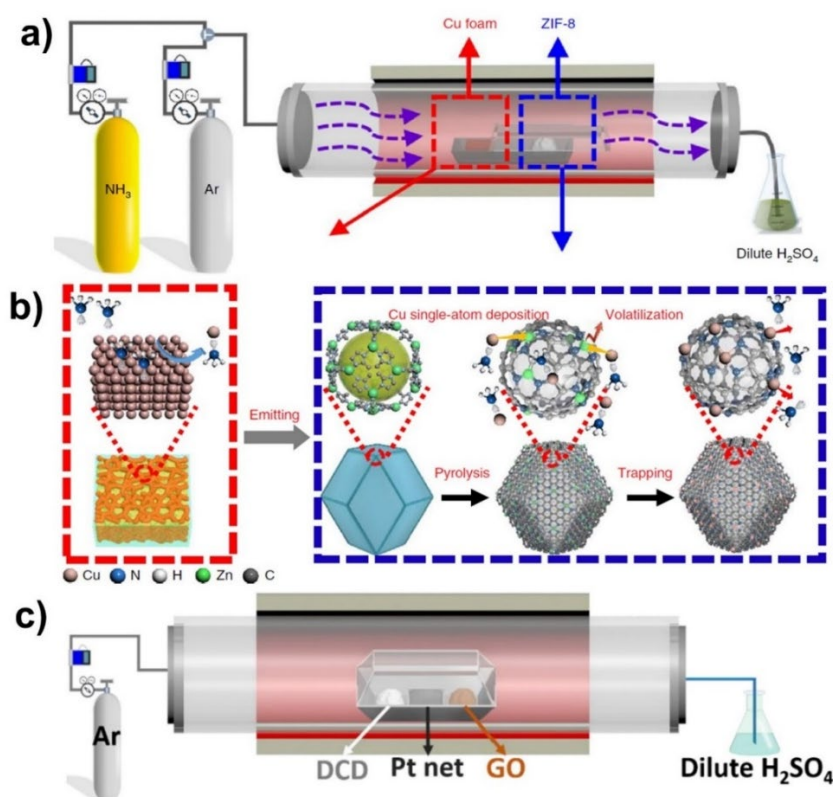


Figure 2-13. Schematic illustration of the preparation of Cu-SAs/N-C ^[103]. (a) Apparatus diagram; (b) Proposed reaction mechanism. (c) Apparatus diagram for synthesizing Pt SAs/DG^[104].

Photo-Chemical Method

Zheng *et al.* firstly reported the atomically dispersed Pd catalyst (Pd₁/TiO₂) on ultrathin TiO₂ nanosheets through a room temperature photochemical deposition strategy^[105]. Ultraviolet (UV) light was applied to induce the deposition of atomic Pd. In details, UV irradiation can generate electron-hole pairs on TiO₂ nanosheets, electrons were trapped in Ti-3d orbitals to form Ti³⁺ sites, and holes broke the Ti-O bonds between glycolate and TiO₂, resulting in the formation of -OCH₂CH₂O• radicals (EG), which play an essential role in preparing Pd₁/TiO₂. Thereafter, the introduced H₂PdCl₄ was absorbed onto TiO₂, liberating two Cl⁻ of PdCl₂²⁻ under the UV treatment to yield intermediate PdCl₂ units. The subsequent replacement was occurred between Cl⁻ in PdCl₂ unit and

the OH⁻ group in EG, forming the PdCl₁/TiO₂ intermediate. Further UV treatment could remove the remaining Cl⁻, thus stabilizing isolated Pd atom on TiO₂ by forming more Pd-O bond. Yao *et al.* also reported defect-induced Pt–Co–Se coordinated sites (CoSe_{2-x}Pt) by the photochemical method^[106]. In their research, the plasma induced defects can evidently increase the loading amount of Pt (2.25 wt%) by photochemically depositing Pt precursor under UV irradiation (shown in Figure 2-14). Moreover, Wu *et al.* applied iced-chemistry to prepare atomically dispersed Pt via ultraviolet (UV) irradiating the frozen chloroplatinic acid (H₂PtCl₆) aqueous solution. The iced-photochemical reduction ensured the high loading amount of Pt (2.6 wt%) and the isolated states of Pt single atoms on the mesoporous carbon. In a sharp contrast, the conventional photochemical reduction of H₂PtCl₆ aqueous solution led to the formation of Pt nanocrystals^[107]. More recently, the photochemical method is also successfully used to fabricate isolated diatomic Pt and Ru on g-C₃N₄^[108].

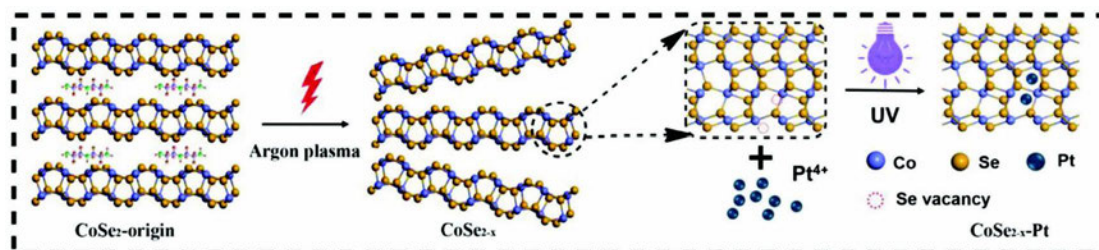
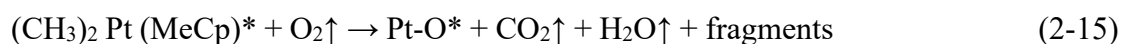


Figure 2-14. Schematic illustration of the Ar-plasma-induced exfoliation of CoSe₂-origin and the loading of single Pt by UV irradiation^[106].

Atomic Layer Deposition (ALD)

Atomic layer deposition (ALD) is a tool for the atomic precise design and synthesis of catalysts. Recently, ALD is also proved to be a powerful method for precise and facile synthesis of SACs by the sequential and self-limiting surface reactions^[109-113]. Through simply controlling the number of ALD cycles, the density, size, morphology and loading of Pt on graphene can be precisely regulated. Sun *et al.* reported the isolated single Pt atoms anchored to graphene nanosheet by using the ALD technology for methanol oxidation reaction^[109]. The synthesized single-atom catalysts presented a dramatically enhanced catalytic activity (up to 10 times) over that of the commercial Pt/C catalyst. Figure 2-15 (a to d) represents a typically schematic illustration of the ALD deposition. Generally, the ALD process includes two half-reactions. During the first half-reaction (Figure 2-15a and b), the metal precursor (MeCpPtMe₃, methylcyclopentadienyl-trimethylplatinum) will react with the substrate (graphene nanosheet), in which a fraction of reactive ligands of the metal precursor will be partially removed by reaction with active sites (functional groups or defect, here is a monolayer of oxygen containing function group), leading to a Pt-containing monolayer to be formed on the substrate surface. In the second half-reaction (Figure 2-15c and d), the Pt-containing monolayer reacts with the subsequent oxygen pulse, thus forming a new adsorbed oxygen layer on the Pt surface by removing the remaining ligands of the Pt-containing monolayer. The corresponding half-reactions are shown as below.



Here, ‘*’ represents an active surface species, and Pt-O* represents oxygen molecules (or dissociated oxygen ions) that are adsorbed on the Pt surface. The two half-reactions consist of a complete cycle of ALD method, producing atomically dispersed metal species on the selected substrates. Increasing the cycles of ALD could lead to the formation of clusters or even particles.

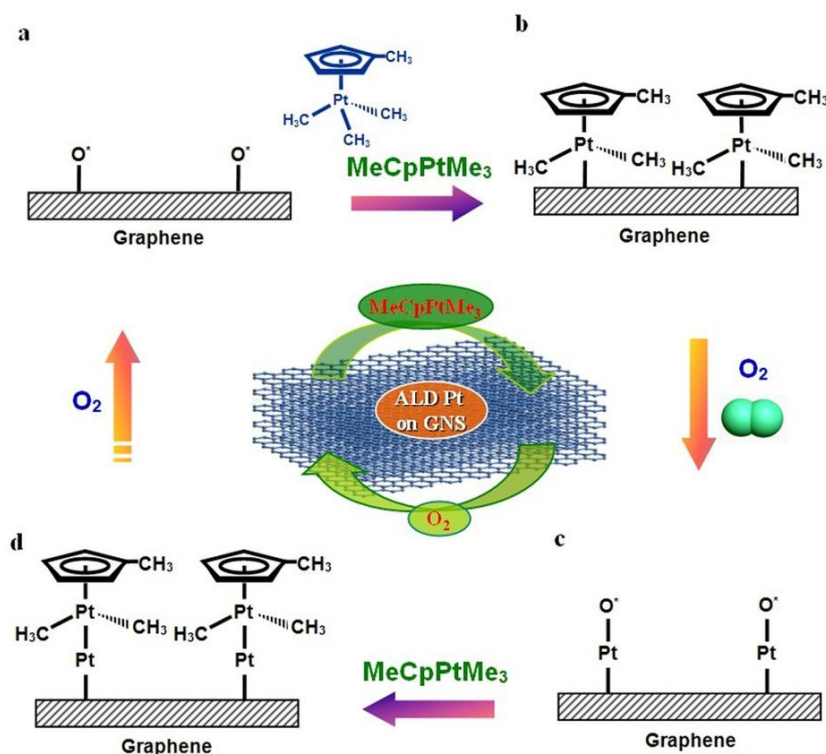


Figure 2-15. Schematic illustration of the ALD method for synthesizing atomically dispersed Pt on graphene nanosheet^[109].

2.3.2 AMS Nanomaterials for Hydrogen Production

For electrocatalytic HER, downsizing Pt nanoparticles to isolated Pt species anchored on support is an effective tactic for both maximizing metal utilization and decreasing the cost. Sun *et al.* reported a Pt AMS supported on N-doped graphene nanosheets (Pt_1/NGN) by the atomic layer deposition (ALD) technique^[114]. The catalytic activity was significantly enhanced, which is 37 times higher than that of the commercial platinum/carbon catalysts. DFT calculations illustrate that the partially unoccupied 5d orbital density of states (DOS) of Pt 5d character contributes to the excellent catalytic activity. Other than precious Pt-based catalysts, downsizing nonprecious metals into monodispersed metal species could also achieve a remarkably improved water oxidation property that their corresponding nanocatalysts do not possess. Recently, Yao and co-workers reported an active site of atomic Ni anchored on carbon matrix for

superb HER^[115, 116]. Electrochemical tests exhibited a much-decreased overpotential of 70 mV for achieving 10 mA cm⁻², which is comparable to the commercial Pt/C catalyst, shown in Figure 2-16a and b. XAS and DFT analysis demonstrated that the excellent HER and OER performance was ascribed to the unique configurations of atomic Ni in the defects of DG (defective graphene) substrate.

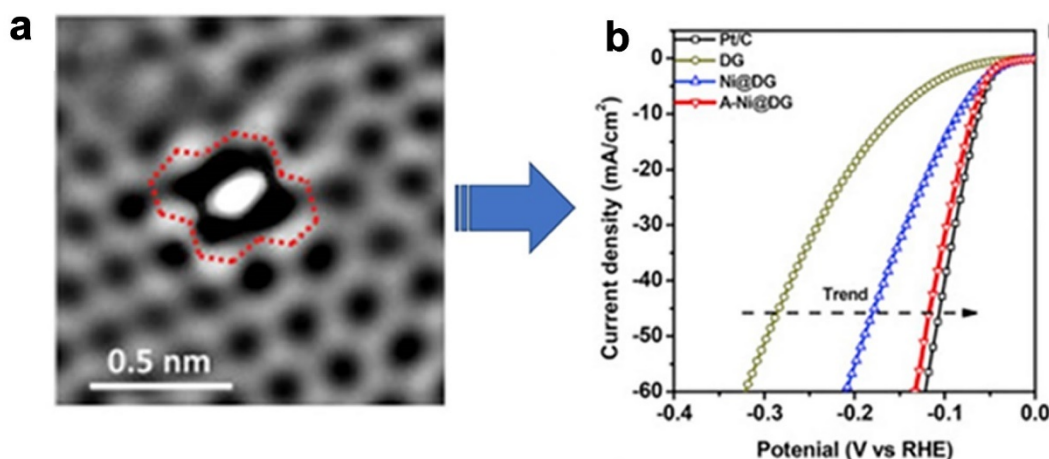


Figure 2-16. The zoomed-in image of the defective area with atomic Ni trapped (a) and corresponding HER performance (b)^[115].

However, the preparation of single metal atoms often suffers from particle agglomeration due to the extremely high surface energies. Therefore, fabrication of AMS nanomaterials with high loading is still a big challenge. Recently, defect engineering has emerged as a new perspective and has been demonstrated by several groups^[19, 24, 117, 118]. The introduction of defects can effectively tune the electrocatalytic abilities of catalysts by regulating their electronic structures, and thus improving the catalytic activity^[23-26]. For instance, transition-metal dichalcogenides (e.g., MoS₂) have also been verified to increase their intrinsic hydrogen evolution activity through defect-induced asymmetric electronic structure distribution^[17, 119, 120]. Besides, defects can also be served as unique anchor sites and disperse single metal atoms on various supports. Trapping atomic metal species with defects can effectively stabilize these single metal atoms against migration and aggregation, enhance the stability of defects during electrocatalysis, and even restructured their local electronic distribution through the

diverse coordinated configurations^[23, 121-123]. Recently, Yao *et al.* reported an atomic Pt catalyst via defect engineering strategy^[124]. Remarkably, a high loading of 2.25 wt% atomic Pt is obtained, without forming Pt particles or clusters.

2.3.3 AMS Nanomaterials for Hydrogen Storage

As discussed previously, neither molecular physisorption nor atomic chemisorption can meet the targets of the DOE. The inherent issues of the two hydrogen storage methods are ascribed to the unsuitable adsorption enthalpies of hydrogen. The reported solutions are mainly focused on how to improve weak molecular physisorption, or to decrease the strong atomic chemisorption, so as to form a moderate binding energy. However, none of current materials can meet the practical application requirements. The ideal hydrogen storage materials should be reversibly operated under mild temperatures with fast charging/discharging kinetics. This means that hydrogen can be stored in molecular form, but in a weak chemisorption manner, called molecular chemisorption. This fascinating hydrogen storage method simultaneously endows materials the good reversibility as physical adsorption and moderate stability under room temperature as chemical adsorption, which may stand out as a promising hydrogen storage method.

The molecular chemisorption process can be classified into weak chemisorption involving the gas–solid interactions at the surface. Hence, the structure of adsorption sites at the surface is vital to uncovering underlying mechanism of molecular chemisorption, which is the prerequisite to both materials design and hydrogen adsorption behavior. Early in 1984, Kubas *et al.* experimentally discovered a non-dissociative form of hydrogen adsorbed onto a coordinated transition metal (TM) complex, $\text{W}(\text{CO})_3(\text{P/Pr}_3)_2$ ^[125]. In this TM complex, W atom is linked with five coordinates, and the hydrogen molecule is chemisorbed without dissociation via a side-on coordination binding to W atom. However, the bond length of hydrogen is stretched by approximately 20% longer than that of free H_2 . To explain the dihydrogen binding coordination, the Dewar-Chat-Duncanson model for TM-olefin complexes^[126] is invoked to rationalize the stability of these σ -type complexes, called Kubas-type

interaction. Similar to the Dewar-Chatt-Duncanson model with a three-center two-electron (3c-2e) bond (type I shown in Figure 2-17), the Kubas-type interaction involves σ donation from the filled σ -bonding orbital of H_2 molecule to an unfilled d orbital of a TM. Meanwhile, π back-donation (BD) occurs from a filled d orbital of a TM to the empty σ^* anti-bonding orbital of the H_2 molecule, which determines the stability of molecularly chemisorbed H_2 (type II shown in Figure 2-17).

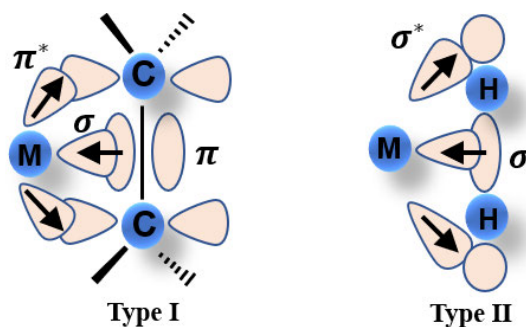


Figure 2-17. Schematic diagram showing three orbital interactions between the central element and ligand^[127]. Type I: TM-olefin complexes. Type II: Kubas-type H_2 complexes.

The non-dissociative molecular chemisorption has ever been mentioned in metal-based hydrogen storage materials. It is known that hydrogen sorption process upon metal atoms includes: physisorption, dissociation, hydrogen atom diffusion, hydride nucleation and growth. Note that the physisorbed H_2 will enter a molecular chemisorption state after crossing an activation barrier. The molecular chemisorption is generally considered as a transition state before the dissociation of hydrogen. A.-S. Martensson, C. Nyberg, and S. Andersson^[128] observed the molecular H_2 chemisorbed at the edge sites of a stepped Ni (100) surface that is covered with a dense layer of atomic hydrogen by use of low-energy electron diffraction (LEED) and EELS in conjunction. In contrast, no such state is observed on the flat Ni (100) surface. The authors ascribed the molecular chemisorption to Kubas-type interaction. They suggested that nickel atoms with lower coordination at the stepped surface possess residual unfilled d states which could stabilize the chemisorbed H_2 , while the

dissociative channel is blocked by the saturated atomic adsorbate layer. The results illustrated that it is the low-coordinated metal atoms possess the capacity of molecular chemisorption.

Recently, Julian Berwanger *et al.*^[129] reported the direct observation of chemical binding forces on single Fe atoms to study the chemical reactivity of atom-assembled Fe clusters from 1 to 15 atoms on the atomic scale. This measurement can be achieved via the scanning probe microscopy with CO-terminated tips which can transition from the physisorption to the chemisorption regime and forms a weak chemical bond with the individual atoms. It is found that the chemisorption strength increases inversely with the atom's reduced coordination number. The results imply that the regulation of atomic coordination number can enhance the interaction force between H₂ and adsorbent atoms.

Based on the self-consistent-field molecular-orbital theory, Niu and co-workers^[130] reported that the hydrogen behaves differently while approaching to a neutral metal atom (Ni) and a metal ion (Ni⁺). For a neutral metal atom, similar to the metal atoms on surfaces and in the bulk, it will transfer an electron to the approaching H₂ molecule to fill the antibonding orbital. This will lead to the bond cleavage of H-H favouring the atomic bonding between individual H atom and metal atom. In contrast, the ability of electron donation to a H₂ molecule becomes energetically inefficient for a transition metal ion due to the higher second ionization potential of the metal atom. Instead, a strong polarization effect will occur between the ion and H₂ molecule, which will enable several H₂ molecules chemisorbed in its molecular form onto a metal ion.

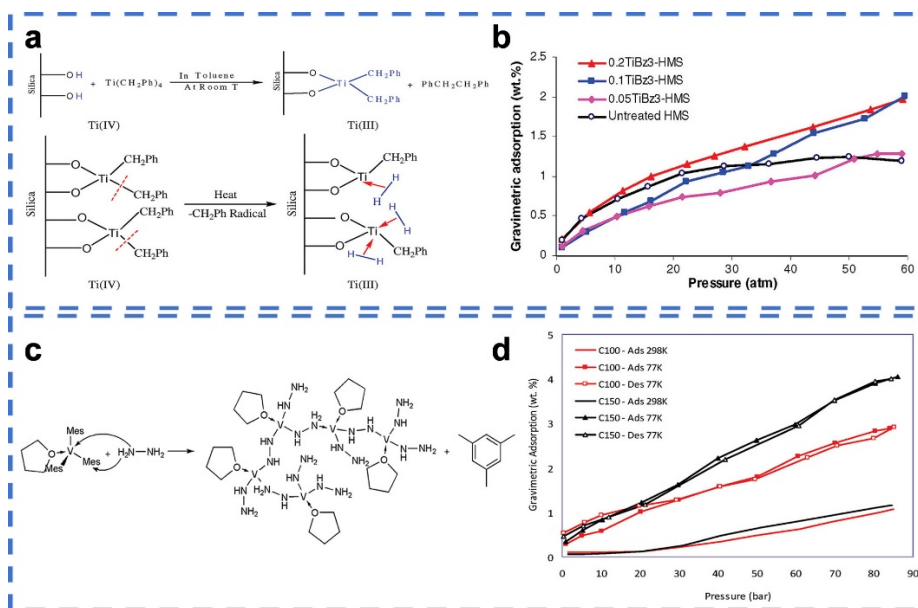


Figure 2-18. Hydrogen storage performance (via molecular chemisorption). (a) Schematic representation of the grafting of benzyl Ti species onto the surface of mesoporous silica. Reprinted with permission from^[131]. (b) Hydrogen adsorption isotherms at 77 K for mesoporous silica treated with various molar equivalents of tribenzyl titanium. Reprinted with permission from^[131]. (c) Possible mechanism for the reaction between $\text{V}(\text{Mes})_3 \cdot \text{THF}$ and N_2H_4 . Reprinted with permission from^[132]. (d) Hydrogen adsorption-desorption isotherms of vanadium hydrazide samples. Reprinted with permission from^[132].

The above analysis indicates that the low-coordinated metal atoms possess the capacity of molecular chemisorption. Previous experimental explorations further confirmed the role of the unique material structure on molecular chemisorption for hydrogen storage. Strategies of material synthesis include grafting TM atoms to surfaces of porous materials (e.g., mesoporous silica)^[131, 133] and bridging the TM atoms with light weight ligands (e.g., hydrazine) to the microporous materials^[132, 134, 135]. In 2008, Antonelli and co-workers reported an organometallic Ti fragment as the H_2 storage material^[131]. The low-coordinated Ti (III) atoms were grafted onto mesoporous silica using tri- and tetrabenzyl Ti precursors. The detailed experimental process is shown in Figure 2-18a.

It can be observed that the low valent Ti atoms are three coordinates with two O atoms and one C atom, which can act as the adsorption sites. The hydrogen storage properties in Figure 2-18b show that the highest gravimetric storage value of 2.02 wt% recorded under the condition of 60 atm and 77 K is the sample with a Ti/Si molar ratio of 0.2 (0.20 Ti/HMS), while only 1.21 wt% hydrogen can be stored by silica precursor under the same conditions. By calculations, an average of 2.7 H₂ molecules are adsorbed onto each Ti atom in 0.20 Ti/HMS. It is notable that hydrogen adsorption isotherms of Ti-grafted samples do not saturate under the condition of 60 atm and 77 K. Increasing the pressure can further increase the numbers of H₂ molecules being adsorbed, according to the Le Chatelier's principle. Moreover, the binding enthalpy for Ti (III) grafted sample, by Clausius-Clapyron equation, is determined to be 22.04 kJ/mol as compared to 3.5kJ/mol for the pristine silica materials. On the one hand, the dramatically enhanced enthalpy reflects the molecular chemisorption mechanism differing from typical physical adsorption characteristic. On the other hand, the large enthalpy guarantees around 1.1 hydrogen molecules are molecularly chemisorbed onto each Ti atom under the room temperature.

In addition to grafting techniques, vanadium hydrazide gels with isolated and coordination-unsaturated V(III) species are also fabricated using trimesitylvanadium (III) as a precursor and hydrazine as a linker^[132]. The possible reaction mechanism is given in Figure 2-18c. The vanadium atom is tri-coordinated with N atoms in vanadium hydrazide gels, though some residual tetrahydrofuran (THF) molecules bound to V atoms. The hydrogen adsorption isotherms (Figure 2-18d) present a linear hydrogen adsorption behavior, reflecting a non-dissociative hydrogen chemisorption, and up to 4.04 wt% of hydrogen are stored for sample C150 under 77 K and 85 bar. Even under room temperature, 49 % of their adsorption can be retained as opposed to 77 K, owing to its greatly enhanced adsorption enthalpies from 3 to 36.5 kJ/mol.

Apparently, developing hydrogen storage in form of molecular chemisorption will construct a new conceptual paradigm in solid-state hydrogen storage fields. The core of rationalizing materials being capable of molecular chemisorption is to fabricate low

coordinated metal atoms with unique coordination configuration. AMS nanomaterials naturally feature the low coordination number and tunable coordination environment, as the promising hydrogen storage candidate via molecular chemisorption fashion. Currently, it remains a big challenge for present fabrication processes. In addition, the underlying adsorption mechanisms via the molecular chemisorption need to be clarified, thus favouring the correlation between structure of adsorption sites with hydrogen adsorption performance.

2.4 Conclusions

In this chapter, recent progresses of hydrogen production and storage materials are summarized, including the mechanism of hydrogen production and storage, the development of materials for hydrogen production and storage. Meanwhile, the remaining issues and challenges to hydrogen production and storage materials are also highlighted. For the HER materials, extensive work has been done on developing various catalyst materials, including noble metal catalysts, non-noble metal catalysts and even metal-free catalysts. However, noble metals are still the mainstream for HER at present. The high cost of the noble metals impedes their commercial application. As to the hydrogen storage, various materials were developed to store hydrogen via chemisorption or physisorption method. In addition, strategies were reported to modify the thermodynamics and kinetics to meet the DOE's targets set for hydrogen storage materials. However, up to now, the development of hydrogen storage materials which could satisfy the DOE's standard is a much more challenging issue.

To realize the commercialization of hydrogen energy, hydrogen should be produced in affordable way, which is still a big issue to be solved. AMS nanomaterials feature the maximization of the metal utilization (up to 100%), the well-defined active centers and unique electronic structures, which stand out as the promising candidate to be used as hydrogen production materials. However, the preparation of isolated metal atoms often suffers from particle agglomeration due to the extremely high surface energies. Therefore, exploiting affordable, scalable and highly efficient AMS nanomaterials is

still a grand challenge. The precise characterization of the local active center and the origin of the structure-property correlation need to be figured out as well.

The current hydrogen storage materials still suffer from poor thermodynamics and/or sluggish kinetics. Herein, we propose a hydrogen storage method via the molecular chemisorption approach, which is different from the conventional physisorption or chemisorption. Afterward, we discussed the great potential of AMS nanomaterials to be used as hydrogen storage materials via molecular chemisorption. Obviously, rationally designing AMS nanomaterials being capable of molecular chemisorption is extremely important. The underlying adsorption mechanisms via the molecular chemisorption need to be uncovered for better design and fabrication of efficient hydrogen storage materials for practical applications.

2.5 References

1. Xiao P, Chen W and Wang X. A Review of Phosphide-Based Materials for Electrocatalytic Hydrogen Evolution. *Adv Energy Mater* 2015; 5: 1500985.
2. Zhang Y, Xiao J, Lv Q Y, et al. Self-supported transition metal phosphide based electrodes as high-efficient water splitting cathodes. *Front Chem Sci Eng* 2018; 12: 494-508.
3. Morales-Guio C G, Stern L-A and Hu X. Nanostructured hydrotreating catalysts for electrochemical hydrogen evolution. *Chem. Soc. Rev.* 2014; 43: 6555-6569.
4. Li C and Baek J-B. Recent Advances in Noble Metal (Pt, Ru, and Ir)-Based Electrocatalysts for Efficient Hydrogen Evolution Reaction. *ACS Omega* 2020; 5: 31-40.
5. Wan X-K, Wu H B, Guan B Y, et al. Confining Sub-Nanometer Pt Clusters in Hollow Mesoporous Carbon Spheres for Boosting Hydrogen Evolution Activity. *Adv. Mater.* 2020; 32: 1901349.

6. Kobayashi D, Kobayashi H, Wu D, et al. Significant Enhancement of Hydrogen Evolution Reaction Activity by Negatively Charged Pt through Light Doping of W. *J. Am. Chem. Soc.* 2020; 142: 17250-17254.
7. Liu Z, Qi J, Liu M, et al. Aqueous Synthesis of Ultrathin Platinum/Non-Noble Metal Alloy Nanowires for Enhanced Hydrogen Evolution Activity. *Angew. Chem. Int. Ed.* 2018; 57: 11678-11682.
8. Shi Y-C, Yuan T, Feng J-J, et al. Rapid fabrication of support-free trimetallic Pt₅₃Ru₃₉Ni₈ nanosponges with enhanced electrocatalytic activity for hydrogen evolution and hydrazine oxidation reactions. *J. Colloid Interface Sci.* 2017; 505: 14-22.
9. Yuan H and He Z. Platinum Group Metal-free Catalysts for Hydrogen Evolution Reaction in Microbial Electrolysis Cells. *The Chemical Record* 2017; 17: 641-652.
10. Eftekhari A. Electrocatalysts for hydrogen evolution reaction. *Int. J. Hydrogen Energy* 2017; 42: 11053-11077.
11. Zou X X and Zhang Y. Noble metal-free hydrogen evolution catalysts for water splitting. *Chem. Soc. Rev.* 2015; 44: 5148-5180.
12. Jaramillo T F, Jørgensen K P, Bonde J, et al. Identification of Active Edge Sites for Electrochemical H₂ Evolution from MoS₂ Nanocatalysts. *Science* 2007; 317: 100-102.
13. Hu W-H, Han G-Q, Liu Y-R, et al. Ultrathin MoS₂-coated carbon nanospheres as highly efficient electrocatalysts for hydrogen evolution reaction. *Int. J. Hydrogen Energy* 2015; 40: 6552-6558.
14. Anto Jeffery A, Nethravathi C and Rajamathi M. Two-Dimensional Nanosheets and Layered Hybrids of MoS₂ and WS₂ through Exfoliation of Ammoniated MS₂ (M = Mo, W). *The Journal of Physical Chemistry C* 2014; 118: 1386-1396.
15. Zhang J, Wang T, Pohl D, et al. Interface Engineering of MoS₂/Ni₃S₂ Heterostructures for Highly Enhanced Electrochemical Overall-Water-Splitting Activity. *Angew. Chem. Int. Ed.* 2016; 55: 6702-6707.

16. Li H, Tsai C, Koh A L, et al. Activating and optimizing MoS₂ basal planes for hydrogen evolution through the formation of strained sulphur vacancies. *Nat. Mater.* 2016; 15: 48-53.
17. Wang X, Zhang Y, Si H, et al. Single-Atom Vacancy Defect to Trigger High-Efficiency Hydrogen Evolution of MoS₂. *J. Am. Chem. Soc.* 2020; 142: 4298-4308.
18. Li Y, Wang H, Xie L, et al. MoS₂ Nanoparticles Grown on Graphene: An Advanced Catalyst for the Hydrogen Evolution Reaction. *J. Am. Chem. Soc.* 2011; 133: 7296-7299.
19. Jia Y, Jiang K, Wang H, et al. The Role of Defect Sites in Nanomaterials for Electrocatalytic Energy Conversion. *Chem-Us* 2019; 5: 1371-1397.
20. Tang T, Wang Z and Guan J. A review of defect engineering in two-dimensional materials for electrocatalytic hydrogen evolution reaction. *Chin. J. Catal.* 2022; 43: 636-678.
21. Zhang L, Jia Y, Yan X, et al. Activity Origins in Nanocarbons for the Electrocatalytic Hydrogen Evolution Reaction. *Small* 2018; 14: 1800235.
22. Swaminathan J, Subbiah R and Singaram V. Defect-Rich Metallic Titania (TiO_{1.23})—An Efficient Hydrogen Evolution Catalyst for Electrochemical Water Splitting. *Acs Catal* 2016; 6: 2222-2229.
23. Yan X, Jia Y and Yao X. Defective Structures in Metal Compounds for Energy-Related Electrocatalysis. *Small Structures* 2021; 2: 2000067.
24. Li W, Wang D, Zhang Y, et al. Defect Engineering for Fuel-Cell Electrocatalysts. *Adv. Mater.* 2020; 32: 1907879.
25. Liang Q, Zhang Q, Zhao X, et al. Defect Engineering of Two-Dimensional Transition-Metal Dichalcogenides: Applications, Challenges, and Opportunities. *Acs Nano* 2021; 15: 2165-2181.
26. Yu K, Lou L-L, Liu S, et al. Asymmetric Oxygen Vacancies: the Intrinsic Redox Active Sites in Metal Oxide Catalysts. *Advanced Science* 2020; 7: 1901970.

27. Zhang K, Kim H-J, Lee J-T, et al. Unconventional Pore and Defect Generation in Molybdenum Disulfide: Application in High-Rate Lithium-Ion Batteries and the Hydrogen Evolution Reaction. *ChemSusChem* 2014; 7: 2489-2495.
28. Liu X and Dai L. Carbon-based metal-free catalysts. *Nature Reviews Materials* 2016; 1: 16064.
29. Cui W, Liu Q, Cheng N, et al. Activated carbon nanotubes: a highly-active metal-free electrocatalyst for hydrogen evolution reaction. *Chem. Commun.* 2014; 50: 9340-9342.
30. Das R K, Wang Y, Vasilyeva S V, et al. Extraordinary Hydrogen Evolution and Oxidation Reaction Activity from Carbon Nanotubes and Graphitic Carbons. *Acs Nano* 2014; 8: 8447-8456.
31. Zheng Y, Jiao Y, Li L H, et al. Toward Design of Synergistically Active Carbon-Based Catalysts for Electrocatalytic Hydrogen Evolution. *Acs Nano* 2014; 8: 5290-5296.
32. Zheng Y, Jiao Y, Zhu Y, et al. Hydrogen evolution by a metal-free electrocatalyst. *Nat Commun* 2014; 5: 3783.
33. Zhang B, Wang H-H, Su H, et al. Nitrogen-doped graphene microtubes with opened inner voids: Highly efficient metal-free electrocatalysts for alkaline hydrogen evolution reaction. *Nano Res* 2016; 9: 2606-2615.
34. Jia Y, Zhang L, Du A, et al. Defect Graphene as a Trifunctional Catalyst for Electrochemical Reactions. *Adv. Mater.* 2016; 28: 9532-9538.
35. Yan X, Jia Y, Odedairo T, et al. Activated carbon becomes active for oxygen reduction and hydrogen evolution reactions. *Chem. Commun.* 2016; 52: 8156-8159.
36. Zheng Y, Jiao Y, Jaroniec M, et al. Advancing the Electrochemistry of the Hydrogen-Evolution Reaction through Combining Experiment and Theory. *Angew. Chem. Int. Ed.* 2015; 54: 52-65.

37. Durbin D J and Malardier-Jugroot C. Review of hydrogen storage techniques for on board vehicle applications. *Int. J. Hydrogen Energy* 2013; 38: 14595-14617.
38. Martin-Calvo A, Gutierrez-Sevillano J J, Matito-Martos I, et al. Identifying Zeolite Topologies for Storage and Release of Hydrogen. *J. Phys. Chem. C* 2018; 122: 12485-12493.
39. Kumar A, Janes T, Espinosa-Jalapa N A, et al. Selective Hydrogenation of Cyclic Imides to Diols and Amines and Its Application in the Development of a Liquid Organic Hydrogen Carrier. *J. Am. Chem. Soc.* 2018; 140: 7453-7457.
40. Zhang J Z, Li J, Li Y, et al., *Hydrogen generation, storage, and utilization*. Vol. 9781118140635. 2014, Hoboken, New Jersey: Wiley-Science Wise.
41. Rusman N a A and Dahari M. A review on the current progress of metal hydrides material for solid-state hydrogen storage applications. *Int. J. Hydrogen Energy* 2016; 41: 12108-12126.
42. Rosi N L, Eckert J, Eddaoudi M, et al. Hydrogen storage in microporous metal-organic frameworks. *Science* 2003; 300: 1127-1129.
43. Cheng H M, Yang Q H and Liu C. Hydrogen storage in carbon nanotubes. *Carbon* 2001; 39: 1447-1454.
44. Langmi H W, Book D, Walton A, et al. Hydrogen storage in ion-exchanged zeolites. *J. Alloys Compd.* 2005; 404: 637-642.
45. Lang C G, Ouyang L Z, Yang L L, et al. Enhanced hydrogen storage kinetics in Mg@FLG composite synthesized by plasma assisted milling. *Int. J. Hydrogen Energy* 2018; 43: 17346-17352.
46. Lang C G, Jia Y, Liu J W, et al. Dehydrogenation and reaction pathway of Perovskite-Type $\text{NH}_4\text{Ca}(\text{BH}_4)_3$. *Progress in Natural Science-Materials International* 2018; 28: 194-199.
47. Germain J, Fréchet J M J and Svec F. Nanoporous Polymers for Hydrogen Storage. *Small* 2009; 5: 1098-1111.

48. Blankenship Ii T S, Balahmar N and Mokaya R. Oxygen-rich microporous carbons with exceptional hydrogen storage capacity. *Nat Commun* 2017; 8: 1545.
49. Züttel A. Materials for hydrogen storage. *Mater. Today* 2003; 6: 24-33.
50. Zhu M, Lu Y, Ouyang L, et al. Thermodynamic Tuning of Mg-Based Hydrogen Storage Alloys: A Review. *Materials* 2013; 6: 4654-4674.
51. Wang H, Lin H J, Cai W T, et al. Tuning kinetics and thermodynamics of hydrogen storage in light metal element based systems – A review of recent progress. *J. Alloys Compd.* 2016; 658: 280-300.
52. Yang F S, Wang G X, Zhang Z X, et al. Design of the metal hydride reactors – A review on the key technical issues. *Int. J. Hydrogen Energy* 2010; 35: 3832-3840.
53. Jia Y, Sun C, Shen S, et al. Combination of nanosizing and interfacial effect: Future perspective for designing Mg-based nanomaterials for hydrogen storage. *Renewable Sustainable Energy Rev.* 2015; 44: 289-303.
54. Bardhan R, Ruminski A M, Brand A, et al. Magnesium nanocrystal-polymer composites: A new platform for designer hydrogen storage materials. *Energy Environ. Sci.* 2011; 4: 4882-4895.
55. Muthukumar P, Satheesh A, Linder M, et al. Studies on hydriding kinetics of some La-based metal hydride alloys. *Int. J. Hydrogen Energy* 2009; 34: 7253-7262.
56. Abd.Khalim Khafidz N Z, Yaakob Z, Lim K L, et al. The kinetics of lightweight solid-state hydrogen storage materials: A review. *Int. J. Hydrogen Energy* 2016; 41: 13131-13151.
57. Vijay Babu A R, Devunuri N, Manisha D R, et al. Magnesium hydrides for hydrogen storage: A mini review. *International Journal of ChemTech Research* 2014; 6: 3451-3455.

58. Uchida H T, Wagner S, Hamm M, et al. Absorption kinetics and hydride formation in magnesium films: Effect of driving force revisited. *Acta Mater.* 2015; 85: 279-289.
59. Lu Y S, Zhu M, Wang H, et al. Reversible de-/hydriding characteristics of a novel $\text{Mg}_{18}\text{In}_1\text{Ni}_3$ alloy. *Int. J. Hydrogen Energy* 2014; 39: 14033-14038.
60. Lang C, Ouyang L, Yang L, et al. Enhanced hydrogen storage kinetics in Mg@FLG composite synthesized by plasma assisted milling. *Int. J. Hydrogen Energy* 2018; 43: 17346-17352.
61. Rudman P S. Hydriding and dehydriding kinetics. *Journal of the Less Common Metals* 1983; 89: 93-110.
62. Reilly J J and Wiswall R H. Reaction of hydrogen with alloys of magnesium and nickel and the formation of Mg_2NiH_4 . *Inorg. Chem.* 1968; 7: 2254-2256.
63. Kyoji D, Sato T, Rönnebro E, et al. A new ternary magnesium–titanium hydride Mg_7TiH_x with hydrogen desorption properties better than both binary magnesium and titanium hydrides. *J. Alloys Compd.* 2004; 372: 213-217.
64. Zhong H C, Wang H, Ouyang L Z, et al. Microstructure and hydrogen storage properties of Mg-Sn nanocomposite by mechanical milling. *J. Alloys Compd.* 2011; 509: 4268-4272.
65. Chen D, Chen L, Wang Y, et al. Ca, Pd, Sn and La effects on the electronic structure of MgH_2 . *Xiyou Jinshu Cailiao Yu Gongcheng/Rare Metal Materials and Engineering* 2004; 33: 485-489.
66. Cui J, Wang H, Liu J, et al. Remarkable enhancement in dehydrogenation of MgH_2 by a nano-coating of multi-valence Ti-based catalysts. *J. Mater. Chem. A* 2013; 1: 5603-5611.
67. Bobet J-L, Akiba E and Darriet B. Effect of substitution of Fe and Ni for Co in the synthesis of Mg_2Co compound using the mechanical alloying method. *J. Alloys Compd.* 2000; 297: 192-198.
68. Dong H, Huang C, Moser D, et al. Structure and stability of high pressure synthesized MgTM_2H_6 ($\text{TM}=\text{Zr}, \text{Nb}$) hydrides. *Acta Mater.* 2015; 96: 237-248.

69. Morinaga M and Yukawa H. Nature of chemical bond and phase stability of hydrogen storage compounds. *Materials Science and Engineering: A* 2002; 329-331: 268-275.
70. Friedrichs O, Sánchez-López J C, López-Cartes C, et al. Nb₂O₅ “Pathway Effect” on Hydrogen Sorption in Mg. *The Journal of Physical Chemistry B* 2006; 110: 7845-7850.
71. Barkhordarian G, Klassen T and Bormann R. Fast hydrogen sorption kinetics of nanocrystalline Mg using Nb₂O₅ as catalyst. *Scr. Mater.* 2003; 49: 213-217.
72. Xie L, Liu Y, Wang Y T, et al. Superior hydrogen storage kinetics of MgH₂ nanoparticles doped with TiF₃. *Acta Mater.* 2007; 55: 4585-4591.
73. Luo Y, Wang P, Ma L-P, et al. Hydrogen sorption kinetics of MgH₂ catalyzed with NbF₅. *J. Alloys Compd.* 2008; 453: 138-142.
74. Jin S-A, Shim J-H, Cho Y W, et al. Dehydrogenation and hydrogenation characteristics of MgH₂ with transition metal fluorides. *J. Power Sources* 2007; 172: 859-862.
75. Mao J, Guo Z, Yu X, et al. Enhanced hydrogen sorption properties of Ni and Co-catalyzed MgH₂. *Int. J. Hydrogen Energy* 2010; 35: 4569-4575.
76. Bérubé V, Radtke G, Dresselhaus M, et al. Size effects on the hydrogen storage properties of nanostructured metal hydrides: A review. *Int. J. Energy Res.* 2007; 31: 637-663.
77. Berube V, Chen G and Dresselhaus M S. Impact of nanostructuring on the enthalpy of formation of metal hydrides. *Int. J. Hydrogen Energy* 2008; 33: 4122-4131.
78. Wang A, Li J and Zhang T. Heterogeneous single-atom catalysis. *Nat Rev Chem* 2018; 2: 65-81.
79. Cui X J, Li W, Ryabchuk P, et al. Bridging homogeneous and heterogeneous catalysis by heterogeneous single-metal-site catalysts. *Nature Catalysis* 2018; 1: 385-397.

80. Zhang Y, Guo L, Tao L, et al. Defect-Based Single-Atom Electrocatalysts. *Small Methods* 2019; 3: 1800406.
81. Ramalingam V, Varadhan P, Fu H-C, et al. Heteroatom-Mediated Interactions between Ruthenium Single Atoms and an MXene Support for Efficient Hydrogen Evolution. *Adv. Mater.* 2019; 31: 1903841.
82. Zhang Z, Zhu Y, Asakura H, et al. Thermally stable single atom Pt/m-Al₂O₃ for selective hydrogenation and CO oxidation. *Nat Commun* 2017; 8: 16100.
83. Lin J, Wang A, Qiao B, et al. Remarkable Performance of Ir₁/FeO_x Single-Atom Catalyst in Water Gas Shift Reaction. *J. Am. Chem. Soc.* 2013; 135: 15314-15317.
84. Liang J-X, Lin J, Liu J, et al. Dual Metal Active Sites in an Ir₁/FeO_x Single-Atom Catalyst: A Redox Mechanism for the Water-Gas Shift Reaction. *Angew. Chem. Int. Ed.* 2020; 59: 12868-12875.
85. Li J, Banis M N, Ren Z, et al. Unveiling the Nature of Pt Single-Atom Catalyst during Electrocatalytic Hydrogen Evolution and Oxygen Reduction Reactions. *Small* 2021; 17: 2007245.
86. Hossain M D, Liu Z, Zhuang M, et al. Rational Design of Graphene-Supported Single Atom Catalysts for Hydrogen Evolution Reaction. *Adv Energy Mater* 2019; 9: 1803689.
87. Yang X-F, Wang A, Qiao B, et al. Single-Atom Catalysts: A New Frontier in Heterogeneous Catalysis. *Acc. Chem. Res.* 2013; 46: 1740-1748.
88. Su J W, Ge R X, Dong Y, et al. Recent progress in single-atom electrocatalysts: concept, synthesis, and applications in clean energy conversion. *J. Mater. Chem. A* 2018; 6: 14025-14042.
89. Zhang H B, Liu G G, Shi L, et al. Single-Atom Catalysts: Emerging Multifunctional Materials in Heterogeneous Catalysis. *Adv Energy Mater* 2018; 8.
90. Li X, Bi W, Zhang L, et al. Single-Atom Pt as Co-Catalyst for Enhanced Photocatalytic H₂ Evolution. *Adv. Mater.* 2016; 28: 2427-2431.

91. Chen Y, Ji S, Wang Y, et al. Isolated Single Iron Atoms Anchored on N-Doped Porous Carbon as an Efficient Electrocatalyst for the Oxygen Reduction Reaction. *Angew. Chem. Int. Ed.* 2017; 56: 6937-6941.
92. Wang X, Chen W, Zhang L, et al. Uncoordinated Amine Groups of Metal–Organic Frameworks to Anchor Single Ru Sites as Chemoselective Catalysts toward the Hydrogenation of Quinoline. *J. Am. Chem. Soc.* 2017; 139: 9419-9422.
93. Wang J, Han G, Wang L, et al. ZIF-8 with Ferrocene Encapsulated: A Promising Precursor to Single-Atom Fe Embedded Nitrogen-Doped Carbon as Highly Efficient Catalyst for Oxygen Electoreduction. *Small* 2018; 14: 1704282.
94. Wang J, Huang Z, Liu W, et al. Design of N-Coordinated Dual-Metal Sites: A Stable and Active Pt-Free Catalyst for Acidic Oxygen Reduction Reaction. *J. Am. Chem. Soc.* 2017; 139: 17281-17284.
95. Wang T, Kou Z, Mu S, et al. 2D Dual-Metal Zeolitic-Imidazolate-Framework-(ZIF)-Derived Bifunctional Air Electrodes with Ultrahigh Electrochemical Properties for Rechargeable Zinc–Air Batteries. *Adv. Funct. Mater.* 2018; 28: 1705048.
96. Ren W, Tan X, Yang W, et al. Isolated Diatomic Ni-Fe Metal–Nitrogen Sites for Synergistic Electoreduction of CO₂. *Angew. Chem. Int. Ed.* 2019; 58: 6972-6976.
97. Han A, Wang B, Kumar A, et al. Recent Advances for MOF-Derived Carbon-Supported Single-Atom Catalysts. *Small Methods* 2019; 0: 1800471.
98. Yin P Q, Yao T, Wu Y, et al. Single Cobalt Atoms with Precise N-Coordination as Superior Oxygen Reduction Reaction Catalysts. *Angew Chem Int Edit* 2016; 55: 10800-10805.
99. Zhao C M, Dai X Y, Yao T, et al. Ionic Exchange of Metal Organic Frameworks to Access Single Nickel Sites for Efficient Electoreduction of CO₂. *J. Am. Chem. Soc.* 2017; 139: 8078-8081.

100. Wang X Q, Chen Z, Zhao X Y, et al. Regulation of Coordination Number over Single Co Sites: Triggering the Efficient Electroreduction of CO₂. *Angew Chem Int Edit* 2018; 57: 1944-1948.
101. Yang Y, Mao K, Gao S, et al. O-, N-Atoms-Coordinated Mn Cofactors within a Graphene Framework as Bioinspired Oxygen Reduction Reaction Electrocatalysts. *Adv. Mater.* 2018; 30: 1801732.
102. Chen W, Pei J, He C-T, et al. Single Tungsten Atoms Supported on MOF-Derived N-Doped Carbon for Robust Electrochemical Hydrogen Evolution. *Adv. Mater.* 2018; 30: 1800396.
103. Qu Y, Li Z, Chen W, et al. Direct transformation of bulk copper into copper single sites via emitting and trapping of atoms. *Nature Catalysis* 2018; 1: 781-786.
104. Qu Y, Chen B, Li Z, et al. Thermal Emitting Strategy to Synthesize Atomically Dispersed Pt Metal Sites from Bulk Pt Metal. *J. Am. Chem. Soc.* 2019; 141: 4505-4509.
105. Liu P, Zhao Y, Qin R, et al. Photochemical route for synthesizing atomically dispersed palladium catalysts. *Science* 2016; 352: 797-800.
106. Zhuang L, Jia Y, Liu H, et al. Defect-Induced Pt–Co–Se Coordinated Sites with Highly Asymmetrical Electronic Distribution for Boosting Oxygen-Involving Electrocatalysis. *Adv. Mater.* 2019; 31: 1805581.
107. Wei H, Huang K, Wang D, et al. Iced photochemical reduction to synthesize atomically dispersed metals by suppressing nanocrystal growth. *Nat Commun* 2017; 8: 1490.
108. Zhou P, Hou X, Chao Y, et al. Synergetic interaction between neighboring platinum and ruthenium monomers boosts CO oxidation. *Chem Sci* 2019.
109. Sun S, Zhang G, Gauquelin N, et al. Single-atom Catalysis Using Pt/Graphene Achieved through Atomic Layer Deposition. *Scientific Reports* 2013; 3.
110. Cheng N, Stambula S, Wang D, et al. Platinum single-atom and cluster catalysis of the hydrogen evolution reaction. *Nat Commun* 2016; 7: 13638.

111. Huang X H, Xia Y J, Cao Y J, et al. Enhancing both selectivity and coking-resistance of a single-atom Pd₁/C₃N₄ catalyst for acetylene hydrogenation. *Nano Res* 2017; 10: 1302-1312.
112. Yan H, Lin Y, Wu H, et al. Bottom-up precise synthesis of stable platinum dimers on graphene. *Nat Commun* 2017; 8.
113. Cheng N and Sun X. Single atom catalyst by atomic layer deposition technique. *Chin. J. Catal.* 2017; 38: 1508-1514.
114. Cheng N C, Stambula S, Wang D, et al. Platinum single-atom and cluster catalysis of the hydrogen evolution reaction. *Nat Commun* 2016; 7.
115. Zhang L, Jia Y, Gao G, et al. Graphene Defects Trap Atomic Ni Species for Hydrogen and Oxygen Evolution Reactions. *Chem-US* 2018; 4: 285-297.
116. Fan L, Liu P F, Yan X, et al. Atomically isolated nickel species anchored on graphitized carbon for efficient hydrogen evolution electrocatalysis. *Nat Commun* 2016; 7: 10667.
117. Wang Q, Lei Y, Wang D, et al. Defect engineering in earth-abundant electrocatalysts for CO₂ and N₂ reduction. *Energy Environ. Sci.* 2019; 12: 1730-1750.
118. Tang C, Wang H-F and Zhang Q. Multiscale Principles To Boost Reactivity in Gas-Involving Energy Electrocatalysis. *Acc. Chem. Res.* 2018; 51: 881-889.
119. Lai Z, Chaturvedi A, Wang Y, et al. Preparation of 1T'-Phase ReS₂xSe₂(1-x) (x = 0–1) Nanodots for Highly Efficient Electrocatalytic Hydrogen Evolution Reaction. *J. Am. Chem. Soc.* 2018; 140: 8563-8568.
120. Yang J, Wang Y, Lagos M J, et al. Single Atomic Vacancy Catalysis. *Acs Nano* 2019; 13: 9958-9964.
121. Wan J, Chen W, Jia C, et al. Defect Effects on TiO₂ Nanosheets: Stabilizing Single Atomic Site Au and Promoting Catalytic Properties. *Adv. Mater.* 2018; 30: 1705369.
122. Rivera-Cárcamo C, Scarfiello C, García A B, et al. Stabilization of Metal Single Atoms on Carbon and TiO₂ Supports for CO₂ Hydrogenation: The Importance

- of Regulating Charge Transfer. *Advanced Materials Interfaces* 2021; 8: 2001777.
123. Zhu J, Tu Y, Cai L, et al. Defect-Assisted Anchoring of Pt Single Atoms on MoS₂ Nanosheets Produces High-Performance Catalyst for Industrial Hydrogen Evolution Reaction. *Small* 2022; 18: 2104824.
 124. Zhuang L, Jia Y, Liu H, et al. Defect-Induced Pt–Co–Se Coordinated Sites with Highly Asymmetrical Electronic Distribution for Boosting Oxygen-Involving Electrocatalysis. *Adv. Mater.* 2018; 0: 1805581.
 125. Kubas G J, Ryan R R, Swanson B I, et al. Characterization of the first examples of isolable molecular hydrogen complexes, $M(CO)_3(PR_3)_2(H_2)$ (M = molybdenum or tungsten; R = Cy or isopropyl). Evidence for a side-on bonded dihydrogen ligand. *J. Am. Chem. Soc.* 1984; 106: 451-452.
 126. Mingos D M P, *Recent Developments in Theoretical Organometallic Chemistry*, in *Adv. Organomet. Chem.*, FGA Stone and R West, Editors. 1977, Academic Press. p. 1-51.
 127. Lang C, Jia Y, Yan X, Ouyang L, Zhu M, Yao X. Molecular chemisorption: a new conceptual paradigm for hydrogen storage. *Chem Synth* 2022; 2:1.
 128. Mårtensson A S, Nyberg C and Andersson S. Observation of Molecular H₂ Chemisorption on a Nickel Surface. *Phys. Rev. Lett.* 1986; 57: 2045-2048.
 129. Berwanger J, Polesya S, Mankovsky S, et al. Atomically Resolved Chemical Reactivity of Small Fe Clusters. *Phys. Rev. Lett.* 2020; 124: 096001.
 130. Niu J, Rao B K and Jena P. Binding of hydrogen molecules by a transition-metal ion. *Phys. Rev. Lett.* 1992; 68: 2277-2280.
 131. Hamaed A, Trudeau M and Antonelli D M. H₂ Storage Materials (22KJ/mol) Using Organometallic Ti Fragments as σ -H₂ Binding Sites. *J. Am. Chem. Soc.* 2008; 130: 6992-6999.
 132. Hoang T K A, Webb M I, Mai H V, et al. Design and Synthesis of Vanadium Hydrazide Gels for Kubas-Type Hydrogen Adsorption: A New Class of Hydrogen Storage Materials. *J. Am. Chem. Soc.* 2010; 132: 11792-11798.

133. Hoang T K A, Hamaed A, Trudeau M, et al. Bis(benzene) and Bis(cyclopentadienyl) V and Cr Doped Mesoporous Silica with High Enthalpies of Hydrogen Adsorption. *The Journal of Physical Chemistry C* 2009; 113: 17240-17246.
134. Xu G, Pareek K, Li N, et al. High capacity hydrogen storage at room temperature via physisorption in a coordinatively unsaturated iron complex. *Int. J. Hydrogen Energy* 2015; 40: 16330-16337.
135. Hoang T K A, Hamaed A, Moula G, et al. Kubas-Type Hydrogen Storage in V(III) Polymers Using Tri- and Tetradentate Bridging Ligands. *J. Am. Chem. Soc.* 2011; 133: 4955-4964.

Chapter 3. Experimental Methodologies

3.1 Materials

Commercial molybdenum disulfide (MoS_2 , 99.5%, $<2\ \mu\text{m}$) was bought from Aladdin, aluminum oxide was purchased from Aladdin, ruthenium trichloride ($\text{RuCl}_3 \cdot x\text{H}_2\text{O}$) was brought from Sigma. Cobalt(II) oxide (CoO , $<2\ \mu\text{m}$, 99.99%, Aladdin) was purchased from Macklin. Titanium oxide nano powders was bought from Aladdin. All the chemicals were used without further purifications or any other treatment.

3.2 Synthesis of Samples

Preparation of defective MoS_2 : 1.5g of commercial molybdenum disulfide (C- MoS_2) and 0.5 g of aluminum oxide (Al_2O_3 , 6~7 μm) were mixed in a stainless vial, and the ball-to-powder ratio was set to 50:1. Then, the high-energy mechanochemical milling (HEMM) was conducted to the mixed powder under Ar atmosphere with a vibration type ball mill at the constant rotation speed of 450 rpm. The $\text{Al}_2\text{O}_3@\text{MoS}_2$ complex was obtained by HEMM for 10 h. After HEMM, the complex was dispersed into 2M HCl solution and stirred over 12 h to remove the Al_2O_3 . Then, the defective MoS_2 was collected by centrifugation and washing, and then was dried in an oven at 80 °C over 12 h.

Preparation of isolated Ru atoms doped defective MoS_2 : typically, 200 mg of defective MoS_2 was dispersed in deionized water by ultrasonication for 10 min. Then, 2 mL of RuCl_3 solution (5.0 mM) was added to the above dispersion and stirred for 2 h. Afterward, the solution was dried at 80 °C and then further annealed under hydrogen atmosphere at 200 °C for 2 h. To prepare the catalysts with different Ru loading amount, different amounts (0.5, 1.0 and 4 mL) of RuCl_3 solution can be added. For comparison, commercial MoS_2 supported Ru particle ($\text{Ru}@C\text{-MoS}_2$) was also prepared using commercial MoS_2 as the support and RuCl_3 solution as the Ru precursor.

Synthesis of $\text{Co}_3\text{O}_4@\text{MoS}_2$: In a typical process, 1 g of bulk MoS_2 and CoO mixtures were put into a stainless ball milling jar containing stainless steel balls. The mass ratio (ball-to-powder) was set to 60:1 at the start. The mechanochemical reaction was then

undertaken under Ar atmosphere at 450 rpm for 12 h using a type of planetary ball mill (QM-3SP4, Nanjing, China) at room temperature. After ball milling, the as obtained homogeneous mixtures were dispersed in HCl (2 M) solution for 24 h to remove the CoO. After filtration and rinse by water and ethanol several times, the obtained product was further dried at 80 °C overnight. The final products were collected and marked as Co@MoS₂-x (x=0.1, 0.2 0.4), here x means the mass of CoO in MoS₂/CoO mixture.

Synthesis of milled MoS₂ (M-MoS₂): the preparation process is similar to that of Co@MoS₂, but without the addition of CoO.

Synthesis of Ni₃O₄@MoS₂ and Fe₃O₄@MoS₂: the HMBM process is similar to the synthesis of Co₃O₄@MoS₂. In brief, 0.4 g of NiO and Fe₂O₃ were ball milled with 0.6 g MoS₂, respectively. Then the ball-milled products were treated with HCl (2M) solution. After following filtering and drying, the final Ni₃O₄@MoS₂ and Fe₃O₄@MoS₂ were obtained.

Synthesis of defective TiO₂: to prepare TiO₂-x (x=200, 300, and 400) samples, the TiO₂ nano powders was annealed under hydrogen atmosphere at various temperature (200, 300, and 400 °C). After annealing , the samples are collected and stored in the glove box filled with Argon.

Preparation of Ti₁@C-x: 0.5 g of Titanyl phthalocyanine (TiOPc) and carbon black (CB) mixtures were loaded into a stainless jars containing stainless steel balls. Here, x represents the loading amount of TiOPc. The synthesis of Ti₁@C-x was conducted via a simple mechanical ball milling in Ar for 10 h using a QM-3SP4 planetary ball miller. The mill was operated at 250 rpm by repeating milling (for 30 min) and cooling (for 30 min). After ball milling, the samples were collected and stored in an Ar-filled glovebox.

3.3 Characterization

X-Ray Powder Diffraction

X-Ray Powder Diffraction (XRD) is used for phase identification analysis and determining crystal structure of crystalline materials. Here, the XRD data was collected on a powder diffractometer (XRD, PANalytical X'PERT) using Cu K α radiation ($\lambda = 1.5406 \text{ \AA}$).

Scanning Electron Microscopy

Surface morphologies of the prepared samples are analyzed by field emission scanning electron microscopy (FE-SEM, TESCAN GAIA3) equipped with energy dispersive X-ray spectroscopy.

Transmission Electron Microscopy

Transmission electron microscopy (TEM) and high-resolution TEM (HRTEM) were conducted using a JEM-2100F (JEOL Co., Japan) microscope.

Brunauer-Emmett-Teller (BET) Surface Area

The nitrogen adsorption/desorption isotherms were measured with a Quadrachrome adsorption instrument.

X-ray Photoelectron Spectroscopy

X-ray photoelectron spectroscopy (XPS) was performed on (ESCALAB 250 Xi) with an ESCALAB 250Xi spectrometer (Thermo Fisher Scientific) using an Al K α (1486.6 eV) excitation source and fitted with CasaXPS software.

Raman Spectroscopy

Raman spectra of the samples were recorded using a Thermo Fisher Micro DXR microscope excited by a He-Ne laser (532 nm) at a resolution of 2 cm^{-1} .

Inductively Coupled Plasma Atomic Emission Spectrometry

The content of gold and ruthenium was determined by inductively coupled plasma atomic emission spectrometry (ICP-AES).

UV-Vis Spectroscopy

The UV–Vis absorption spectra were recorded with a UV–vis spectrophotometer (U-3310) equipped with a diffuse-reflectance attachment.

High-Angle Annular Dark Field -Scanning Transmission Electron Microscopy

Aberration-corrected HAADF-STEM measurements were taken on a JEM-ARM200F instrument at 200 keV. Meanwhile, energy-dispersive X-ray elemental mapping was also collected on the same equipment.

X-Ray Absorption Spectra

X-ray absorption spectra (XAS) were obtained at the National Synchrotron Radiation Research Center (NSRRC), Hsinchu, Taiwan, ROC, and the hard X-ray absorption data for the Mo, Ru K-edge and Ti K T were collected at beamline BL17C.

3.4 Electrochemical Performance Evaluation

The catalyst ink was fabricated by sonicating the active catalyst in 1 mL of 1:1 v/v water/ethanol with 50 μL 5 wt% Nafion solution for more than 1 h to form a homogeneous ink. Then, 4 μL of the catalyst ink was drop-cast onto a freshly polished glassy carbon electrode of 5 mm in diameter. All the electrochemical performance tests were evaluated in a three-electrode system on an electrochemical workstation (CHI660E). A glassy carbon electrode was used as the working electrode, a Hg/HgO electrode (1M KOH) as the reference electrode, and a graphite rod as the counter electrode. Linear sweep voltammetry tests with a scan rate of 5 mVs^{-1} were conducted in 1.0 M KOH. Before test, the catalyst was repeatedly CV cycling in the electrolyte until steady voltammogram curve was obtained. Electrochemical impedance spectroscopy (EIS) was performed with a frequency from 0.01 to 100k Hz and amplitude of 5 mV. Electrochemical active surface areas (ECSA) were obtained by measuring electrochemical double layer capacitance (Cdl) of catalysts.

To evaluate catalytic stability, the prepared ink was dropped onto fresh carbon cloth and

then assessed by measuring the current density versus the time curve of the catalyst at constant voltages in the alkaline condition.

3.5 Hydrogen Storage Performance Test

The hydrogen adsorption performance tests were conducted by ASAP 2020 Micromeritics sorption analyzer under 77 K using 99.9999% purity hydrogen. Before test, the samples were degassed at 180 °C for 6 h under continuously vacuum. The hydrogen storage properties under high pressure were determined by using a homemade HPSA-auto apparatus

3.6 DFT Calculations

Hydrogen evolution reaction

All density functional theory (DFT) calculations of a series of 4×4 supercells monolayer MoS₂ were implemented using the Vienna ab initio simulation package (VASP), where the projector-augmented wave (PAW) method was adopted within the Perdew-Burke-Ernzerhof generalized gradient approximation (GGA) for the exchange-correlation functional^[1, 2]. A plane-wave kinetic energy cutoff energy of 400 eV and a k-points mesh with $4 \times 4 \times 1$ was applied. For all structures, the spin polarized calculations were considered. In addition, the structure optimization was fully conducted until the energy difference tolerance and the total force were less than 1×10^{-6} eV atom⁻¹ and 0.01 eV Å⁻¹, respectively. A vacuum layer of 12 Å along the z direction was introduced to prevent interactions between adjacent sheets.

Calculation of formation energies

The formation energies of S vacancy (E_{sv}) were calculated by the following formula^[3, 4]:

$$E_{sv} = E_{MoS_2-S} - E_S - E_{MoS_2} \quad (3-1)$$

where E_{MoS_2} is the total energy for MoS₂ with S vacancy, E_{MoS_2} is the energy for optimal monolayer MoS₂, and E_S is the energy of one S atom.

The Formation energies of Ru-doped MoS₂ configurations (E_f) were calculated by the following formula ^[3, 4]:

$$E_{sv} = E_{MoS_2-S} - E_S - E_{MoS_2} \quad (3-2)$$

where E_{total} is the total energy for MoS₂ with doped Ru metal atoms. In the cases of the metal supported on MoS₂, E_{MoS_2} is the energy for perfect MoS₂, while for the cases of Ru-doped MoS₂, E_{MoS_2} is the energy for MoS₂ with one Mo or S vacancy. E_{Ru} is the energy of one metal atom in its bulk phase.

At 298 K and 1 atm, Gibbs free energy ΔG of the adsorption species was calculated according to ^[5, 6] :

$$\Delta G = \Delta E + \Delta ZPE - T\Delta S \quad (3-3)$$

where ΔE is the adsorption energy of adsorbed species on the monolayer MoS₂, ΔZPE and $T\Delta S$ are the zero-point energy and entropy difference of species in the adsorbed state and the gas phase, respectively. For the key process of water dissociation on MoS₂, the value of ($\Delta ZPE - T\Delta S$) is ca. 0.47 eV. For the hydrogen generation process, the value of ($\Delta ZPE - T\Delta S$) is ca. 0.22 eV.

Hydrogen Storage

All DFT calculations were carried out using Vienna ab-initio simulation package (VASP) ^[2, 7, 8]. The generalized gradient approximation (GGA) of the Perdew-Burke-Ernzerhof (PBE) type^{9, 10} and the projector augmented wave (PAW) ^[11] method were applied for the exchange-correlation potential and the electron-core interaction respectively. The plane-wave energy cutoff was set to 400 eV and only the Gamma point was included in our calculations. The structure of our model was relaxed until the residual force per atom was less than 0.03 eV/Å and the convergence criteria of energy

was set to 10^{-5} eV to achieve accurate adsorption energy. Grimme method^[12] was applied to include the van der Waals (vdW) interactions. The anatase surface was constructed by using a slab model with 4 TiO₂ layers (144 atoms) along z-direction. The thickness of vacuum space was larger than 15 Å to eliminate influence of period images.

3.7 References

1. G. Kresse and J. Hafner, *Phys. Rev. B*, 1993, **47**, 558-561.
2. G. Kresse and J. Furthmüller, *Phys. Rev. B*, 1996, **54**, 11169-11186.
3. J. Zhang, X. Xu, L. Yang, D. Cheng and D. Cao, *Small Methods*, 2019, **3**, 1900653.
4. J. Ge, D. Zhang, Y. Qin, T. Dou, M. Jiang, F. Zhang and X. Lei, *Appl. Catal., B* 2021, **298**, 120557.
5. V. Wang, N. Xu, J.-C. Liu, G. Tang and W.-T. Geng, *Comput. Phys. Commun.* , 2021, **267**, 108033.
6. L. Zhuang, Y. Jia, H. Liu, X. Wang, R. K. Hocking, H. Liu, J. Chen, L. Ge, L. Zhang, M. Li, C.-L. Dong, Y.-C. Huang, S. Shen, D. Yang, Z. Zhu and X. Yao, *Adv. Mater.* , 2019, **31**, 1805581.
7. G. Kresse and J. Furthmüller, *Comput. Mater. Sci.*, 1996, **6**, 15-50.
8. G. Kresse and J. Hafner, *Phys. Rev. B*, 1994, **49**, 14251-14269.
9. J. P. Perdew, K. Burke and M. Ernzerhof, *Phys. Rev. Lett.*, 1996, **77**, 3865.
10. J. P. Perdew, M. Ernzerhof and K. Burke, *J. Chem. Phys.*, 1996, **105**, 9982-9985.
11. G. Kresse and D. Joubert, *Phys. Rev. B*, 1999, **59**, 1758-1775.
12. S. Grimme, *J. Comput. Chem.*, 2006, **27**, 1787-1799.

Chapter 4. Facile and Scalable Mechanochemical Synthesis of Defective MoS₂ with Single Atoms toward Highly Efficient Hydrogen Evolution

STATEMENT OF CONTRIBUTION TO CO-AUTHORED PUBLISHED PAPER


This chapter includes a co-authored paper. The status of the co-authored paper, including all authors, are:

Chengguang Lang, Wenbin Jiang, Cheng-Jie Yang, Hao Zhong, Peirong Chen, Chung-Li Dong, Yue Lin, Xuecheng Yan, Liuzhang Ouyang, Yi Jia, Xiangdong Yao

My contribution to the paper involved:

- Literature survey
- Concept and design
- Analysis and interpretation of data
- Drafting and writing

(Signed)  (Date) 31/07/2022
Chengguang Lang

(Countersigned)  (Date) 02/08/2022
Corresponding author of paper: Prof. Xiangdong Yao

(Countersigned)  (Date) 31/07/2022
Supervisor: Dr. Xuecheng Yan

4.1 Introduction

Electrocatalytic water splitting is considered as a sustainable and environmental process for hydrogen generation, while the electrocatalytic efficiency largely relies on the catalytic activity of electrocatalysts ^[1-3]. Recently, constructing active sites via defect engineering has emerged as a new perspective and it has been demonstrated to be an effective strategy to enhance the hydrogen evolution performance by several groups ^[4-7]. The introduction of defects can effectively tune the electrocatalytic performance of catalysts by regulating their electronic structures, and thus improving the catalytic activity^[8-11]. For instance, Yao *et al.* reported a defective graphene (DG) via N doping and removal for electrochemical hydrogen evolution reaction (HER), which exhibits significantly improved HER activities as compared to both the pristine graphene and N-doped graphene. Further HAADF-STEM images and DFT calculations reveal that 7557 defects are the major active sites for the HER^[12]. Similarly, transition-metal dichalcogenides (e.g., MoS₂) have also been found to increase the intrinsic hydrogen evolution activity through defect-induced asymmetric electronic structure distribution^[13-15]. Different methods such as plasma engraving^[16], H₂ annealing^[17], chemical etching^[14], electrochemical desulfurization^[18] and laser irradiation^[19], have been successfully developed with the aim of generating defects, or alternatively, bottom-up approaches were followed to directly synthesized MoS₂ nanostructures with abundant defects^[20, 21]. However, the execution of above-mentioned defect preparation methods is not only complicated and/or time-consuming, but also expensive and in high demand of apparatus^[39]. In addition, none of these methods can satisfy the demands for large-scale commercial preparation. Therefore, it is particularly imperative to explore a facile and applicable strategy for the scalable fabrication of HER catalysts with well-defined structures.

Currently, high-energy mechanochemical ball milling (HMBM) is gaining increasingly research attention in catalyst preparation because of its eco-friendly, scalable, and reproducible nature^[22-24]. HMBM is a mechanical process that enables the purposeful

execution of physical and chemical transformations in powder materials^[25]. Typically, under the shear force and impact force, the HMBM process involves constant deformation, fracturing and cold welding of materials during repeated collisions with a ball, which is not only widely used in the materials fabrication, but also used in the modification of materials, such as exfoliation, refinement and even the creation of defects^[26, 27]. For example, Kim *et al.* reported the synthesis of single atoms catalysts via the ball milling strategy^[28]. By ball milling Pt precursors (K_2PtCl_4) with nitrogen-doped carbon supports, the Pt single atom catalyst is directly obtained with a loading amount of 1.92 wt%, exhibiting 17-fold enhancement in mass activity as compared to the commercial 20 wt% Pt/C for the electrochemical hydrogen evolution. In addition, the HMBM is extensively used for the preparation of few-layer 2D materials, like graphene, BN, and C_3N_4 ^[29-33]. Besides the synthesis and modification of materials, the merits of easy operation, short fabrication time, mild operation conditions (room temperature and atmospheric pressure) and low-cost, naturally endow HMBM with great potential for commercial applications.

Herein, the high-energy mechanochemical ball milling strategy is adopted for the mass preparation of defective molybdenum disulfide (MoS_2). Meanwhile, atomically dispersed Ru atoms are also introduced to further modify the defective MoS_2 ($Ru_1/D-MoS_2$). The XANES results reveal that the atomic Ru doping could generate S vacancies, which can break the symmetry of electronic density around the Ru atoms, leading to the redistribution of local charge. This unique asymmetric structure of center Ru atoms in the $Ru_1/D-MoS_2$ catalyst could remarkably enhance its catalytic activity in an alkaline electrolyte, greatly exceeding the nanoparticle counterparts, demonstrating its extremely high industrial potential. Further DFT calculations indicate that the asymmetrical electronic distribution of $Ru_1/D-MoS_2$ can effectively optimize the adsorption energy of intermediates to accelerate water dissociation and increase the electron transport along the $Ru_1@D-MoS_2$ sheet, and therefore resulting in the remarkably improved HER catalytic activity.

4.2 Results and discussion

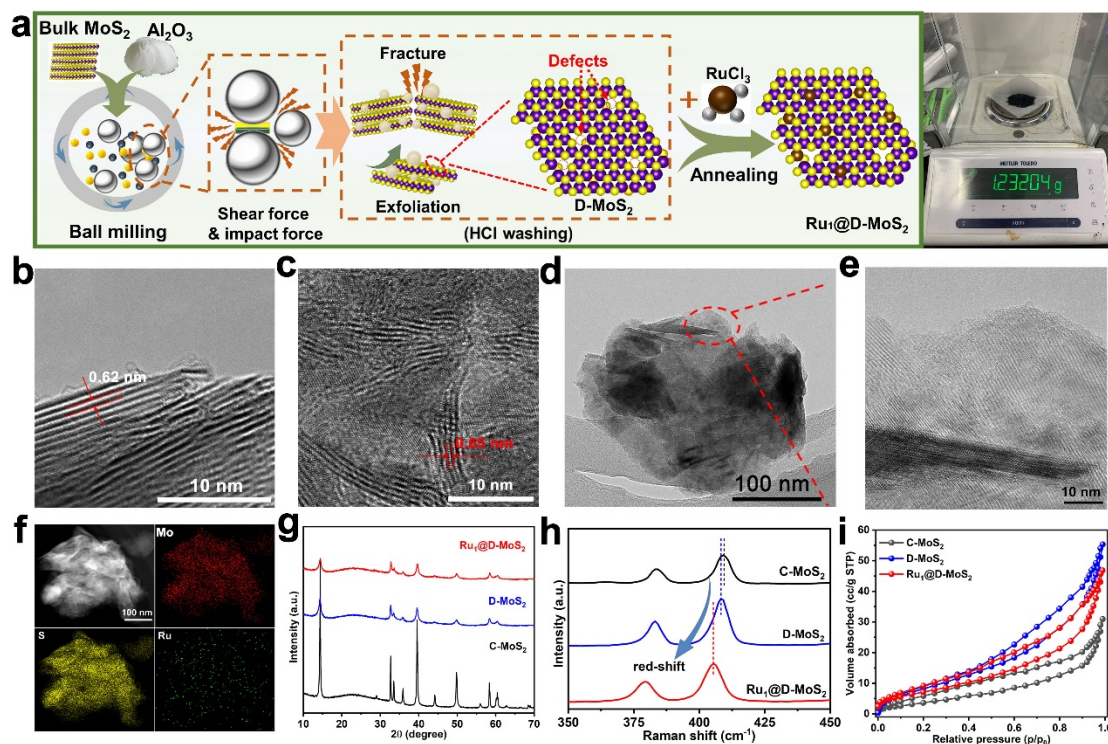


Figure 4-1. Preparation and morphology characterization of $\text{Ru}_1@\text{D-MoS}_2$. (a) Schematic illustration for the synthetic process of $\text{Ru}_1@\text{D-MoS}_2$. (b) HRTEM image of commercial MoS_2 . (c) HRTEM image of D-MoS_2 . (d and e) TEM (d) and HRTEM (e) image of $\text{Ru}_1@\text{D-MoS}_2$. (f) EDS mapping of $\text{Ru}_1@\text{D-MoS}_2$. (g) XRD patterns of C-MoS_2 , D-MoS_2 and $\text{Ru}_1@\text{D-MoS}_2$. (h) Representative Raman spectra for C-MoS_2 , D-MoS_2 and $\text{Ru}_1@\text{D-MoS}_2$, respectively. (i) The Brunauer–Emmett–Teller (BET) measurements for C-MoS_2 , D-MoS_2 and $\text{Ru}_1@\text{D-MoS}_2$, respectively.

The schematic illustration of the preparation of Ru doped defective MoS_2 ($\text{Ru}_1@\text{D-MoS}_2$) is shown in Figure 4-1a. Here, different from the reported defect preparation methods, such as plasma engraving^[16], H_2 annealing^[17], and chemical etching^[14], HMBM strategy is applied to exclude chalcogen atoms for the mass preparation of defective MoS_2 . To effectively downsize the particle size and create defects in the bulk MoS_2 , we introduce the rigid Al_2O_3 as an efficient pulverization during HMBM. The

introduction of Al₂O₃ friction can exert a friction force to enhance the shear effect, which can easily break the weak interplanar van der Waals interactions and strengthen the relative motion between the MoS₂ layers, thus facilitating the exfoliation of bulk MoS₂. Simultaneously, the impact force generated by milling balls can enable the insertion of Al₂O₃ into MoS₂, which can effectively fracture the bulk MoS₂ and create abundant defects. Specifically, 1.5 g of commercial MoS₂ (~2 μm) was ball milled with rigid Al₂O₃. After the ball milling, the mixture was dispersed into 2M HCl solution to remove the Al₂O₃. Then the defective MoS₂ was obtained after drying for 12 h in an oven. To obtain atomic Ru doped defective MoS₂, 2 mL of RuCl₃ (5.0 mM) solution was dropped into the prepared D-MoS₂ solution. After stirring for 6 h, the solution was dried via heating at 80 °C. Afterward, the atomic catalyst Ru@D-MoS₂-2 mL (named as Ru₁@D-MoS₂) was obtained via annealing the sample at 200 °C under hydrogen atmospheres.

The as-obtained catalysts were firstly characterized by TEM analysis. After HMBM, the high-resolution TEM (HRTEM) image of D-MoS₂ in Figure 4-1c shows that the layer spacing is 0.65 nm, which is larger than that of the C-MoS₂ (0.62 nm) shown in Figure 4-1b, indicating the exfoliation of MoS₂ during HEBM process. TEM and the corresponding EDS elemental-mapping analyses were also performed on the Ru₁@D-MoS₂ (Figure 4-1d-f). As shown in Figure 4-1d and e, no Ru particle or clusters can be observed. In addition, the EDS elemental mapping reveals the homogeneous distribution of Mo, S and Ru atoms over the entire nanosheet (Figure 4-1f). The X-ray diffraction (XRD), Brunauer–Emmett–Teller (BET) area and Raman spectra are also applied to identify the structural changes, as shown in Figure 4-1 g-i. Obviously, the XRD intensity of the D-MoS₂ is significantly lower than that of the C-MoS₂, indicating the remarkably decreased particle size after HMBM. After loading Ru atoms, no Ru-containing crystal peaks can be detected, which is consistent with the TEM results (Figure 4-1d-f), suggesting the monodispersing of Ru atoms. Moreover, the Brunauer–Emmett–Teller (BET) analysis obtained from the N₂ adsorption/desorption is also

applied to reflect the specific surface area (Figure 4-1i). The BET specific surface area of D-MoS₂ was measured to be 33.3 m² g⁻¹, which is much larger than that of C-MoS₂ (14.9 m² g⁻¹), implying the much decreased particle size, which is in line with the XRD results. With the loading of Ru atoms, the specific surface area is slightly decreased (27.6 m² g⁻¹), but still larger than that of C-MoS₂. Meanwhile, the Raman spectra of C-MoS₂, D-MoS₂ and Ru₁@D-MoS₂ in Figure 4-1h show two distinct peaks at approximately 380 and 405 cm⁻¹, corresponding to the in-plane E_{2g}^1 and out-of-plane A_{1g} vibration modes of 2H-MoS₂ [16, 34]. The clearly observed red shift of E_{2g}^1 peak and A_{1g} peak is ascribed to the resulted defects in the D-MoS₂ [14]. Incorporating atomic Ru species lead to further red shift of the characteristic Raman spectra for Ru₁@D-MoS₂, which can be attributed to the generated S-vacancy defects [35-37].

To directly observe that Ru atoms, high-angle annular dark field-scanning transmission electron microscopy (HAADF-STEM) with sub-angstrom resolution was performed. Figure 4-2a clearly verifies the filling of single Ru atoms (brighter white dots) uniformly dispersed in the MoS₂ plane. It can be observed that the majority of Ru atoms occupy positions of the Mo atoms, and a few Ru atoms occupy the S positions. The occupation of Ru single atoms was further verified by the intensity profile (Figure 4-2b) along the line 1 and 2 in Figure 4-2a [38]. Figure 4-2c presents the corresponding schematic diagram of Ru occupation. Additionally, X-ray photoelectron spectroscopy (XPS) was applied to study the changes in elemental chemical states. In the high-resolution Mo 3d XPS spectrum (Figure 4-2d), the Mo 3d double peaks at 232.4 and 229.3 eV are assigned to the Mo IV 3d 5/2 and Mo IV 3d 3/2 in C-MoS₂, whereas the signal at 226.5 eV is attributed to the S 2s electrons [14]. The S 2p spectrum (Figure S4-1) also shows a doublet positioned at 162.1 eV and 163.3 eV, respectively, revealing the -2 oxidation state of S in the C-MoS₂. By comparison, the Mo 3d and S 2p peaks of D-MoS₂ present the negative shift (Figure 4-2d and Figure S4-1). The results indicate that the generated defects altered the electronic structures of Mo and S, and the electron density around the Mo and S increases [14]. Incorporating Ru species will cause peaks of

Mo 3d and S 2p in Ru₁@D-MoS₂ shifting to lower binding energies (Figure 4-2d, S4-1), showing the generation of S vacancies (SVs). The trend is also observed for samples Ru@D-MoS_{2-x} (x=0.5, 1, 4), shown in Figure S4-2 and S4-3. Besides, the Ru 3d_{3/2} peak in Figure S4-4 confirms the presence of Ru species in the structure of Ru₁@D-MoS₂ and is positively charged. The results further confirm that Ru atoms are successfully doped into MoS₂ lattice, transferring electrons to surround Mo and S atoms.

The atomic coordination structure of the prepared catalysts was analyzed by XANES spectroscopy, and extended X-ray absorption fine structure (EXAFS) spectroscopy. Figure 4-2e displays the Mo K-edge XANES spectra for Mo foil, C-MoS₂, D-MoS₂, and Ru₁@D-MoS₂. The results indicate that Mo species in Ru₁@D-MoS₂ were in a lower oxidation state than those in C-MoS₂, and D-MoS₂, according to the lower energy for absorption edge and weaker intensity for white line. The results are also consistent with the XPS results. As shown in Figure 4-2f, the Mo K-edge FT-EXAFS shows two peaks at ~1.98 Å and ~2.68 Å, respectively, which are assigned to Mo–S and Mo–Mo scattering features. Notably, the FT-EXAFS spectrum for Ru₁@D-MoS₂ exhibits much weaker Mo–S peak intensity as compared to C-MoS₂ and D-MoS₂, attributed to the decrease of coordination number by the generation of abundant SVs and the interactions between Ru species and MoS₂ [39, 40]. The Ru K-edge XANES spectra for Ru powder and Ru₁@D-MoS₂ are present in Figure 4-2g. Obviously, the absorption intensity of the Ru K-edge in Ru₁@D-MoS₂ is evidently higher than Ru powder, reflecting that the Ru atoms have more positive charge, in good agreement with the XPS results. By transferring electrons from Ru species into the MoS₂ substrates, Mo species are reduced and accompanied with the formation of S vacancies [39, 41]. The corresponding FT-EXAFS spectrum for Ru₁@D-MoS₂ shows a prominent peak at ~1.63 Å, which is attributed to the Ru–S scattering feature, demonstrating the monodispersing Ru atoms in Ru₁@D-MoS₂ (Figure 4-2h). The emergence of Ru–Mo scattering feature is consistent with substitutional doping of Ru into the Mo location. Further FT-EXAFS fitting analysis (Figure 4-2i, Figure S4-5, Table S4-1) identifies that the isolated Ru

atoms coordinate with five S atoms, while one S atom is lost thus forming the SVs.

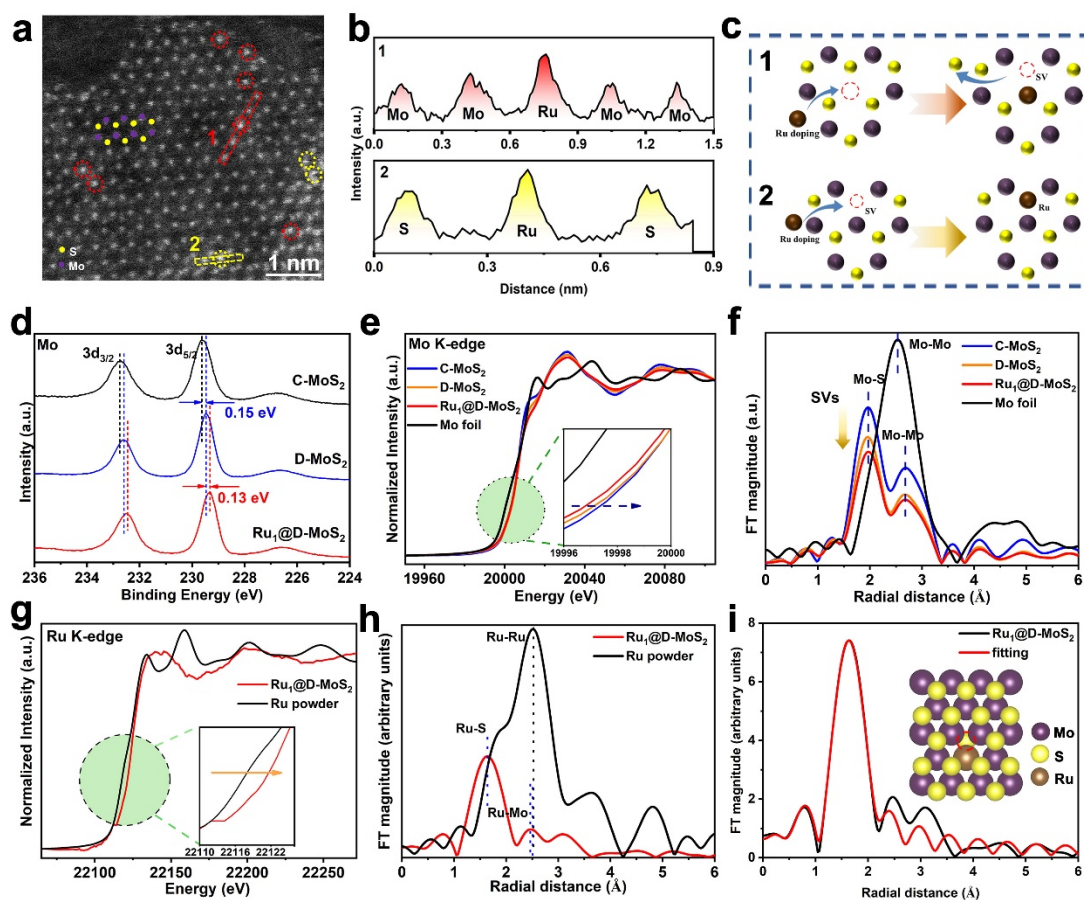


Figure 4-2. Characterization of atomically dispersed Ru₁@D-MoS₂ catalysts. (a) Aberration-corrected atomic resolution HAADF-STEM image of Ru₁@D-MoS₂. (b) Intensity profile along the line 1 and 2 in Fig. 1a. (c) The schematic diagram of Ru occupation corresponding to line 1 and 2. (d) High-resolution X-ray photoelectron spectroscopy of Mo 3d of C-MoS₂, D-MoS₂ and Ru₁@D-MoS₂, (e) Normalized XAFS spectra of the Mo K-edge for the C-MoS₂, D-MoS₂ and Ru₁@D-MoS₂ samples. (f) Corresponding FT-EXAFS spectra from (e). (g) Normalized NEXAFS spectra of the Ru K-edge for the C-MoS₂, D-MoS₂ and Ru₁@D-MoS₂ samples. (h) Corresponding FT-EXAFS spectra from (g). (i) The fitting of k₃-weighted Fourier transforms EXAFS spectra of the Ru K-edge for Ru₁@D-MoS₂. Inset is the model of Ru₁@D-MoS₂. The dashed circle represents the S vacancy.

To study the influence of vacancy and single Ru filling on the HER, the electrocatalytic performance of as-prepared catalysts were evaluated systematically by a series of electrochemical tests. The linear sweep voltammetry (LSV) in a 1 M KOH electrolyte, was carried out in a typical three-electrode setup. As shown in Figure 4-3a, the bulk C-MoS₂ shows a poor HER activity, with an overpotential of 364 mV at the current density of 10 mA cm⁻², in good agreement with the reported results^[16, 41]. Mechanically induced defective MoS₂ via HMBM (D-MoS₂) can effectively enhance the HER activity, reducing the overpotential of about 100 mV relative to C-MoS₂ at the current density of 10 mA cm⁻², due to the increased edges and defects. Monodispersed Ru atoms decorated D-MoS₂ (Ru₁@D-MoS₂) possesses the best hydrogen evolution performance, showing an overpotential of 107 mV at 10 mA cm⁻². The HER performance of C-MoS₂ with the loading of Ru (donated as Ru@C-MoS₂) is also studied for comparison. The TEM images (Figure S4-11) confirmed the formation of Ru particles. Obviously, the Ru@C-MoS₂ showed a higher HER activity as compared to C-MoS₂ but is still inferior to Ru₁@MoS₂. These results suggest that single Ru atoms coupled with defective MoS₂ can maximize the alkaline HER activity. In addition, the Ru₁@D-MoS₂ exhibits a smaller Tafel slope of 96 mV dec⁻¹ than that of the Ru@C-MoS₂ (136 mV dec⁻¹), suggesting a faster hydrogen evolution dynamics (Figure 4-3b). The electrochemically effective surface areas (ECSA) normalized LSV curves were performed as well to highlight the intrinsic activity (Figure 4-3c, Figure S4-7 and S4-8,). As exhibited in Figure 4-3d and c, the Ru₁@MoS₂ shows the lowest overpotential as compared to C-MoS₂, D-MoS₂, Ru₁@D-MoS₂, and Ru@C-MoS₂ at the given ECSA-normalized current density, reflecting the high intrinsic activity of Ru₁@MoS₂. Furthermore, the electrochemical impedance spectroscopy (EIS) tests are also conducted to evaluate the electrode kinetics during the HER process. Figure S4-6 shows the corresponding Nyquist plots of these electrodes. As can be seen, the Ru₁@MoS₂ possesses the lowest charge transfer resistance. The improvement of electrical conductivity mainly originates from the optimized electronic structure with Ru doping.

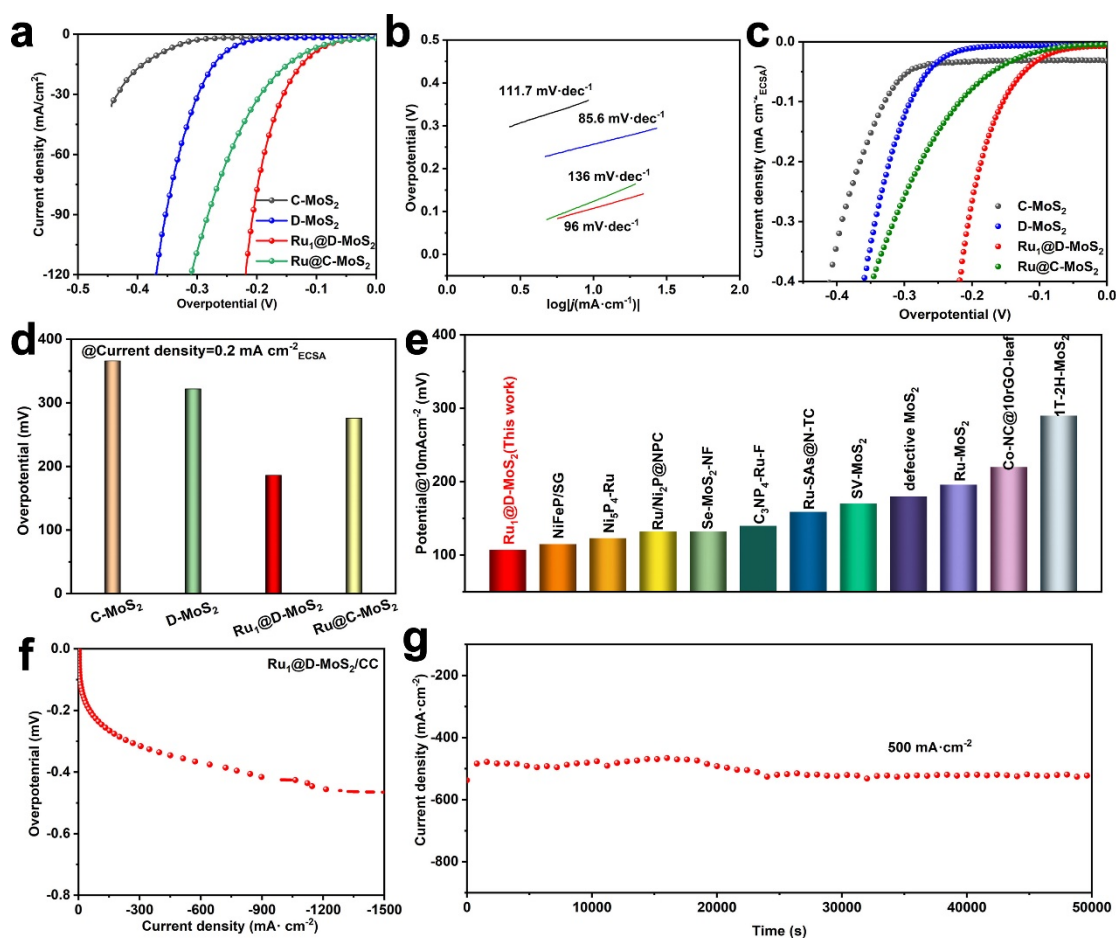


Figure4-3. Catalytic HER performances. (a) Linear sweep voltammetry (LSV) curves (scan rate: 5 mV s^{-1}) of C-MoS₂, D-MoS₂, Ru₁@D-MoS₂, and Ru@C-MoS₂ as catalysts toward HER in 1.0 M KOH. (b) Tafel plots derived from the LSV curves for HER. (c) ECSA-normalized polarization curves of C-MoS₂, D-MoS₂, Ru₁@D-MoS₂, and Ru@C-MoS₂. (d) Overpotential at ECSA-normalized current density of 0.04 mA cm^{-2} for Ru₁@D-MoS₂ in comparison with those of C-MoS₂, D-MoS₂, Ru₁@D-MoS₂, and Ru@C-MoS₂. (e) Comparison of the η_{10} values between Ru₁@D-MoS₂ and other hydrogen evolution electrocatalysts. (f) HER polarization curves of Ru₁@MoS₂ coated on carbon cloth. (g) Stability test of Ru₁@MoS₂ at 500 mA cm^{-2} .

The electrochemical performance of D-MoS₂ with different loading amount of Ru is also investigated systematically. The corresponding Ru contents are determined using ICP-AES (Table S4-2). As shown in Figure S4-9, through the regulation of the loading amount of Ru, the HER performance shows an enhancement tendency with the increase

of Ru content. The Ru₁@D-MoS₂ with the Ru loading amount of 1.41 wt% presents the highest HER activity, while further increasing the content of Ru will lead to the decay of HER activity due to the formation of Ru clusters (Figure S4-10). The results indicate that the atomic Ru is much superior to metallic bulk Ru in improving the HER activity of MoS₂ support. It should be noted that the created S vacancy is essential for the single Ru trapping. Even the same RuCl₃ solution dosage is used, much more Ru species can be trapped on defective MoS₂, while large Ru particles are formed on the C-MoS₂ (Figure S4-11). Moreover, Figure 4-3e compares the $\eta_1 = 10$ value of Ru₁@MoS₂ with previously reported catalysts. The demonstrated activity of Ru₁@MoS₂ is comparable to those of other previously reported state-of-the-art hydrogen evolution electrocatalysts (also summarized in Table S4-3). The stability is of vital importance in electrocatalysis. To investigate the long-term stability, Ru₁@MoS₂ ink was drop-cast onto carbon cloth and examined by a chronoamperometric (CP) test at a current density of 500 mA cm⁻² in a 1.0 M KOH (Figure 4-3f and g). As demonstrated in Figure 4-3g, the Ru₁@MoS₂ shows excellent catalytic stability for alkaline HER.

Combined the above structure characterization and experimental data, we assume that the dramatically improved HER activities of Ru₁@D-MoS₂ is ascribed to the unique coordinated configuration of Ru atoms in defective MoS₂. Afterward, the density functional theory (DFT) calculations were applied to clarify the refined atomic configuration of the isolated Ru atoms within MoS₂ nanosheet. Firstly, the formation energy of the Ru atom replacing the Mo site (named as Ru₁(Mo)@MoS₂) was calculated, shown in Figure S4-12. The results exhibit that Ru atoms tend to replace Mo sites with an exothermic energy of -4.05 eV, indicating the substitutional doping of Ru is a thermodynamically driven process. In contrast, the positive formation energy for Ru replacing S site (named as Ru₁(S)@MoS₂) is energetically unfavorable, suggesting that Ru atoms tend to occupy the Mo site instead of S site, which is consistent with the HAADF-STEM image and XANES. The formation energy of SVs in MoS₂ (named as MoS₂-Sv) and Ru₁@D-MoS₂ was calculated as well. As shown in

Figure S4-12, the decrease in the formation energy of SVs by 1.55 eV after Ru doping indicate the feasibility of using Ru doping to create SVs.

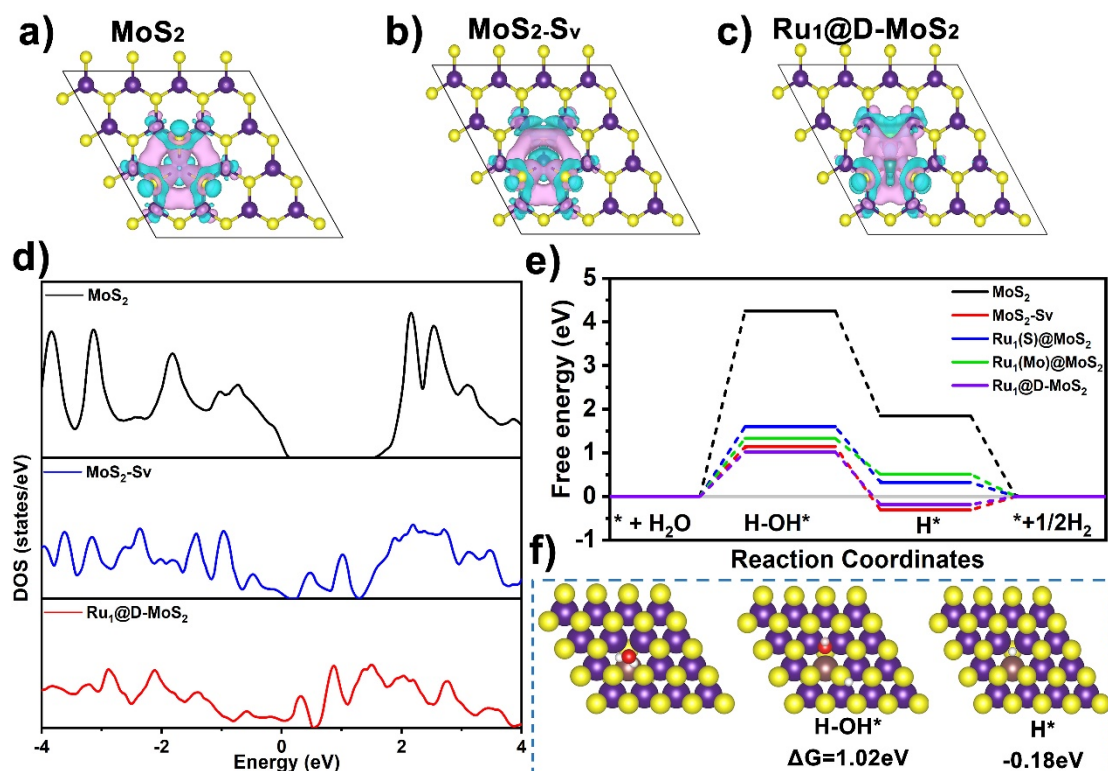


Figure 4-4. DFT calculations. (a-c) The geometries of MoS₂, MoS₂-Sv, and Ru₁@D-MoS₂ and their 3D charge density differences calculated by DFT. (d) Comparison of the total DOS for MoS₂, MoS₂-Sv, and Ru₁@D-MoS₂. (e) Free energy diagrams of the MoS₂, MoS₂-Sv, Ru₁(S)@MoS₂, Ru₁(Mo)@MoS₂ and Ru₁@D-MoS₂ under alkaline solution. (f) The optimized structures of the intermediates on Ru₁@D-MoS₂.

Meanwhile, Figure 4-4a–c displays the 3D charge density differences of C-MoS₂, D-MoS₂, and Ru₁@D-MoS₂. The Bader charge was applied to analyze the electron loss/gain (Figure S4-13). As shown in Figure 4-4b and Figure S4-13, after removing a S atom, the residual electrons restrained at the S-vacancies flow toward the surrounding Mo atoms, resulting in a higher electron density nearby, leaving the S-vacancies electron-deficient, which agrees well with the XPS and XAS results. Moreover, the loading of Ru atoms will lead to further deviation of the charge, due to the difference of the electronegativity among Ru (2.2), S (2.58), and Mo (2.16) (Figure S4-13). To

demonstrate the effect of electronically asymmetric distribution on the HER intermediates, the charge density differences of C-MoS₂, D-MoS₂, and Ru₁@D-MoS₂ with H₂O and H* are calculated, respectively (Figures S14–S15). Figure S4-14 shows that H₂O has a stronger interaction with the Ru₁@D-MoS₂ compared to C-MoS₂ and D-MoS₂, favoring the dissociation of H₂O. In contrast, the charge density difference in Figure S4-15 exhibits a moderate interaction between H* on Ru₁@D-MoS₂. Figure 4-4d also compares the total density of states (DOS) of C-MoS₂, D-MoS₂, and Ru₁@D-MoS₂. The results show that the Ru₁@D-MoS₂ has the highest electronic state density near the Fermi level (EF), suggesting the Ru site greatly facilitates the fast electron transfer with the assistance of the S vacancy.

In alkaline conditions, the HER process includes two steps: i) the initial H₂O dissociation to form H* and OH[−] (ΔG_{H_2O}), and ii) the next hydrogen generation (ΔG_{H^*}), which have been widely accepted as a descriptor to evaluate the HER activity of various catalysts. DFT calculations are performed to explore the intrinsic catalytic activity for the HER, based on the models shown in Figure 4-4a–c. Besides, the Ru atom substituted S site (Ru₁(S)@MoS₂) and Ru atom substituted Mo site (Ru₁(Mo)@MoS₂) models are compared as well (Figure S4-12). The Gibbs free energy (ΔG) diagrams are shown in Figure 4-4e. The H₂O dissociation is generally the rate-determining step for the HER in alkaline media, due to its high energy barrier^[42, 43]. Unfortunately, the C-MoS₂ exhibits an unfavorable water dissociation energy barrier (ΔG_{H_2O}) of 3.78 eV, and such a high energy barrier hinders the water dissociation into H*, resulting in sluggish alkaline HER kinetics. In contrast, creating S vacancy or Ru atoms substituting (Mo or S site) can effectively decrease the ΔG_{H_2O} , but the corresponding energy barriers for HER are still high. Coupling S vacancy with single Ru atom could further lower the free energy barrier of H₂O dissociation to 0.55 eV, implying that the Mo(Ru) with the redistribution of electron density has a stronger water affinity, facilitating the water dissociation (Figure 4-4f and S4-16). The free energy of atomic hydrogen adsorption (ΔG_{H^*}) is also calculated to evaluate the hydrogen evolution activity (Figure 4-4e)^[44].

Obviously, the Ru₁@D-MoS₂ shows a moderate ΔG_{H^*} close to 0, favoring the balance of the adsorption and desorption of H. As a result, the Ru₁@D-MoS₂ exhibits the best HER performance.

4.3 Conclusions

To summarize, a facile and scalable high-energy mechanochemical ball milling strategy is developed to synthesize defective MoS₂ catalysts decorated with single metal atoms. The resulting Ru₁@D-MoS₂ only demands a low overpotential of 107 mV in alkaline electrolytes to deliver a current density of 10 mA cm⁻², which is superior to most previously reported catalysts. The XAFS analysis demonstrates that the single Ru occupies the Mo site coupled with a S vacancy, which could induce the asymmetrical transition of the local electron structure. DFT calculations also revealed that the outstanding HER activity of Ru₁@D-MoS₂ is mainly attributed to the unique asymmetrical coordination configuration of S vacancy coupled single-atom Ru, which could not only efficiently accelerate water dissociation and alter the adsorption/desorption of H^{*} by optimizing intermediates binding, but also greatly increase the electrical conductivity, and therefore leading to its remarkably improved HER catalytic activity. This work validates the potential of HEME in the commercial preparation of high performance HER catalysts.

4.4 References

1. Mahmood N, Yao Y, Zhang J-W, et al. Electrocatalysts for Hydrogen Evolution in Alkaline Electrolytes: Mechanisms, Challenges, and Prospective Solutions. *Advanced Science* 2018; 5: 1700464.
2. Mohammed-Ibrahim J and Sun X. Recent progress on earth abundant electrocatalysts for hydrogen evolution reaction (HER) in alkaline medium to achieve efficient water splitting – A review. *Journal of Energy Chemistry* 2019; 34: 111-160.

3. Gong M, Wang D-Y, Chen C-C, et al. A mini review on nickel-based electrocatalysts for alkaline hydrogen evolution reaction. *Nano Res* 2016; 9: 28-46.
4. Jia Y, Jiang K, Wang H, et al. The Role of Defect Sites in Nanomaterials for Electrocatalytic Energy Conversion. *Chem-Us* 2019; 5: 1371-1397.
5. Tang T, Wang Z and Guan J. A review of defect engineering in two-dimensional materials for electrocatalytic hydrogen evolution reaction. *Chin. J. Catal.* 2022; 43: 636-678.
6. Zhang L, Jia Y, Yan X, et al. Activity Origins in Nanocarbons for the Electrocatalytic Hydrogen Evolution Reaction. *Small* 2018; 14: 1800235.
7. Swaminathan J, Subbiah R and Singaram V. Defect-Rich Metallic Titania ($\text{TiO}_{1.23}$)—An Efficient Hydrogen Evolution Catalyst for Electrochemical Water Splitting. *Acs Catal* 2016; 6: 2222-2229.
8. Yan X, Jia Y and Yao X. Defective Structures in Metal Compounds for Energy-Related Electrocatalysis. *Small Structures* 2021; 2: 2000067.
9. Li W, Wang D, Zhang Y, et al. Defect Engineering for Fuel-Cell Electrocatalysts. *Adv. Mater.* 2020; 32: 1907879.
10. Liang Q, Zhang Q, Zhao X, et al. Defect Engineering of Two-Dimensional Transition-Metal Dichalcogenides: Applications, Challenges, and Opportunities. *Acs Nano* 2021; 15: 2165-2181.
11. Yu K, Lou L-L, Liu S, et al. Asymmetric Oxygen Vacancies: the Intrinsic Redox Active Sites in Metal Oxide Catalysts. *Advanced Science* 2020; 7: 1901970.
12. Jia Y, Zhang L, Du A, et al. Defect Graphene as a Trifunctional Catalyst for Electrochemical Reactions. *Adv. Mater.* 2016; 28: 9532-9538.
13. Lai Z, Chaturvedi A, Wang Y, et al. Preparation of 1T'-Phase $\text{ReS}_2\text{xSe}_2(1-\text{x})$ ($\text{x} = 0-1$) Nanodots for Highly Efficient Electrocatalytic Hydrogen Evolution Reaction. *J. Am. Chem. Soc.* 2018; 140: 8563-8568.
14. Wang X, Zhang Y, Si H, et al. Single-Atom Vacancy Defect to Trigger High-Efficiency Hydrogen Evolution of MoS_2 . *J. Am. Chem. Soc.* 2020; 142: 4298-4308.
15. Yang J, Wang Y, Lagos M J, et al. Single Atomic Vacancy Catalysis. *Acs Nano*

2019; 13: 9958-9964.

16. Li H, Tsai C, Koh A L, et al. Activating and optimizing MoS₂ basal planes for hydrogen evolution through the formation of strained sulphur vacancies. Nat. Mater. 2016; 15: 48-53.

17. Ye G, Gong Y, Lin J, et al. Defects Engineered Monolayer MoS₂ for Improved Hydrogen Evolution Reaction. Nano Lett. 2016; 16: 1097-1103.

18. Li G, Fu C, Wu J, et al. Synergistically creating sulfur vacancies in semimetal-supported amorphous MoS₂ for efficient hydrogen evolution. Appl. Catal., B 2019; 254: 1-6.

19. Meng C, Lin M-C, Du X-W, et al. Molybdenum Disulfide Modified by Laser Irradiation for Catalyzing Hydrogen Evolution. ACS Sustainable Chemistry & Engineering 2019; 7: 6999-7003.

20. Xie J, Qu H, Xin J, et al. Defect-rich MoS₂ nanowall catalyst for efficient hydrogen evolution reaction. Nano Res 2017; 10: 1178-1188.

21. Yang L, Zhou W, Lu J, et al. Hierarchical spheres constructed by defect-rich MoS₂/carbon nanosheets for efficient electrocatalytic hydrogen evolution. Nano Energy 2016; 22: 490-498.

22. Kumar M, Xiong X, Wan Z, et al. Ball milling as a mechanochemical technology for fabrication of novel biochar nanomaterials. Bioresour. Technol. 2020; 312: 123613.

23. Muñoz-Batista M J, Rodriguez-Padron D, Puente-Santiago A R, et al. Mechanochemistry: Toward Sustainable Design of Advanced Nanomaterials for Electrochemical Energy Storage and Catalytic Applications. ACS Sustainable Chemistry & Engineering 2018; 6: 9530-9544.

24. Danielis M, Colussi S, De Leitenburg C, et al. Outstanding Methane Oxidation Performance of Palladium-Embedded Ceria Catalysts Prepared by a One-Step Dry Ball-Milling Method. Angew. Chem. Int. Ed. 2018; 57: 10212-10216.

25. Khumalo M V and Khoathane M C, *Effect of Mechanical Alloying in Polymer/Ceramic Composites*, in *Handbook of Consumer Nanoproducts*. 2021, Springer Singapore: Singapore. p. 1-22.

26. Bor A, Jargalsaikhan B, Uranchimeg K, et al. Particle morphology control of metal powder with various experimental conditions using ball milling. *Powder Technol.* 2021; 394: 181-190.
27. Shuai C, He C, Peng S, et al. Mechanical Alloying of Immiscible Metallic Systems: Process, Microstructure, and Mechanism. *Adv. Eng. Mater.* 2021; 23: 2001098.
28. Jin H, Sultan S, Ha M, et al. Simple and Scalable Mechanochemical Synthesis of Noble Metal Catalysts with Single Atoms toward Highly Efficient Hydrogen Evolution. *Adv. Funct. Mater.* 2020; 30: 2000531.
29. Zhu K, Wang W, Meng A, et al. Mechanically exfoliated g-C₃N₄ thin nanosheets by ball milling as high performance photocatalysts. *RSC Advances* 2015; 5: 56239-56243.
30. Wang Z, Zhu Y, Ji D, et al. Scalable Exfoliation and High-Efficiency Separation Membrane of Boron Nitride Nanosheets. *ChemistrySelect* 2020; 5: 3567-3573.
31. Yi M and Shen Z. A review on mechanical exfoliation for the scalable production of graphene. *J. Mater. Chem. A* 2015; 3: 11700-11715.
32. Shi D, Yang M, Chang B, et al. Ultrasonic-Ball Milling: A Novel Strategy to Prepare Large-Size Ultrathin 2D Materials. *Small* 2020; 16: 1906734.
33. Li X, Shen J, Wu C, et al. Ball-Mill-Exfoliated Graphene: Tunable Electrochemistry and Phenol Sensing. *Small* 2019; 15: 1805567.
34. Zhang W, Liao X, Pan X, et al. Superior Hydrogen Evolution Reaction Performance in 2H-MoS₂ to that of 1T Phase. *Small* 2019; 15: 1900964.
35. Wu W, Niu C, Wei C, et al. Activation of MoS₂ Basal Planes for Hydrogen Evolution by Zinc. *Angew. Chem. Int. Ed.* 2019; 58: 2029-2033.
36. Shi Y, Zhou Y, Yang D-R, et al. Energy Level Engineering of MoS₂ by Transition-Metal Doping for Accelerating Hydrogen Evolution Reaction. *J. Am. Chem. Soc.* 2017; 139: 15479-15485.
37. Deng J, Li H, Xiao J, et al. Triggering the electrocatalytic hydrogen evolution activity of the inert two-dimensional MoS₂ surface via single-atom metal doping. *Energy Environ. Sci.* 2015; 8: 1594-1601.

38. Wang L, Zhang W, Wang S, et al. Atomic-level insights in optimizing reaction paths for hydroformylation reaction over Rh/CoO single-atom catalyst. *Nat Commun* 2016; 7: 14036.
39. Jiang K, Luo M, Liu Z, et al. Rational strain engineering of single-atom ruthenium on nanoporous MoS₂ for highly efficient hydrogen evolution. *Nat Commun* 2021; 12: 1687.
40. Zhang T, Chen Z, Walsh A G, et al. Single-Atom Catalysts Supported by Crystalline Porous Materials: Views from the Inside. *Adv. Mater.* 2020; 32: 2002910.
41. Luo Z, Ouyang Y, Zhang H, et al. Chemically activating MoS₂ via spontaneous atomic palladium interfacial doping towards efficient hydrogen evolution. *Nat Commun* 2018; 9: 2120.
42. Wang J, Zhang Z, Song H, et al. Water Dissociation Kinetic-Oriented Design of Nickel Sulfides via Tailored Dual Sites for Efficient Alkaline Hydrogen Evolution. *Adv. Funct. Mater.* 2021; 31: 2008578.
43. Chen G, Wang T, Zhang J, et al. Accelerated Hydrogen Evolution Kinetics on NiFe-Layered Double Hydroxide Electrocatalysts by Tailoring Water Dissociation Active Sites. *Adv. Mater.* 2018; 30: 1706279.
44. Zhang L, Zhuang L, Liu H, et al. Beyond Platinum: Defects Abundant CoP₃/Ni₂P Heterostructure for Hydrogen Evolution Electrocatalysis. *Small Science* 2021; 1: 2000027.

4.5 Supporting Information

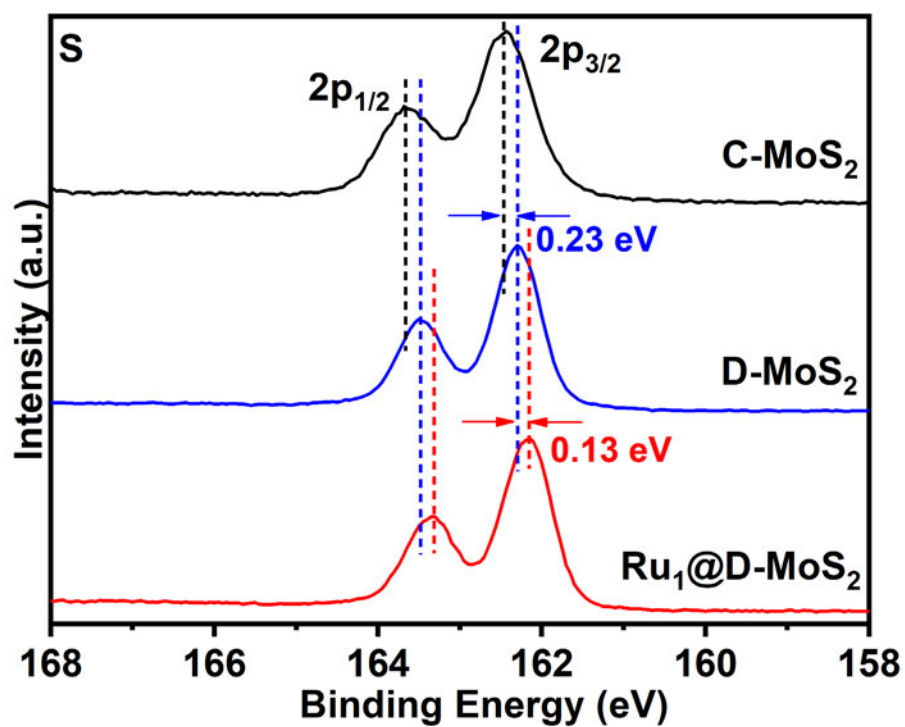


Figure S4-1. High-resolution S 2p XPS spectra of C-MoS₂, D-MoS₂ and Ru₁@D-MoS₂, respectively.

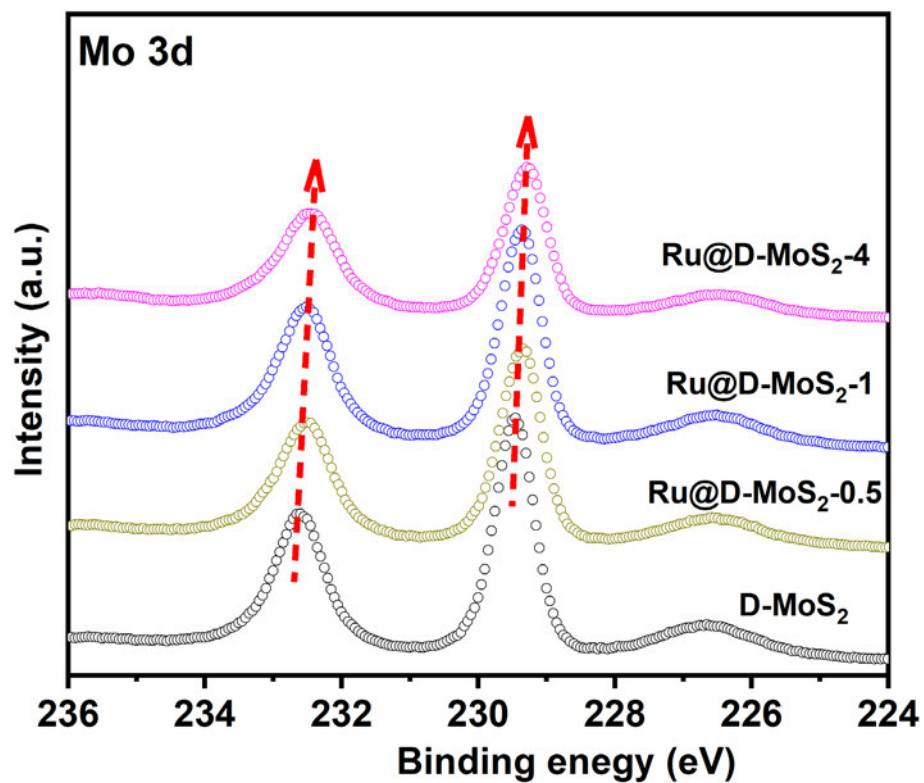


Figure S4-2. High-resolution Mo 3d XPS spectrum.

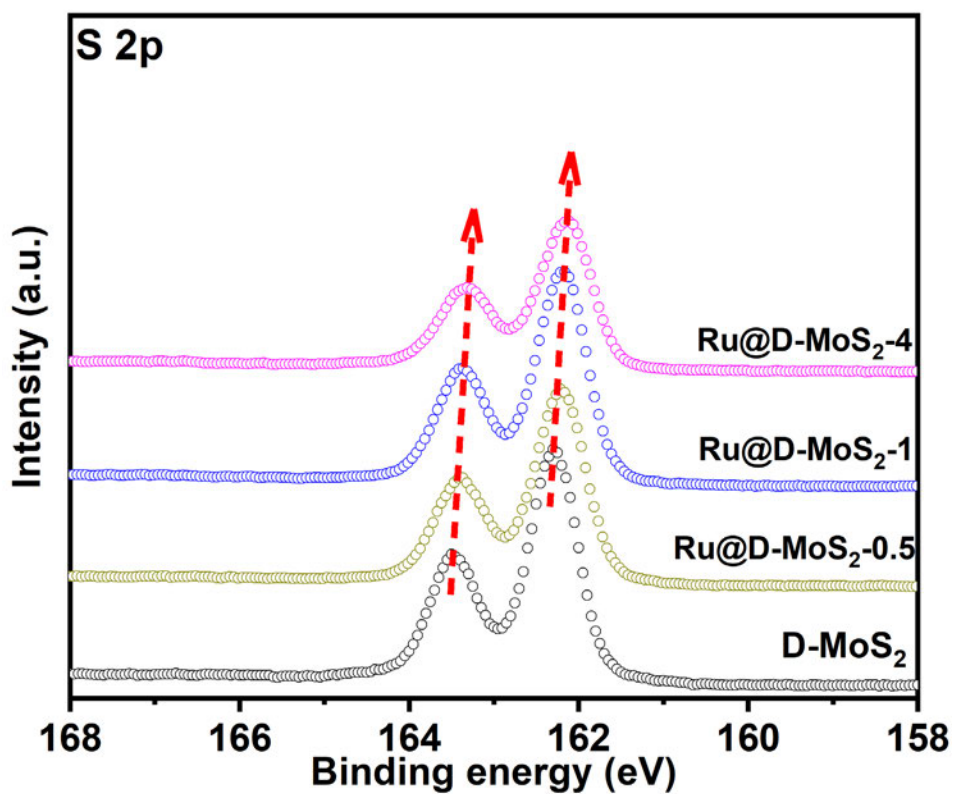


Figure S4-3. High-resolution S 2p XPS spectrum.

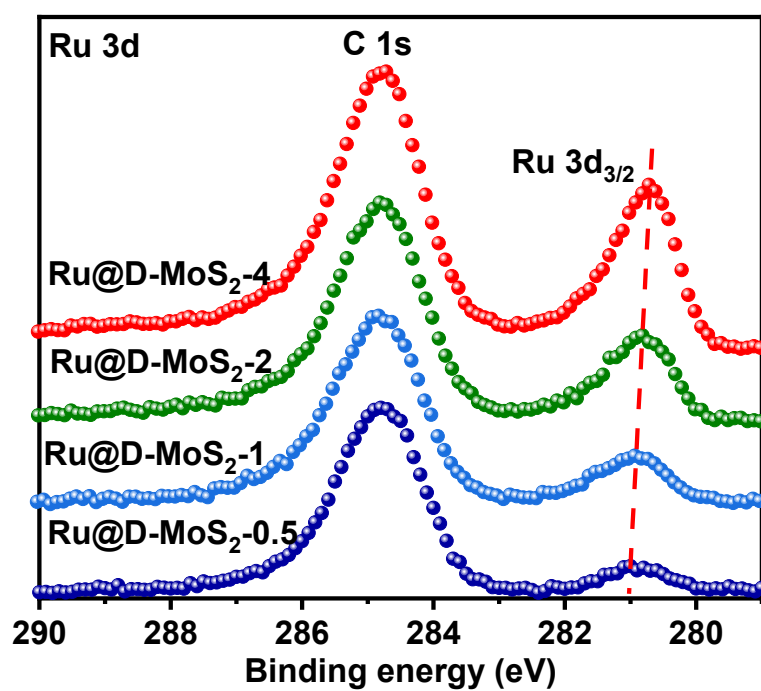


Figure S4-4. High-resolution Ru 3d XPS spectrum.

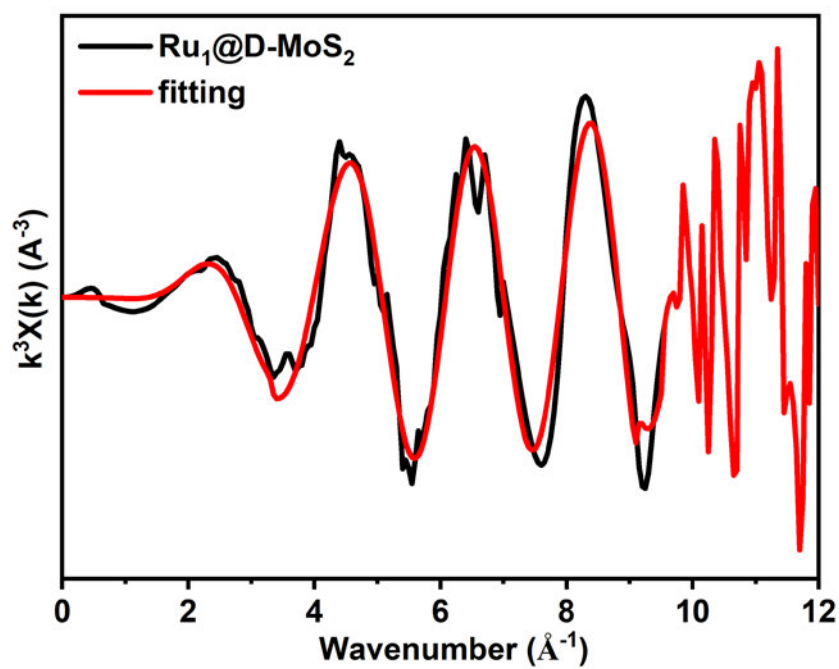


Figure S4-5. EXAFS k space fitting curve (circle) and the experimental one (line) of Ru₁@D-MoS₂.

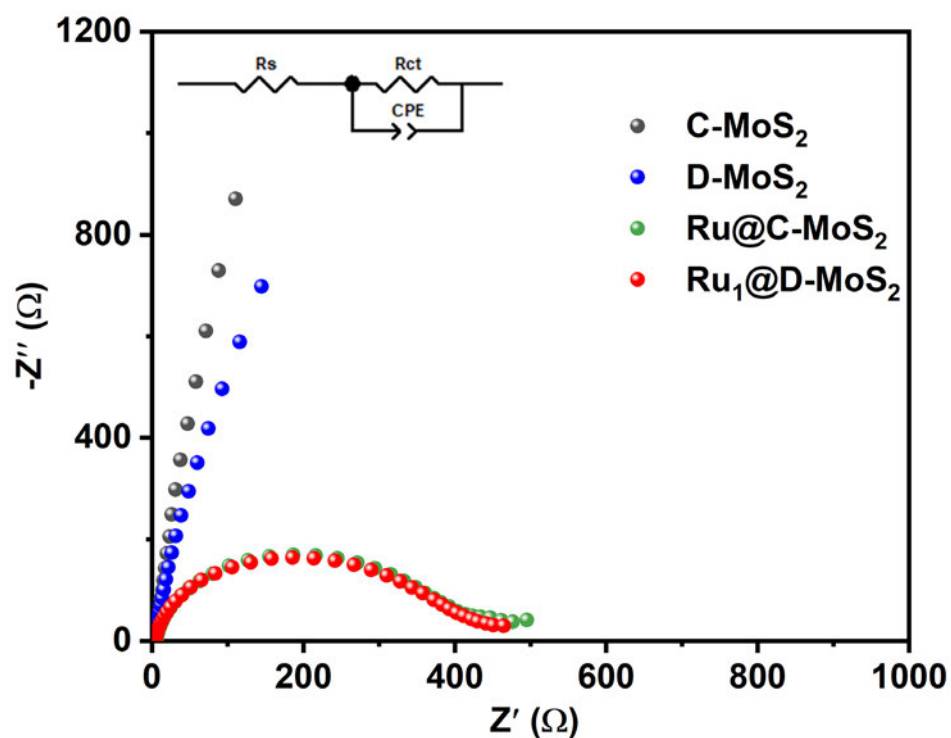


Figure S4-6. Nyquist plot of electrochemical impedance spectra for C-MoS₂, D-MoS₂, Ru₁@D-MoS₂ and Ru@C-MoS₂, respectively.

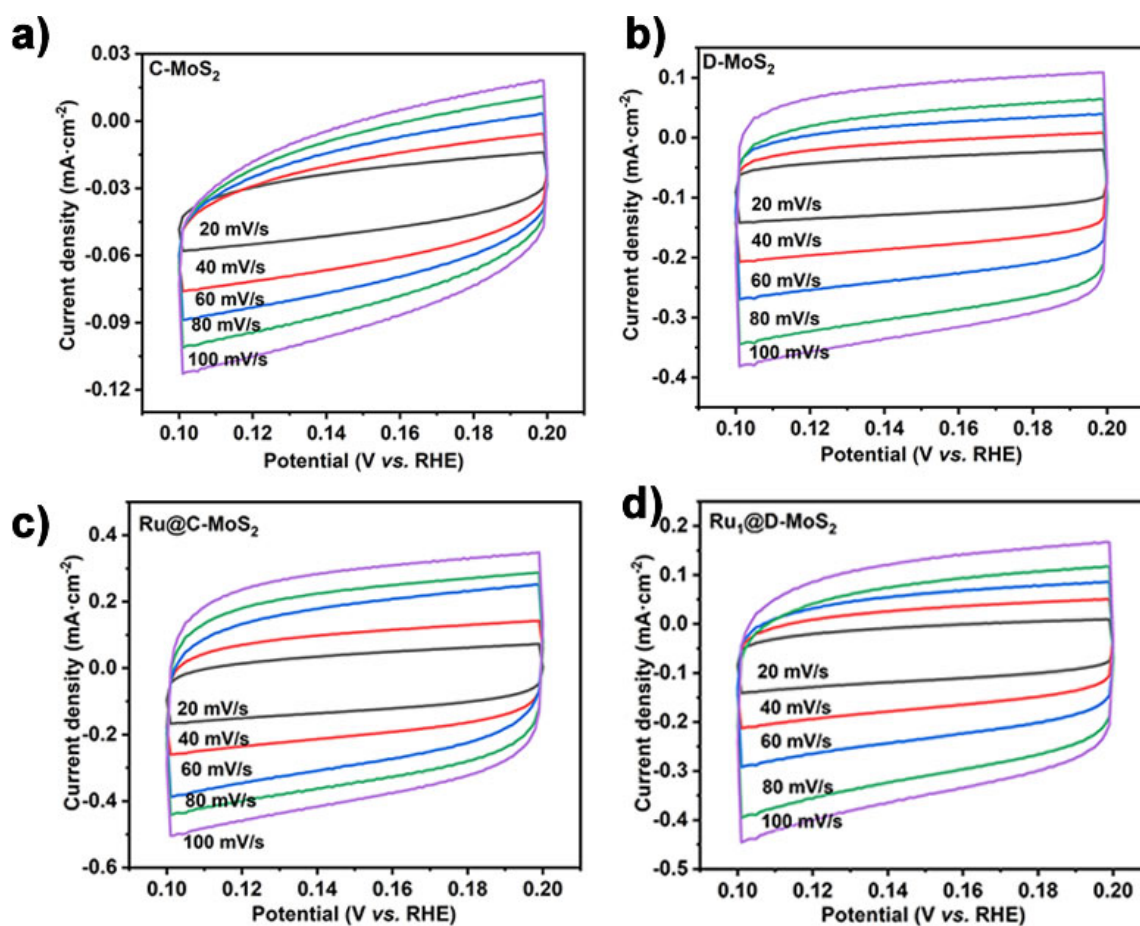


Figure S4-7. CV curves at various scan rates of (a) C-MoS₂, (b)D-MoS₂, (c)Ru₁@D-MoS₂ and (d) Ru@C-MoS₂ in 1M KOH.

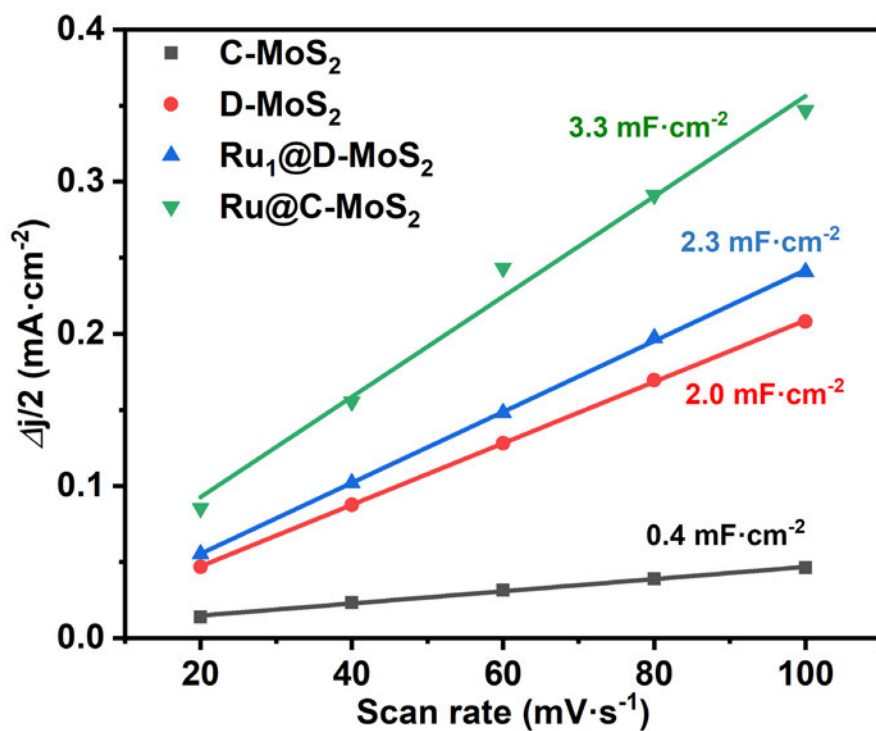


Figure S4-8. Linear fits of half capacitive currents versus scan rates for the extraction of C_{dl}.

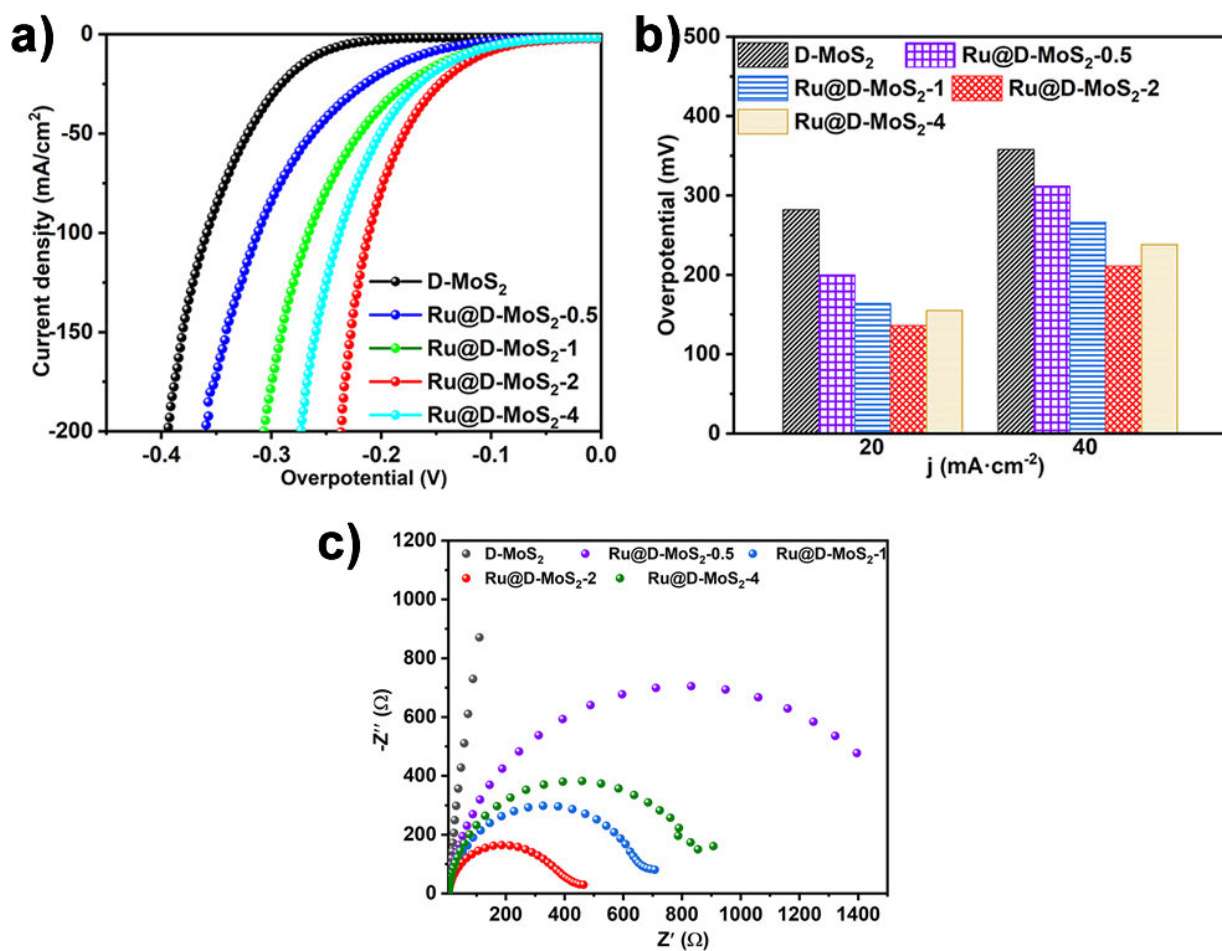


Figure S4-9. (a) Electrochemical HER performance of Ru@MoS_{2-x} (x=0,0.5,1,2,4). (b) Comparison of overpotential values at the current density of 20 and 40 mA cm⁻². (c) Nyquist plot of electrochemical impedance spectra.

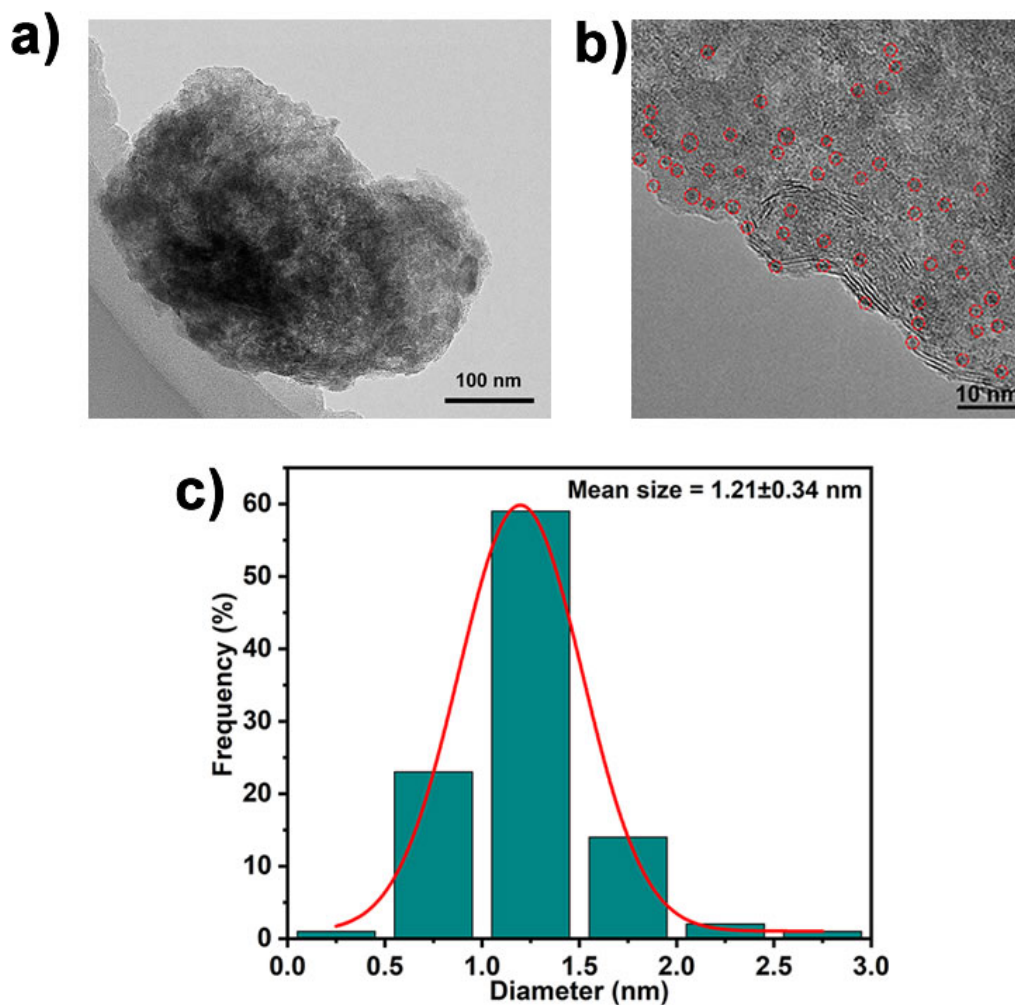


Figure S4-10. (a) and (b) TEM and HR-TEM image images of Ru@D-MoS₂-4. (c) Size distribution Ru particles. It is observed that the nano clusters of Ru are formed and uniformly distributed the entire MoS₂ sheet. The average particle diameter was determined to be 1.21 nm.

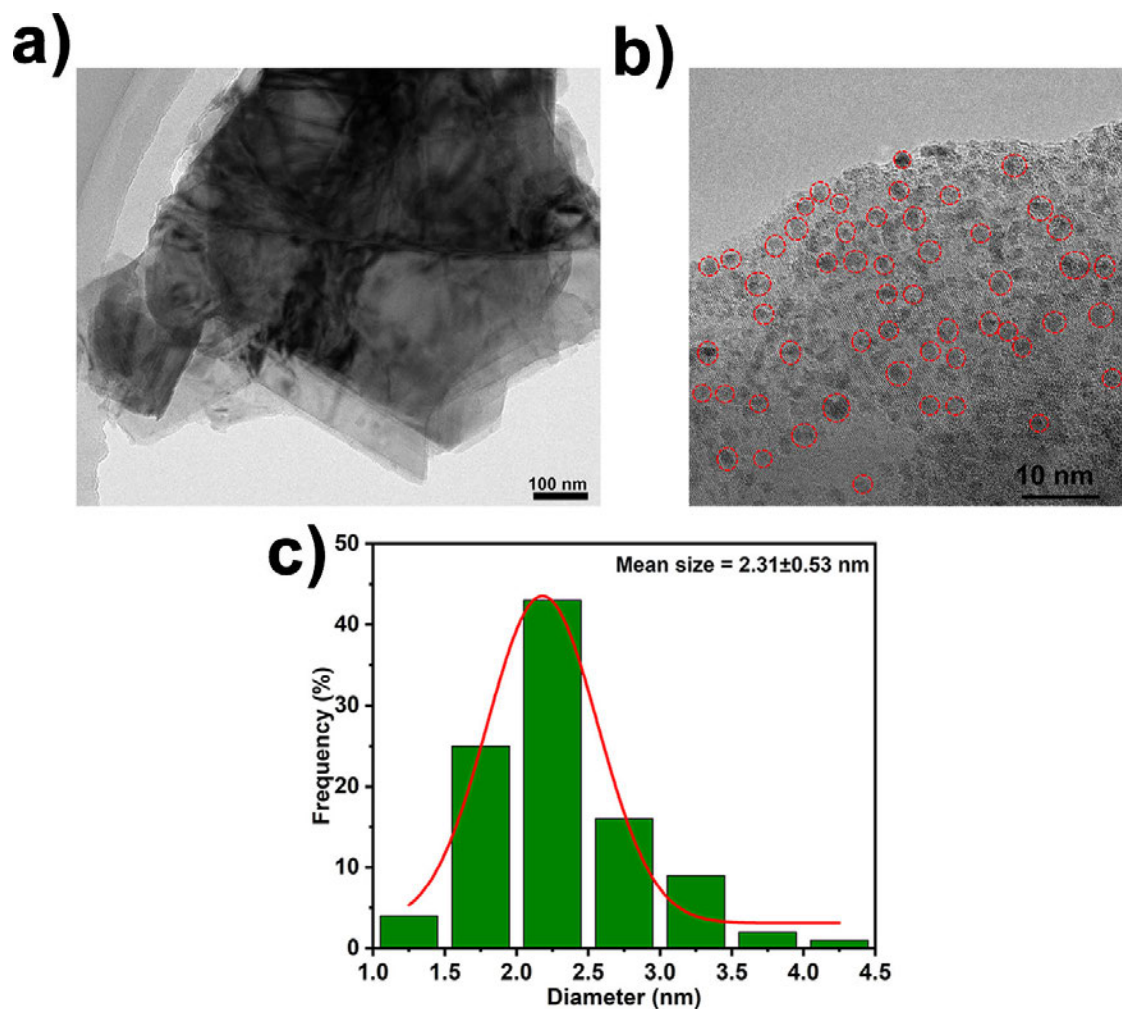


Figure S4-11. (a) and (b) TEM and HR-TEM image images of Ru@C-MoS₂. (c) Size distribution of Ru particles. Obviously, the Ru articles are observed on the entire commercial MoS₂ sheet. The average particle diameter was determined to be 2.31 nm.

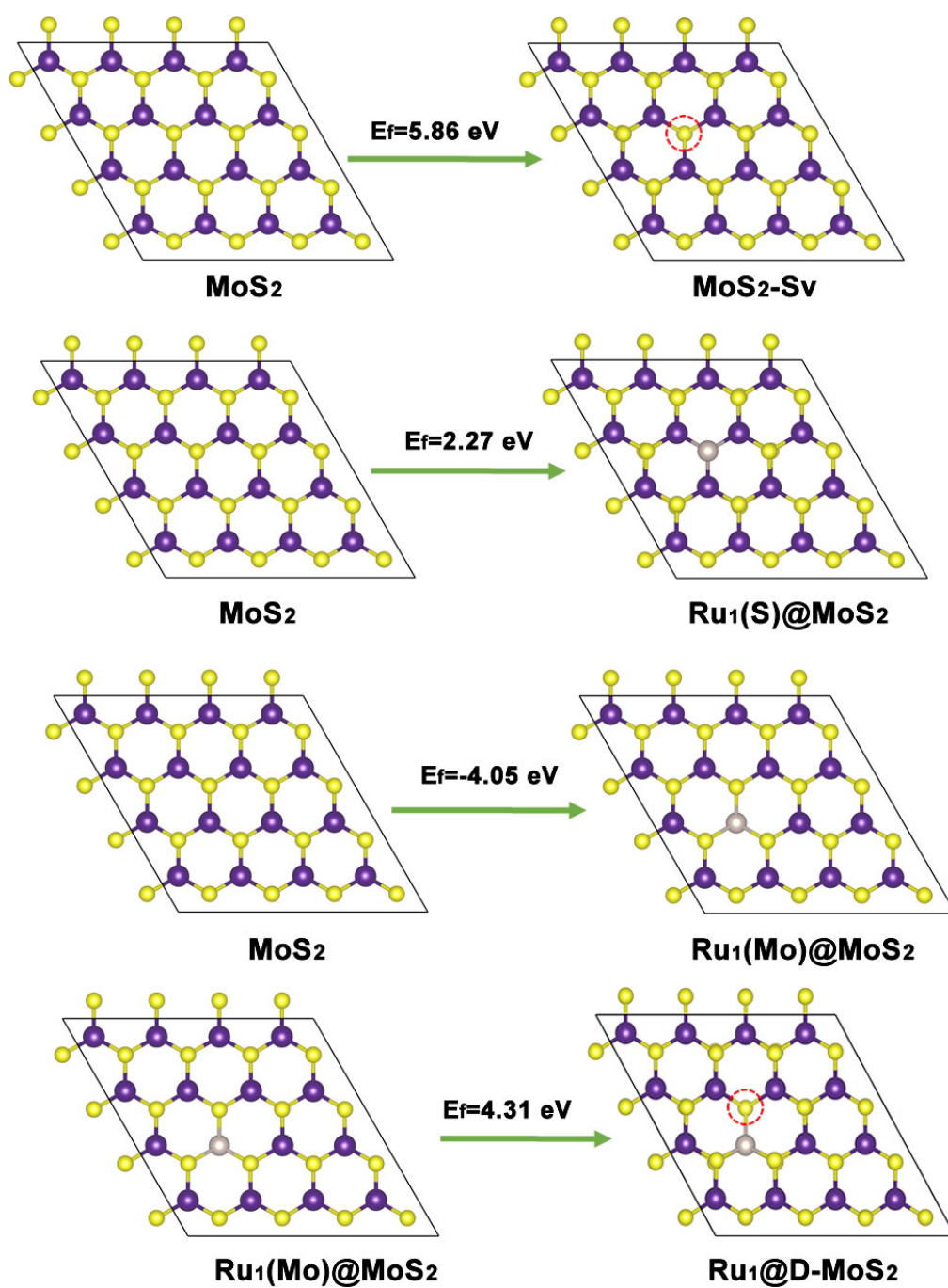


Figure S4-12. Formation energies (E_f) for 2H-MoS₂ with S vacancy and Ru atoms. (a) formation of S vacancy, (b) Ru replacing S site, (c) Ru replacing Mo sites, and (d) formation of S vacancy after Ru replacing Mo site. The dashed circle represents the S vacancy.

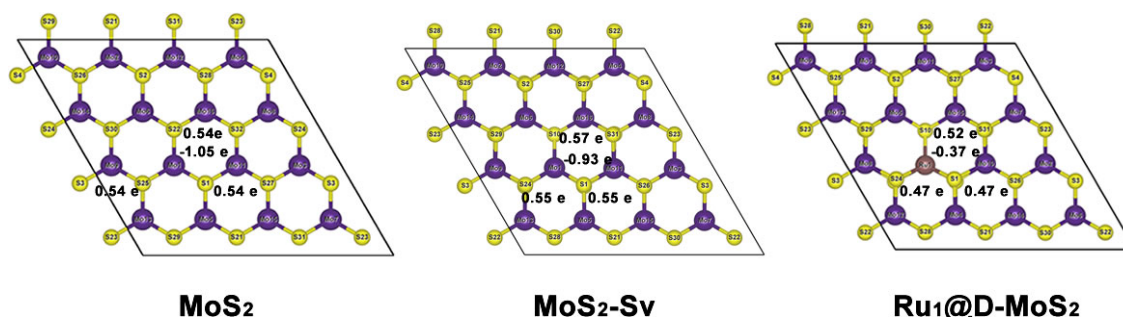


Figure S4-13. The Bader charge numbers of atoms in MoS₂, MoS₂-Sv and Ru₁@D-MoS₂.

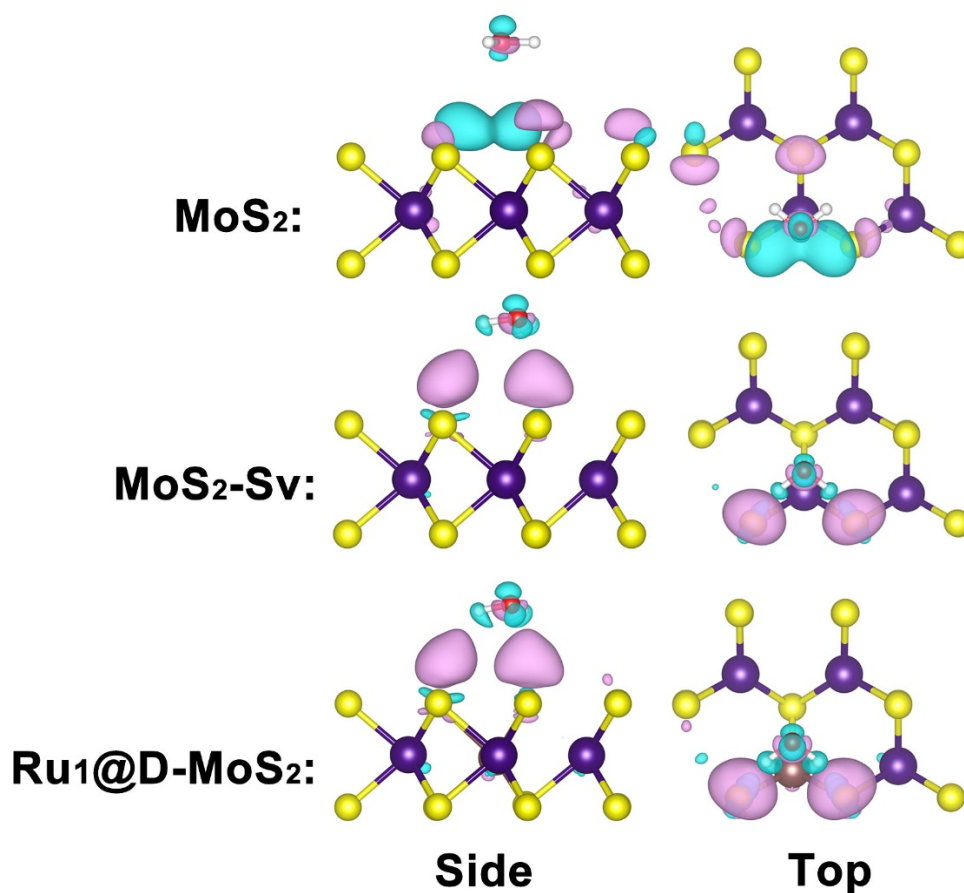


Figure S4-14. The 3D charge density differences of H₂O adsorption on C-MoS₂, D-

MoS₂, and Ru₁@D-MoS₂ respectively. Regarding the charge density differences, pink and cyan represent positive and negative regions, respectively.

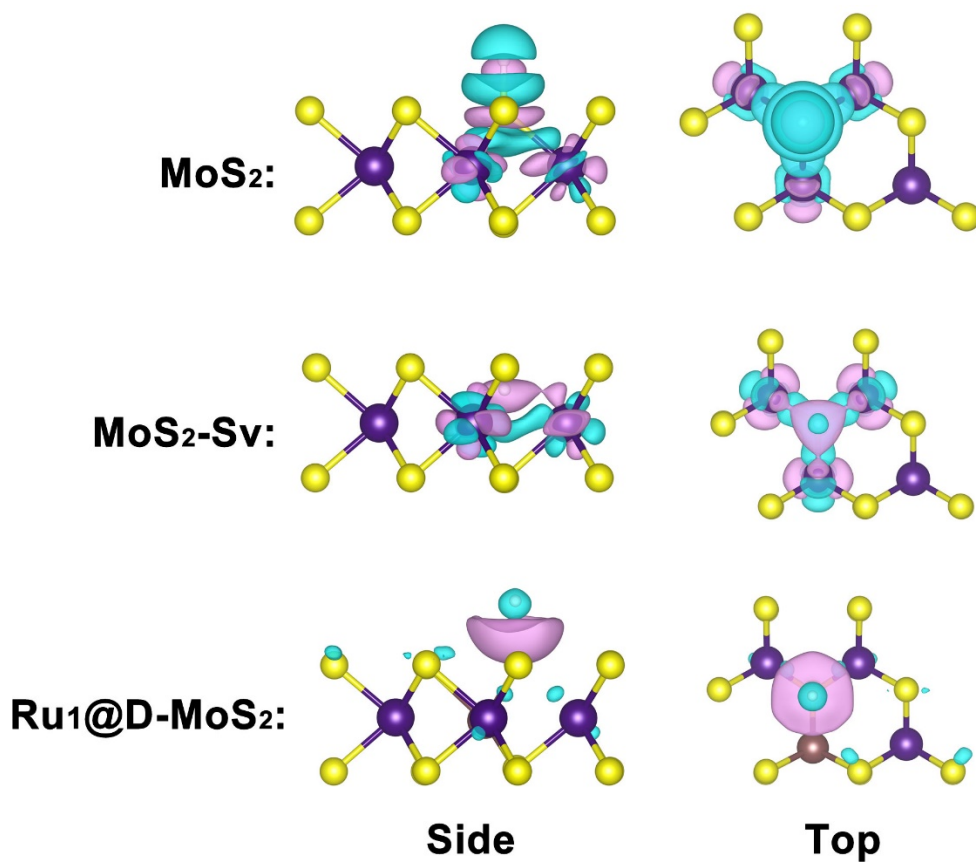


Figure S4-15. The 3D charge density differences of H* adsorption on C-MoS₂, D-MoS₂, and Ru₁@D-MoS₂.

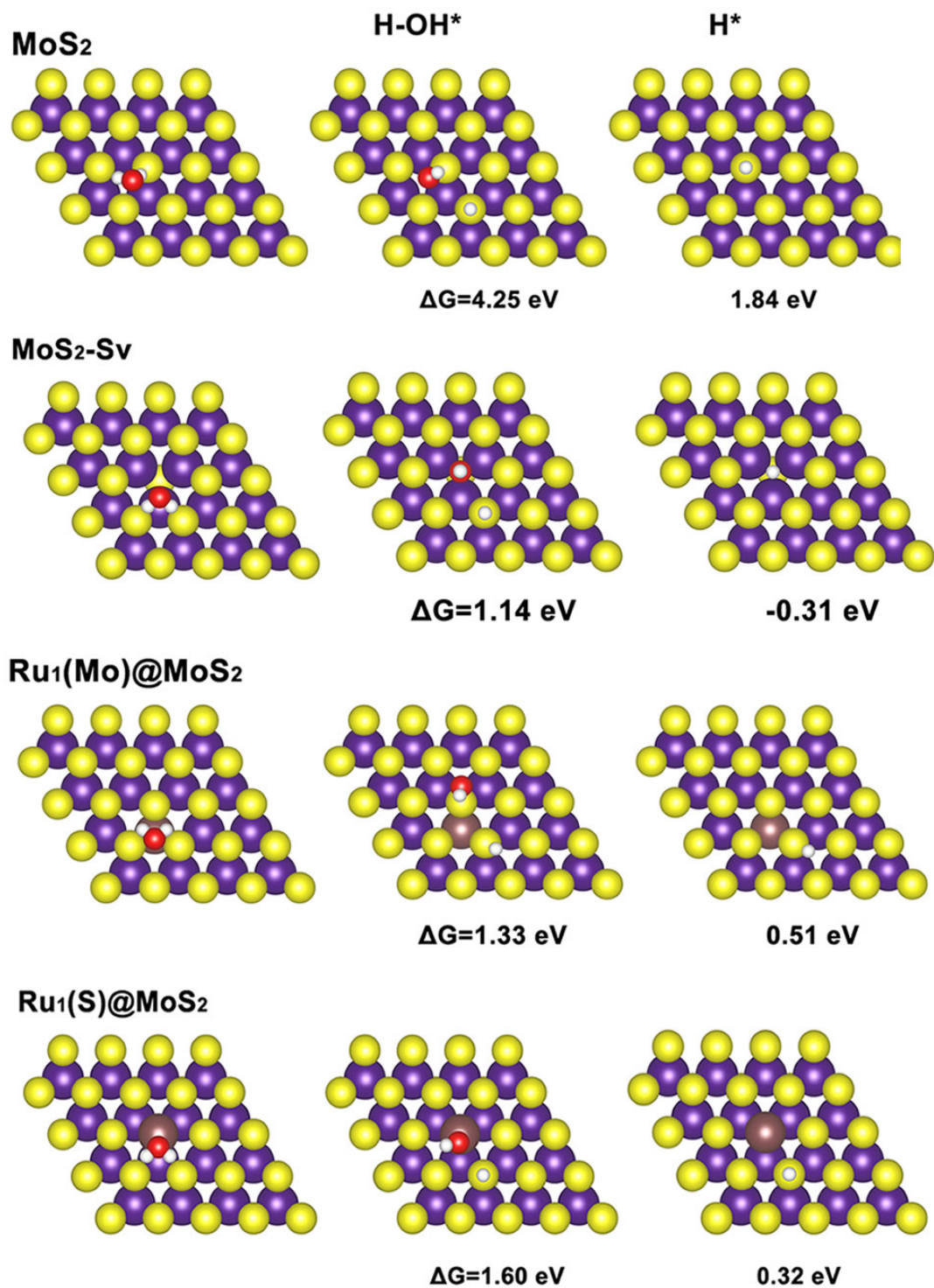


Figure S4-16. The optimized structures of the intermediates on MoS₂, MoS₂-Sv, Ru₁(Mo)@MoS₂ and Ru₁(S)MoS₂.

Table S4-1. The EXAFS fitting parameters of Ru R-space for Ru₁@D-MoS₂

Sample	path	N	σ^2 (Å ²)	R/Å
Ru ₁ @D-MoS ₂	Ru-S	5	0.00465	2.20488

Note: N is the coordination number; σ^2 , Debye-Waller factor to account for both thermal and structural disorders; R is the distance between absorber and backscatter atoms.

Table S4-2. Elemental contents determined by ICP-MS for different catalysts.

Samples	Ru@D-MoS ₂ -0.5	Ru@D-MoS ₂ -1	Ru@D-MoS ₂ -2	Ru@D-MoS ₂ -4
wt. %	0.35	0.68	1.41	2.72

Table S4-3. Electrocatalytic HER performance of our synthesized Ru₁@D-MoS₂ compared with that of other reported HER electrocatalysts

Catalysts	Overpotential(mV) at 10 mAcm ⁻²	References.
Ru₁@D-MoS₂	107	This work
The Ni ₅ P ₄ -Ru	123	Adv. Mater. 2020, 32, 1906972
Ru-SAs@N-TC	159	Adv. Funct. Mater. 2020, 30, 2003007
Ru-MoS ₂	196	Small Methods 2019, 1900653
Co-NC@10rGO-leaf	220	Chem Eng J. 2021, 426, ,131270,
C ₃ N ₄ -Ru-F	140	J. Mater. Chem. A, 5 (2017), 18261-18269
Ru/Ni ₂ P@NPC	132	ACS Sustain. Chem. Eng. 2019, 7, 21, 17714– 17722
NiFeP/SG	115	Nano energy. 2019. 58. 870-876
defective MoS ₂	180	Adv. Mater. 2013, 25, 5807–5813
Se-MoS ₂ -NF	132	Nat Commun. 2020, 11, 3315
SV-MoS ₂	170	Nature Mater. 2016, 15, 48–53
1T–2H MoS ₂	290	Adv. Energy Mater. 2018, 8, 1801345.

Chapter 5. Mechanochemical preparation of defective MoS₂ with Co and O co-doping for electrochemical hydrogen evolution

STATEMENT OF CONTRIBUTION TO CO-AUTHORED PUBLISHED PAPER


This chapter includes a co-authored paper. The status of the co-authored paper, including all authors, are:

Chengguang Lang, Lei Zhang, Cheng-Jie Yang, Hao Zhong, Peirong Chen, Chung-Li Dong, Jun Chen, Aijun Du, Xuecheng Yan, Liuzhang Ouyang, Yi Jia, Xiangdong Yao

My contribution to the paper involved:

- Literature survey
- Concept and design
- Analysis and interpretation of data
- Drafting and writing

(Signed)  (Date) 31/07/2022
Chengguang Lang

(Countersigned)  (Date) 02/08/2022
Corresponding author of paper: Prof. Xiangdong Yao

(Countersigned)  (Date) 31/07/2022
Supervisor: Dr. Xuecheng Yan

5.1 Introduction

Hydrogen is a clean energy carrier and also an alternative to fossil fuels owing to its high enthalpy and zero environmental emission characteristics during combustion. Currently, over 90% of global hydrogen supply is produced by the reformation of fossil fuels, which involves the CO₂ emission and still in short supply^[1, 2]. To replenish the present hydrogen supply and relief the impact on environment, water splitting via hydrogen evolution reaction (HER) is favorable due to its simplicity, sustainability, and high purity for industrial hydrogen production^[3]. Despite tremendous efforts have been made in the past decade, platinum-based materials are still considered to be the most effective electrocatalysts for the HER^[4, 5]. To make the hydrogen produced from water splitting more cost-competitive, it is thus highly desirable to exploit low-cost, highly efficient electrocatalysts to replace the expensive Pt-based catalysts.

Recently, earth-rich and cheap molybdenum disulfide (MoS₂) has received great attention as the HER catalyst. Theoretical calculations demonstrated that the edges of MoS₂ have a low hydrogen adsorption free energy, resembling that of Pt^[6, 7]. For example, Chorkendorff *et al.* have experimentally proved that the electrochemically active center of MoS₂ arises from the unsaturated sulfur atoms along its edges, while the basal planes are catalytical inert^[8]. However, bulk MoS₂ suffers from low active-edge-site density and poor conductivity. Therefore, different strategies have been proposed to enhance the activity of MoS₂. The reported modifications mainly involve the domination of particle size and shape, electronic structure by doping heteroatoms or introducing defects, heterogeneous interface, and stress engineering^[9-12]. Downsizing the MoS₂ is a straightforward method to increase the active edge-sites, such as nanoparticles, nanoflakes, and layer thickness^[13-16]. For example, Jin Song *et al.* reported a chemically exfoliated MoS₂ with significantly enhanced electrocatalytic performance via lithium intercalation^[14]. The observed overpotential at 10 mA cm⁻² significantly decreased from 320 mV (as-grown MoS₂) to 195 mV. Engineering vacancy defects onto bulk MoS₂ can not only improve the conductivity but also

manipulate the number of active sites and the hydrogen adsorption free energy. For example, Zheng *et al.* reported a strained S vacancy engineer via exposing MoS₂ to Ar plasma ^[17]. Combining DFT calculations, it is found that the strained S-vacancy sites can manipulate the gap states even closer to the Fermi level, thus yielding an optimal ΔG_H . Besides the plasma engraving, chemical etching agent (such as H₂O₂) is also found to be able to create S-vacancy defects on the basal plane ^[18]. By regulating the etching duration, etching solution, and etching temperature, a homogeneously distributed single S-vacancies onto the MoS₂ is obtained, leading to an overpotential decreased from 220 mV to 131 mV at the current density of 10 mA cm⁻². Heteroatom doping can not only activate their adjacent S atoms but also increase the electrical conductivity. Bao *et al.* reported an atomically dispersed Co atom into the in-plane domain of MoS₂ ^[19]. The incorporation of Co atoms can moderate the H adsorption energy to enhance the HER activity. The resulted mPF-Co-MoS₂ electrocatalyst exhibits a high HER activity with the overpotential of only 156 mV at a current density of 10 mA cm⁻². However, the execution of above-mentioned defect preparation methods is not only complicated, but also expensive and in high demand of apparatus, such as high temperature/pressure, strong reducing agents, or poisonous reactants. Besides, the batch preparation of catalysts with these methods still needs to be further evaluated. It is also highly desirable to find a way for mass fabrication. Moreover, for the industrial application, the stability of the catalysts also needs to be examined at a current density of 500 mA cm⁻² in alkaline solutions for the large-scale hydrogen production.^[20, 21]

Herein, we propose an economic and efficient strategy to exclude chalcogen atoms for the mass preparation of defective MoS₂ (Co,O@MoS₂-0.4) via high-energy mechanochemical ball milling (HMBM). Through the HMBM with CoO, the size effect, defect engineering and heteroatom doping can be simultaneously achieved. During grinding, the CoO can act as auxiliary agent to shatter the bulk MoS₂, thus exposing more active edges and concurrently creating more defects (active sites). Besides the reduced size, heteroatomic Co is incorporated into the MoS₂ lattice during the

mechanochemical milling, which can further activate the inert surface of MoS₂. All these multi-dimensional regulations contribute to an optimal catalytic activity toward the HER, resulting in an overpotential of 94 mV at the current density of 10 mA cm⁻². Furthermore, the stability tests indicate that the prepared catalyst Co_{0.4}O@MoS₂-0.4 holds great promise for commercial large-scale hydrogen production.

5.2 Results and discussion

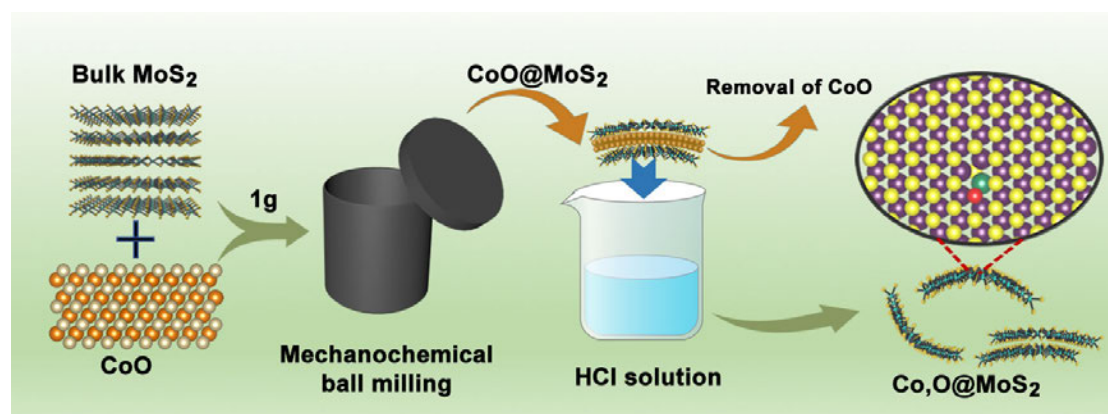


Figure 5-1. Schematic drawing of scalable catalyst preparation for hydrogen production.

The heteroatom decorated, curved MoS₂ nanosheets (Co_{0.4}O@MoS₂) were prepared via a simple one-step high-energy mechanochemical ball milling process. A schematic of the process is shown in Figure 5-1. Here, the commercial MoS₂ (C-MoS₂, ~2 μm) was directly used as the starting material. Our previous work indicates that the use of oxide additive (rigid Al₂O₃, hardness: 2160 kg mm⁻²) during HMBM can effectively refine the particle size and create defects. In this work, we use CoO with low hardness (279 kg mm⁻²) to replace the Al₂O₃. Note that the CoO can function as grinding additive and Co source. The mechanochemical reaction was carried out using a type of planetary ball mill at room temperature which can generate shear force and impact force. Afterward, the CoO particles were etched by HCl solution. By regulating the mass ratio of CoO to MoS₂, different Co_{0.4}O@MoS_{2-x} (x represents the mass of CoO) catalysts are

fabricated, of which the Co₂O₃@MoS₂-0.4 (named thereafter Co₂O₃@MoS₂) exhibits the best HER performance. The experimental results indicate that the introduction of CoO can not only promote the exfoliation and refinement of the bulk MoS₂, but also bend the 2D lamellar structure of MoS₂.

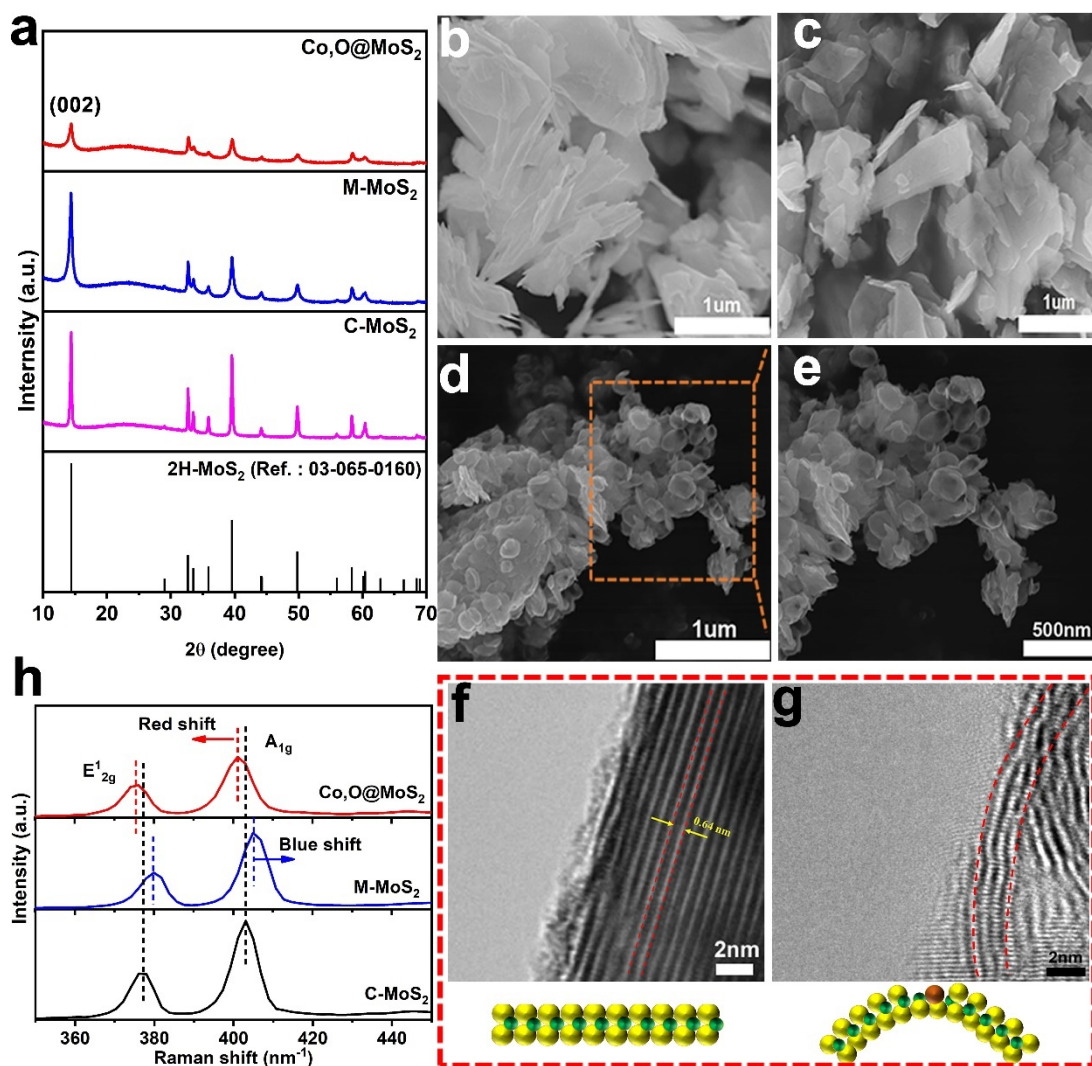


Figure 5-2. (a) XRD patterns of C-MoS₂, M-MoS₂ and Co₂O₃@MoS₂. (b-c) SEM images of C-MoS₂ (b), M-MoS₂ (c) and Co₂O₃@MoS₂ (d). (e) The enlarged SEM image of Co₂O₃@MoS₂. (f and g) HRTEM images of C-MoS₂ and M-MoS₂. (h) Representative Raman spectra for C-MoS₂, M-MoS₂ and Co₂O₃@MoS₂, respectively.

The powder X-ray diffraction (PXRD) was firstly used to characterize the synthesized

samples. As shown in Figure 5-2a, strong reflections of C-MoS₂ in the PXRD pattern indicate the crystal structure of 2H [22]. After HMBM, the ball milled MoS₂ (M-MoS₂) displays a peak broadening and weakening, implying the decreased number of stacked and smaller crystallite size compared to C-MoS₂ [23, 24]. Compared with the M-MoS₂, the dramatically weakened XRD peak intensity of the Co₃O₄@MoS₂ implies that the introduction of CoO can remarkably promote the grain refinement of bulk MoS₂ (Figure S5-1). It can be noted that the existing characteristic peaks of 2H phase for Co₃O₄@MoS₂ indicate no phase transformation occurs. The scanning electron microscopy (SEM) and transmission electron microscopy (TEM) are also applied to reveal the morphology changes of MoS₂ with and without CoO. As shown in Figure 5-2b, the milled MoS₂ without CoO (M-MoS₂) maintained the 2D lamellar structure. In contrast, the Co₃O₄@MoS₂ presents a curved morphology (Figure 5-2d and e). High-resolution transmission electron microscopy (HRTEM, Figure 5-2f and g) further validates the atomically curved MoS₂ from the cross-sectional view. This could be explained that the ductile MoS₂ could be coated onto the CoO (Figure S5-2) and then curled under shear force during milling. The MoS₂ preserved the curved morphology after HCl solution etching. The curved morphology caused by lattice bending inevitably generates out-of-plane lattice strains, which is conceived to be beneficial for the HER^[17, 25, 26]. Simultaneously, the size of Co@MoS₂ in Figure 5-2e is significantly smaller than that of M-MoS₂ (Figure 5-2c), which is consistent with the XRD results.

We further conducted the structure characterization using Raman spectroscopy. As shown in Figure 5-2f, two prominent Raman bands at approximately 380 and 405 cm⁻¹ represent the in-plane E_{2g}¹ and out-of-plane A_{1g}¹ vibration modes of 2H-MoS₂, respectively [27, 28]. Note that, the Raman characteristic peaks of Co@MoS₂-x (Figure 5-2f and S5-3) and M-MoS₂ presents opposite shift trends. As compared with the C-MoS₂, the M-MoS₂ shows a blueshift, which is related to the reduced particle size and layers^[29, 30]. Conversely, a red shift can be observed for the Co₃O₄@MoS₂-x, which can be ascribed to the heteroatom doping as well as the strain^[17, 18]. The chemical state of

the as-obtained MoS₂ catalysts was also characterized by X-ray photoelectron spectroscopy (XPS). In Mo 3d XPS spectrum (Figure S5-4), two major peaks are distinctly observed at 229.6 and 232.7 eV, which are assigned to the Mo 3d 5/2 and Mo 3d 3/2 in C-MoS₂ [31, 32], respectively. Obviously, the valence state of Mo in M-MoS₂ did not present observable changes, indicating that the HEMM process without CoO cannot generate abundant defects on MoS₂. In contrast, the peaks of Mo 3d for Co,O@MoS₂ shift to lower energy. Similar phenomena are also observed from the S 2s XPS spectrum (Figure S5-5). Both shifts of Mo 3d and S 2s peaks to lower energy indicate that the electron density around the Mo and S sites increases, which can be ascribed to the created defects and heteroatom incorporation. Meanwhile, the detected Co 2p signal provides solid evidence for Co incorporation into the Co@MoS₂ (Figure S5-6). The value of Co 2p_{3/2} was measured to be 779.1 eV, indicating that Co atoms are chemically bonded into MoS₂ instead of metallic Co (778 eV) [33-35] or CoO (780.7 eV) [36, 37]. The results confirmed that atomic diffusion occurred during the HMBM process, and Co atoms were incorporated into lattice of MoS₂ driven by mechanical force. Moreover, the gradually enhanced peak intensity of Co 2p_{3/2} with the increase of CoO reflects the higher content of cobalt atoms. Inductively coupled plasma-atomic emission spectrometry (ICP-AES) is also conducted to quantitatively identify the content of Co, shown in Table S5-1. The results show that the increase of CoO will lead to the enhancement of Co loading amount in MoS₂. Accordingly, the heteroatom incorporation further affirms the red shift in the Raman spectra. Besides, O 1s XPS of Co,O@MoS₂ is also detected (Figure S5-7), which can be deconvoluted into two peaks. The O 1s peak at 531.5 eV ascribes to the binding energy of M(Co/Mo)-O bonds, indicating O atoms are also successfully incorporated [38-40]. The O 1s peak at 532.4 eV is assigned to the adsorbed water molecules [35, 41, 42].

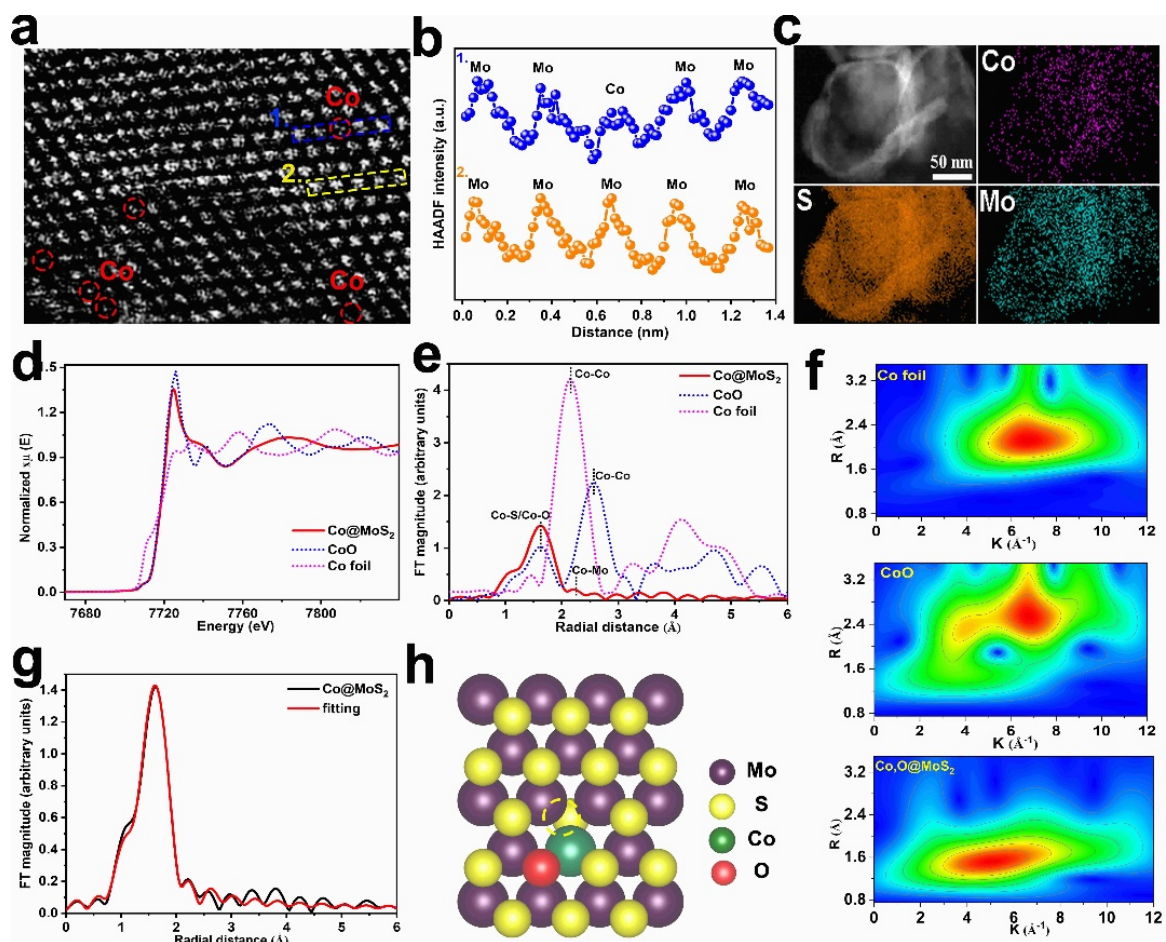


Figure 5-3. Structure characterizations of Co,O@MoS₂. (a) Aberration-corrected atomic resolution HAADF-STEM image of Co,O@MoS₂. (b) Intensity profiles along line 1 and 2 indicated in image (a). (c) EDS mapping of Co,O@MoS₂. (d) Normalized Co K-edge X-ray absorption near-edge structure spectra (XANES) of the Co K-edge for the Co foil, CoO and Co,O@MoS₂, respectively. (e) Fourier transform (FT) k^3 -weighted XANES of Co,O@MoS₂, CoO and Co foil. (f). Wavelet transform (WT) for the k^3 -weighted EXAFS signals of Co,O@MoS₂, CoO and Co foil, respectively. (g). The corresponding experimental and best-fitted EXAFS spectra in R space for Co,O@MoS₂. (h) The simulation model of Co,O@MoS₂. The dashed circle represents the S vacancy.

In addition, the atomic-resolution aberration-corrected HAADF-STEM was performed to verify the coordination of Co atoms in the MoS₂ lattice, and also to observe the dispersion status of Co directly. As shown in Figure 5-3a and b, Co atoms are present

as darker dots and Mo atoms are shown as brighter dots, due to the lower atomic number of Co in comparison to Mo. Furthermore, the energy-dispersive X-ray spectroscopy (EDS) analysis in Figure 5-3c validates the homogeneous elemental distribution of Co atoms in Co,O@MoS₂. Meanwhile, the chemical state and coordination environment of the Co,O@MoS₂ was examined by X-ray absorption near-edge structure (XANES) spectroscopy and extended X-ray absorption fine structure (EXAFS) spectroscopy. Figure S5-8 and S5-9 show the Mo K-edge XANES and the EXAFS spectra of C-MoS₂, M-MoS₂ and Co,O@MoS₂ samples. It can be seen that the intensity of white line of M-MoS₂ and Co,O@MoS₂ is weaker than that of C-MoS₂, indicating the generation of defects. In contrast, Co,O@MoS₂ shows the lowest intensity of white line, ascribing to the defects and heteroatom doping. The corresponding FT-EXAFS spectra (Figure S5-9) are also applied to validate the existence of defects. The decrease of peak intensity for Mo-S coordination in Figure S5-9b indicates the HMBM process can create defects in the MoS₂ and the Co,O@MoS₂ possesses the highest defects density. Moreover, the Mo–Mo radial of Co,O@MoS₂ presents a small shift as compared to C-MoS₂, while the shift is not observed for the M-MoS₂. Such changes indicate the existence of strain [25]. The results are consistent with the XPS results (Figure S5-4). Figure 5-3d also compares the XANES spectra of Co foil, CoO and Co,O@MoS₂-0.4 at the Co K-edge. The XANES spectra reveal that the absorption energy of Co,O@MoS₂ is lower than that of CoO but higher than that of the Co foil. The results imply that Co is positively charged, and the valence state of Co is between the Co foil (0) and CoO (+2), which agrees well with the XPS results, further confirming the atomic Co doping. Difference in local coordination geometry was further demonstrated by their Fourier-transformed R-space spectra (Figure 5-3e). A predominant peak for Co,O@MoS₂ is situated at around 1.62 Å, corresponding to Co–S/O scattering path, while no Co–Co coordination peak at 2.2 Å can be detected. In contrast, the CoO and Co foil display a dominant Co–Co path at 2.6 Å and 2.2 Å respectively [43, 44]. The absence of Co–Co contribution in the spectra of Co,O@MoS₂ further validates the atomic dispersion of Co atoms, which is in line well with the HAADF-STEM observation. Furthermore, EXAFS wavelet

transform (WT) analysis was employed for discernment of the atomic Co dispersion. The WT plot (Figure 5-3f) of Co₂O@MoS₂ shows the WT maximum at around 5.0 Å⁻¹ is attributed to the Co–S/O bond by comparing with the Co foil and CoO, while no intensity maximum corresponded to Co–Co can be observed. The quantitative structural parameters of Co sites in Co₂O@MoS₂ are obtained from the least-squares EXAFS fitting analysis. As shown in Figure 5-3g, the k space and R space best fitting curves matched well with the experimental results. The fitting result of Co₂O@MoS₂ (Figure 5-3g and Table S5-2) shows the co-presence of Co–S and Co–O scattering path with coordination numbers of 4.0 and 0.6, respectively. These results indicate that Co atoms are coordinated with four S atoms and one O atom in Co₂O@MoS₂. Figure 5-3h shows the corresponding atomic structure model.

The HER electrocatalytic activity of prepared MoS₂-based catalysts was examined using a typical standard three-electrode system in a 1 M KOH solution. Figure 5-4a and Figure S5-10 show the representative linear sweep voltammograms (LSV) curves for 20% Pt/C electrode, commercial MoS₂, CoO particle, M-MoS₂, and Co₂O@MoS_{2-x}. Due to its limited electrochemical active edges, the commercial MoS₂ exhibits very low HER activity, confirming that the commercial MoS₂ mainly consists of the inactive basal plane. The HMBM process can effectively exfoliate and refine the MoS₂ particles, thus exposing more active edges. Accordingly, the catalytic activity of the milled MoS₂ (M-MoS₂) is about 100 mV smaller than that of the commercial MoS₂ at 10 mA cm⁻². Extraordinarily, the MoS₂ mechanochemically modified with CoO can further optimize the HER catalytic activity. Through regulating the mass ratio of CoO/MoS₂, the modified MoS₂ exhibits excellent catalytic activity with the increase of cobalt oxide content (Figure S5-10). Typically, the Co₂O@MoS_{2-0.4} shows a lowest overpotential of 94 mV at 10 mA cm⁻², which is 130 mV and 230mV smaller than that of the M-MoS₂ and C-MoS₂, respectively (Figure 5-3a and Figure S5-12). The Tafel slope, as a pivotal kinetic parameter, is usually used to investigate the rate-determining step of an electrochemical process. By fitting the LSV curves, the Co₂O@MoS_{2-0.4} shows the

lowest Tafel slope of 76 mV dec⁻¹ among the as-prepared catalysts, whereas that for the C-MoS₂ is as large as 103 mV dec⁻¹ (Figure 5-4b). The decrease from 103 to 76 mV dec⁻¹ indicates that the isolated Co atoms incorporation could alter the rate-limiting step from the H adsorption to electrochemical desorption step, reflecting the Volmer–Heyrovsky mechanism [45].

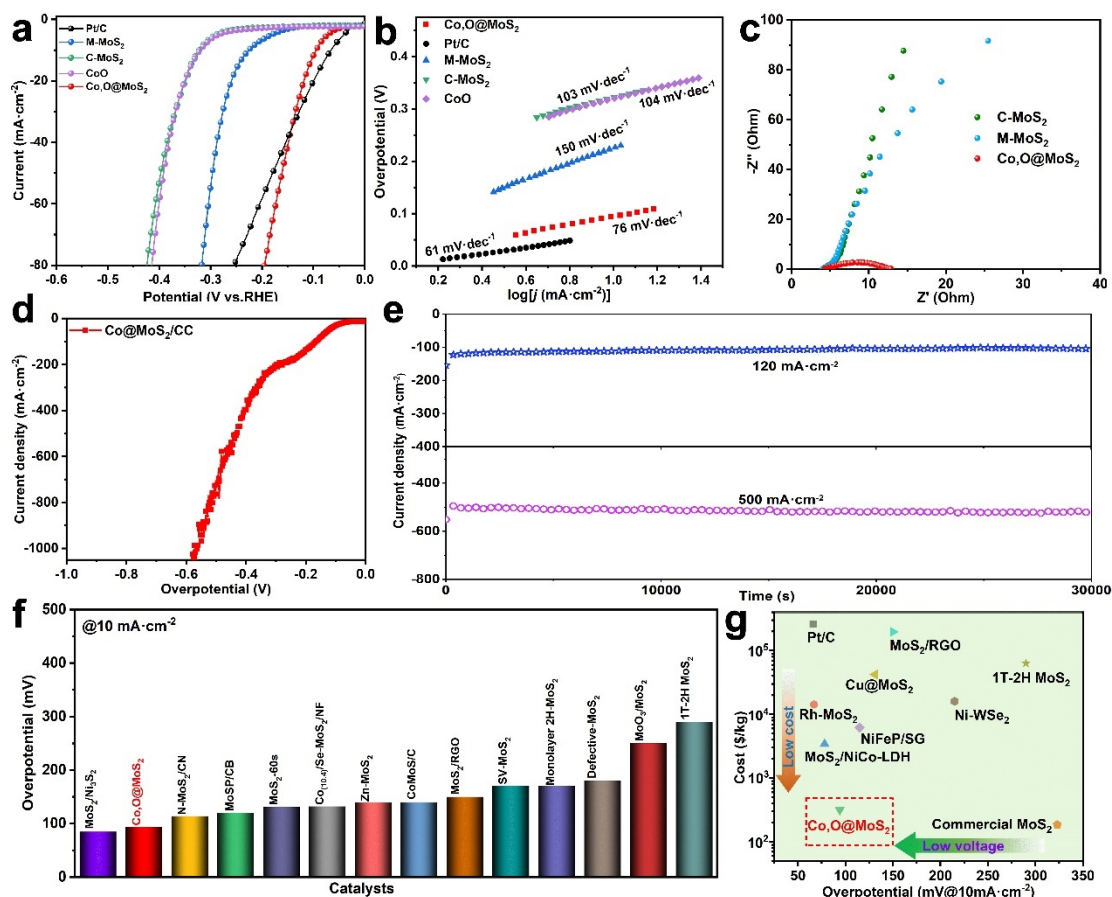


Figure 5-4. Catalytic HER performances. (a) Linear sweep voltammetry (LSV) curves of C-MoS₂, CoO, M-MoS₂, Co,O@MoS₂ and 20 wt% Pt/C in 1.0 M KOH at a scan rate of 5 mV s⁻¹. (b) Tafel plots derived from the LSV curves in (a). (c) Nyquist plot of electrochemical impedance spectra for C-MoS₂, M-MoS₂ and Co,O@MoS₂. (d) HER polarization curves of Co,O@MoS₂ coated on carbon cloth. (e) Long-term stability test of Co,O@MoS₂ at 500 mA cm⁻². (f) Comparison of the η₁₀ values between Co,O@MoS₂ and hydrogen evolution electrocatalysts. (g) Stability test of Ru₁@MoS₂ at 500 mA cm⁻².

Electrochemical impedance spectroscopy (EIS) tests were conducted to further investigate the charge transfer kinetics. As shown in Figure 5-4c and Figure S5-13, the charge transfer resistances (R_{ct}) of the Co,O@MoS₂-x decline substantially compared with C-MoS₂ and M-MoS₂, of which Co@MoS₂-0.4 exhibits smallest R_{ct} value of 7.4 Ω . The results suggest that the Co@MoS₂-0.4 possesses the best charge-transfer properties than the other samples, thus has superior HER kinetics. The electrochemical active surface area (ECSA) was also evaluated from the double-layer capacitance (C_{dl}) to understand the improvement of the HER activity, shown in Figure S5-11 and S5-12. Remarkably, the Co@MoS₂-0.4 yields the highest C_{dl} value of 31.9 mF cm⁻², whereas the C-MoS₂, M-MoS₂, Co,O@MoS₂-0.1, and Co,O@MoS₂-0.2 are determined to be 3.5, 9.6, 10.1, and 14.1 mF·cm⁻², respectively. The results indicate that introducing more CoO can remarkably extend the electrochemical active area during HMBM, thus rendering more catalytic active sites. In addition, stability performance was evaluated via dropping the Co,O@MoS₂ onto carbon cloth (Figure 5-4d and e). Under the current density of 120 mA cm⁻², the Co,O@MoS₂ shows a negligible decrease after 30000 s. Considering the industrial applications, we further examined the stability under a high current density of 500 mA cm⁻² (Figure 5-4e). The high current density remained after continuous test of 30000 s, reflecting the robust structure of Co,O@MoS₂ even at high current density. The features of low overpotential, low EIS, large C_{dl} as well as good stability at high current density demonstrate that Co,O@MoS₂ is an excellent HER catalyst. Combining the abundance and cheapness of C-MoS₂, our synthetic strategy of CoO-assisted HMBM provides a commercially feasible method for hydrogen production via water splitting. Moreover, compared with previously reported MoS₂-based catalysts, the Co,O@MoS₂-0.4 also shows outstanding HER activity (Figure 5-4f, Table S5-3). The fabrication methods via ball milling for the Co,O@MoS₂ show noticeable superiority over other methods, such as the simple process, low equipment requirement, and large-scale preparation. Then we further evaluate the cost of fabricated catalysts. Figure 5-4g (Table S5-4) displays the overpotential (@10mA cm⁻²) vs. cost. Apparently, the Co,O@MoS₂ indicates the comprehensive advantages of

properties and price, which provides a promising and practical way toward large-scale production of advanced HER catalysts for commercial application.

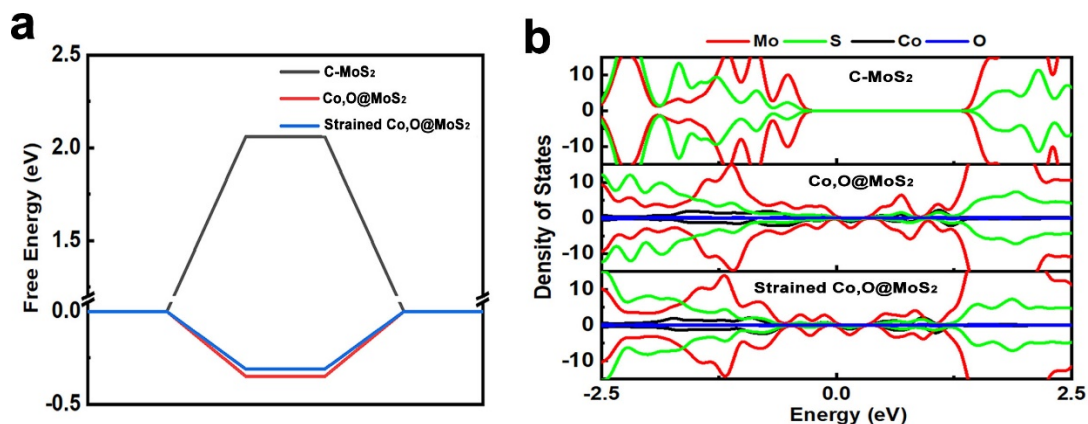


Figure 5-5. (a) The hydrogen adsorption free energy diagrams of the C-MoS₂, Co,O@MoS₂, strained Co,O@MoS₂. (b) Comparison of the DOS for C-MoS₂, Co,O@MoS₂, and strained Co,O@MoS₂, respectively.

DFT calculations were also carried out to gain further insights into the influence of Co doping and strain on the HER activity. For an ideal HER catalyst, the free energy of hydrogen adsorption (ΔG_{H^+}) should be close to 0 eV. As shown in Figure 5-5a, the ΔG_{H^+} on the surface of Co,O@MoS₂ and strain Co,O@MoS₂ is calculated to be -0.35 eV, and -0.31 eV, respectively, which is much smaller than that on the pristine MoS₂ (2.06 eV). Thus, the strained Co,O@MoS₂ is expected to show better HER activity than that of the Co,O@MoS₂, and the Co doping can sufficiently enhance the HER activity of MoS₂, which is in line with our experimental findings. To understand such enhancement of HER activity, the density of states (DOS) of the pristine MoS₂, Co,O@MoS₂ and strained Co,O@MoS₂ are calculated and shown in Figure 5-5b. The Co doping leads to more states around the Fermi level which not only promotes the interaction between the catalyst and reactants but also improve the electric conductivity of MoS₂. When strain is applied, the states near to the Fermi level is slightly reduced and pushed into deeper level, which consequently weakens the strong binding of hydrogen and the Co,O@MoS₂ surface.

5.3 Conclusions

In summary, we reported a sustainable batch preparation method for producing MoS₂-based HER electrocatalysts. The catalytic activity of the commercial bulk MoS₂ can be modulated by ball milling with CoO via integrating the strain, heteroatom doping and particle sizes. The Co₂O₃@MoS₂ demonstrated the most outstanding HER activity of all the fabricated catalysts, with a low overpotential of 94 mV at 10 mA cm⁻² under strong alkaline conditions. Moreover, the catalysts exhibit decent catalytic stability under both low-current density and high-current density. Furthermore, the cheap and earth abundant MoS₂ also provides the electrocatalytic HER with significant economic performance. Evaluated from the aspect of performance and cost, our results show the great potential of the developed method in industrialized sustainable hydrogen production.

5.4 References

1. Symes M D and Cronin L. Decoupling hydrogen and oxygen evolution during electrolytic water splitting using an electron-coupled-proton buffer. *Nature Chemistry* 2013; 5: 403-409.
2. Mahmood N, Yao Y, Zhang J-W, et al. Electrocatalysts for Hydrogen Evolution in Alkaline Electrolytes: Mechanisms, Challenges, and Prospective Solutions. *Advanced Science* 2018; 5: 1700464.
3. Hossain M D, Liu Z, Zhuang M, et al. Rational Design of Graphene-Supported Single Atom Catalysts for Hydrogen Evolution Reaction. *Adv Energy Mater* 2019; 9: 1803689.
4. Wang D, Li Q, Han C, et al. Single-atom ruthenium based catalyst for enhanced hydrogen evolution. *Appl. Catal., B* 2019; 249: 91-97.
5. Cheng N, Stambula S, Wang D, et al. Platinum single-atom and cluster catalysis of the hydrogen evolution reaction. *Nat Commun* 2016; 7: 13638.

6. Huang X, Leng M, Xiao W, et al. Activating Basal Planes and S-Terminated Edges of MoS₂ toward More Efficient Hydrogen Evolution. *Adv. Funct. Mater.* 2017; 27: 1604943.
7. Yin Y, Han J, Zhang Y, et al. Contributions of Phase, Sulfur Vacancies, and Edges to the Hydrogen Evolution Reaction Catalytic Activity of Porous Molybdenum Disulfide Nanosheets. *J. Am. Chem. Soc.* 2016; 138: 7965-7972.
8. Jaramillo T F, Jørgensen K P, Bonde J, et al. Identification of Active Edge Sites for Electrochemical H₂ Evolution from MoS₂ Nanocatalysts. *Science* 2007; 317: 100-102.
9. Mao J, Wang Y, Zheng Z, et al. The rise of two-dimensional MoS₂ for catalysis. *Frontiers of Physics* 2018; 13: 138118.
10. Ding Q, Song B, Xu P, et al. Efficient Electrocatalytic and Photoelectrochemical Hydrogen Generation Using MoS₂ and Related Compounds. *Chem-Us* 2016; 1: 699-726.
11. Cao Y. Roadmap and Direction toward High-Performance MoS₂ Hydrogen Evolution Catalysts. *Acs Nano* 2021; 15: 11014-11039.
12. Meng C, Chen X, Gao Y, et al. Recent Modification Strategies of MoS₂ for Enhanced Electrocatalytic Hydrogen Evolution. *Molecules* 2020; 25: 1136.
13. Huang H, Huang J, Liu W, et al. Ultradispersed and Single-Layered MoS₂ Nanoflakes Strongly Coupled with Graphene: An Optimized Structure with High Kinetics for the Hydrogen Evolution Reaction. *ACS Appl. Mat. Interfaces* 2017; 9: 39380-39390.
14. Lukowski M A, Daniel A S, Meng F, et al. Enhanced Hydrogen Evolution Catalysis from Chemically Exfoliated Metallic MoS₂ Nanosheets. *J. Am. Chem. Soc.* 2013; 135: 10274-10277.
15. Li Y, Wang H, Xie L, et al. MoS₂ Nanoparticles Grown on Graphene: An Advanced Catalyst for the Hydrogen Evolution Reaction. *J. Am. Chem. Soc.* 2011; 133: 7296-7299.
16. Wang T, Gao D, Zhuo J, et al. Size-Dependent Enhancement of Electrocatalytic

- Oxygen-Reduction and Hydrogen-Evolution Performance of MoS₂ Particles. *Chemistry – A European Journal* 2013; 19: 11939-11948.
17. Li H, Tsai C, Koh A L, et al. Activating and optimizing MoS₂ basal planes for hydrogen evolution through the formation of strained sulphur vacancies. *Nat. Mater.* 2016; 15: 48-53.
 18. Wang X, Zhang Y, Si H, et al. Single-Atom Vacancy Defect to Trigger High-Efficiency Hydrogen Evolution of MoS₂. *J. Am. Chem. Soc.* 2020; 142: 4298-4308.
 19. Deng J, Li H, Wang S, et al. Multiscale structural and electronic control of molybdenum disulfide foam for highly efficient hydrogen production. *Nat Commun* 2017; 8: 14430.
 20. Luo Y, Tang L, Khan U, et al. Morphology and surface chemistry engineering toward pH-universal catalysts for hydrogen evolution at high current density. *Nat Commun* 2019; 10: 269.
 21. Zhang C, Luo Y, Tan J, et al. High-throughput production of cheap mineral-based two-dimensional electrocatalysts for high-current-density hydrogen evolution. *Nat Commun* 2020; 11: 3724.
 22. Liang Z, Xue Y, Guo Y, et al. Rationalizing and controlling the phase transformation of semi-metallic 1T'-phase and semi-conductive 2H-phase MoS₂ as cocatalysts for photocatalytic hydrogen evolution. *Chem. Eng. J.* 2020; 396: 125344.
 23. Bang G S, Nam K W, Kim J Y, et al. Effective Liquid-Phase Exfoliation and Sodium Ion Battery Application of MoS₂ Nanosheets. *ACS Appl. Mat. Interfaces* 2014; 6: 7084-7089.
 24. Amini M, Ramazani S.A A, Faghihi M, et al. Preparation of nanostructured and nanosheets of MoS₂ oxide using oxidation method. *Ultrason. Sonochem.* 2017; 39: 188-196.
 25. Jiang K, Luo M, Liu Z, et al. Rational strain engineering of single-atom ruthenium on nanoporous MoS₂ for highly efficient hydrogen evolution. *Nat*

- Commun 2021; 12: 1687.
26. Lee J H, Jang W S, Han S W, et al. Efficient Hydrogen Evolution by Mechanically Strained MoS₂ Nanosheets. *Langmuir* 2014; 30: 9866-9873.
 27. Li H, Zhang Q, Yap C C R, et al. From Bulk to Monolayer MoS₂: Evolution of Raman Scattering. *Adv. Funct. Mater.* 2012; 22: 1385-1390.
 28. Attanayake N H, Dheer L, Thenuwara A C, et al. Ni- and Co-Substituted Metallic MoS₂ for the Alkaline Hydrogen Evolution Reaction. *ChemElectroChem* 2020; 7: 3606-3615.
 29. Han C, Zhang Y, Gao P, et al. High-Yield Production of MoS₂ and WS₂ Quantum Sheets from Their Bulk Materials. *Nano Lett.* 2017; 17: 7767-7772.
 30. Liang C, Sui X, Wang A, et al. Controlled Production of MoS₂ Full-Scale Nanosheets and Their Strong Size Effects. *Advanced Materials Interfaces* 2020; 7: 2001130.
 31. Yang Y, Fei H, Ruan G, et al. Edge-Oriented MoS₂ Nanoporous Films as Flexible Electrodes for Hydrogen Evolution Reactions and Supercapacitor Devices. *Adv. Mater.* 2014; 26: 8163-8168.
 32. Ye R, Del Angel-Vicente P, Liu Y, et al. High-Performance Hydrogen Evolution from MoS₂(1-x)P_x Solid Solution. *Adv. Mater.* 2016; 28: 1427-1432.
 33. Liang L, Jin H, Zhou H, et al. Cobalt single atom site isolated Pt nanoparticles for efficient ORR and HER in acid media. *Nano Energy* 2021; 88: 106221.
 34. Pan Y, Sun K, Liu S, et al. Core-Shell ZIF-8@ZIF-67-Derived CoP Nanoparticle-Embedded N-Doped Carbon Nanotube Hollow Polyhedron for Efficient Overall Water Splitting. *J. Am. Chem. Soc.* 2018; 140: 2610-2618.
 35. Yuan X, Ge H, Wang X, et al. Controlled Phase Evolution from Co Nanochains to CoO Nanocubes and Their Application as OER Catalysts. *ACS Energy Letters* 2017; 2: 1208-1213.
 36. Liao L, Zhang Q, Su Z, et al. Efficient solar water-splitting using a nanocrystalline CoO photocatalyst. *Nat. Nanotechnol.* 2014; 9: 69-73.
 37. Shi W, Guo F, Zhu C, et al. Carbon dots anchored on octahedral CoO as a stable

- visible-light-responsive composite photocatalyst for overall water splitting. *J. Mater. Chem. A* 2017; 5: 19800-19807.
38. Liu J, Wang Z, Li J, et al. Structure Engineering of MoS₂ via Simultaneous Oxygen and Phosphorus Incorporation for Improved Hydrogen Evolution. *Small* 2020; 16: 1905738.
 39. Ullah N, Xie M, Chen L, et al. Novel 3D graphene ornamented with CoO nanoparticles as an efficient bifunctional electrocatalyst for oxygen and hydrogen evolution reactions. *Mater. Chem. Phys.* 2021; 261: 124237.
 40. Xie J, Zhang J, Li S, et al. Controllable Disorder Engineering in Oxygen-Incorporated MoS₂ Ultrathin Nanosheets for Efficient Hydrogen Evolution. *J. Am. Chem. Soc.* 2013; 135: 17881-17888.
 41. Lin H, Li Y, Li H, et al. Multi-node CdS hetero-nanowires grown with defect-rich oxygen-doped MoS₂ ultrathin nanosheets for efficient visible-light photocatalytic H₂ evolution. *Nano Res* 2017; 10: 1377-1392.
 42. Wang X, Liu Y, Zhang T, et al. Geometrical-Site-Dependent Catalytic Activity of Ordered Mesoporous Co-Based Spinel for Benzene Oxidation: In Situ DRIFTS Study Coupled with Raman and XAFS Spectroscopy. *Acs Catal* 2017; 7: 1626-1636.
 43. Guo W, Luo H, Fang D, et al. In situ revealing the reconstruction behavior of monolayer rocksalt CoO nanosheet as water oxidation catalyst. *Journal of Energy Chemistry* 2022; 70: 373-381.
 44. Pan Y, Lin R, Chen Y, et al. Design of Single-Atom Co–N₅ Catalytic Site: A Robust Electrocatalyst for CO₂ Reduction with Nearly 100% CO Selectivity and Remarkable Stability. *J. Am. Chem. Soc.* 2018; 140: 4218-4221.
 45. Xu Q, Liu Y, Jiang H, et al. Unsaturated Sulfur Edge Engineering of Strongly Coupled MoS₂ Nanosheet–Carbon Macroporous Hybrid Catalyst for Enhanced Hydrogen Generation. *Adv Energy Mater* 2019; 9: 1802553.

5.5 Supporting Information

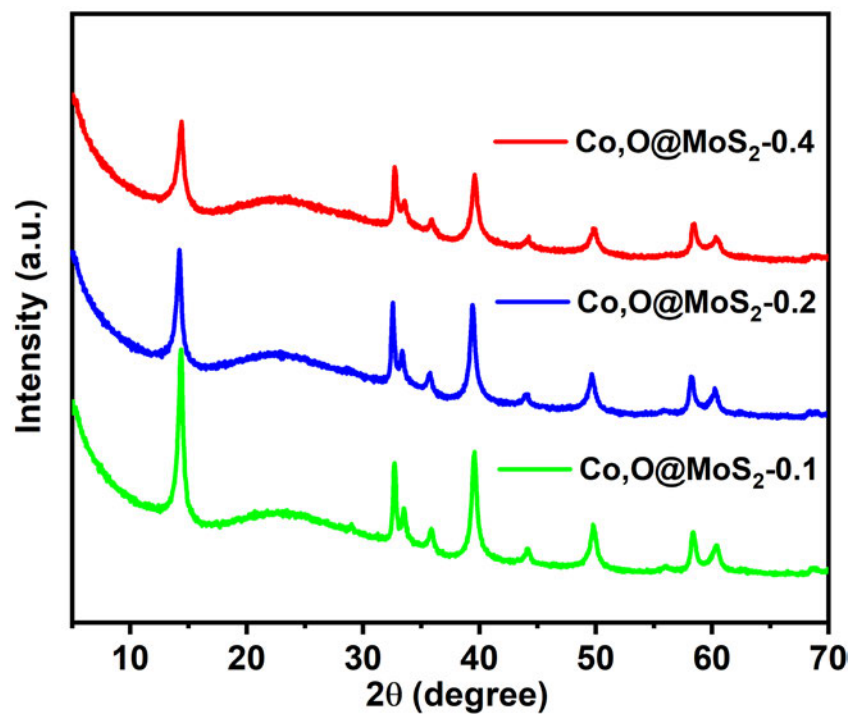


Figure S5-1. XRD patterns of Co,O@MoS_{2-x} (x=0.1, 0.2 and 0.4).

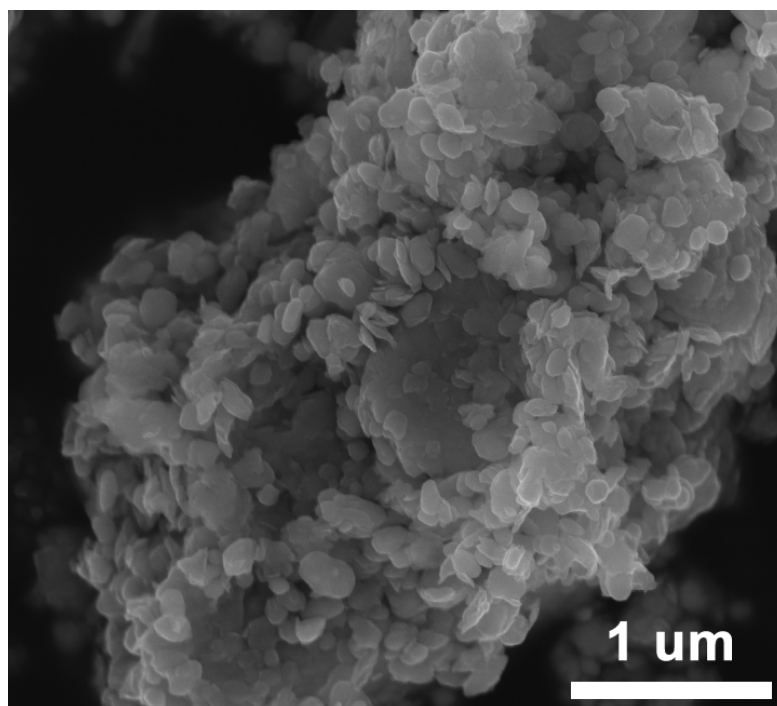


Figure S5-2. The SEM images of Co,O@MoS₂-0.4 after milling.

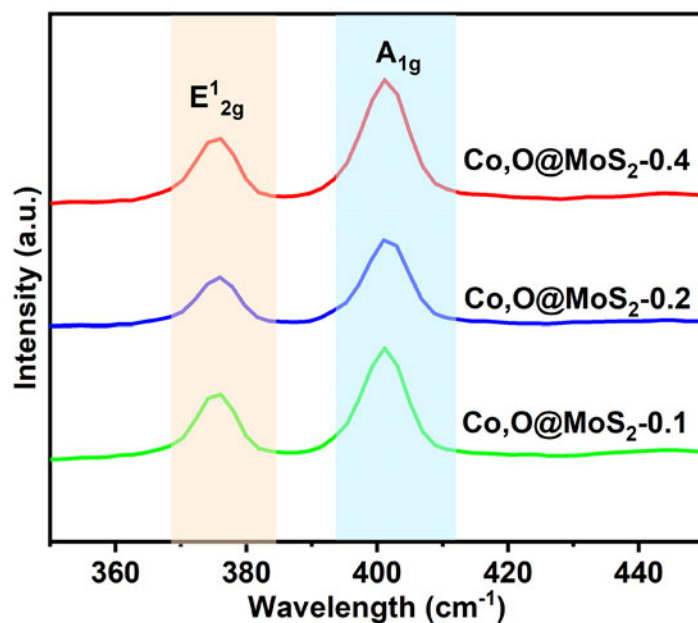


Figure S5-3. Representative Raman spectra for Co,O@MoS₂-x (x=0.1, 0.2 and 0.4).

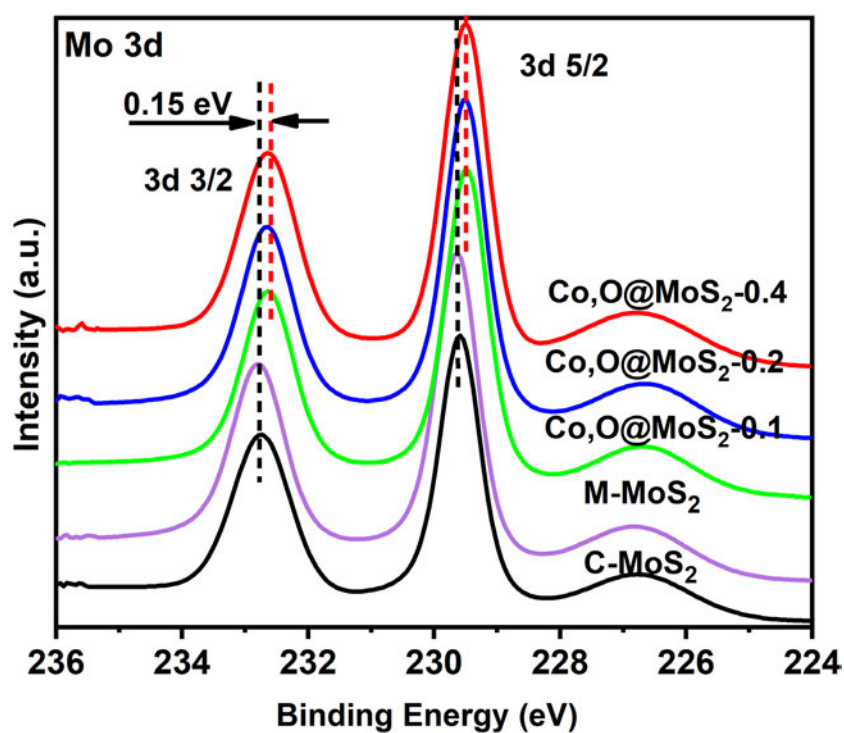


Figure S5-4. High-resolution Mo 3d XPS spectra of C-MoS₂, M-MoS₂, and Co,O@MoS₂-x (x=0.1, 0.2 and 0.4), respectively.

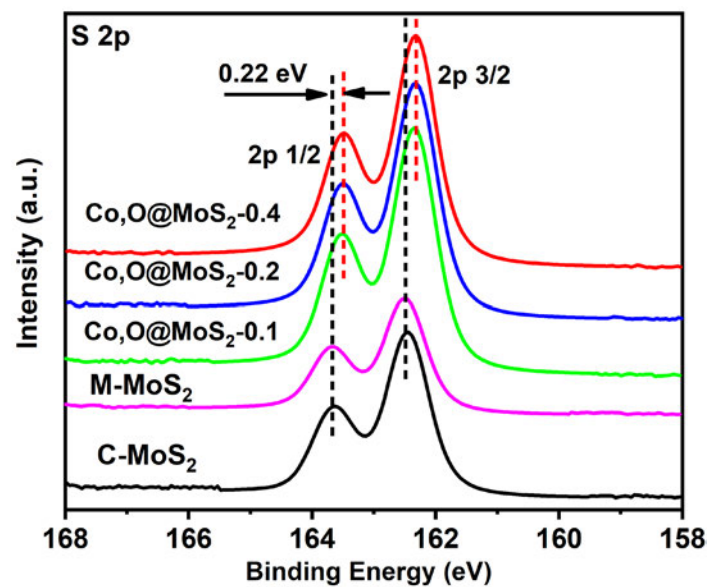


Figure S5-5. High-resolution S 2p XPS spectra of C-MoS₂, M-MoS₂, and Co,O@D-MoS₂-x (x=0.1, 0.2 and 0.4), respectively.

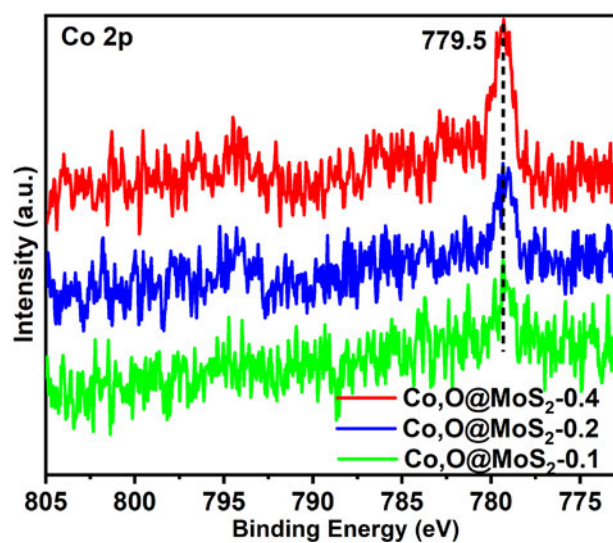


Figure S5-6. High-resolution Co 2p XPS spectra of Co,O@MoS₂-x (x=0.1, 0.2 and 0.4), respectively.

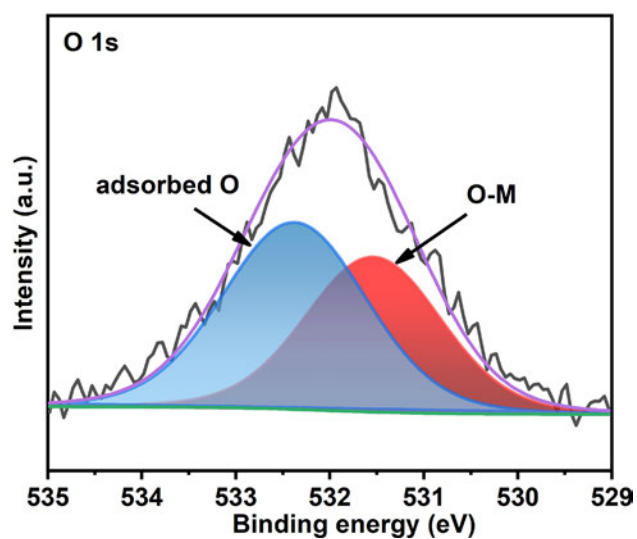


Figure S5-7. High-resolution O 1s XPS spectra of Co,O@MoS₂.

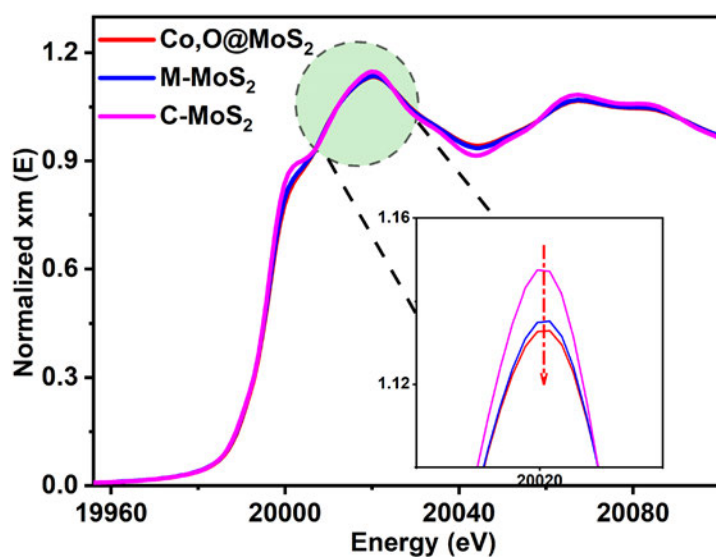


Figure S5-8. Normalized XAFS spectra of the Mo K-edge for the C-MoS₂, M-MoS₂ and Co,O@MoS₂ samples.

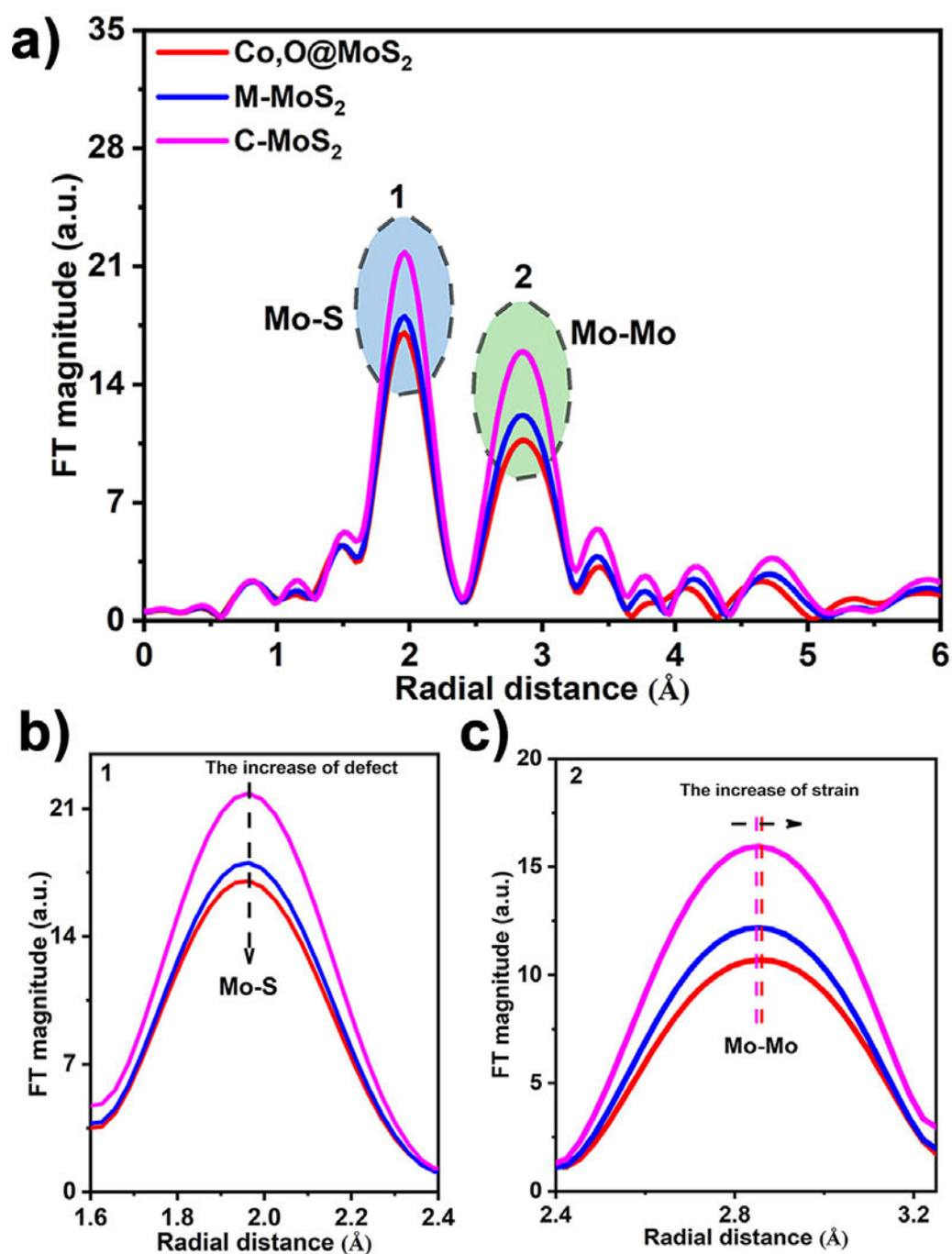


Figure S5-9. Fourier transform of Mo K-edge EXAFS spectra (a). (b) and (c) are the enlarged spectra corresponding to region 1 and 2 in (a).

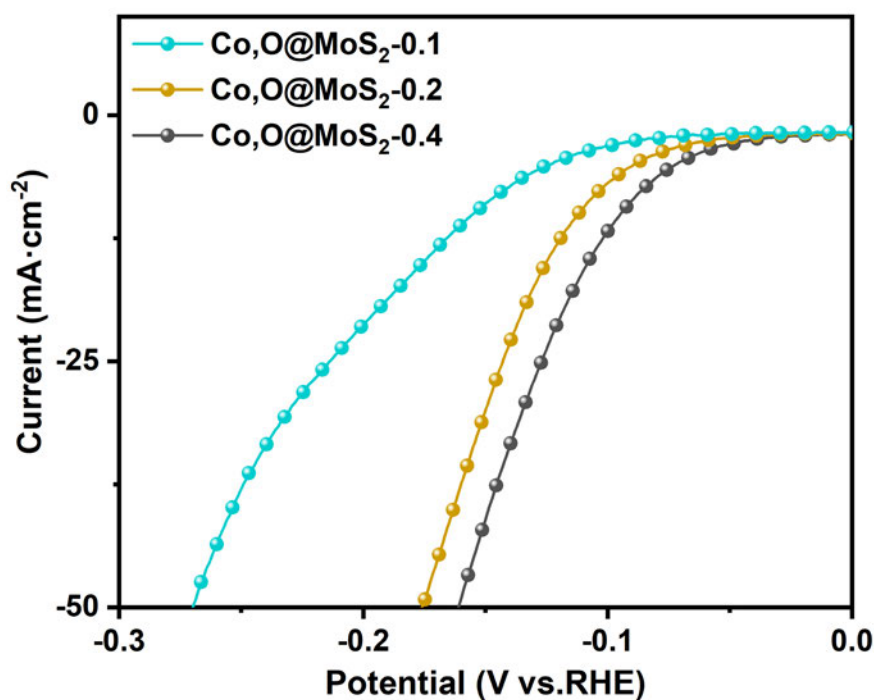


Figure S5-10. (a) Electrochemical HER performance of Co,O@MoS₂-x (x=0.1, 0.2 and 0.4).

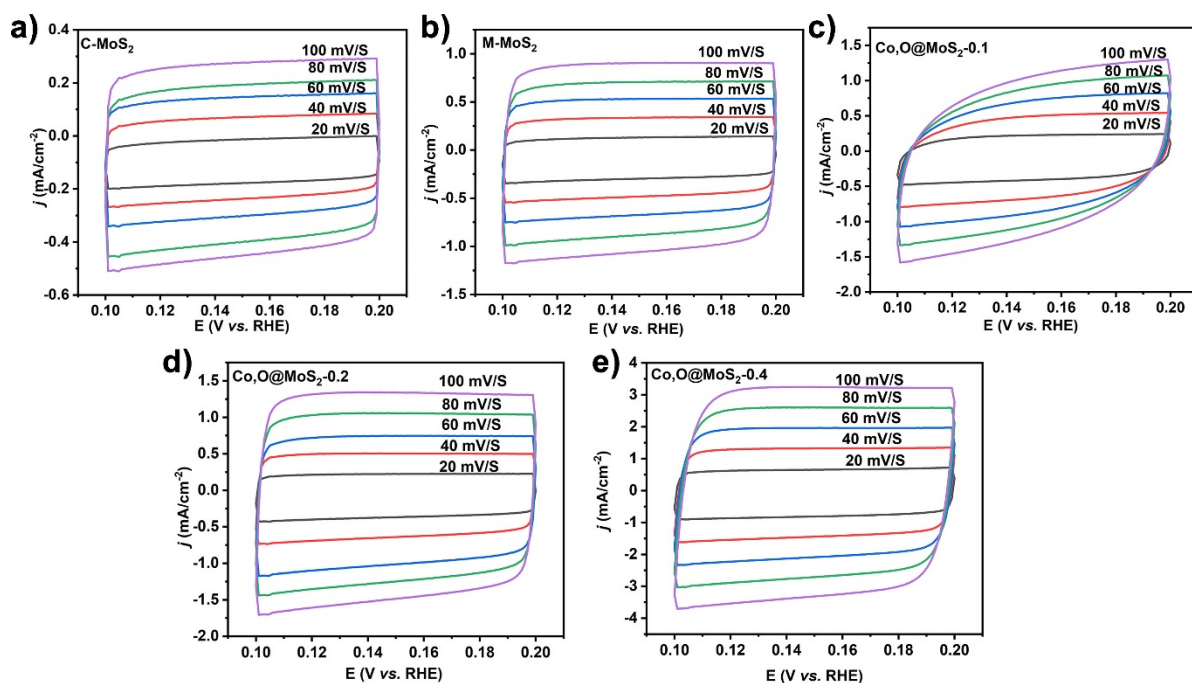


Figure S5-11. CV curves at various scan rates of (a) C-MoS₂, b) M-MoS₂, (c) Co,O@MoS₂-0.1, Co,O@MoS₂-0.2 and Co,O@MoS₂-0.4 in 1M KOH.

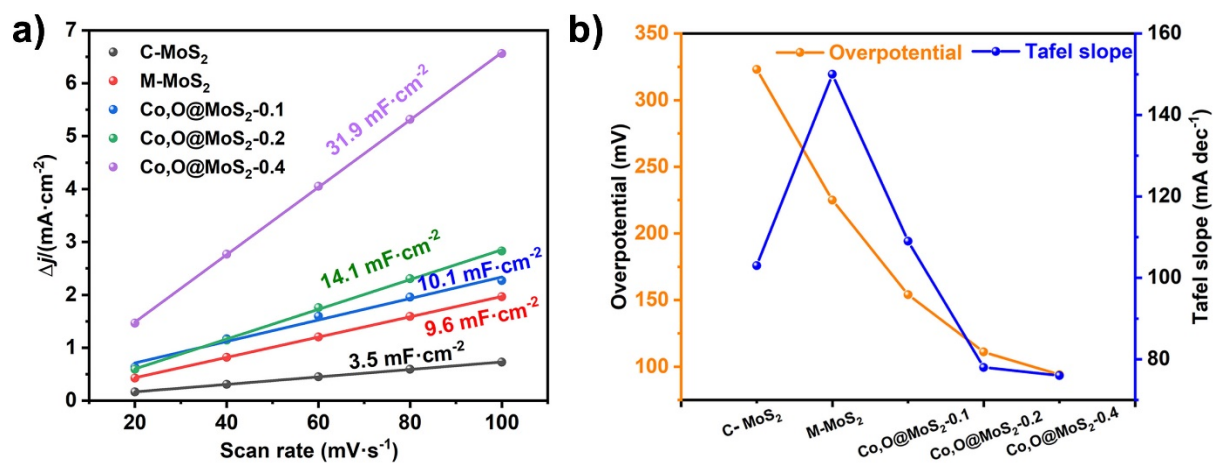


Figure S5-12. (a) Linear fits of half capacitive currents versus scan rates for the extraction of Cdl. (b) Comparison of Tafel slope and overpotential values at the current density of 10 mA cm⁻².

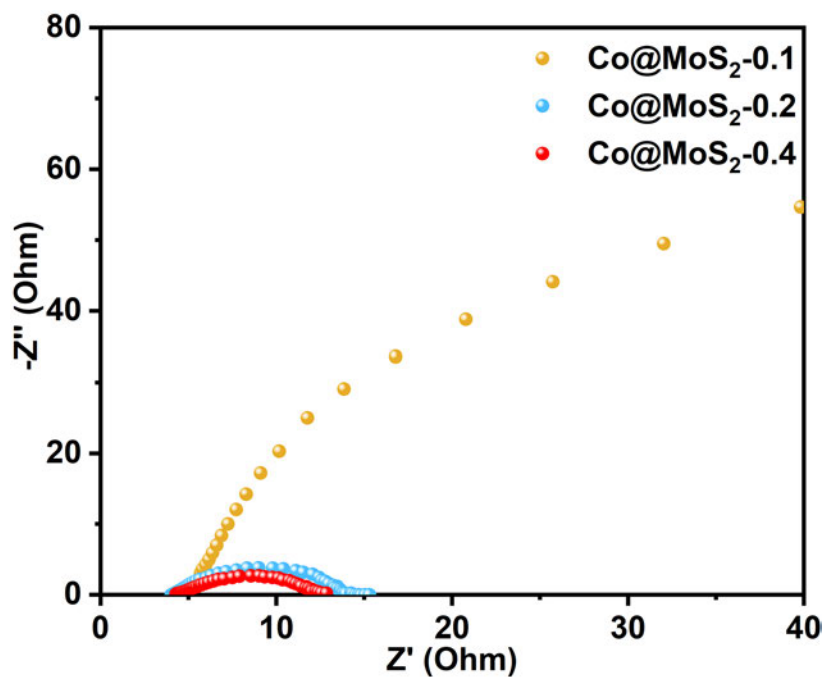


Figure S5-13. Nyquist plot of electrochemical impedance spectra for Co₂O₃@MoS₂-x (x=0.1, 0.2 and 0.4).

Table S5-1. Elemental contents determined by ICP-MS for different catalysts.

Samples	Co ₂ O ₃ @MoS ₂ -0.1	Co ₂ O ₃ @MoS ₂ -0.2	Co ₂ O ₃ @MoS ₂ -0.4
Content (wt%)	0.13	0.24	0.44

Table S5-2. The EXAFS fitting parameters of Co R-space for Co₂O₃@D-MoS₂.

Sample	path	N	σ^2 (Å ²)	R/Å
Co ₂ O ₃ @MoS ₂	Co-O	1	0.00497	1.81532
	Co-S	4	0.0051	2.19372

Note: N is the coordination number; σ^2 , Debye-Waller factor to account for both thermal and structural disorders; R is the distance between absorber and backscatter atoms.

Table S5-3. Electrocatalytic HER performance of our synthesized Co₂O₃@D-MoS₂ compared with that of other reported MoS₂-based HER electrocatalysts.

Catalysts	Overpotential at 10 mA·cm ⁻² (mV)	Electrolyte	Ref.
Co ₂ O ₃ @MoS ₂	94	1 M KOH	This work
Monolayer 2H-MoS ₂	170	0.5 M H ₂ SO ₄	<i>Adv. Mater.</i> 2013 , 25, 5807–5813.
1T–2H MoS ₂	290	1 M KOH	<i>Adv. Energy Mater.</i> 2018 , 8, 1801345.
SV-MoS ₂	170	0.5 M H ₂ SO ₄	<i>Nature Mater.</i> 2016 , 15, 48–53
MoS ₂ -60 s	131	0.5 M H ₂ SO ₄	<i>J. Am. Chem. Soc.</i> 2020 , 142, 4298–4308
defective MoS ₂	180	0.5 M H ₂ SO ₄	<i>Adv. Mater.</i> 2013 , 25, 5807–5813
Zn-MoS ₂	140	0.5 M H ₂ SO ₄	<i>J. Am. Chem. Soc.</i> 2017 , 139, 15479–15485
MoS ₂ /Ni ₃ S ₂	85	1 M KOH	<i>Int. J. Hydrog. Energy.</i> 2020, 45, 13149–13162.
Co _(10.4) /Se-MoS ₂ -NF	132	0.5 M H ₂ SO ₄	<i>Nat Commun.</i> 2020 , 11, 3315
CoMoS/C	140	0.5 M H ₂ SO ₄	<i>ACS Appl. Mater. Interfaces</i> 2015 , 7, 27242
MoSP/CB	120	0.5 M H ₂ SO ₄	<i>Adv. Mater.</i> 2016 , 28, 1427–1432
N-MoS ₂ /CN	114	0.5 M H ₂ SO ₄	<i>J. Am. Chem. Soc.</i> 2019 , 141, 18578–18584.
MoS ₂ /RGO	150	0.5 M H ₂ SO ₄	<i>J. Am. Chem. Soc.</i> 2011 , 133, 7296–7299
MoO ₃ /MoS ₂	250	0.5 M H ₂ SO ₄	<i>ACS Appl. Energy Mater.</i> 2020 , 3, 5333–5342.

Table S5-4. Comparison of the cost vs. activity at 10 mAcm⁻².

Catalysts	Overpotential at 10 mA·cm ⁻² (mV)	Electrolyte	Price (\$/Kg)	Ref.
Rh-MoS ₂	67	0.5 M H ₂ SO ₄	14246	[3]
MoS ₂ /NiCo-LDH	78	1 M KOH	3432	[4]
20wt% Pt/C	66	1 M KOH	263000	This work
Co ₃ O ₄ @MoS ₂	94	1 M KOH	318	This work
MoS ₂ /RGO	150	0.5 M H ₂ SO ₄	196469	[5]
Cu@MoS ₂	131	0.5 M H ₂ SO ₄	42254	[6]
1T-2H MoS ₂	290	1 M KOH	63264	[7]
NiFeP/SG	115	1 M KOH	6267	[8]
C- MoS ₂	323	1 M KOH	186	This work
Ni-WSe ₂	215	1 M KOH	16052	[9]

Reference:

1. Yu, X., et al., *An Mn-doped NiCoP flower-like structure as a highly efficient electrocatalyst for hydrogen evolution reaction in acidic and alkaline solutions with long duration*. *Nanoscale*, 2021. **13**(25): p. 11069-11076.
2. Zhou, Q., et al., *Engineering additional edge sites on molybdenum dichalcogenides toward accelerated alkaline hydrogen evolution kinetics*. *Nanoscale*, 2019. **11**(2): p. 717-724.
3. Meng, X., et al., *Distance Synergy of MoS₂-Confined Rhodium Atoms for Highly Efficient Hydrogen Evolution*. *Angewandte Chemie International Edition*, 2020. **59**(26): p. 10502-10507.

4. Hu, J., et al., *Nanohybridization of MoS₂ with Layered Double Hydroxides Efficiently Synergizes the Hydrogen Evolution in Alkaline Media*. Joule, 2017. **1**(2): p. 383-393.
5. Li, Y., et al., *MoS₂ Nanoparticles Grown on Graphene: An Advanced Catalyst for the Hydrogen Evolution Reaction*. Journal of the American Chemical Society, 2011. **133**(19): p. 7296-7299.
6. Ji, L., et al., *One-pot synthesis of porous 1T-phase MoS₂ integrated with single-atom Cu doping for enhancing electrocatalytic hydrogen evolution reaction*. Applied Catalysis B: Environmental, 2019. **251**: p. 87-93.
7. Wang, S., et al., *Ultrastable In-Plane 1T-2H MoS₂ Heterostructures for Enhanced Hydrogen Evolution Reaction*. Advanced Energy Materials, 2018. **8**(25): p. 1801345.
8. Li, R.-Q., et al., *Monolithic electrode integrated of ultrathin NiFeP on 3D strutted graphene for bifunctionally efficient overall water splitting*. Nano Energy, 2019. **58**: p. 870-876.
9. Kadam, S.R., et al., *Ni-WSe₂ nanostructures as efficient catalysts for electrochemical hydrogen evolution reaction (HER) in acidic and alkaline media*. Journal of Materials Chemistry A, 2020. **8**(3): p. 1403-1416.

Chapter 6. Crossover from physisorption to chemisorption: a rational design for H₂ storage

STATEMENT OF CONTRIBUTION TO CO-AUTHORED PUBLISHED PAPER

This chapter includes a co-authored paper. The status of the co-authored paper, including all authors, are:

Chengguang Lang, Lei Zhang, Cheng-Jie Yang, Hao Zhong, Hanwu Dong, Chung-Li Dong, Aijun Du, Xuecheng Yan, Liuzhang Ouyang, Yi Jia, Xiangdong Yao

My contribution to the paper involved:

- Literature survey
- Concept and design
- Analysis and interpretation of data
- Drafting and writing

(Signed)  (Date) 31/07/2022
Chengguang Lang

(Countersigned) _____ (Date) 02/08/2022
Corresponding author of paper: Prof. Xiangdong Yao

(Countersigned)  (Date) 31/07/2022
Supervisor: Dr. Xuecheng Yan

6.1 Introduction

The ever-growing energy demand versus the depleting of fossil fuel reserves and the environmental pollution urge us to promote the carbon neutralization by the use of clean energy^[1-4]. Among all new energy sources, hydrogen holds significant promise as a clean energy carrier owing to its characteristics of high enthalpy, zero emission, and renewability^[2, 5, 6]. However, as a vital component in ‘hydrogen economy’, hydrogen storage and transportation is still a big challenge at present^[7-9]. Thus, the exploration of effective hydrogen storage solutions is a matter of utmost urgency.

Currently, great efforts have been devoted to solid-state hydrogen storage materials due to their high safety and promising hydrogen storage capacity^[10-12]. Generally, based on the intrinsic hydrogen adsorption fashions, the existed solid-state hydrogen storage materials can be categorized into two types: molecular physisorption-type materials and atomic chemisorption-type materials. The former is typically characterized by high specific surface area and favorable porosity such as metal organic frameworks (MOFs), carbon nanotubes (CNTs), activated carbons (ACs), etc.^[13-17]. Hydrogen adsorption via molecular physisorption fashion relies on the Van der Waals force between H₂ molecules and material surface^[18]. Such weak interaction (generally lower than 0.15 eV) can only stabilize considerable hydrogen under low temperatures. Elevating the temperature will dramatically reduce the hydrogen storage capacity. In contrast, the atomic chemisorption-type materials store hydrogen via chemically binding the atomic H, such as metal hydrides, complex hydrides, liquid organic hydrides^[19-21]. In this case, hydrogen desorption requires extra energy input to break the strong bonding. For example, the decomposition of MgH₂ can be triggered while the temperature is higher than 300 °C^[22, 23]. Efforts are also devoted to improving the hydrogen storage properties of such materials. Basically, previous designs and modifications related to hydrogen storage materials involve improving weak molecular physisorption, or to decreasing the strong atomic chemisorption, such as heteroatom doping, alloying, and forming composite^[24-26]. However, no materials to date can satisfy the hydrogen storage targets

for practical application. Therefore, theoretical breakthrough is essential for exploiting a new class of materials for hydrogen storage.

Herein, we found that the uniquely unsaturated Ti atom can bind H₂ molecules via molecular chemisorption method. Differing from the weak Van der Waals force and strong chemical bonding, the molecular chemisorption involves a strong electronic interaction between Ti atom and molecular H₂. Further DFT calculations indicate that this electronic interaction can effectively enhance the binding energy of hydrogen molecules on adsorption sites as compared to physisorption. In addition, compared with the dissociated chemisorption, the molecular chemisorption maintains the molecular form of hydrogen adsorbed, favoring hydrogen desorption. It is found that the binding energy of H₂ for four-coordinates Ti atom was determined to be 0.3 eV, which is evidently larger than that of the five-coordinates Ti atom (0.18 eV). This work provides a new method for designing hydrogen storage material with moderate adsorption energy.

6.2 Results and Discussion

Understanding the interactions between hydrogen molecule and material surface is of great importance, which determines the binding affinities of potential hydrogen storage materials, and thus their extent of potential for practical use. Previously, the hydrogen adsorption behaviors are investigated by DFT calculations while approaching to a neutral metal atom (such as Ni) and a low valence metal ion (such as Ni⁺)^[34]. The results indicate that the dissociation of hydrogen molecule is blocked due to the higher second ionization potential of the Ni⁺ atom, and several H₂ molecules to be chemisorbed in the form of molecular onto Ni⁺ ion under the strong polarization effect. In contrast, hydrogen molecule will be dissociated and chemisorbed by neutral metal atom (Ni). The results imply that the low valence TM ions have greater potential than neutral TM atoms for hydrogen storage.

However, isolated TM ion cannot exist itself in nature and prefers to be hexa-coordinate

in the solid state, which is adverse to hydrogen adsorption. Therefore, rational design and delicate synthesis of metal atom with unique coordination structure is vital to achieve hydrogen storage materials with optimal adsorption energy (Figure 6-1a).

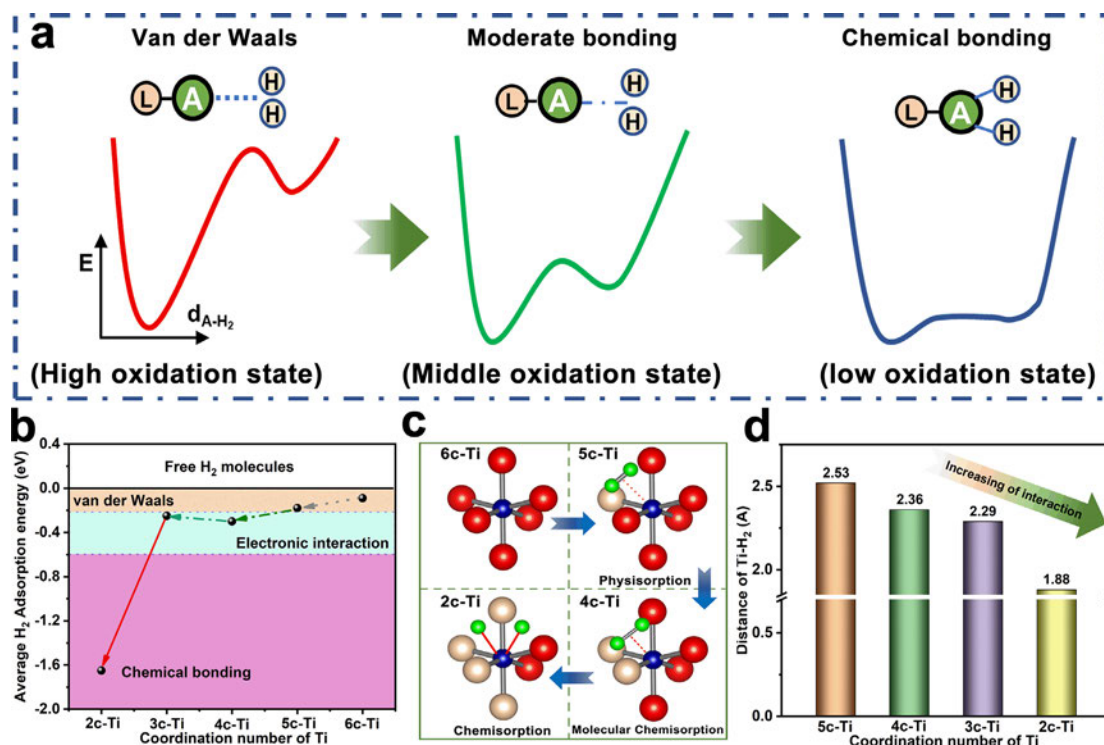


Figure 6-1. (a) Types of hydrogen interaction with adsorption sites. (b) The average adsorption energy of H₂ onto Ti atoms with different coordination number. (c) Corresponding Structural model of hydrogen adsorption. (d) The distance between Ti and hydrogen. The red, blue, green, and grey balls represent O atom, Ti atom, H atom and O vacancy, respectively.

In this work, using TiO₂ as an example material, we investigate the binding energy of H₂ molecule adsorbed onto interfacial titanium atom with different coordination numbers shown in Figure 6-1b. For perfect TiO₂, the interface of TiO₂ is covered with both 6-coordinates and 5-coordinates Ti atoms. H₂ molecule will automatically attracted by five-coordinates Ti atom with a binding energy of 0.18 eV. Decreasing the coordination number of Ti to 5 and 4, the binding energy of H₂ is increased to 0.3 and 0.25 eV, respectively. Further regulating the coordination number to two, the molecular

H₂ will be dissociated into hydrogen atoms while approaching to Ti atom and adsorbed in the form of strong chemisorption. The resulted hydrogen adsorption energy is determined to be 1.65 eV. Figure 6-1c shows the corresponding structural model of hydrogen adsorption. Moreover, the distance of H₂ to Ti atom is also determined, shown in Figure 6-1d. Obviously, the distance is decreased with the reduce of coordination number, implying that the enhanced interaction between H₂ molecule and low-coordinates Ti atom.

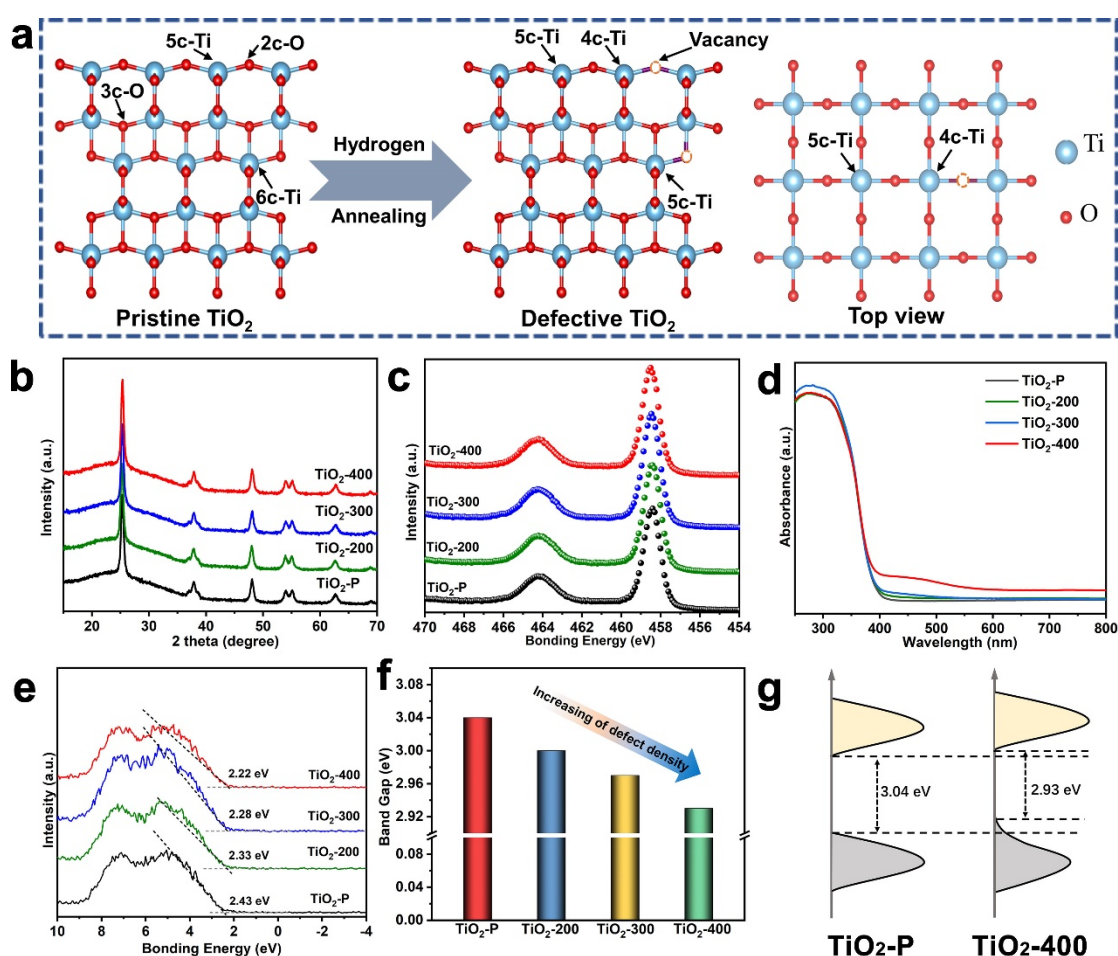


Figure 6-2. (a) Schematic illustration of synthetic defective titanium oxide. (b) XRD patterns of TiO₂-P and annealed TiO₂ under H₂ atmosphere. (c) High-resolution XPS spectra of Ti 2p of TiO₂ before and after annealing. (d) and (e). UV-vis absorption spectra and Valence band XPS (VB-XPS) spectra of TiO₂-P and annealed TiO₂-x. (f) the band gap of TiO₂-P and annealed TiO₂-x. (g) band energy diagram of TiO₂-P and annealed TiO₂-400.

Inspired by the theoretical calculation results, we then synthesized the defective TiO₂ by an annealing process under H₂ atmosphere. A schematic diagram illustrates the preparation process (Figure 6-2a). For perfect pristine TiO₂ (TiO₂-P), each Ti atom is coordinated with six O atoms. There should exist five-coordinated Ti atoms on the surface of TiO₂. Even lower coordinated Ti atoms can be found on the vertices and edges of TiO₂ particles. Annealing process under H₂ atmosphere will decrease the coordination number of Ti by removing the O atoms. Therefore, the five-coordinated Ti atoms on the surface are possible changing to 4-coordinates after annealing.

The structure of TiO₂ was firstly examined using the X-ray diffraction (XRD). The XRD patterns shown in Figure 6-2b suggest that the pristine TiO₂ (TiO₂-P) is anatase nanocrystal and the crystal structure of titanium oxide has not changed after annealing at the selected annealing temperature [35, 36]. The X-ray photoelectron spectroscopy (XPS) measurement was performed for the TiO₂-P and annealed TiO_{2-x} samples (Figure 6-2c). The oxidation state of titanium did not change significantly. However, no obvious differences can be observed in the Ti 2p XPS spectra. This may be explained by the defect density below the detective limitation of the XPS analysis, easy oxidization of Ti^{x+} by a proper oxidant such as O₂, and/or the insufficient sensitivity of the XPS analysis toward the defects in the reduced TiO₂[37-40].

To validate the existence of defects after annealing, ultraviolet-visible (UV-vis) spectra and the valence-band X-ray photoelectron spectroscopy (VB-XPS) are also conducted for the TiO₂-P and TiO_{2-x} samples. The ultraviolet-visible (UV-vis) spectra displayed in Figure 6-2d show that all the samples have similar strong absorption peaks in the UV region before 400 nm, which is originated from the intrinsic band gap absorption of TiO₂. As compared to TiO₂-P, the annealed samples expand the absorption edge of TiO₂ in UV-visible range with slightly red-shift. The enhanced absorbance in the visible region is ascribed to the electronic transition from the valence band (VB) to the localized states of oxygen vacancy associated low-valent Ti^{x+}. The results further

confirm the existence of oxygen vacancies, and the density of O vacancies is increased with the increase of the annealing temperature. Moreover, the VB-XPS of pure TiO_2 displays a VB maximum energy of 2.43 eV below the Fermi level (Figure 6-2e). After annealing, an upward shift for TiO_{2-x} sample can be observed due to the existence of surface oxygen vacancies, in which the TiO_2 -400 exhibited a VB of 2.22 eV. The corresponding band gaps were also calculated, shown in Figure 6-2f. Clearly, with the increase of annealing temperature, the band gap of TiO_2 decreases gradually, reflecting the increases of oxygen vacancy which is in line with the UV-vis spectra results. According to the UV-vis and VB-XPS spectral analyses (Figure 6-2d and 6-2e, Figure S6-1), the energetic band structure diagram of the modified TiO_2 is determined and illustrated in Figure 6-2g.

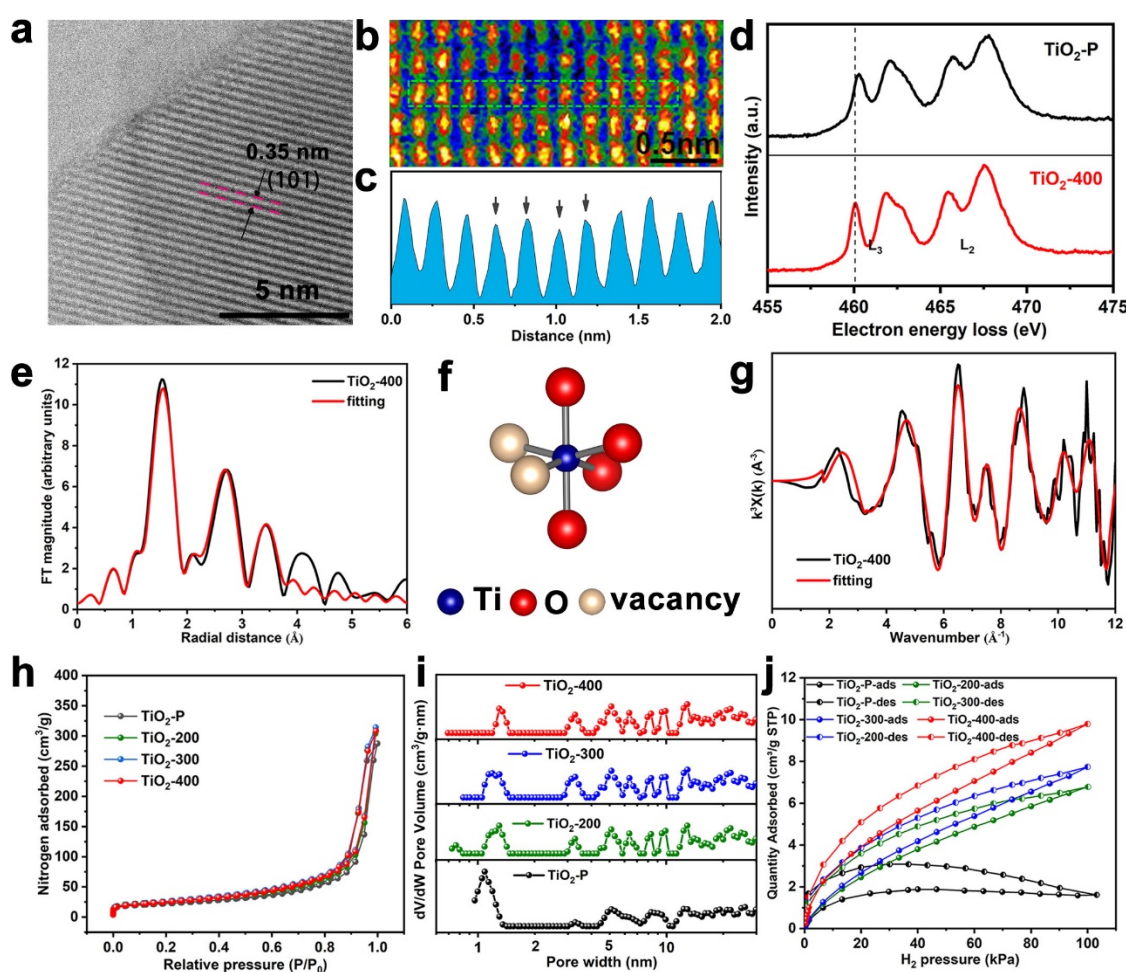


Figure 6-3. (a) HR-TEM image of TiO_2 -400. (b) HAADF-STEM images and (c) corresponding intensity line profile extracted from HAADF-STEM image of TiO_2 -

400. (d) EELS spectra of TiO₂-P and TiO₂-400. (e) Experimental and best-fitted EXAFS spectra in R space for TiO₂-400. (f) Schematic model of tetra-coordinated Ti atom. (g) Experimental and best-fitted EXAFS spectra in k space for TiO₂-400. (h) Nitrogen adsorption desorption isotherms and (i) corresponding pore size distribution of TiO₂-P and annealed TiO₂-x. (h) Hydrogen adsorption curves for all TiO₂ samples under liquid temperature.

The morphology of TiO₂-P and annealed TiO₂-x is characterized by the SEM and TEM. In Figure S6-2, the SEM image indicates that the TiO₂-P nanoparticles were loosely aggregated with particle size of around 20 nm. After annealing, the particle size did not change significantly (Figure S6-3). High-resolution TEM (HRTEM) image in Figure 6-3a shows that the TiO₂ nanoparticles after annealing remain crystallized. The characteristic lattice fringes of 0.35 nm can be indexed as the (1 0 1) planes of the anatase. Further atomic scale structures are probed for the TiO₂-400 by using the high-angle annular dark-field scanning transmission electron microscopy (HAADF-STEM). As shown in Figure 6-3b, the slightly distortion can be observed in the corresponding intensity line profiles of the bottom panel (indicated by black arrows) of Figures 6-3c, which is ascribed to the existence of oxygen vacancies ^[41]. In contrast, such distortion is not observed in TiO₂-P (Figure S6-4). Electron energy loss spectroscopy (EELS) is further conducted to obtain a qualitative interpretation of chemical bonding. Figure 6-3d shows that the Ti L peaks at high energy (460–470 eV) of TiO₂-400 shift to lower energies compared with TiO₂-P. The results indicate a reduced valence state of titanium and confirm the existence of oxygen defects. These phenomena further imply that the surface oxygen atoms of TiO₂ are removed after high temperature treatment, resulting in the reduction of the surface of the sample.

X-ray absorption fine structure (XAFS) analysis was further conducted to understand the coordination environment of TiO₂ before and after annealing. Figure S6-5 shows the Ti K-edge X-ray absorption near edge structure (XANES) spectra. The TiO₂-P and

annealed $\text{TiO}_2\text{-x}$ samples display similar XANES spectra with the anatase TiO_2 , implying the similar local structure environment. Besides, the lower intensity of the white line for annealing TiO_2 implies the lower oxidation state of Ti as compared to $\text{TiO}_2\text{-P}$, suggesting the coordination number of interface Ti atoms is reduced after annealing. Further Fourier transform (FT) of extended XAFS (FT-EXAFS) and corresponding least-squares EXAFS fitting in k space and R space were carried out to obtain quantitative structural parameters of the Ti atoms in the TiO_2 samples. The EXAFS fitting parameters are listed in Table S6-2, and the fitting curves are depicted in Figure 6-3e to 6-3g and Figure S6-6 to S6-8. The k space and R space best fitting curves matched well with the experimental results. A main peak can be observed at around 1.50, corresponding to the Ti-O scattering path (Figure 6-3e, and Figure S6-6 to S6-8). Meanwhile, the EXAFS fitting parameters shown in Table S6-2 indicate that the coordination number is decreased with the increase of the annealing temperature, and the optimized geometric configuration for interfacial Ti atoms in $\text{TiO}_2\text{-400}$ was determined to possess a coordination number of 4 (Figure 6-3f), confirming the existence of four-coordinated Ti.

Nitrogen adsorption desorption isotherms were also used to measure the surface areas and pore size distributions of as-obtained TiO_2 , shown in Figure 6-3h and 6-3i. It can be seen that the specific surface area of the material did not change significantly after annealing (Figure 6-3h and Table S6-1). However, the porosity has changed. Figure 6-3i demonstrates that, with the increase of annealing temperature, the pore volume of micropores decreased and transformed to mesoporous. These results indicate that annealed TiO_2 samples are not in favor of hydrogen storage via physisorption, due to the reduction of micropore volume.

We further conducted the hydrogen adsorption test to evaluate the hydrogen storage performance of the synthesized TiO_2 . Figure 6-3j presents the hydrogen adsorption curves of $\text{TiO}_2\text{-P}$ and $\text{TiO}_2\text{-x}$ from 0 to 1 bar. Obviously, different from the prediction

from the BET results, the annealed TiO₂ exhibits an increased hydrogen adsorption capacity as compared to TiO₂-P. In addition, the hydrogen capacity adsorbed is increased with the annealing temperature. The TiO₂-400 shows the highest hydrogen adsorption amount of 10 cm³/g, which is about 5 times higher than that of TiO₂-P. Combining the BET results, we conclude that the defective TiO₂ does not rely on the conventional physisorption to storage hydrogen. Moreover, the reversible desorption indicates that the adsorbed hydrogen is not stored in the form of strong dissociative chemisorption. Note that, the annealing process only changes the coordination number of the surface titanium atoms by creating O-vacancy. Therefore, the significantly increased hydrogen capacity is ascribed to the increased affinity of the low-coordinated interfacial Ti atom (LC-Ti) to hydrogen molecules. Besides, the lower the coordination number, the stronger the interaction between Ti atom and hydrogen molecules.

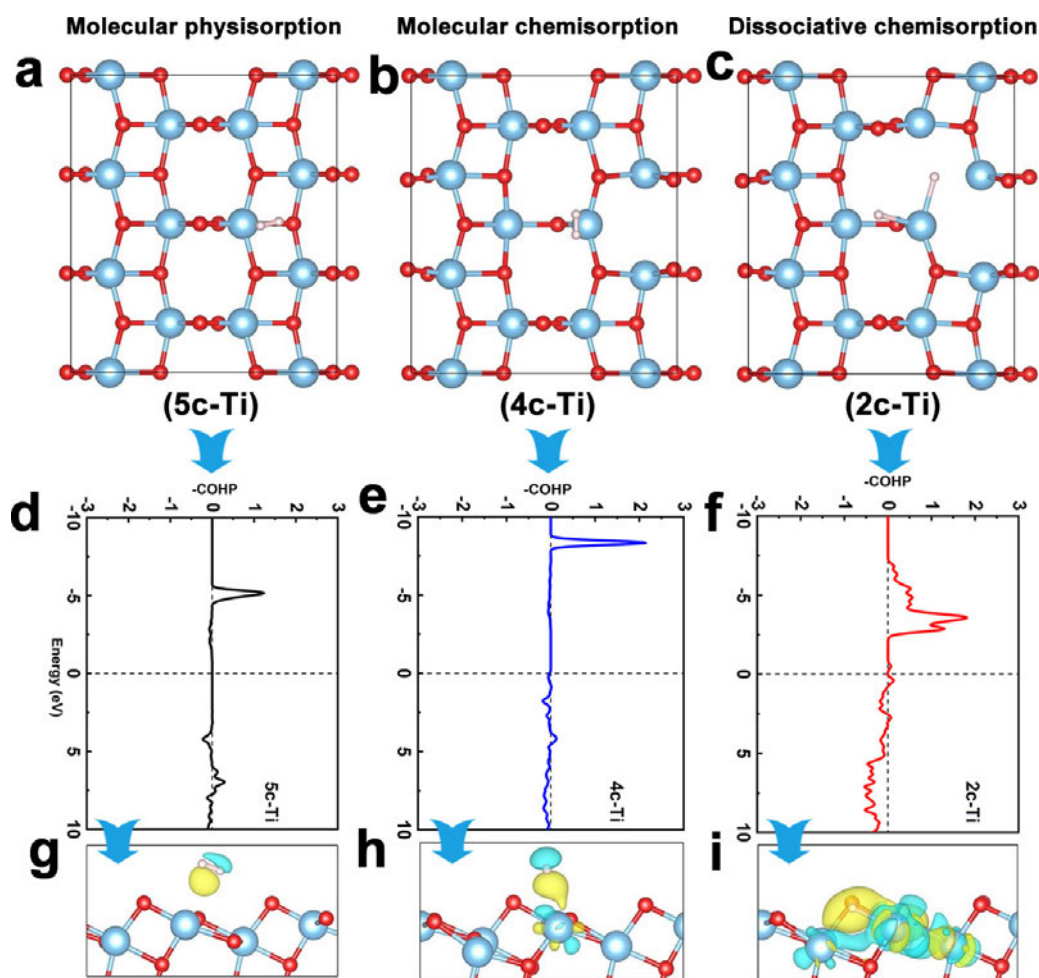


Figure 6-4. (a-c) Structural model of hydrogen adsorbed onto Ti atom with different coordination. (d-f) Crystal orbital Hamilton population (COHP) charts of H₂ adsorbed onto 5c-Ti, 4c-Ti and 2c-Ti, respectively. (g-i) The charge densities of H₂ adsorbed onto 5c-Ti, 4c-Ti and 2c-Ti, respectively. Yellow and cyan color represents the accumulation and depletion of charge density.

To get insight to the adsorption behavior of hydrogen molecule, DFT calculations were conducted to reveal the interactions between H₂ molecules and interfacial Ti atoms. Figure 6-4a to 6-4c display the adsorption configurations of hydrogen molecule on Ti atoms with different coordination numbers, which represents three different hydrogen uptake mechanisms. By regulating the coordination number of titanium atoms, the transformation from the van der Waals interaction to strong chemical interaction is successfully realized, indicating that titanium atoms with different coordination numbers have different affinity for hydrogen.

Then, the crystal orbital Hamilton population (COHP) was employed to visualize and analyze the bonding characters between hydrogen molecule and Ti atoms. Moreover, the charge density difference of Ti and H₂ was further investigated separately to distinguish the strength of the interaction. COHP is a partitioning of the band-structure energy in terms of orbital-pair contributions. The bonding and antibonding interactions typically appear as positive and negative COHP values, respectively. Generally, the more bonding states occupied and the lower energy level the bonding states take, the stronger the interaction will be. As shown in Figure 6-4d, below the Fermi level, the bonding states at 5c-Ti site is located around -5 eV with a low population intensity. The corresponding charge redistribution in Figure 6-4g shows that electrons concentrate around H₂ molecule while there is no obvious charge transferring between the surface and H₂, suggesting the weak physical interaction between H₂ and TiO₂ surface. When H₂ molecule approaches 4cTi and 3c-Ti site, the COHP below the Fermi level is similar to that at 5c-Ti site but shifts to lower energy level of -8.3 eV and with a higher intensity

(Figure 6-4e and Figure S6-9), implying that the interactions are stronger than that of 5c-Ti. Such enhancement is also reflected by the charge redistribution, of which small amount of electrons transfer from Ti to H₂ (Figure 6-4h). It is noted that the hydrogen adsorbed remains intact, suggesting a mediate binding strength. In contrast, there is massive charge transferring from the surface to the H₂ at 2c-Ti (Figure 6-4f). As a result, the hydrogen molecule is dissociated into hydrogen atoms, displaying a strong interaction between H₂ and 2c-Ti site (Figure 6-4c). Accordingly, the COHP confirms the massive bonding states occupied in 2c-Ti site (Figure 6-4i), reflecting the strong chemical bonding characteristic.

6.3 Conclusions

To summarize, we have demonstrated a kind of defective TiO₂ for hydrogen storage via a defect engineering technique. By regulating the coordination of Ti atom, the hydrogen storage fashion can be realized with the transformation from physical adsorption to chemical adsorption. Differing from the weak physical adsorption and strong chemical adsorption, Ti atom with certain coordination number can store hydrogen in a molecular chemisorption manner. The new hydrogen adsorption method exhibits a significantly enhanced adsorption energy to hydrogen compared with the physical adsorption, enabling the hydrogen to be stored stably at room temperature. Accordingly, the TiO₂-400 shows the highest hydrogen uptake of 10 cm³/g, which is about 5 times higher than that of the TiO₂-P. Further DFT calculations indicate that the Ti atom with certain coordination number can store hydrogen with moderate bond energy. While the lower coordinated titanium atoms exhibit the feature of metallic titanium, which could dissociate the molecule to form the strong chemical bond. This work will construct a new conceptual paradigm in the solid-state hydrogen storage field.

6.4 References

1. He J, Li Z, Zhang X, et al. Towards carbon neutrality: A study on China's long-term low-carbon transition pathways and strategies. *Environmental Science and Ecotechnology* 2022; 9: 100134.
2. Espegren K, Damman S, Pisciella P, et al. The role of hydrogen in the transition from a petroleum economy to a low-carbon society. *Int. J. Hydrogen Energy* 2021; 46: 23125-23138.
3. Yuan X, Su C-W, Umar M, et al. The race to zero emissions: Can renewable energy be the path to carbon neutrality? *J. Environ. Manage.* 2022; 308: 114648.
4. Phang S J, Wong V-L, Tan L-L, et al. Recent advances in homojunction-based photocatalysis for sustainable environmental remediation and clean energy generation. *Applied Materials Today* 2020; 20: 100741.
5. Tarhan C and Çil M A. A study on hydrogen, the clean energy of the future: Hydrogen storage methods. *Journal of Energy Storage* 2021; 40: 102676.
6. Baykara S Z. Hydrogen: A brief overview on its sources, production and environmental impact. *Int. J. Hydrogen Energy* 2018; 43: 10605-10614.
7. Ratnakar R R, Gupta N, Zhang K, et al. Hydrogen supply chain and challenges in large-scale LH₂ storage and transportation. *Int. J. Hydrogen Energy* 2021; 46: 24149-24168.
8. Moradi R and Groth K M. Hydrogen storage and delivery: Review of the state of the art technologies and risk and reliability analysis. *Int. J. Hydrogen Energy* 2019; 44: 12254-12269.
9. Mohan M, Sharma V K, Kumar E A, et al. Hydrogen storage in carbon materials—A review. *Energy Storage* 2019; 1: e35.
10. Boateng E and Chen A. Recent advances in nanomaterial-based solid-state hydrogen storage. *Materials Today Advances* 2020; 6: 100022.
11. Shahi R R, Gupta A K and Kumari P. Perspectives of high entropy alloys as hydrogen storage materials. *Int. J. Hydrogen Energy* 2022.
12. Luo Q, Li J, Li B, et al. Kinetics in Mg-based hydrogen storage materials:

- Enhancement and mechanism. *Journal of Magnesium and Alloys* 2019; 7: 58-71.
13. Lyu J, Kudiiarov V and Lider A. An Overview of the Recent Progress in Modifications of Carbon Nanotubes for Hydrogen Adsorption. *Nanomaterials* 2020; 10: 255.
 14. Sdanghi G, Canevesi R L S, Celzard A, et al. Characterization of Carbon Materials for Hydrogen Storage and Compression. *C* 2020; 6: 46.
 15. Gangu K K, Maddila S, Mukkamala S B, et al. Characteristics of MOF, MWCNT and graphene containing materials for hydrogen storage: A review. *Journal of Energy Chemistry* 2019; 30: 132-144.
 16. Shet S P, Shanmuga Priya S, Sudhakar K, et al. A review on current trends in potential use of metal-organic framework for hydrogen storage. *Int. J. Hydrogen Energy* 2021; 46: 11782-11803.
 17. Lim K L, Kazemian H, Yaakob Z, et al. Solid-state Materials and Methods for Hydrogen Storage: A Critical Review. *Chemical Engineering & Technology* 2010; 33: 213-226.
 18. Farrukh S, Fan X, Mustafa K, et al., *Physisorption, in Nanotechnology and the Generation of Sustainable Hydrogen*, S Farrukh, et al., Editors. 2021, Springer International Publishing: Cham. p. 73-82.
 19. Schneemann A, White J L, Kang S, et al. Nanostructured Metal Hydrides for Hydrogen Storage. *Chem. Rev.* 2018; 118: 10775-10839.
 20. Li H-W, Yan Y, Orimo S-I, et al. Recent Progress in Metal Borohydrides for Hydrogen Storage. *Energies* 2011; 4: 185-214.
 21. Lang C, Jia Y and Yao X. Recent advances in liquid-phase chemical hydrogen storage. *Energy Storage Materials* 2020; 26: 290-312.
 22. Cui J, Wang H, Liu J, et al. Remarkable enhancement in dehydrogenation of MgH_2 by a nano-coating of multi-valence Ti-based catalysts. *J. Mater. Chem. A* 2013; 1: 5603-5611.
 23. Lang C, Ouyang L, Yang L, et al. Enhanced hydrogen storage kinetics in

- Mg@FLG composite synthesized by plasma assisted milling. *Int. J. Hydrogen Energy* 2018; 43: 17346-17352.
24. Abe J O, Popoola A P I, Ajenifuja E, et al. Hydrogen energy, economy and storage: Review and recommendation. *Int. J. Hydrogen Energy* 2019; 44: 15072-15086.
 25. Nagar R, Vinayan B P, Samantaray S S, et al. Recent advances in hydrogen storage using catalytically and chemically modified graphene nanocomposites. *J. Mater. Chem. A* 2017; 5: 22897-22912.
 26. Kim K C. A review on design strategies for metal hydrides with enhanced reaction thermodynamics for hydrogen storage applications. *Int. J. Energy Res.* 2018; 42: 1455-1468.
 27. Kresse G and Furthmüller J. Efficiency of ab-initio total energy calculations for metals and semiconductors using a plane-wave basis set. *Comput. Mater. Sci.* 1996; 6: 15-50.
 28. Kresse G and Furthmüller J. Efficient iterative schemes for ab initio total-energy calculations using a plane-wave basis set. *Phys. Rev. B* 1996; 54: 11169-11186.
 29. Kresse G and Hafner J. Ab initio molecular-dynamics simulation of the liquid-metal--amorphous-semiconductor transition in germanium. *Phys. Rev. B* 1994; 49: 14251-14269.
 30. Perdew J P, Burke K and Ernzerhof M. Generalized gradient approximation made simple. *Phys. Rev. Lett.* 1996; 77: 3865.
 31. Perdew J P, Ernzerhof M and Burke K. Rationale for mixing exact exchange with density functional approximations. *J. Chem. Phys.* 1996; 105: 9982-9985.
 32. Kresse G and Joubert D. From ultrasoft pseudopotentials to the projector augmented-wave method. *Phys. Rev. B* 1999; 59: 1758-1775.
 33. Grimme S. Semiempirical GGA-type density functional constructed with a long-range dispersion correction. *J. Comput. Chem.* 2006; 27: 1787-1799.
 34. Niu J, Rao B K and Jena P. Binding of hydrogen molecules by a transition-metal ion. *Phys. Rev. Lett.* 1992; 68: 2277-2280.

35. Lv Y, Yuan R, Cai B, et al. High-Efficiency Perovskite Solar Cells Enabled by Anatase TiO₂ Nanopyramid Arrays with an Oriented Electric Field. *Angew. Chem. Int. Ed.* 2020; 59: 11969-11976.
36. Ni Q, Dong R, Bai Y, et al. Superior sodium-storage behavior of flexible anatase TiO₂ promoted by oxygen vacancies. *Energy Storage Materials* 2020; 25: 903-911.
37. Liu M, Li H and Wang W. Defective TiO₂ with oxygen vacancy and nanocluster modification for efficient visible light environment remediation. *Catal. Today* 2016; 264: 236-242.
38. Dong K, Liang J, Wang Y, et al. Plasma-induced defective TiO₂-x with oxygen vacancies: A high-active and robust bifunctional catalyst toward H₂O₂ electrosynthesis. *Chem Catalysis* 2021; 1: 1437-1448.
39. Xin X, Xu T, Yin J, et al. Management on the location and concentration of Ti³⁺ in anatase TiO₂ for defects-induced visible-light photocatalysis. *Appl. Catal., B* 2015; 176-177: 354-362.
40. Teleki A and Pratsinis S E. Blue nano titania made in diffusion flames. *PCCP* 2009; 11: 3742-3747.
41. Jia G, Wang Y, Cui X, et al. Wet-chemistry hydrogen doped TiO₂ with switchable defects control for photocatalytic hydrogen evolution. *Matter* 2022; 5: 206-218.

6.5 Supporting Information

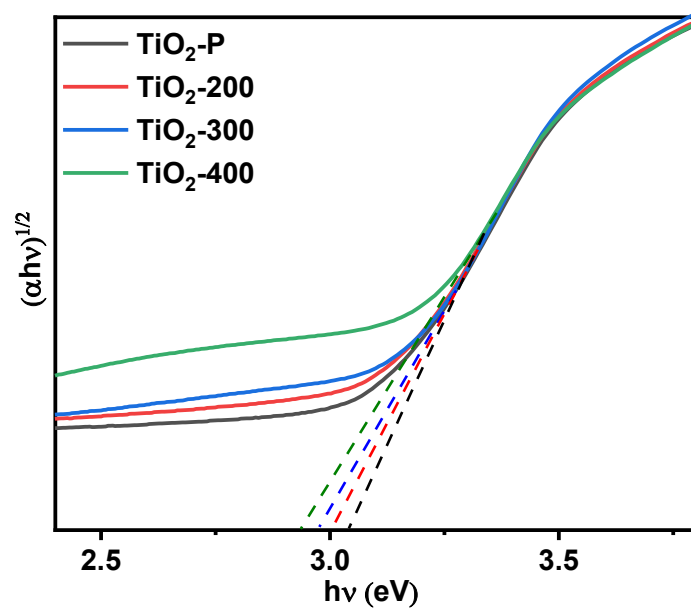


Figure S6-1. Tauc plot constructed from UV–vis absorption spectra of $(\alpha h\nu)^{1/2}$ versus the energy of light.

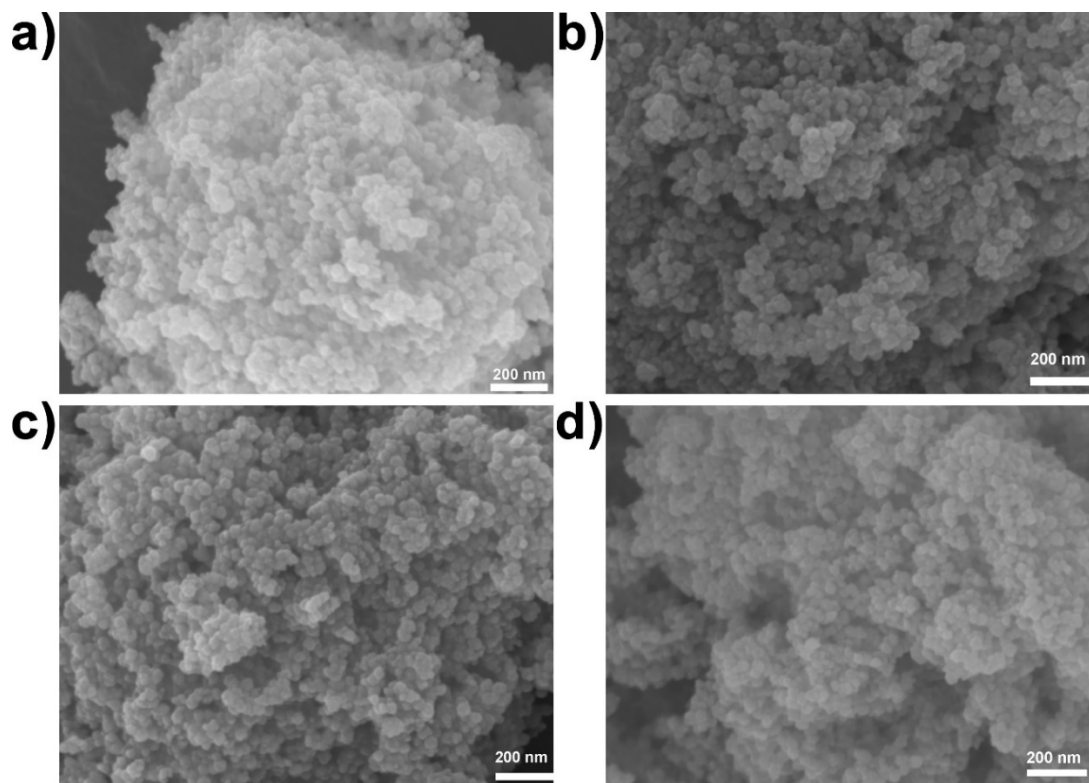


Figure S6-2. SEM images of $\text{TiO}_2\text{-P}$ (a), $\text{TiO}_2\text{-200}$ (b), $\text{TiO}_2\text{-300}$ (c) and $\text{TiO}_2\text{-400}$ (d), respectively.

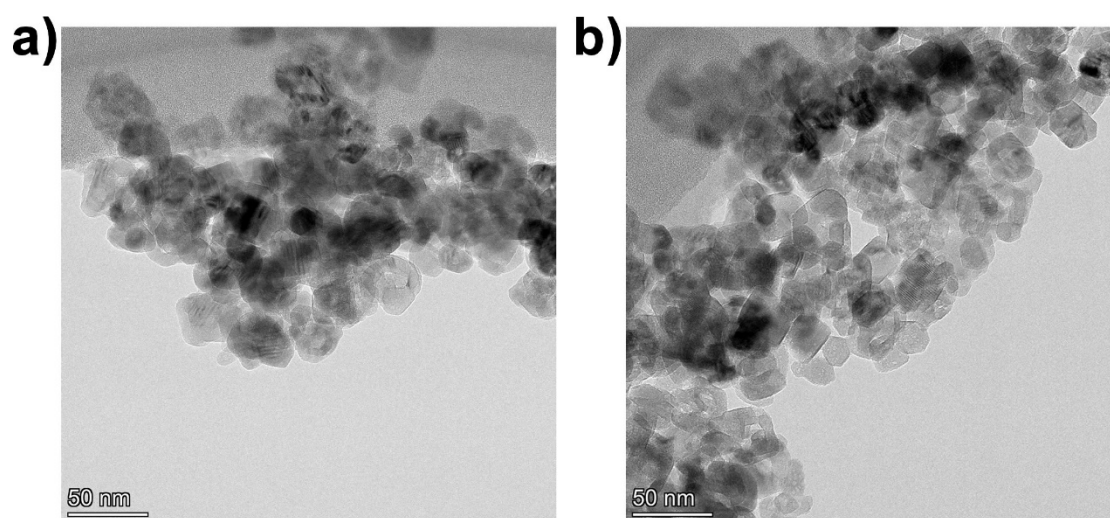


Figure S6-3. TEM images of TiO₂-P (a), and TiO₂-400.

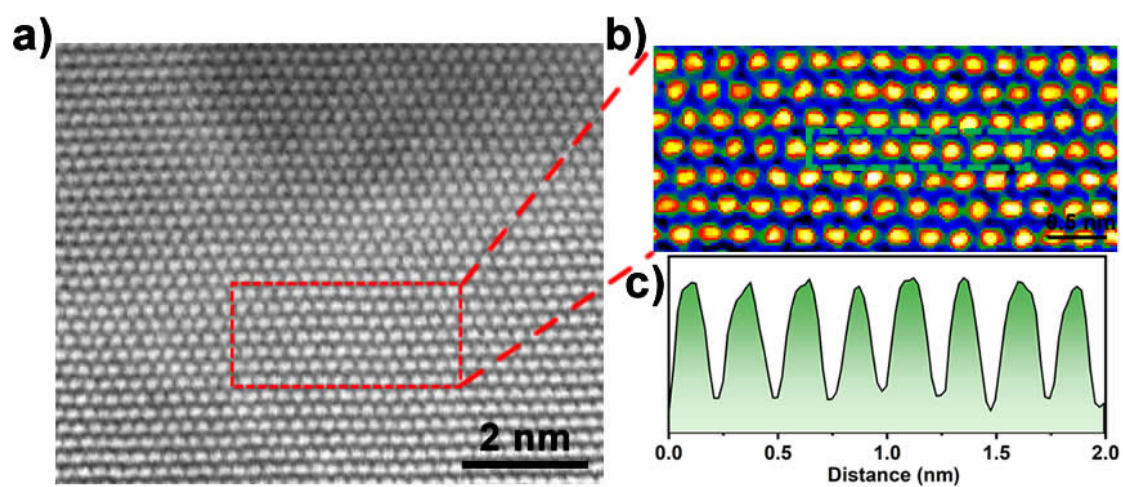


Figure S6-4. (a) and (b) HAADF-STEM images of TiO₂-P; (c) corresponding intensity line profile extracted from HAADF-STEM image of TiO₂-P in (b).

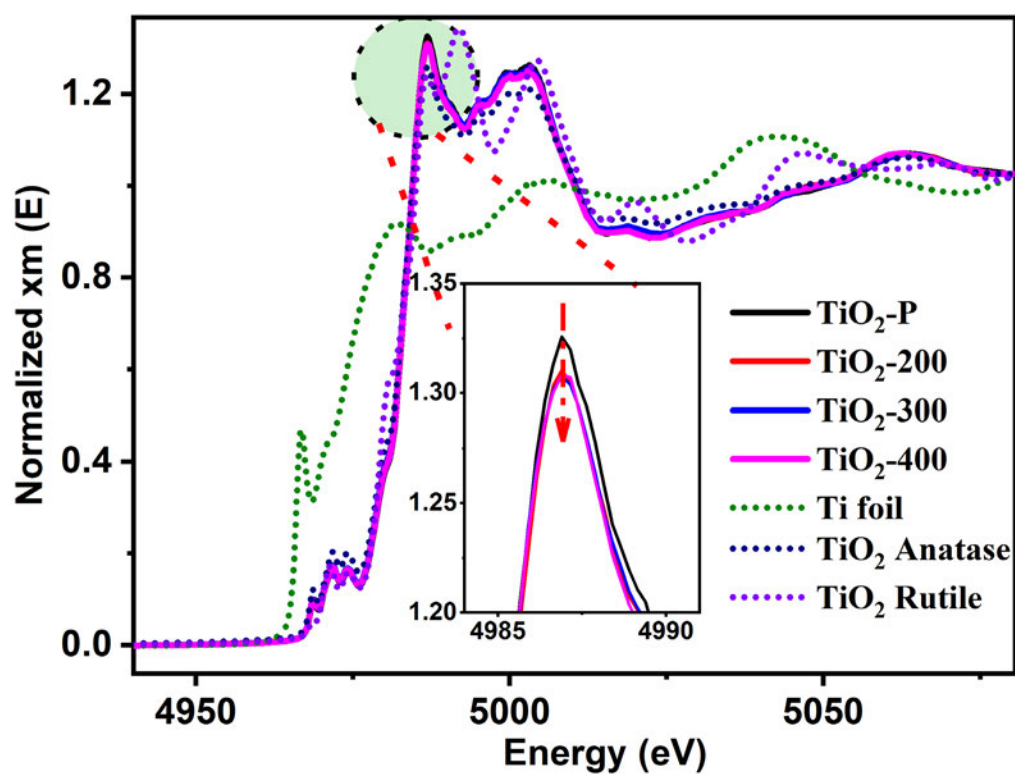


Figure S6-5. XANES spectra of $\text{TiO}_2\text{-P}$, $\text{TiO}_2\text{-x}$ ($x=200$, 300 and 400) and corresponding references. Inset is the enlarged part of white lines corresponding to $\text{TiO}_2\text{-P}$ and $\text{TiO}_2\text{-x}$ sample.

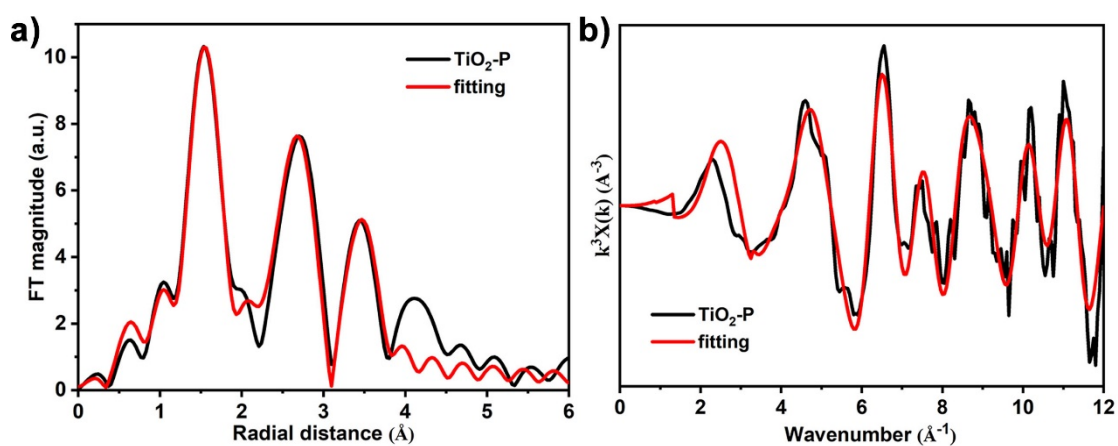


Figure S6-6. The FT EXAFS fitting spectrum of $\text{TiO}_2\text{-P}$ at R-space (a) and k-space (b), respectively.

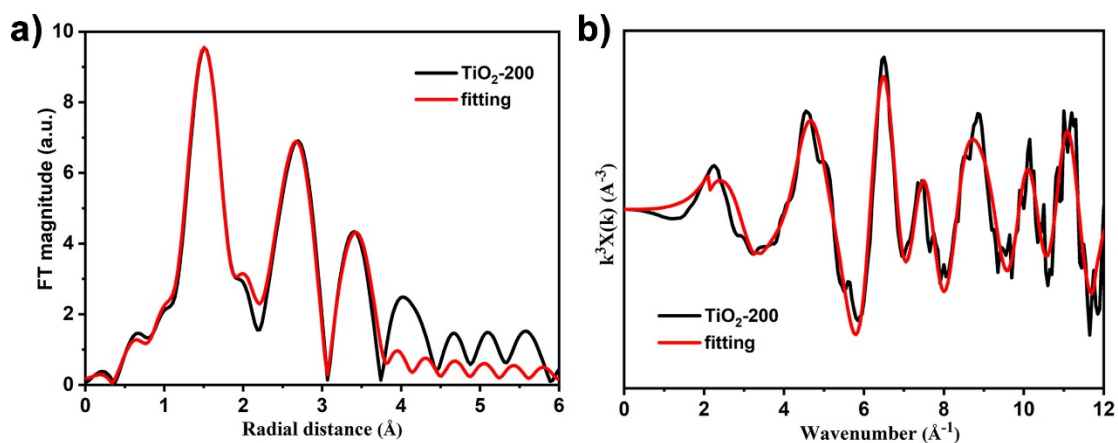


Figure S6-7. The FT EXAFS fitting spectrum of TiO₂-200 at R-space (a) and k-space (b), respectively.

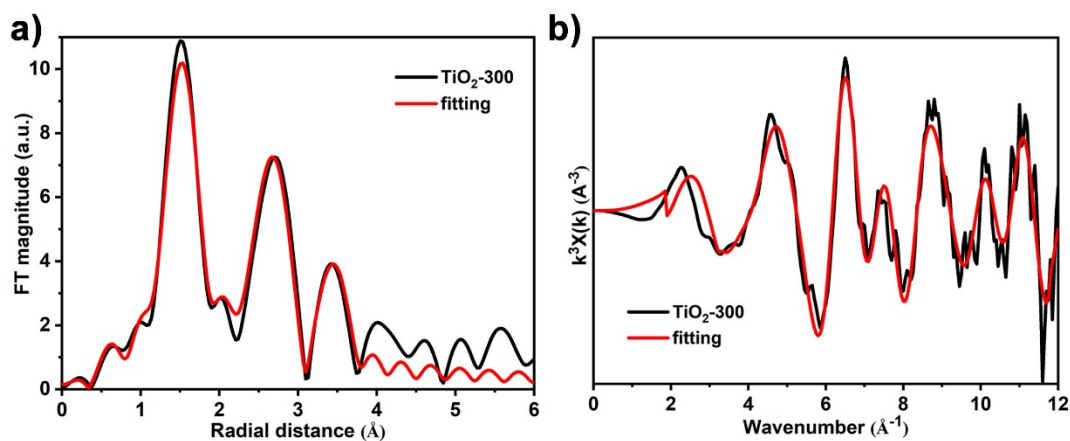


Figure S6-8. The FT EXAFS fitting spectrum of TiO₂-300 at R-space (a) and k-space (b), respectively.

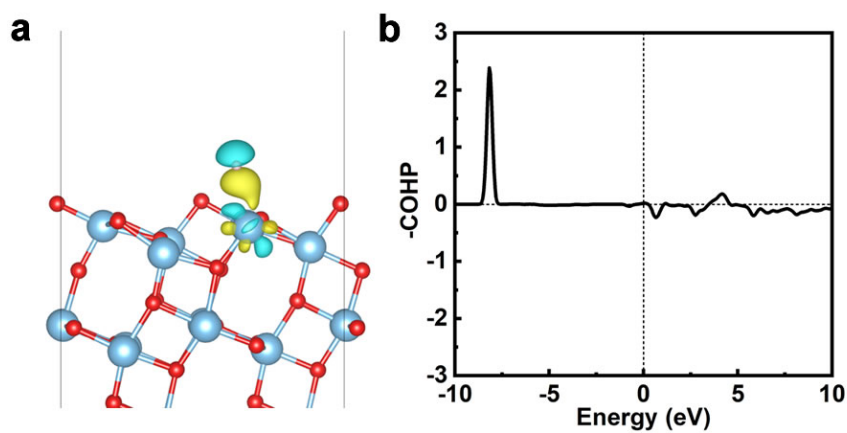


Figure S6-9. The charge densities (a) and Crystal orbital Hamilton population charts (b) of H₂ adsorbed onto 3c-Ti.

Table S6-1. BET surface area of TiO₂-P and TiO₂-x (x=200, 300 and 400) samples.

Samples	TiO ₂ -P	TiO ₂ -200	TiO ₂ -300	TiO ₂ -400
BET surface area (m ₂ /g)	80	91	92	88

Table S6-2. The EXAFS fitting parameters

Sample	Paths	Bond length (Å)	C.N.	s ²
P-TiO ₂	Ti-O1	1.96842	3.56	0.0011
	Ti-O2	2.11385	1.8	0.0010
	Ti-Ti	3.04002	2.8	0.0027
	Ti-Ti	3.89306	3.2	0.0036
TiO ₂ -200	Ti-O1	1.91364	2.94	0.0022
	Ti-O2	2.11941	1.4	0.0030
	Ti-Ti	3.03353	2.8	0.0035
	Ti-Ti	3.88810	3.6	0.0053
TiO ₂ -300	Ti-O1	1.89280	1.98	0.0005
	Ti-O2	2.06695	2.34	0.0050
	Ti-Ti	3.04500	3.2	0.0041
	Ti-Ti	3.87353	3.6	0.0061
TiO ₂ -400	Ti-O1	1.91873	1.98	0.0005
	Ti-O2	2.0657	1.8	0.0030
	Ti-Ti	3.04464	3.2	0.0045
	Ti-Ti	3.84201	3.2	0.0042

Chapter 7. Isolated Ti atom grafting carbon material for advanced hydrogen storage

STATEMENT OF CONTRIBUTION TO CO-AUTHORED PUBLISHED PAPER

This chapter includes a co-authored paper. The status of the co-authored paper, including all authors, are:

Chengguang Lang, Lei Zhang, Cheng-Jie Yang, Hao Zhong, Yue Lin, Chung-Li Dong, Aijun Du, Xuecheng Yan, Liuzhang Ouyang, Yi Jia, Xiangdong Yao

My contribution to the paper involved:

- Literature survey
- Concept and design
- Analysis and interpretation of data
- Drafting and writing

(Signed) _____

Chengguang Lang

(Date) 30/07/2022

(Countersigned) _____ (Date) 02/08/2022

Corresponding author of paper: Prof. Xiangdong Yao

(Countersigned) _____ (Date) 31/07/2022

Supervisor: Dr. Xuecheng Yan

7.1 Introduction

Hydrogen features the cleaning, abundance, high-energy-density, and efficiency, which is considered as the ideal energy carrier to reduce the dependence on or even to replace the current fossil energy^[1, 2]. Due to the low-density nature of hydrogen gas at ambient conditions, the secure and efficient hydrogen storage is extremely vital for the end use^[3, 4]. Although decades of efforts have been devoted, the roadblocks to commercialize hydrogen technology are still the hydrogen storage and delivery steps^[5, 6]. Solid-state storage via materials is considered as a promising solution because of its high gravimetric/volumetric energy densities, and security^[7]. However, the unfavorable thermodynamics and/or sluggish kinetics during hydrogen adsorption/desorption processes^[8], as well as reversibility^[9] greatly restrict the practical use of solid-state hydrogen storage materials.

Currently, the search and development for solid state materials with suitable hydrogen storage properties is still the primary goal. Ideal hydrogen storage materials are expected to have a moderate interaction with hydrogen, which enable the hydrogen to be stored/released under moderate temperature and pressure. Previous designs and modifications related to hydrogen storage materials mainly involve improving the weak molecular physisorption^[4, 10, 11], or to decrease the strong atomic chemisorption^[12-14], which still unsatisfied for the practical applications. Our previous work has confirmed that the low-coordinated Ti atoms on the surface of TiO₂ can adsorb hydrogen molecule via molecular chemisorption fashion. However, the adsorption sites are limited. Grafting isolated Ti atoms onto carbon substrates is considered as an effective strategy, and the corresponding hydrogen adsorption properties are also systematically investigated. Chakraborty *et al.* reported an atomic titanium-decorated graphene for high-capacity hydrogen storage via DFT simulations^[15]. The Ti atoms can be adsorbed stably on the hollow site with a binding energy of 1.40 eV. It is found that the decorated Ti atom can dramatically enhance the binding strength of molecular hydrogen to 0.23–0.60 eV. These results indicate that construction of atomic metal sites onto carbon

matrix can stand out as a promising and novel method for fabricating efficient hydrogen storage materials.

Herein, we prepared an atomic Ti doped carbon nanomaterial via a simple high-energy mechanochemical ball milling (HMBM) method. The HAADF-STEM images demonstrate the homogeneously dispersed single Ti atoms onto carbon matrix. The hydrogen adsorption tests confirmed that the introduction of isolated Ti atom can act as the hydrogen adsorption site, which can effectively increase the hydrogen uptake under near ambient temperature. For $\text{Ti}_1\text{@CB-170}$, each Ti atom can adsorb up to two H_2 molecules under 50 bars, via a molecular chemisorption manner. This work will provide valuable insight into designing and constructing hydrogen adsorption sites which enable the hydrogen to be adsorbed stably under near room temperature.

7.2 Results and Discussion

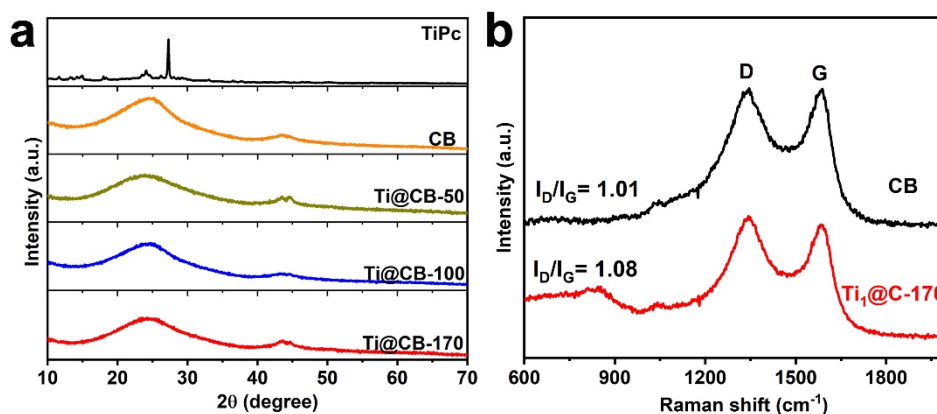


Figure 7-1. (a) XRD patterns of TiOPc, CB and as-prepared $\text{Ti}_1\text{@C-x}$ ($x=50, 100$ and 170). (b) Raman spectra of CB and $\text{Ti}_1\text{@CB-170}$.

The atomic Ti doped carbon black (CB) samples were prepared via a high-energy mechanochemical ball milling method. In brief, titanyl phthalocyanine (TiOPc) and carbon black are selected as the Ti source and support matrix, respectively. Afterward,

the high-energy ball milling was carried out under the Ar atmosphere to prepare the atomically dispersed Ti atoms anchored on CB matrix (named as $\text{Ti}_1@\text{CB-x}$, x represents the loading amount of TiOPc). It should be noted that the ball milled samples have high activity and may spontaneously ignite when exposed to air. Therefore, all samples are carefully collected and stored in a glove box filled with Ar gas.

The structure of the as-prepared $\text{Ti}_1@\text{CB}$ samples was firstly investigated by X-ray diffraction (XRD). The results are shown in Figure 7-1a. Obviously, the diffraction peak of TiOPc disappeared after ball milling and no extra peaks can be observed, indicating the successfully grafting of Ti atoms onto carbon matrix driven by the mechanical force. The surface chemical structure of the atomic Ti doped CB nanomaterials was studied using Raman spectroscopy. As shown in Figure 7-1b, the D peak observed at 1349 cm^{-1} for both CB and $\text{Ti}_1@\text{CB-170}$ indicate the existence of a large number of structural defects^[16]. Meanwhile, the ratios of I_D/I_G for $\text{Ti}_1@\text{CB-x}$ ($x=50, 100, 170$) are relatively high as compared to that of the CB (Figure 7-1b and Figure S7-1), implying that the introduction of atomic Ti will generate more structural defects.

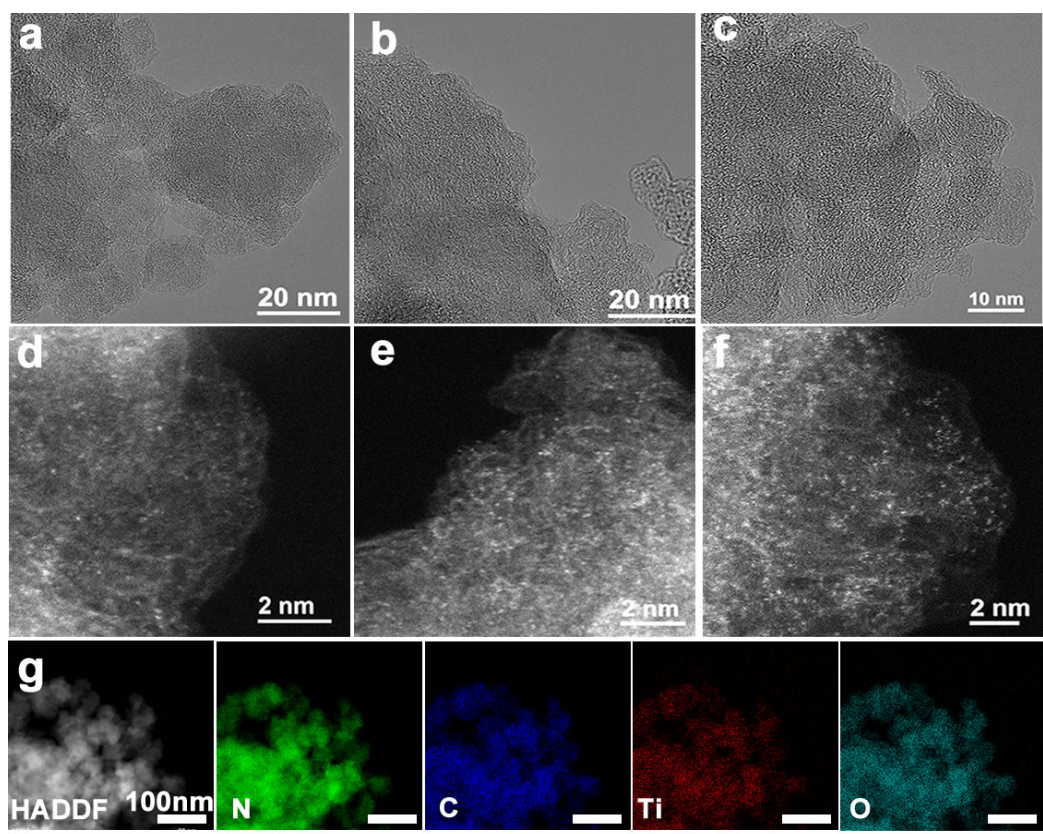


Figure 7-2. (a to c) HRTEM images of $\text{Ti}_1\text{@C-50}$, $\text{Ti}_1\text{@C-100}$ and $\text{Ti}_1\text{@C-170}$, respectively. (b) HAADF-STEM images of $\text{Ti}_1\text{@C-50}$, $\text{Ti}_1\text{@C-100}$ and $\text{Ti}_1\text{@C-170}$, respectively. (c) Corresponding EDS mapping of $\text{Ti}_1\text{@CB-170}$.

We then conducted the TEM characterizations, shown in Figure 7-2 (a to c). As can be seen, no big particles or clusters can be observed, which is consistent with the XRD results. Subsequently, the high-angle annular dark field–scanning TEM (HAADF–STEM) with sub-angstrom resolution was conducted to probe the atomic dispersion of individual Ti atoms (shown in Figure 7-2d to 7-2e). It can be noticed that the bright spots in the HAADF–STEM images correspond to isolated Ti atoms that are homogeneously distributed throughout the entire CB matrix (Figure 7-2d, Figure S7-2 and S7-3). The results indicate the successful synthesis of individual Ti atom grafted carbon material.

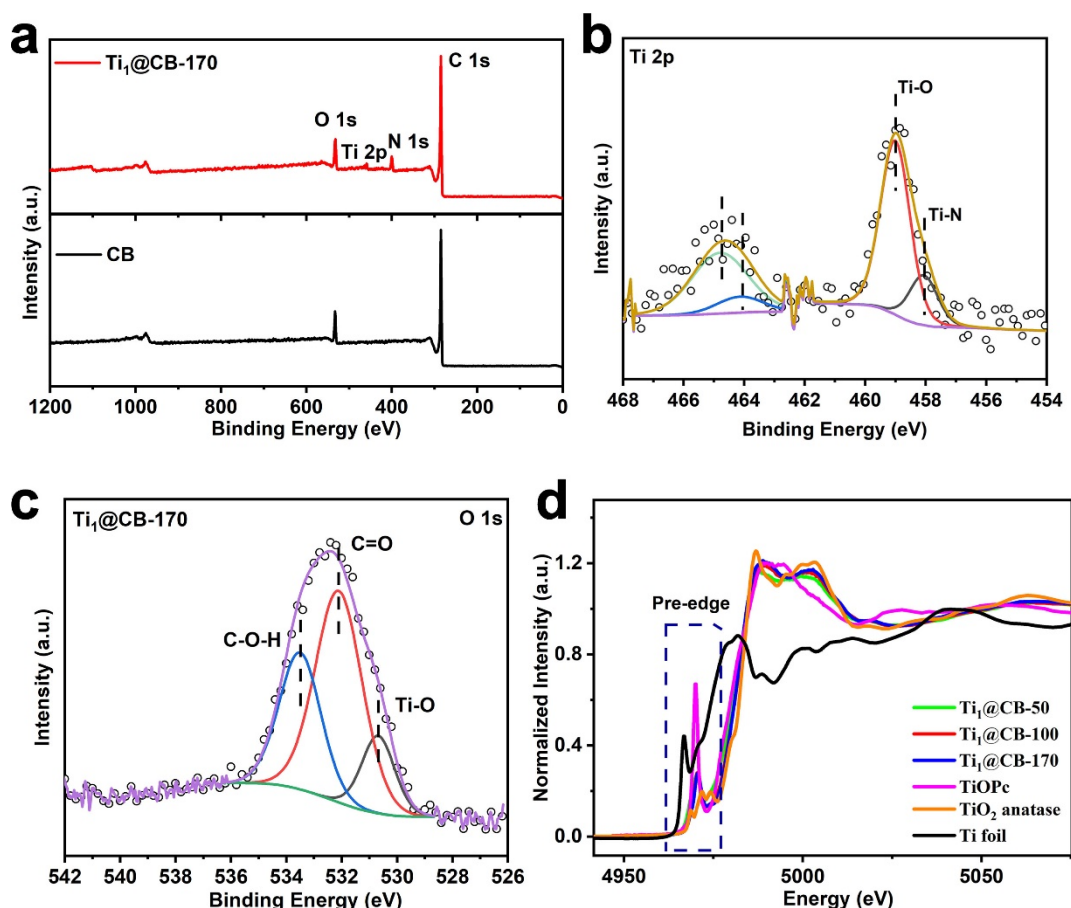


Figure 7-3. (a) Survey scan XPS spectra of CB and $\text{Ti}_1\text{@CB-170}$. (b) Ti 2p high resolution XPS spectrum of $\text{Ti}_1\text{@CB-170}$. (c) O1s high resolution XPS spectrum of $\text{Ti}_1\text{@CB-170}$. (d) Ti K-edge x-ray absorption near-edge structure (XANES) spectra of Ti foil, $\text{Ti}_1\text{@CB-x}$, TiOPc, anatase TiO_2 .

The chemical states of Ti doped CB samples were investigated by the X-ray photoelectron spectroscopy (XPS). As shown in Figure 7-3a and Figure S7-4, the appearance of Ti and N peaks in the survey scan XPS spectra indicate that the TiOPc molecules are successfully grafted onto CB matrix. The high-resolution spectra of these peaks provided more details of the Ti doped CB samples. Figure 7-3b and Figure S7-5 present the Ti 2p high-resolution XPS spectra. The continuous enhancement of Ti peak intensity indicates the increase of the Ti content. The total atomic Ti loadings in $\text{Ti}_1\text{@CB-50}$, $\text{Ti}_1\text{@CB-100}$ and $\text{Ti}_1\text{@CB-170}$ are estimated by inductively coupled plasma-atomic emission spectrometry (ICP-AES), and the results are given in Table S7-1. The deconvoluted XPS spectrum of $\text{Ti}_1\text{@CB-170}$ in the region Ti 2p (Figure 7-3b)

indicates the existence of two kinds of chemical bonds. The dominant peak at 459 eV can be ascribed to Ti-O, while the peak at 458 eV is assigned to the Ti-N^[17, 18]. O 1s high-resolution spectra were also analyzed for the CB and Ti₁@CB-170 samples. Compared with CB, a new peak centered at 530.6 eV is observed (Figure 7-3c and Figure S7-6), which is ascribed to the contribution of Ti-O^[16, 19], in consistent with the Ti 2p XPS results. The N 1s spectrum in Figure S7-7 also confirms the existence of Ti-N positioned at 399.5 eV^[20, 21]. Besides, the peaks of pyridinic N (398.5 eV)^[21] and graphitic-N (400.8 eV)^[22, 23] are also detected, indicating that the TiOPc molecules were destroyed during HEME process and some N atoms have been transferred to CB substrate. These XPS results reflect that the formation of individual Ti atom is via the decomposition of TiOPc during HMBM and the reassembling of Ti atom with N and O atoms, and the O atoms coordinated to Ti account for the majority of species in Ti₁@CB-170 sample.

Additionally, X-ray absorption spectroscopy (XAS) was applied to investigate the local structure and coordination information of Ti atoms in atomic Ti doped CB samples and the standard samples (Ti foil, TiOPc, and anatase TiO₂). The corresponding normalized X-ray absorption near-edge structure (XANES) spectra are presented in Figure 7-3d. Obviously, the absorption edge energy of Ti₁@CB is located between Ti foil and TiO₂ and close to the TiOPc precursor, implying the similar local structure environment to TiOPc. Moreover, the slightly higher oxidation state of Ti₁@CB samples compared to TiOPc indicates that partial N atoms coordinated to Ti atom are substituted by O atoms during ball milling, which is in line with the XPS results. The pre-edge of XANES spectrum is also a “fingerprint” feature to reveal the structural changes. The XANES of anatase TiO₂ in Figure 7-3d displays an evident triple pre-edge feature before the main peak, which is assigned to the distorted TiO₆ configuration^[19, 24]. In contrast, the Ti bond structure in the Ti₁@CB only presents a single pre-edge peak, indicating a typical non-central symmetry feature^[17, 19].

The Fourier transform of extended XAFS (FT-EXAFS) is also conducted for the

prepared samples, shown in Figure S7-8. The peaks associated with the Ti–Ti bond around 2.5 Å or 3.0 Å present in TiO₂ or Ti foil are not detected in the Ti₁@CB samples, indicating that the Ti atoms existed in the Ti₁@CB samples as individual atoms. The main peaks for Ti₁@CB samples are centered between the Ti–O peak (TiO₂) and Ti–N/O (Ti), and the increase of titanium content will cause the main peaks to shift to the Ti–O peak of TiO₂. The results are in good agreement with the XPS analysis. Considering the lower oxidation state of the Ti₁@CB samples compared to that of TiO₂, we conclude that the single Ti atom in Ti₁@CB sample is 5-coordinates and coordinated with both O atoms and N atoms.

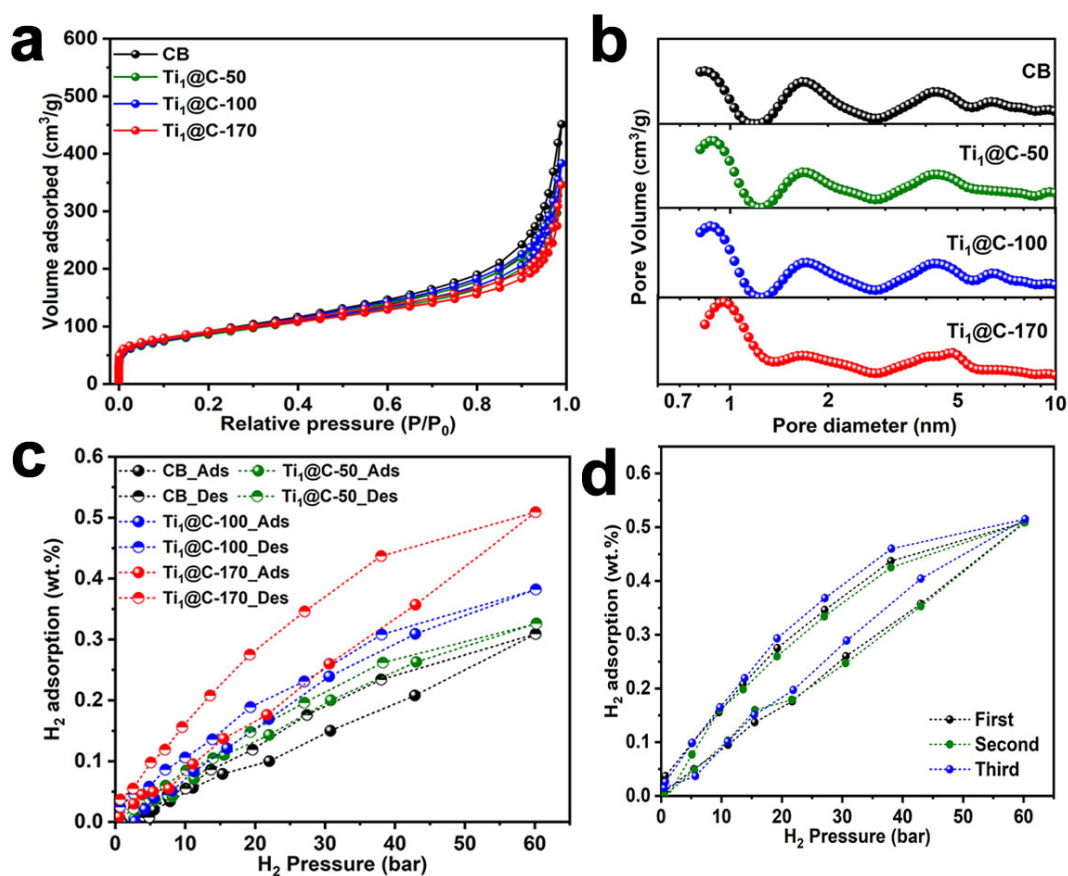


Figure 7-4. (a) Nitrogen adsorption-desorption isotherms and (b) corresponding pore size distribution of CB and Ti₁@CB-x. (c) Hydrogen adsorption-desorption curves for CB and Ti₁@CB-x samples at -20 °C. (d) Hydrogen adsorption-desorption cycling curves.

The nitrogen adsorption/desorption isotherms measurements were conducted to study the porosity of the as-prepared samples. As shown in Figure 7-4a, the CB and Ti₁@CB-x (x=50, 100 and 170) display similar isotherm curves, and the detailed specific surface areas of the samples are given in Table S7-2. It can be seen that the specific surface area (SSA) of the samples did not change significantly. A steep enhancement of nitrogen uptake in Figure 7-4a can be observed at a relatively low pressure (P/P₀), which is ascribed to the existence of micropores in the carbon matrix. Moreover, the isotherm curves of atomic Ti doped carbon (Ti₁@CB-x) at low pressure are similar to that of CB, illustrating the similar proportion of micropores. The pore size distribution (PSD) curves are also analyzed and depicted in Figure 7-4b. Obviously, all the samples display the similar pore size distribution. The results indicate that the introduction of TiOPc during high-energy mechanochemical ball milling does not significantly change the porosity of the as-prepared samples.

The hydrogen storage performance of the atomic Ti doped carbon nanomaterials was evaluated via hydrogen adsorption/desorption tests. Figure 7-4c shows the hydrogen adsorption/desorption curves of CB and Ti₁@CB-x from 0 to 60 bars. As can be seen, the introduction of atomic Ti onto CB matrix can remarkably improve the hydrogen storage capacity. The amount of hydrogen uptake is increased with the increase of the loading amount of Ti atoms. The Ti₁@CB-170 exhibits the highest hydrogen adsorption amount of 0.51 wt%, which is 1.65 times as that of CB. According to the BET analysis, the atomic Ti doped CB samples have the same SSA and pore size, which demonstrate that the hydrogen uptake of Ti₁@CB-x contributed by physisorption is same to that of CB. Therefore, the increase of hydrogen uptake can be attributed to the isolated Ti atoms on CB matrix, and the interactions between Ti atom and hydrogen molecule is stronger than the physisorption. Besides, the linear relationship between the loading amount of Ti atom and hydrogen absorption amount, further confirms that the atomic Ti on the CB matrix acts as the hydrogen adsorption site. Moreover, the reversible desorption performance in Figure 7-4c also indicates the hydrogen uptake by the atomic

Ti is not stored in form of strong dissociative chemisorption. We also probed the relationships between the Ti content and hydrogen adsorption, shown Figure S7-9. It is found that hydrogen uptake of each Ti atom increases with the increase of hydrogen pressure, and up to two H₂ molecules can be adsorbed on each Ti atom, which is twice the amount of hydrogen absorbed by metal Ti. The maximum adsorption number (N_{\max}) of H atoms for each isolated Ti atoms can be described by the 18-electron rule, $N_{\max} = (18 - n_v - 5)$, where n_v is the number of valence electrons of the Ti atom, and five is the number of electrons contributed by the five coordination atoms nearest to Ti [15, 25, 26]. According to the DFT calculations^[27], the 5-coordinated Ti can adsorb four intact hydrogen molecules.

The hydrogen adsorption/desorption measurement is also repeated to evaluate the stability of the Ti₁@CB-170. As shown in Figure 7-4d, the Ti₁@CB-170 exhibits good cycling stability. After hydrogen adsorption/desorption test, the coordination environment of Ti atom in Ti₁@CB-170 is also characterized by the XAS. Figure S7-10 compared the XAS spectrum of the Ti₁@CB-170 before and after hydrogen adsorption/desorption cycling test, the results indicate that the coordination structure remains unchanged.

7.3 Conclusions

In summary, we applied a facile high-energy mechanochemical ball milling method fabricated solid-state hydrogen storage materials with atomic Ti sites. The HADDF-STEM images confirm the isolated Ti atoms confined into the CB matrix. Further XAS characterizations imply that the atomic Ti is coordinated with both O and N atoms. The hydrogen uptake tests suggest that the atomic Ti functions as the hydrogen adsorption site, which can remarkably enhance the hydrogen storage capacity. It is found that the interaction between hydrogen molecule and Ti atom is stronger than the physisorption, which enable the hydrogen adsorbed stably under near room temperature. This work

will pave a way toward the design and construction of solid-state materials with abundant hydrogen adsorption sites for hydrogen storage at ambient temperatures.

7.4 References

1. Gencer A, Aydin S, Surucu O, et al. Enhanced hydrogen storage of a functional material: Hf_2CF_2 MXene with Li decoration. *Appl. Surf. Sci.* 2021; 551: 149484.
2. Lin H-J, Li H-W, Shao H, et al. In situ measurement technologies on solid-state hydrogen storage materials: a review. *Materials Today Energy* 2020; 17: 100463.
3. Liu H, Lu C, Wang X, et al. Combinations of V_2C and Ti_3C_2 MXenes for Boosting the Hydrogen Storage Performances of MgH_2 . *ACS Appl. Mat. Interfaces* 2021; 13: 13235-13247.
4. Jain V and Kandasubramanian B. Functionalized graphene materials for hydrogen storage. *Journal of Materials Science* 2020; 55: 1865-1903.
5. Kumar P, Singh S, Hashmi S a R, et al. MXenes: Emerging 2D materials for hydrogen storage. *Nano Energy* 2021; 85: 105989.
6. Jia Y, Sun C, Shen S, et al. Combination of nanosizing and interfacial effect: Future perspective for designing Mg-based nanomaterials for hydrogen storage. *Renewable Sustainable Energy Rev.* 2015; 44: 289-303.
7. Rusman N a A and Dahari M. A review on the current progress of metal hydrides material for solid-state hydrogen storage applications. *Int. J. Hydrogen Energy* 2016; 41: 12108-12126.
8. Abd.Khalim Khafidz N Z, Yaakob Z, Lim K L, et al. The kinetics of lightweight solid-state hydrogen storage materials: A review. *Int. J. Hydrogen Energy* 2016; 41: 13131-13151.
9. Lang C, Jia Y and Yao X. Recent advances in liquid-phase chemical hydrogen storage. *Energy Storage Materials* 2020; 26: 290-312.
10. Shet S P, Shanmuga Priya S, Sudhakar K, et al. A review on current trends in potential use of metal-organic framework for hydrogen storage. *Int. J. Hydrogen*

- Energy 2021; 46: 11782-11803.
11. Weng Q, Zeng L, Chen Z, et al. Hydrogen Storage in Carbon and Oxygen Co-Doped Porous Boron Nitrides. *Adv. Funct. Mater.* 2021; 31: 2007381.
 12. He T, Cao H and Chen P. Complex Hydrides for Energy Storage, Conversion, and Utilization. *Adv. Mater.* 2019; 31: 1902757.
 13. Liu Y, Yang Y, Gao M, et al. Tailoring Thermodynamics and Kinetics for Hydrogen Storage in Complex Hydrides towards Applications. *The Chemical Record* 2016; 16: 189-204.
 14. Møller K T, Sheppard D, Ravnsbæk D B, et al. Complex Metal Hydrides for Hydrogen, Thermal and Electrochemical Energy Storage. *Energies* 2017; 10: 1645.
 15. Liu Y, Ren L, He Y, et al. Titanium-decorated graphene for high-capacity hydrogen storage studied by density functional simulations. *J. Phys.: Condens. Matter* 2010; 22: 445301.
 16. Liang S, Zhu C, Zhang N, et al. A Novel Single-Atom Electrocatalyst Ti₁/rGO for Efficient Cathodic Reduction in Hybrid Photovoltaics. *Adv. Mater.* 2020; 32: 2000478.
 17. Han Z, Zhao S, Xiao J, et al. Engineering d-p Orbital Hybridization in Single-Atom Metal-Embedded Three-Dimensional Electrodes for Li–S Batteries. *Adv. Mater.* 2021; 33: 2105947.
 18. Xing M, Zhang J and Chen F. New approaches to prepare nitrogen-doped TiO₂ photocatalysts and study on their photocatalytic activities in visible light. *Appl. Catal., B* 2009; 89: 563-569.
 19. Lu X, Xu K, Tao S, et al. Engineering the electronic structure of two-dimensional subnanopore nanosheets using molecular titanium-oxide incorporation for enhanced photocatalytic activity. *Chem Sci* 2016; 7: 1462-1467.
 20. Liu H, Zhang S, Chen Y, et al. Rational design of TiO₂@ nitrogen-doped carbon coaxial nanotubes as anode for advanced lithium ion batteries. *Appl. Surf. Sci.*

- 2018; 458: 1018-1025.
21. Deng D, Chen X, Yu L, et al. A single iron site confined in a graphene matrix for the catalytic oxidation of benzene at room temperature. *Science Advances* 2015; 1: e1500462.
 22. Liu L, Yang F, Ge L, et al. Facile and low-cost preparation of Co and N co-doped hierarchical porous carbon as a functional separator for Li-S batteries. *Electrochim. Acta* 2022; 401: 139380.
 23. Kiuchi H, Kondo T, Sakurai M, et al. Characterization of nitrogen species incorporated into graphite using low energy nitrogen ion sputtering. *PCCP* 2016; 18: 458-465.
 24. Farges F, Brown G E and Rehr J J. Ti $K\alpha$ -edge XANES studies of Ti coordination and disorder in oxide compounds: Comparison between theory and experiment. *Phys. Rev. B* 1997; 56: 1809-1819.
 25. Chung C, Ihm J and Lee H. Recent progress on Kubas-type hydrogen-storage nanomaterials: from theories to experiments. *Journal of the Korean Physical Society* 2015; 66: 1649-1655.
 26. Kiran B, Kandalam A K and Jena P. Hydrogen storage and the 18-electron rule. *The Journal of Chemical Physics* 2006; 124: 224703.
 27. Zhao Y, Kim Y-H, Dillon A C, et al. Hydrogen Storage in Novel Organometallic Buckyballs. *Phys. Rev. Lett.* 2005; 94: 155504.

7.5 Supporting Information

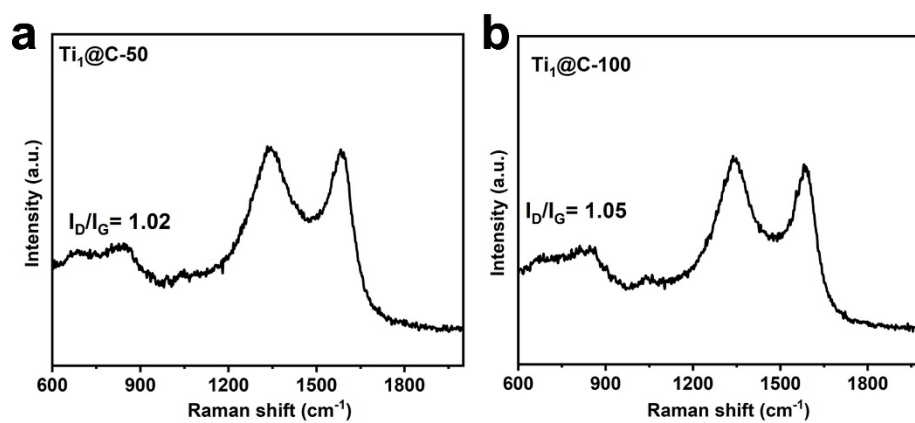


Figure S7-1. Raman spectra of $\text{Ti}_1\text{@CB-50}$ (a) and $\text{Ti}_1\text{@CB-100}$ (b), respectively.

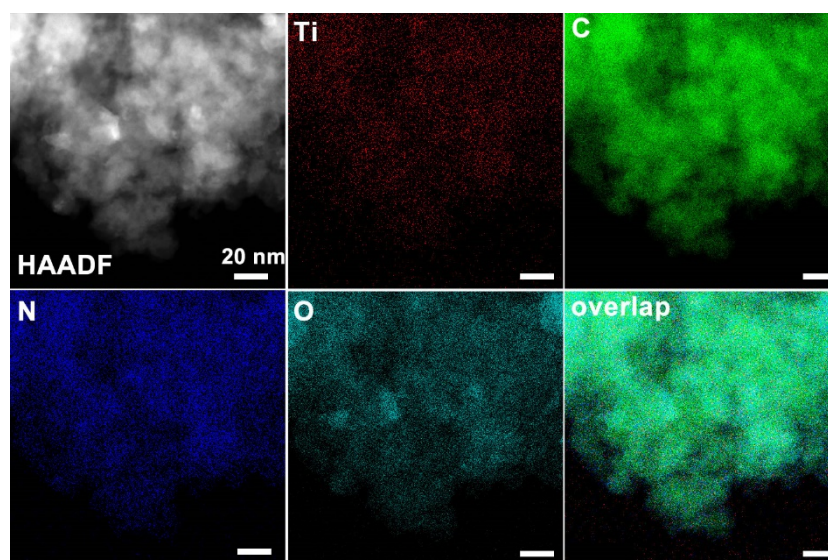


Figure S7-2. EDS mapping of $\text{Ti}_1\text{@CB-50}$.

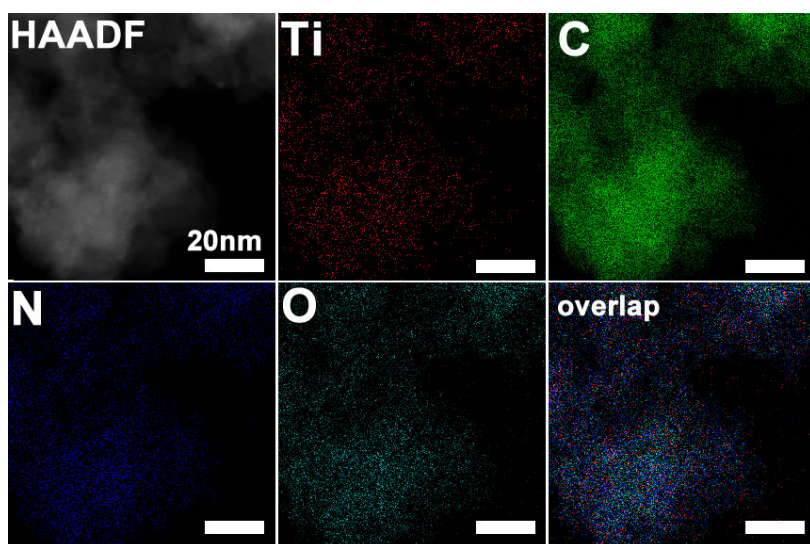


Figure S7-3. EDS mapping of $\text{Ti}_1\text{@CB-100}$.

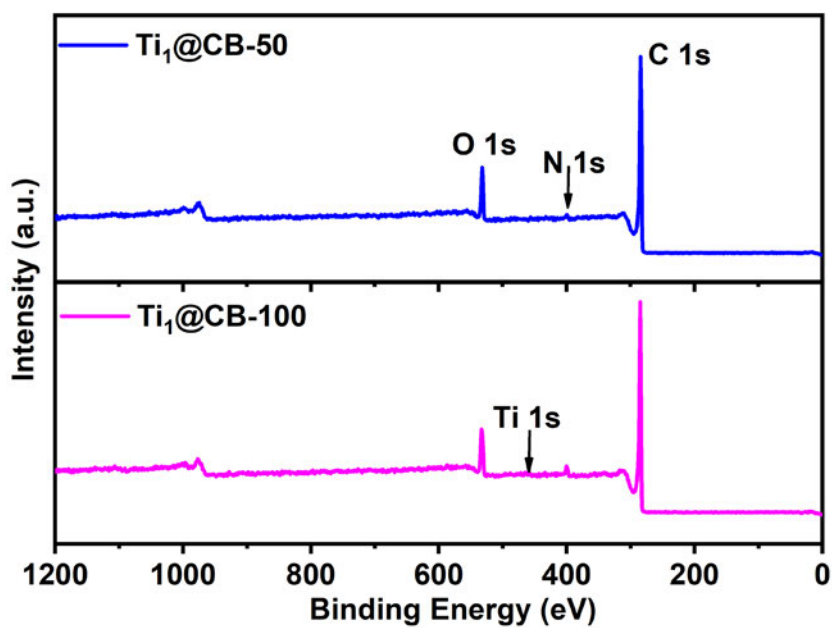


Figure S7-4. Survey scan XPS spectra for $\text{Ti}_1\text{@CB-50}$ and $\text{Ti}_1\text{@CB-100}$, respectively.

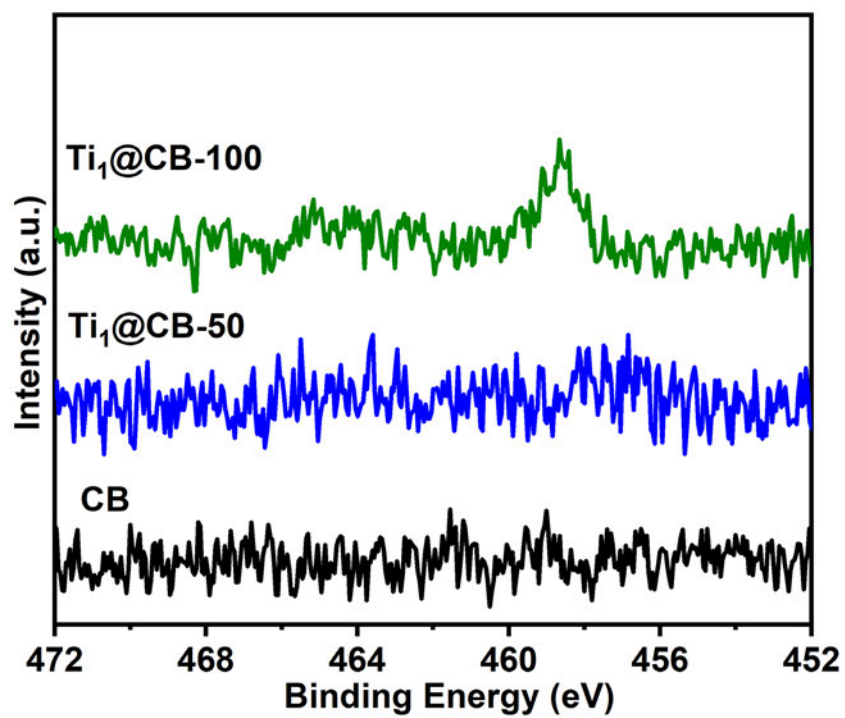


Figure S7-5. Ti 2p high-resolution XPS spectrum of CB, $\text{Ti}_1\text{@CB-50}$ and $\text{Ti}_1\text{@CB-100}$.

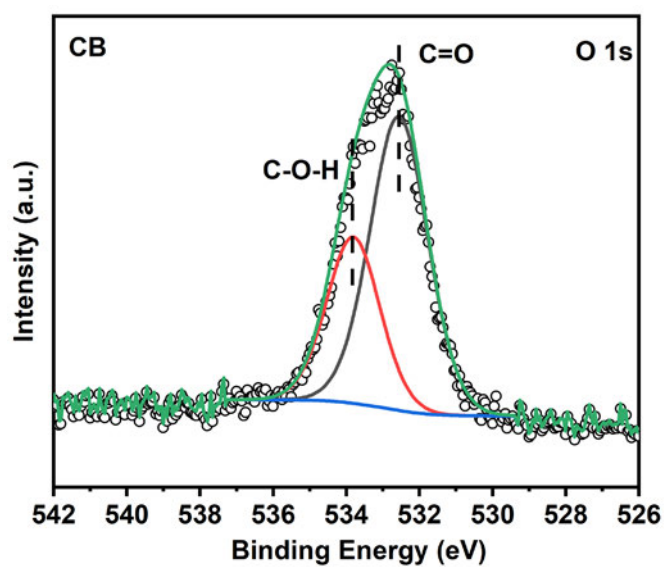


Figure S7-6. O 1s high-resolution XPS spectrum of CB.

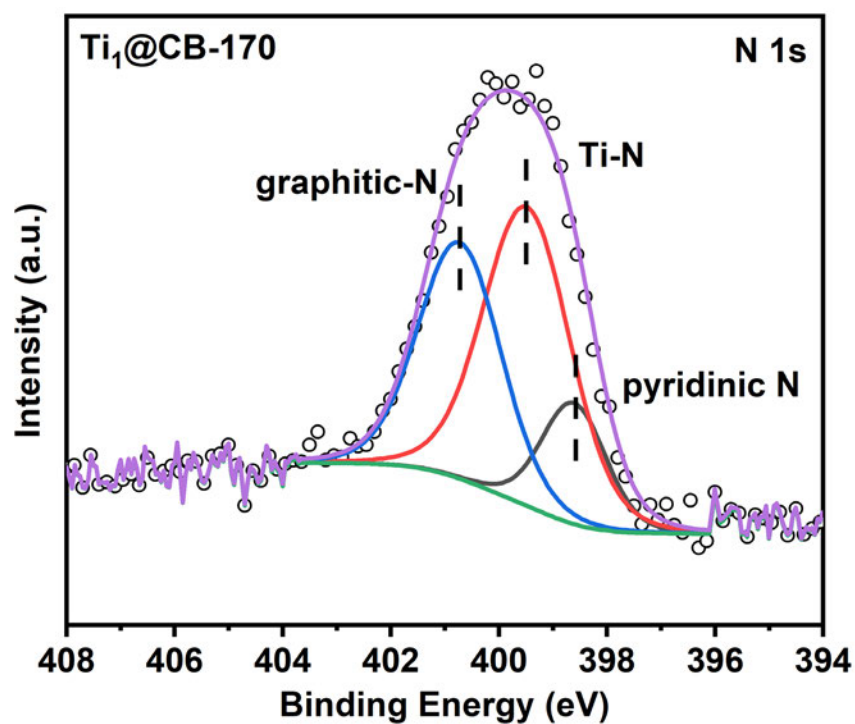


Figure S7-7. N 1s high-resolution XPS spectrum of $\text{Ti}_1\text{@CB-170}$.

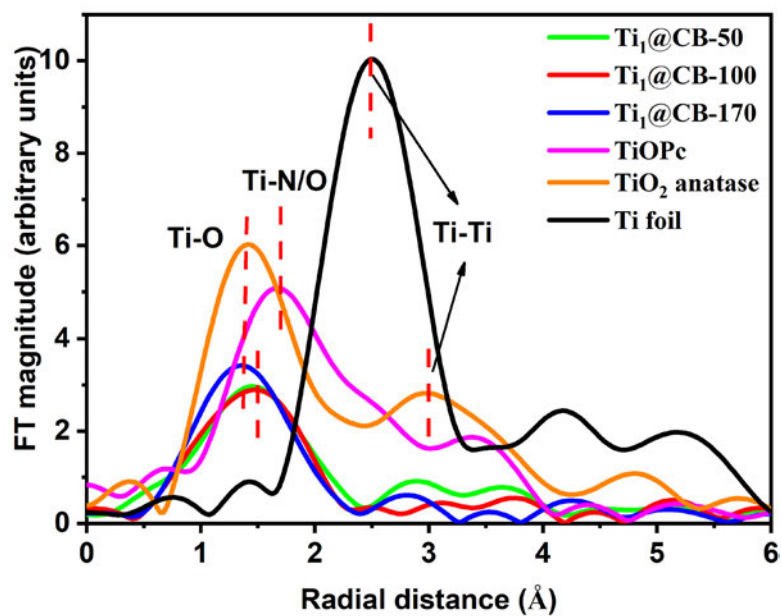


Figure S7-8. Fourier-transformed EXAFS spectra of $\text{Ti}_1\text{@CB}$ catalysts in comparison with TiOPc , Ti foil and TiO_2 .

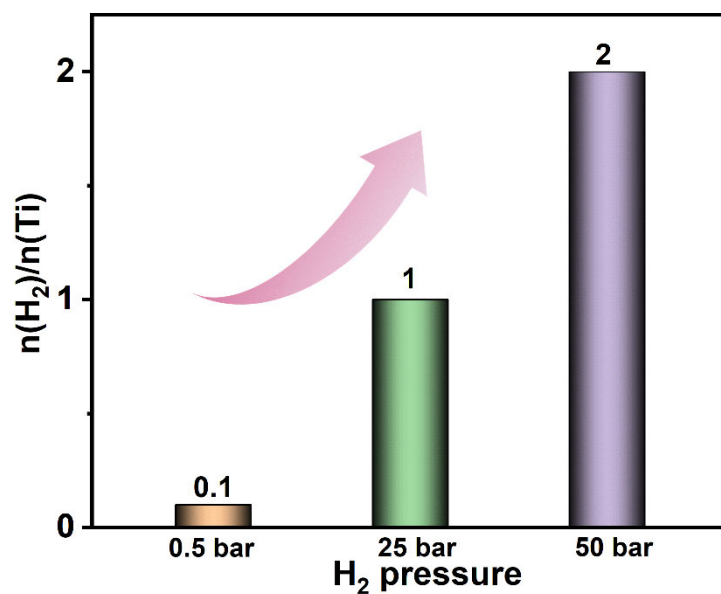


Figure S7-9. Hydrogen adsorption of single Ti atom under hydrogen pressure.

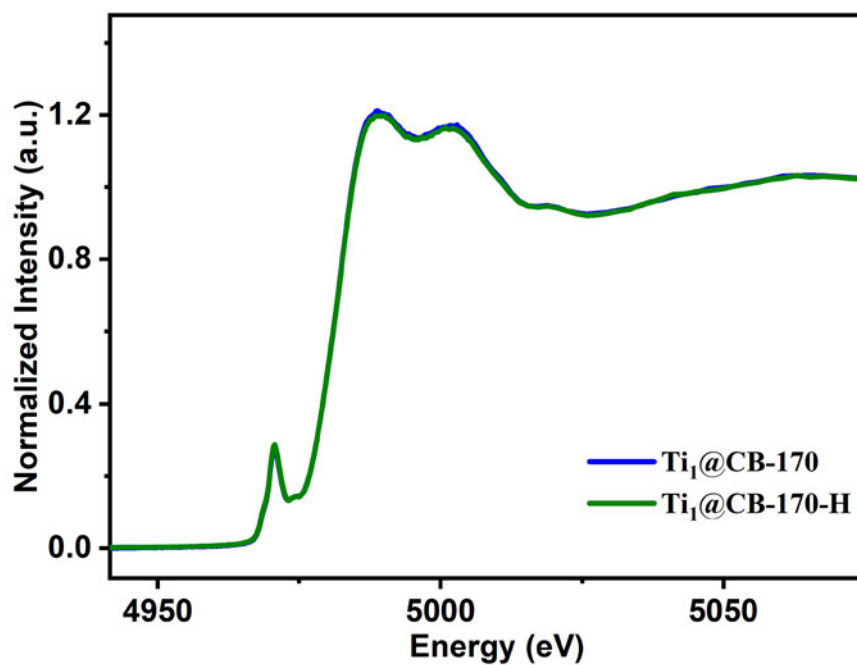


Figure S7-10. Ti K-edge X-ray absorption near-edge structure (XANES) spectra of Ti₁@CB-170 before and after H₂ cycling test.

Table S7-1. Elemental contents determined by ICP-AES for different samples.

Samples	Ti ₁ @CB-50	Ti ₁ @CB-100	Ti ₁ @CB -170
Wt. %	0.497	1.17	1.98

Table S7-2. BET surface area of CB and Ti₁@CB-x (x=50, 100 and 1700) samples.

Samples	CB	Ti ₁ @CB-50	Ti ₁ @CB-100	Ti ₁ @CB -170
BET surface area (m ² /g)	347.8	331.1	344.8	351.3

Chapter 8. Conclusions and Perspectives

8.1 Conclusions

In summary, this PhD project aims to design and fabricate efficient and inexpensive AMS nanomaterials that are expected to create new knowledge of atomic interface catalysis for hydrogen production and storage. From the studies presented in the thesis, conclusions can be summarized as follows.

Firstly, a facile high-energy mechanochemical ball milling strategy is developed for batch preparation of atomic Ru doped defective MoS₂ catalysts for hydrogen evolution. The introduction of atomic Ru atom will generate a S vacancy. Such coordination pattern could induce the asymmetrical transition of local electron structure, which could efficiently accelerate water dissociation. The synergetic effect between single-atom Ru sites and SVs demonstrates an excellent catalytic activity of the prepared catalyst. The synthesized Ru₁@D-MoS₂ only requires a low overpotential of 107 mV in alkaline electrolytes to deliver a current density of 10 mA cm⁻². This disadvantage is that the catalyst preparation still involves the use of noble metal Ru.

Secondly, to substitute the noble metal Ru, atomic Co is introduced to modify the commercial MoS₂ via a simple mechanochemical strategy. Through ball milling with CoO, the catalytic activity of the commercial bulk MoS₂ can be modulated via integrating the strain, heteroatom doping and particle sizes. The synthesized Co_{0.4}O@MoS₂-0.4 demonstrated the highest HER activity, with a low overpotential of 94 mV at 10 mA cm⁻² under strong alkaline conditions. Moreover, the decent catalytic stability under high-current density, low cost and excellent catalytic activity endow the catalyst promising to be used in industrialized sustainable hydrogen production.

Thirdly, combining the experimental studies and DFT calculations, we investigated the relationship between coordination number of Ti and hydrogen adsorption energy via a defect engineering method. By regulating the coordination of Ti atoms, the hydrogen storage fashion can be realized with the transformation from physical adsorption to chemical adsorption. The four-coordinated Ti atoms on the surface of TiO₂ possess moderate adsorption energy to hydrogen, which can store hydrogen in a molecular

chemisorption manner. Accordingly, the TiO₂-400 displays the highest hydrogen uptake of 10 cm³/g, which is about 5 times higher than that of the TiO₂-P.

Lastly, to increase the hydrogen adsorption sites, the atomic Ti doped carbon substrate was synthesized as solid-state hydrogen storage materials. Hydrogen uptake performance tests indicate that the atomic Ti site functions as the hydrogen adsorption site, which can remarkably enhance the hydrogen storage capacity. The interaction between hydrogen molecule and Ti atom is stronger than the physisorption, which enable the hydrogen adsorbed stable under near room temperature.

In this thesis, through designing and synthesizing AMS nanomaterials for the application of hydrogen production and storage, we gain deep understandings of the role of AMS in hydrogen production and storage, which will provide new approaches for designing excellent HER catalysts and solid hydrogen storage materials in the future.

8.2 Recommendations for Future Work

Despite several achievements have been made to AMS nanomaterials in this project, there remain several challenges need to be investigated and addressed, which deserve continuous research attention.

(1) Though various methods have been developed to synthesize AMS nanomaterials, the density of AMS is low, which greatly limits the efficiency of AMS nanomaterials. Therefore, it is desirable to develop new methods for the batch preparation of AMS nanomaterials with high density of AMS. In addition, the stability of the configuration of AMS during long-term operation under harsh reaction conditions cannot be ignored.

(2) The efficiency of AMS nanomaterials greatly depends on the coordination structure of atomic metal sites. Rationally designing and regulating the coordination structure is vital for a specific application. Currently, it is still an obstacle to precisely fabricate AMS nanomaterials with specific coordination structures. Therefore, new synthetic strategies should be developed to precisely control the configuration of AMS.

(3) Previous DFT calculations have indicated the great potential of AMS nanomaterials for hydrogen storage. The research work in this thesis is only a preliminary exploration. There are still many scientific problems to be solved and studied, such as the influence of metal species, coordination environment, and substrates on hydrogen storage. Furthermore, accurate theoretical calculations combined with matching adsorption models should be provided to explore the critical interactions. Meanwhile, advanced *in-situ* characterization tools (e.g., neutron diffraction, nuclear magnetic resonance (NMR) and *in-situ* XAS) should be applied for interpreting the hydrogen adsorption behaviors.